SCALE-UP OF EMULSIFICATION IN IN-LINE ROTOR–STATOR MIXERS

by

STEVEN HALL

A thesis submitted to the

University of Birmingham

for the degree of

DOCTOR OF ENGINEERING

Centre for Formulation Engineering
School of Chemical Engineering
College of Engineering and Physical Sciences
University of Birmingham
September 2012

ABSTRACT

The power draw and emulsification performance of in-line rotor-stator mixers were investigated experimentally and theoretically, to predict droplet size as a function of process and formulation variables and to establish scale-up rules. The effect of process conditions, three mixer scales and thirteen rotor-stator geometry configurations on emulsification performance were investigated. Emulsions of a wide range of silicone oil viscosities of varying phase volumes, dispersed in aqueous surfactant and non-surfactant solutions were studied.

For lab to factory scale in-line rotor-stator mixers, the most appropriate scaling parameter for mean drop size was tip speed at constant residence time for single and multiple passes. At a single scale, the stator open area was the rotor-stator geometry parameter which had the greatest effect on power draw and emulsification in turbulent flow. Mean drop size was a strong function of the rotor speed, dispersed phase viscosity, interfacial tension, and less dependent upon the mixer flow rate, continuous phase viscosity and dispersed phase volume fraction (for surfactant systems). Correlation of mean drop size with energy dissipation rate indicated that droplet break-up mainly depends on turbulent inertial stresses.

Energy dissipation rate profiles were calculated theoretically using numerical simulations to calculate power draw and to solve population balance model equations. This is the first study in open literature where power consumption and drop size distributions in three scales of in-line rotor-stator mixer are reported.

ACKNOWLEDGEMENTS

First of all, I would like to thank my supervisor, Professor Andrzej Pacek, for his invaluable comments, guidance and encouragement throughout this study. Likewise, I wish to thank Professor Adam Kowalski from Unilever R&D Port Sunlight, for his continued support and advice, and numerous suggestions which have improved this work. I owe a debt of gratitude to Dr Mike Cooke from The University of Manchester, for his tireless assistance, and for many insightful discussions.

I wish to thank Dr Magdalena Jasinska and Professor Jerzy Baldyga from Warsaw University of Technology for their expertise and direction in numerical simulations and modelling. I would also like to acknowledge the help of Mark Flanagan and Geraint Roberts (both Unilever R&D Port Sunlight), Dr Tom Rodgers (The University of Manchester), and Dr Adi Utomo, Dr Ourania Gouseti and David Ryan from the University of Birmingham.

I would like to express thanks to the workshop at CEAS at The University of Manchester, in particular Craig Shore, for modifying and maintaining the rig, and David Rothman of Silverson Machines Ltd. for kindly loaning equipment.

I would like to thank the EPSRC and Unilever for funding this project, the “Royal Commission for the Exhibition of 1851” for the award of an Industrial Fellowship (2009-2012), and Dr Richard Greenwood for managing this programme.

Finally, I would like to thank my family and friends for their support, encouragement and understanding during four challenging years of study.

TABLE OF CONTENTS

LIST OF FIGURES

LIST OF TABLES

NOMENCLATURE

Symbol	Description
A	Constant, -
A_c	Cross-sectional area of stator hole or opening, m^2
A_F	Fraction of outer stator open area, -
A_h	Area of stator holes/openings, m^2
A_s	Surface area of stator, m^2
a_i	Length-based breakage rate, s^{-1}
a_s	Specific surface area of the dispersion, m^2
B	Number of batch vessel turnovers, -
B_d	Birth rate of drops of size d, s^{-1}
b	Exponent, -
$b_i^{-(k)}$	Length-based fragmentation distribution function, m^k
$b(L\|L_i)$	Length-based daughter drop size distribution, m^{-1}
C	Fluid component passed through the mixer, -
C	Constant in Eq. (6.11), -
$C, C_1 \dots C_x$	Dimensionless empirical constants, -
C_g	Constant in multi-fractal turbulence breakage kernel, -
C_h	Homogenisation coefficient in Eq. (2.86), -
C_i	Fluid component passed through the mixer i times, -
C_P	Specific heat capacity at constant pressure, $J\ (kg \cdot K)^{-1}$
C_X	Constant in multi-fractal turbulence breakage kernel, -
$C_{\varepsilon 1}$	Constant in standard $k-\varepsilon$ turbulence model, -
$C_{\varepsilon 2}$	Constant in standard $k-\varepsilon$ turbulence model, -
C_μ	Constant in standard $k-\varepsilon$ turbulence model, -
c	Concentration, $g\ m^{-3}$
c_v	Coefficient of variance, -
D	Rotor diameter (outer rotor), m
D_{AB}	Diffusivity coefficient, $m^2\ s^{-1}$
D_d	Birth rate of drops of size d, s^{-1}
$D_{r,i}$	Inner rotor diameter, m
$D_{r,o}$	Outer rotor diameter, m

$D_{s,i}$	Inner stator diameter, m
$D_{s,o}$	Outer stator diameter, m
D_{T}	Turbulent diffusivity of drops, $m^2\ s^{-1}$
d	Tooth diameter in Eq. (2.27), m
d	Droplet diameter, m
$d_{0,1}$	Diameter below which 10% of the sample population reside, m
$d_{0,5}$	Number median diameter, m
$d_{0,9}$	Diameter below which 90% of the sample population reside, m
d_{10}	Number mean diameter, m
d_{32}	Volume surface mean diameter (Sauter mean drop diameter), m
d_{43}	Moment volume mean diameter, m
d_c	Distance between stator hole centres, m
d_e	Distance between stator hole edges, m
d_h	Stator hole diameter, m
$d_h{}'$	Effective stator hole diameter, m
d_i	Drop size after i passes through the mixer, m
d_i, d_j, d_k	Diameter of drops in class size i, j, k, m
d_{max}	Maximum stable drop diameter, m
d_{min}	Minimum stable drop diameter, m
$\bar{d}$	Mean droplet diameter, m
$\bar{d}_g$	Geometric mean diameter, m
Δd_i	Bin width for class size i, m
E	Spectral energy density function, $m^3\ s^{-2}$
E_0	Gibbs elasticity, $N\ m^{-1}$
E_{sd}	Surface dilational modulus, $N\ m^{-1}$
E_V	Energy density, $J\ m^{-3}$
F	Power factor, -
F'_N	Discrete number cumulative distribution, -
F'_V	Discrete volume cumulative distribution, -
F_N	Continuous number cumulative distribution, -
F_V	Continuous volume cumulative distribution, -
f'_N	Number frequency of the ith interval, -
f'_V	Volume frequency of the ith interval, -
f_N	Continuous number frequency distribution, -
f_V	Continuous volume frequency distribution, -

G_V	Growth rate, $m^3\ s^{-1}$
g	Acceleration due to gravity, $m^2\ s^{-1}$
$g(d)$, $g(v)$	Breakage rate of drops of size d and v, s^{-1}
H	Velocity head, $m\ s^{-1}$
H_f	Distance between teeth centre in Eq. (2.27), m
HI	Homogenisation index, -
h	Height of the fluid level, m
h	Number of rotor-stator units/pairs in Eqs. (2.29) and (2.30), -
h_r	Rotor height, m
h_s	Stator height, m
I	Current, A
I	Drop size index, -
i	Number of passes, -
K_1, K_2	Constants in breakage kernel in Eq. (2.111), -
K_s	Metzner-Otto constant, -
k	Wavenumber, m^{-1}
k	Constant, $(Pa{\cdot}s)^n$
k	Turbulent kinetic energy per unit mass, $m^2\ s^{-2}$
k_0	'Laminar flow' power constant, -
k_1	'Flow' power constant, -
k_B	Boltzmann constant, $J\ K^{-1}$
k_{max}	Maximum turbulent kinetic energy per unit mass, $m^2\ s^{-2}$
L	Integral scale of turbulence (size of large eddies), m
L	Diameter of annular mixing space in Eq. (2.29), m
L	Particle size in QMOM models, m
L_i	Abscissa of quadrature approximation, m
l	Free radial distance in Eq. (2.30), m
M	Mass flow rate, $kg\ s^{-1}$
m_k	Moment of the distribution of the order k = 0,1,2,3
N	Rotor speed, s^{-1}
N	Order of quadrature approximation, -
N_b	Number of drops breaking, -
N_s	Number of samples, -
N_T	Total number of drops, -
n	Power law index, -

$n(v,t)$	Number of drops of size v per unit volume at time t, -
n_b	Number of rotor blades, -
n_h	Number of stator holes, -
n_{hr}	Number of stator holes per row, -
n_i	Number of drops in class size i, -
n_r	Number of stator rows, -
n_{ri}	Refractive index, -
P	Power, W
$P_{Bearings}$	Power due to the bearings, W
P_{Energy}	Power from energy balance, W
P_F	'Flow rate' power term, W
P_F	Ratio of outer stator perimeter of holes to area of the stator, m^{-1}
P_{Flow}	Power due to the fluid flow, W
P_{Fluid}	Power due to the fluid motion, W
P_{Heat}	Power by calorimetry, W
P_h	Perimeter of stator openings, m
P_L	'Losses' power term, W
P_{Motor}	Power due to the motor, W
P_{max}	Maximum power draw, W
P_P	Pumping power, W
P_T	'Torque on rotor shaft' power term, W
P_{Torque}	Power by torque, W
P_{Total}	Total power drawn, W
P_w	Wetted perimeter of stator opening, m
$P_N(d)$	Number probability density function, -
$P_V(d)$	Volume probability density function, -
p	Pressure, Pa
Δp	Pressure difference across the mixing head, Pa
Po_I	'Power number' power constant for in-line mixers in Eq. (2.17), -
Po_{Q_L}	'Local flow rate' power number, -
Po_U	'Unrestricted flow' power constant, -
Po_Z	'Zero flow' power constant, -
Q	Volumetric flow rate (impeller pumping capacity), $m^3 s^{-1}$
Q_{in}	Inlet flow rate, $m^3 s^{-1}$
Q_{is}	Inward flow rate through inner stator, $m^3 s^{-1}$

Q_L	Local volumetric flow rate, $m^3 s^{-1}$
Q_{max}	Maximum volumetric flow rate, $m^3 s^{-1}$
Q_{os}	Outward flow rate through outer stator, $m^3 s^{-1}$
Q_{out}	Outlet flow rate, $m^3 s^{-1}$
q	Height of mixer pin in Eq. (2.29), axial width of the pins in Eq. (2.30), m
R	Residuals, -
R_h	Hydraulic radius of the stator opening, m
R^2	Coefficient of determination, -
r_c	Radius of cylinder into which drop is deformed, m
r_s	Radius of syringe, m
S	Number of stages in Eq. (2.27), -
S_{ij}	Mean strain rate, s^{-1}
S_{max}	Maximum strain rate, s^{-1}
s	Skewness for a log-normal distribution, -
T	Torque, N m
T_B	Torque measured for friction in the bearings, N m
$T_{B,Z}$	'Running zero' torque measured for friction in the bearings, N m
T_Z	'Running zero' torque, N m
t	Time, s
t_b	Droplet breakage time, s
t_D	Diffusion adsorption time scale, s
t_{def}	Droplet deformation time scale, s
t_m	Mixing time, s
t_R	Total residence time in the mixing head, s
t_s	Stator thickness, m
U	Fluid velocity, $m s^{-1}$
U_h	Fluid velocity in the stator holes, $m s^{-1}$
U_i,U_j	Fluid velocity in i, j, direction, $m s^{-1}$
U_K	Kolmogorov velocity scale, $m s^{-1}$
U_{max}	Maximum fluid velocity, $m s^{-1}$
U_T	Tip speed, $m s^{-1}$
$\langle U_{id} \rangle$	Reynolds averaged ith component of the dispersed phase velocity, $m s^{-1}$
V	Voltage, V
V_d	Droplet volume, m^3
V_H	Volume of mixing head (Swept outer rotor volume), m^3

V_h	Homogenisation volume, m^3
V_T	Volume of mixing tank, m^3
v	Volume of daughter drops, m^3
v'	Volume of parent drops, m^3
v_F	Volume fraction, -
W	Rotor blade width, m
w	Span for a log-normal distribution, -
w_i	Weight of quadrature approximation, m^{-3}
x	Exponent, -
x_B	Rotor blade thickness in Eq. (2.28), m
x_i,x_j	Cartesian coordinates, -
y	Exponent, -
Z	Number of teeth in Eq. (2.27) , -
z	Distance between two rotor pins in Eqs. (2.29) and (2.30), m

Greek symbols

$\propto$	Relative rate of surface/interface extension, -
$\propto$	Multi-fractal scaling exponent, -
$\propto_{min}$	Constant in multi-fractal turbulence breakage kernel, -
β	Constant, -
$\beta(v\|v')$	Probability density function for daughter drop size distribution, -
Γ	Surface excess concentration, g m^{-2}
$\dot{\gamma}$	Shear rate, s^{-1}
$\dot{\gamma}_{max}$	Maximum shear rate, s^{-1}
δ	Rotor-stator gap width, m
ε	Mean energy dissipation rate per unit mass of fluid, W kg^{-1}
ε_F	'Flow rate' energy dissipation rate per unit mass of fluid, W kg^{-1}
ε_{max}	Maximum energy dissipation rate per unit mass of fluid, W kg^{-1}
ε_T	'Torque on rotor shaft' energy dissipation rate per unit mass of fluid, W kg^{-1}
ε_t	Total energy dissipation rate per unit mass of fluid in Eq. (2.86), W kg^{-1}
η	Pumping efficiency, -
η_K	Kolmogorov length scale of turbulence, m
θ	Temperature, K
θ_b	Temperature due to bearing friction, K
θ_c	Temperature correction between the temperature probes, K

θ_i	Inlet temperature, K
θ_o	Outlet temperature, K
$\Delta\theta$	Temperature difference across the mixing head, K
μ	Fluid viscosity, Pa·s
μ_A	Apparent viscosity of the continuous phase, Pa·s
μ_c	Continuous phase viscosity, Pa·s
μ_d	Dispersed phase viscosity, Pa·s
μ_d^{eff}	Effective dispersed phase viscosity, Pa·s
ν	Kinematic fluid viscosity, $m^2\ s^{-1}$
$\nu(v')$	Number of daughter drops formed by breakage of a drop of size v', -
ν_c	Kinematic viscosity of the continuous phase, $m^2\ s^{-1}$
ν_t	Turbulent kinematic viscosity, $m^2\ s^{-1}$
ρ	Fluid density, kg m^{-3}
ρ_c	Continuous phase density, kg m^{-3}
ρ_d	Dispersed phase density, kg m^{-3}
σ	Surface/interfacial tension, N m^{-1}
σ_{eff}	Effective interfacial tension, N m^{-1}
σ_g	Geometric standard deviation, -
σ_k	Constant in standard $k-\varepsilon$ turbulence model, -
σ_{rms}	Root mean squared difference, -
σ_s	Standard deviation, m
σ_ε	Constant in standard $k-\varepsilon$ turbulence model, -
τ	Residence time, s
τ_c	Cohesive stresses resisting droplet deformation, kg $m^{-1}\ s^{-2}$
τ_d	Disruptive stresses acting on the droplet, kg $m^{-1}\ s^{-2}$
τ_{IR}	Internal recirculation residence time, s
$\tau_{IR,max}$	Maximum internal recirculation residence time in the mixing head, s
$\tau_{IR,min}$	Minimum internal recirculation residence time in the mixing head, s
τ_K	Kolmogorov time scale, s
τ_s	Cohesive surface tension stresses, kg $m^{-1}\ s^{-2}$
τ_v	Cohesive viscous stresses, kg $m^{-1}\ s^{-2}$
Φ	Dispersed phase volume fraction, -
ϕ_F	Correction factor in Eq. (3.15), -

Dimensionless groups

Ca_{cr}	Critical capillary number, $\dot{\gamma}\,\mu_c d_{max}/\sigma$
Fr	Froude number, N^2D/g
N_c	Circulation number, $\mathrm{Q}t_m/V_T$
N_Q	Flow number, Q/ND^3
Po or N_P	Power number, $P/\rho N^3 D^5$
Re	Reynolds number, $\rho ND^2/\mu$
Re_h	Reynolds number in the stator holes, $\rho U_h d_h/\mu$
Re_{pl}	'Power law' Reynolds number, $\rho N^{2-n}D^2/k$
Re_δ	'Rotor-stator gap' Reynolds number, $\rho(\pi ND)\delta/\mu$
Vi	Viscosity group, $(\rho_c/\rho_d)^{1/2}\,\mu_d ND/\sigma$
We	Weber number, $\rho_c N^2 D^3/\sigma$
We_{eff}	Effective Weber number, $\rho_c N^2 D^3/\sigma_{eff}$
μ^*	Viscosity ratio, μ_d/μ_c

CHAPTER 1. INTRODUCTION

1.1 Background

Rotor-stator mixers can be broadly classified as energy intensive mixing devices, widely used in a variety of industrial processes. These devices are also known as 'high shear mixers', and the key benefit of these mixers is their ability to focus high levels of energy dissipation rate and shear rate on a relatively small volume of fluid, since kinetic energy generated by the rotor is dissipated in the small stator volume (Utomo et al., 2009).

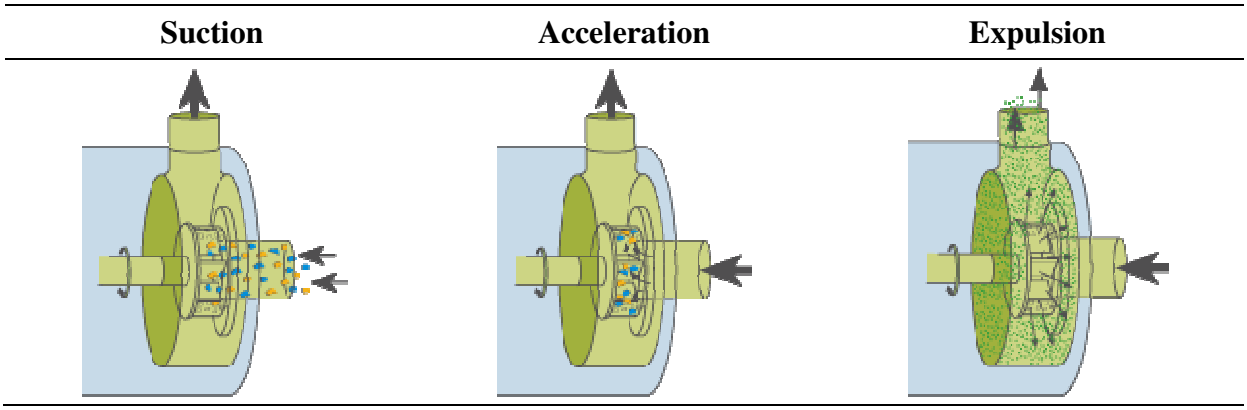

Figure 1.1: In-line rotor-stator mixer operation (from Silverson, 2012).

These mixers consist of a rotor-stator assembly, known as the mixing head, comprised of a rotor that rotates at very high velocities within a stationary stator, where the rotor is in close proximity to the stator. These mixers suck fluid into the mixing head, accelerate it in the rotor-stator gap, and expel it through the stator openings in high velocity jets (Figure 1.1). Rotor tip speeds are typically an order of magnitude greater than in stirred tanks at 10-50 m s^{-1} (Atiemo-Obeng and Calabrese, 2004), with energy dissipation rates up to three orders of

magnitude greater. Rotor-stator gap clearances are as small as 100 μm (Karbstein and Schubert, 1995), with residence times of milliseconds to seconds (Myers et al., 1999).

Typically, high shear mixers are relatively inexpensive, versatile and robust in factory environments. Furthermore, these mixers can combine multiple process stages into a single unit operation, leading to increased process intensification, and they can significantly reduce processing times hence they are often more efficient than other mixing devices.

1.2 Design

There are many different designs of high shear mixer available from a variety of manufacturers, which are broadly classified according to their flow pattern as colloid mills, axial discharge, radial discharge and toothed devices (Atiemo-Obeng and Calabrese, 2004).

1.2.1 Colloid mills

Colloid mills are characterised by a very narrow shear gap, and a cone-shaped rotor and stator (Figure 1.2a), with smooth surfaces to promote laminar flow and grooved surfaces to promote turbulent flow (Karbstein and Schubert, 1995). A variable gap width ensures velocity gradients in the direction of flow to create elongational stresses essential for breakage of very viscous drops (Utomo, 2009), but due to their low pumping capability, they are often used with external pumps in continuous processes.

(a) In-line colloid mill	(b) In-line radial discharge mixer
	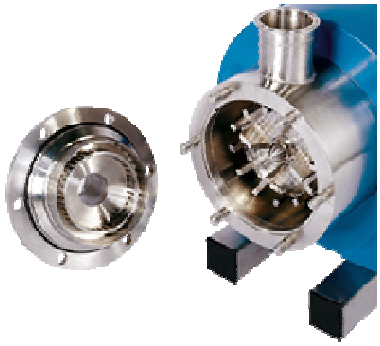

Figure 1.2: Rotor-stator mixer designs (from Klausen Trading Company, 2012; Silverson, 2012).

1.2.1 Radial discharge mixers

Radial discharge mixers (Figure 1.2b) pump fluid radially through a stationary stator containing holes or slots. These mixers have a good pumping capacity, are flexible to manufacture different products (Deutsch, 1998), and are robust and reliable in factory environments (Rothman, 2011). Batch and in-line mixers are offered at lab and industrial scales, with mixers available for specific applications, such as hygienic design or powder processing.

1.2.1.1 Silverson rotor-stator mixers

Silverson Machines Ltd. specialise in the manufacture of batch or in-line radial discharge rotor-stator mixers (Silverson, 2012).

Batch mixers include the laboratory scale L4R (Figure 1.3a), which may be fitted with tubular mixing units to mix small volumes (up to 0.5 L), or with an in-line work head capable of pumping 20 L min^{-1} (Silverson, 2012). Factory mixers can process up to 30,000 L, and are available as bottom entry mixers designed to process highly viscous materials and powders, and batch/in-line mixing rigs to disintegrate/disperse solids (Figure 1.3d).

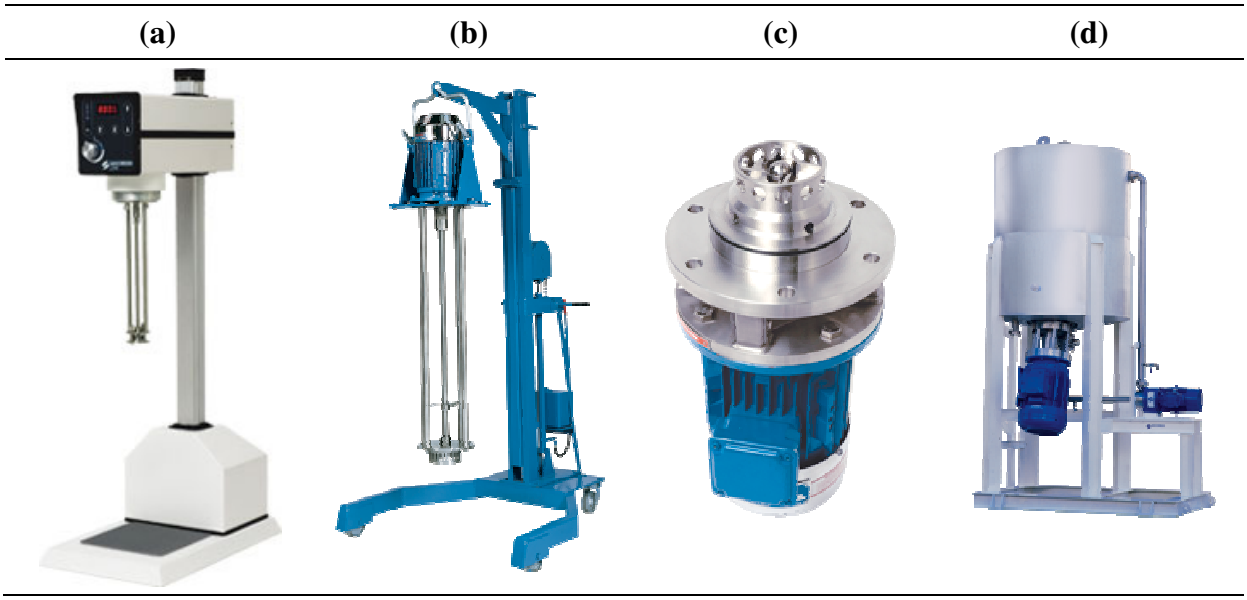

Figure 1.3: Silverson batch mixers: (a) Laboratory mixer; (b) Factory mixer; (c) Bottom entry mixer; (d) Batch/in-line mixers (from Silverson, 2012).

In-line mixers are offered from the laboratory scale, which can self-pump 1,500 L h^{-1}, to the factory scale which can process 20,000 L h^{-1} (Figure 1.4). In-line mixers for specific applications include ultra-hygienic mixers to comply with hygienic manufacturing regulations, and mixers which incorporate a hopper to feed powder or liquid into the inlet pipeline or the mixing head for rapid dispersion (Silverson, 2012).

Both batch and in-line Silverson mixers are fitted with interchangeable heads to enable different stator designs to be integrated for different process requirements (Figure 1.5). In-line mixers are also available with single and multiple stage rotor-stator configurations.

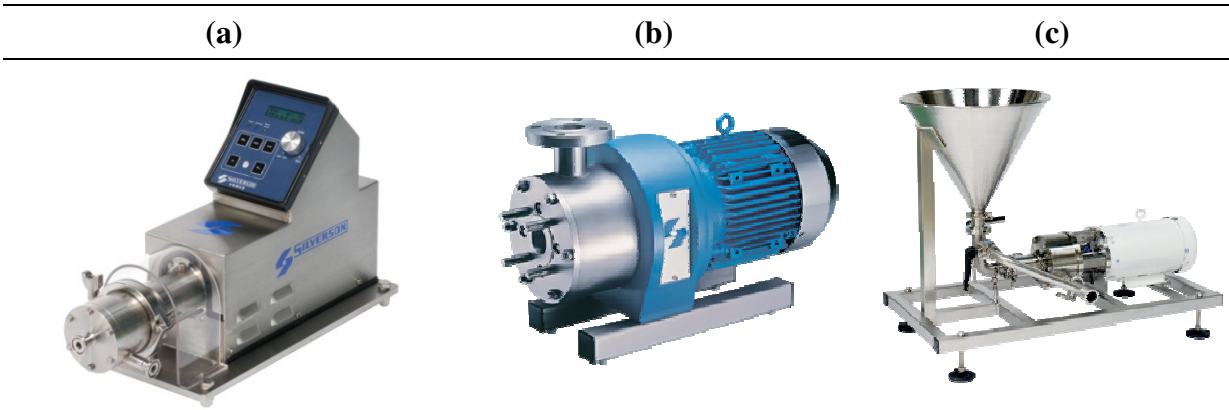

Figure 1.4: Silverson in-line mixers: (a) Laboratory mixer; (b) Factory mixer; (c) Flashmix mixer (from Silverson, 2012).

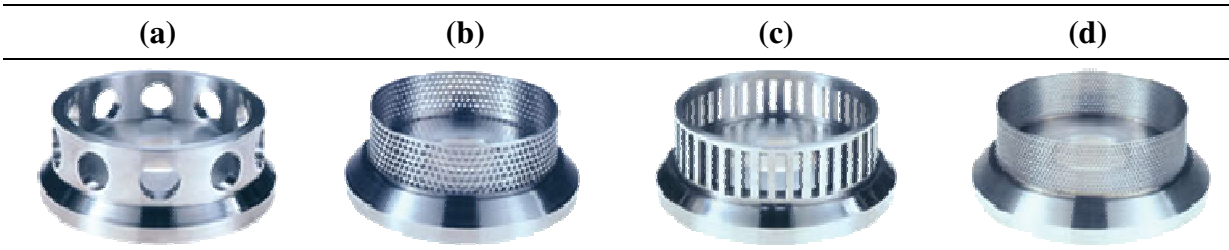

Figure 1.5: Stators for Silverson in-line mixers: (a) General Purpose Disintegrating Head; (b) Square Hole High Shear Screen; (c) Slotted Disintegrating Head; (d) Emulsor Screens (from Silverson, 2012).

1.2.2 Axial discharge mixers

Axial discharge mixers such as the in-line Chemineer Greerco mixer have two rotors and two stators which discharge flow axially through apertures and create shear flow (Figure 1.6). These mixers have an adjustable rotor-stator gap by changing the washers or bushings (Atiemo-Obeng and Calabrese, 2004), and can process high throughputs.

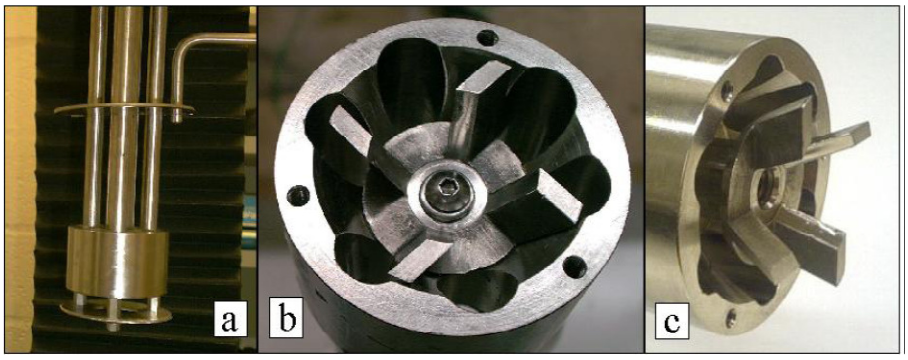

Figure 1.6: In-line Chemineer Greerco axial discharge mixer (from Padron, 2001).

1.2.3 Toothed devices

Toothed devices have a more complex design with slots or teeth incorporated into both the rotor and stator to provide multiple channels for fluid flow (Atiemo-Obeng and Calabrese, 2004). The toothed design is available from manufacturers including IKA, with multiple sets of rotors and stators (Figure 1.7).

Single stage mixing head	**Multi-stage rotors and stators**
	

Figure 1.7: Toothed mixers (from IKA, 2012).

1.3 Operation

Rotor-stator mixers are either batch or in-line devices. Batch mixers are commonly used to process smaller fluid volumes and are often used in industries to enable process

equipment to be multipurpose and provide flexibility for new products (Baker, 1993). However, as the rotors are relatively small and shrouded by the stator, batch mixers have poor bulk circulation resulting in reduced distributive mixing (Atiemo-Obeng and Calabrese, 2004), which is particularly an issue in large vessels. In addition, when vessel size increases, a point is reached where it is more efficient to use an in-line mixer rather than a batch mixer with a large rotor, since power consumption increases sharply with rotor diameter (to the fifth power), and an excessively large motor is required at large scales (Rothman, 2011).

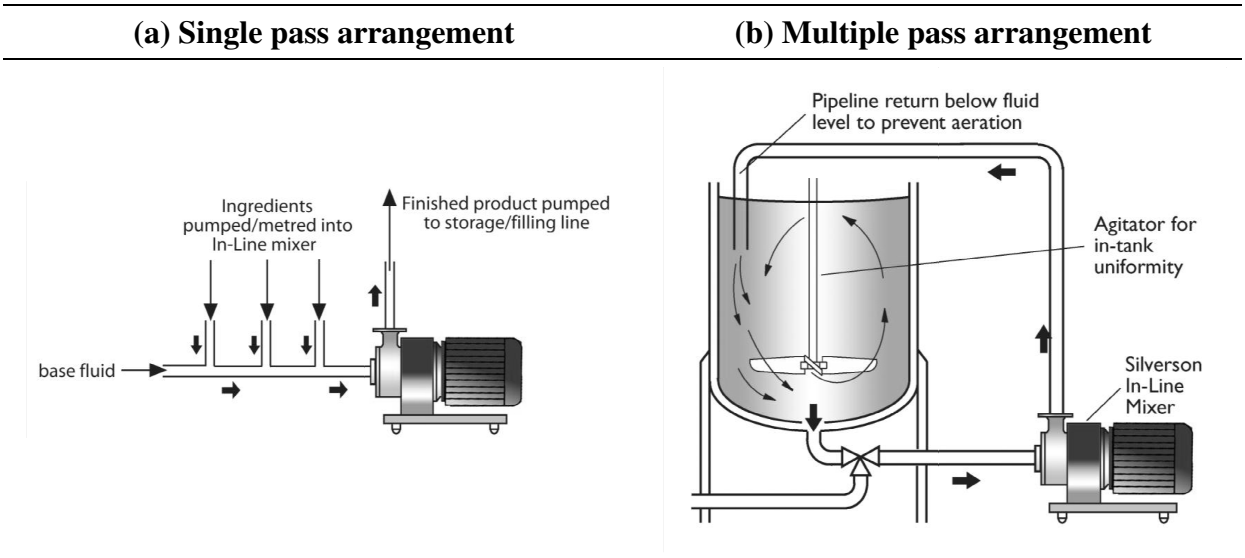

Figure 1.8: In-line rotor-stator mixer operating modes (Rothman, 2009).

Problems associated with batch rotor-stator mixers can be avoided by installing the mixer into a recycle loop around a mixing vessel and employing an in-line rotor-stator mixer, to separate distributive mixing (blending) in the stirred vessel and dispersive mixing (droplet break-up) by the rotor-stator mixer (Baker, 1993), to enable efficient mixing of more demanding highly viscous and non-Newtonian fluids (Kowalski, 2009).

In-line mixers may also be incorporated into a continuous process line and operated in a single pass mode (Figure 1.8a). Typically industry is moving towards single pass systems as

they are more energy efficient and reduce manufacturing timescales. The main disadvantage of this configuration is product quality is only controlled by rotor speed and flow rate, whereas in multiple pass systems, the number of passes is an additional parameter available to control the microstructure.

For single and multiple passes, the dispersed phase can either be injected into the pipeline upstream of the mixing head (Figure 1.9a), or directly into the mixing head (Figure 1.9b). These operating methods can more effectively disperse solids/liquids and they increase the flexibility of rotor-stator mixers.

(a) Material addition upstream of the mixing head	**(b) Material addition by injection into the mixing head**
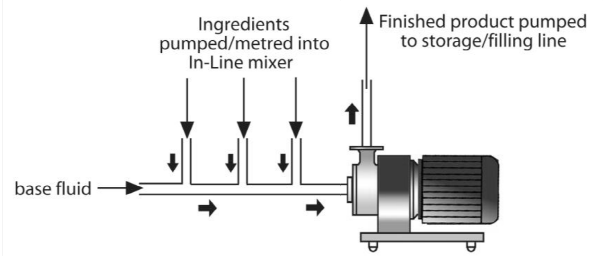	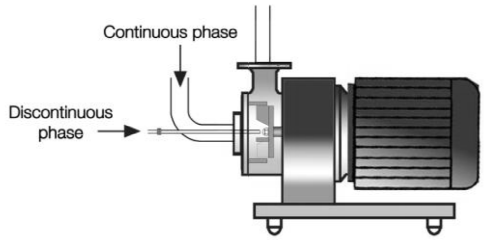

Figure 1.9: Material addition methods into in-line rotor-stator mixers (Rothman, 2009).

1.4 Applications

Rotor-stator devices have numerous applications in energy intensive industrial processes including processing of multiphase products (Utomo et al., 2009). High shear mixers are used to disperse liquids-in-liquids (Schubert and Engel, 2004), to de-agglomerate and uniformly disperse solids including nano-particles in liquids (Pacek et al., 2007), to suspend fine air bubbles in liquids (Muller-Fischer et al., 2007), as well as milling, coagulation, cell disruption, chemical reaction and blending (Atiemo-Obeng and Calabrese, 2004).

Industries employing rotor-stator mixers include fine chemicals, foods, cosmetics, pharmaceuticals, and personal care, to produce various products such as shampoos, deodorants, salad dressings, bitumen, latexes, adhesives and pesticides. One of the most common applications of rotor-stator mixers is in emulsification and some specific applications are summarised in Table 1.1.

Table 1.1: Examples of rotor-stator mixer emulsification applications.

Application	**Description**
Foods	Adler-Nissen et al. (2004) used a lab scale rotor-stator to produce high phase volume (80 wt.%) emulsions, similar to mayonnaise, of canola vegetable oil dispersed in an aqueous phase containing egg yolk emulsifier. Tip speed was varied from 1.3 to 9.4 m s^{-1}, to investigate the effect of shear stress on droplet size distributions of oil-in-water emulsions.
Pharmaceuticals	Maa and Hsu (1996) utilised a rotor-stator device to manufacture the primary emulsion in the double emulsion microencapsulation process used for pharmaceutical and food applications. A Virtishear homogeniser (Virtis, Templest IQ) flow-through rotor-stator emulsified an oil phase of PMMA (poly(methyl methacrylate))/$MeCl_2$ solution injected into an aqueous BSA (bovine serum albumin) solution.
Cosmetics	Masmoudi et al. (2005) used a rotor-stator mixer in the preparation of five pharmaceutical and cosmetic oil-in-water emulsions, representing creams. The oil phase of 20% v/v oil and 5% w/v emulsifier, was added to the aqueous phase at 75°C using a Polytron rotor-stator mixer.
Personal Care	Yuan et al. (2009) used a Polytron PT2100 homogeniser (Kinematica AG) to prepare a model fragrance encapsulated by polymerised monomers dissolved in fragrance. A fragrance/monomer solution phase, comprised of 80 wt.% fragrance oil, was dispersed in an aqueous solution containing 2 wt.% of one of eight non-ionic surfactants.
Fine Chemicals	Fradette et al. (2007) mixed an aqueous phase containing three non-ionic surfactants in standard low-sulphur diesel oil, to form a water-in-diesel emulsion identical to a commercial European diesel formulation called Aquazole™. An Ultra-Turrax T25 rotor-stator (IKA) up to 24,000 rpm was used.

1.5 Context, aims and objectives

Despite the extensive application of rotor-stator devices, little emphasis has been placed on understanding the underlying processing principles, and the current knowledge in 2004 was summarised:

"The current understanding of rotor-stator devices has almost no fundamental basis. There are few theories by which to predict, or systematic experimental protocols by which to assess, the performance of these mixers. In fact, there are very few archival publications on rotor-stator processing" (Atiemo-Obeng and Calabrese, 2004).

Traditionally, scale-up, process development and mixer operation was based on experience, manufacturer's advice, or trial and error, rather than on a scientific and engineering understanding of the process (Atiemo-Obeng and Calabrese, 2004). This approach results in higher development costs, start-up problems, lost time to market and considerable material wastage due to the numerous trials required from laboratory scale to the factory scale (Calabrese et al., 2000).

Moreover, understanding of in-line rotor-stator devices is further limited because the majority of in-line mixers are pilot plant and factory scale machines, so there has been a lack of mixers available for research, combined with the high cost and inherent difficulties of undertaking continuous large scale experiments.

The overall aim of this study is to investigate the application of in-line Silverson rotor-stator mixers in the emulsification process. The goal is to further the understanding of droplet break-up and develop mechanistic models to predict, design and assess the performance of in-line Silverson mixers to manufacture emulsion-based products. The aims are to:

- Characterise power draw as a function of the rotor-stator design, scale and operating/flow conditions, to acquire power draw constants to enable prediction of the energy inputted into the fluid.
- Assess the emulsification performance and develop models enabling the prediction of emulsion droplet size as a function of processing and formulation variables.
- Establish the most appropriate scaling up rules for these devices.
- Identify the influence of the rotor and stator geometry on emulsion droplet size and determine the emulsification efficiency for different rotor-stator configurations.
- Apply numerical simulations to calculate flow fields inside the mixing head and solve population balance equations to predict emulsion droplet size.

1.6 Business case

Within the sponsor company, Unilever, rotor-stator mixers are central to emulsion manufacturing since they are ubiquitous in many processes, and are the only equipment available to create some products. Hence, the company wishes to understand these devices further, and attempt to standardise manufacture using in-line Silverson rotor-stator mixers by improving the scale-up of products from the laboratory to the factory in the fastest, most efficient and cost-effective method.

The basis of this research was experimental using generic emulsion-based formulations, with a degree of computational modelling to develop a fundamental understanding and a predictive capability. This research aims to build on previous Unilever work to develop a formal design procedure based on mechanistic models for in-line rotor-stator mixers so that the results may be applied to future products and processes.

1.7 Thesis outline

The layout of this thesis consists of nine chapters:

- Chapter 1 provides background on rotor-stator mixers, their design, operation and applications, as well as the context and objectives for this research.
- Chapter 2 reviews the current literature on rotor-stator mixers, and presents some theoretical background on the topics of power draw, emulsification and modelling droplet break-up.
- Chapter 3 gives details of the materials, experimental equipment and rig arrangement, and the experimental procedures.
- Chapter 4 presents power draw measured by two methods and fits to a model equation. The power constants of three mixer scales and various rotor-stator geometry are discussed.
- Chapter 5 discusses the effect of process and formulation variables on single pass droplet size distributions (DSDs). Average droplet size was correlated with parameters such as dispersed phase viscosity, rotor speed and flow rate.
- Chapter 6 discusses the effect of number of passes on drop size distributions, together with the prediction of droplet size from solving population balance equations using numerical simulations.
- Chapter 7 explains the effect of scaling up parameters on drop size distributions from the lab scale to the factory scale for single and multiple passes, and non-surfactant and surfactant systems.
- Chapter 8 explains the effect of rotor and stator geometry on droplet size distributions and emulsification efficiency, including the effect of injection of the dispersed phase on average droplet size.

- Chapter 9 summarises the key findings from this study and suggests topics for future work.

1.8 Publications and presentations

Findings from this study have been published in the following book chapters and journals:

1. Pacek, A. W., Hall, S., Cooke, M., and Kowalski, A. J., (2013). "Emulsification in rotor-stator mixers", in *Emulsion Formation and Stability*, Tadros, T. F., (Ed.), Wiley-VCH, Germany, *Accepted*.
2. Hall, S., Cooke, M., Pacek, A. W., Kowalski, A. J., and Rothman, D., (2011). "Scaling Up of Silverson Rotor-Stator Mixers", *The Canadian Journal of Chemical Engineering*, **89(5)**, 1040-1050.
3. Hall, S., Cooke, M., El-Hamouz, A., and Kowalski, A. J., (2011). "Droplet break-up by in-line Silverson rotor-stator mixer", *Chemical Engineering Science*, **66(10)**, 2068-2079.
4. Kowalski, A. J., Cooke, M., and Hall, S., (2011). "Expression for turbulent power draw of an in-line Silverson high shear mixer", *Chemical Engineering Science*, **66(3)**, 241-249.

Parts of this work have been presented at:

1. Hall, S., Pacek, A. W., Kowalski, A. J., Cooke, M., and Rothman, D., (2012). "The effect of scale on liquid-liquid dispersion in in-line Silverson rotor-stator mixers", *Proceedings of the 14th European Conference on Mixing*, Baldyga, J., (Ed.), Warsaw, Poland, September 10-13, 2012, Warsaw University of Technology, Warsaw, pp. 139-144.

2. Hall, S., Pacek, A. W., Kowalski, A. J., Cooke, M., and Rothman, D., (2012). "Liquid-liquid dispersion in in-line Silverson rotor–stator mixers: experiments and simulations", *Mixing XXIII*, Mayan Riviera, Mexico.
3. Hall, S., Cooke, M., Pacek, A. W., and Kowalski, A. J., (2011). "Single and multiple pass emulsification by in-line Silverson rotor-stator mixers", *7th International Symposium on Mixing in Industrial Processes*, Beijing, China.
4. Rodgers, T. L., Cooke, M., Hall, S., Pacek, A. W., and Kowalski, A. J., (2011). "Rotor-Stator Mixers", *Proceedings of the 10th International Conference on Chemical and Process Engineering*, Florence, Italy.
5. Hall, S., Pacek, A. W., Kowalski, A. J., and Cooke, M., (2010). "Emulsification by in-line rotor-stator mixers", *Proceedings of the 5th World Congress of Emulsions*, Lyon, France, Paper No. 140.
6. Hall, S., Cooke, M., Pacek, A. W., Kowalski, A. J., and Rothman, D., (2010). "Scaling Up of Silverson Rotor-Stator Mixers", *Mixing XXII*, Victoria, BC, Canada.
7. Hall, S., Pacek, A. W., Kowalski, A. J., and Cooke, M., (2009). "Concurrent Product-Process Design Using Rotor-Stator Devices", *10th UK Particle Technology Forum*, Birmingham, UK.

CHAPTER 2. LITERATURE REVIEW

2.1 Power draw

Power draw is an important parameter in mixing processes, and is defined as the amount of energy required to generate fluid movement by agitation in a given time period (Ascanio et al., 2004). Power draw can significantly contribute towards the operating cost of chemical processing; therefore knowledge of power draw allows the process to be developed to operate more efficiently. Accurate prediction of power draw is also needed to ensure the required degree of energy input into the process is achieved, and for installation of the correct size of motor, gearbox and shaft (Cooke, 2005). Furthermore, power draw affects many processes such as heat and mass transfer, and is commonly used as a parameter for scaling up processes including emulsification.

The power applied to a mixing system produces a circulating flow, Q, and a velocity head, H, given by (Hemrajani and Tatterson, 2004):

$$Q \propto ND^3 \tag{2.1}$$

$$H \propto N^2D^2 \tag{2.2}$$

The velocity head (H) provides the kinetic energy that generates shear in mixing, while the impeller pumping capacity (Q) describes internal recirculation and is known as the pumping number or flow number, N_Q (Hemrajani and Tatterson, 2004):

$$N_Q = \frac{Q}{ND^3} \tag{2.3}$$

Flow number depends on the impeller type and ranges from 0.3 to 0.8 in turbulent flow (Hemrajani and Tatterson, 2004).

The power drawn by an impeller in a Newtonian fluid is given by (Uhl and Gray, 1966; Edwards et al., 1997):

$$\frac{P}{\rho N^3 D^5} = fn\left(\frac{\rho N D^2}{\mu}, \frac{N^2 D}{g}, \frac{W}{D}, \ldots\right) \tag{2.4}$$

The term on the left hand side of Eq. (2.4) is the power number, which is the ratio of the pressure differences producing the flow to inertial forces, and is a characteristic of the impeller geometry:

$$Po = \frac{P}{\rho N^3 D^5} \tag{2.5}$$

Typical Po values in a stirred vessel range from 0.3 for a Lightnin A310 to 5-6 for a Rushton turbine (Cooke, 2005).

Power draw is also a function of the Froude number, the ratio of inertial to gravitational forces, and is generally only considered in situations where an extreme vortex occurs (Uhl and Gray, 1966):

$$Fr = \frac{N^2 D}{g} \tag{2.6}$$

In mixing processes, the Reynolds number is an important dimensionless term used to describe the ratio of inertial to viscous forces, defined for an impeller:

$$Re = \frac{\rho N D^2}{\mu} \tag{2.7}$$

The other terms on the right hand side of Eq. (2.4), such as W/D, are geometrical parameters which are ignored for geometrically similar systems.

For a single phase Newtonian fluid, the typical relationship between Po and Re is known as a 'power curve' (Figure 2.1), which is valid for a specific impeller/vessel geometry.

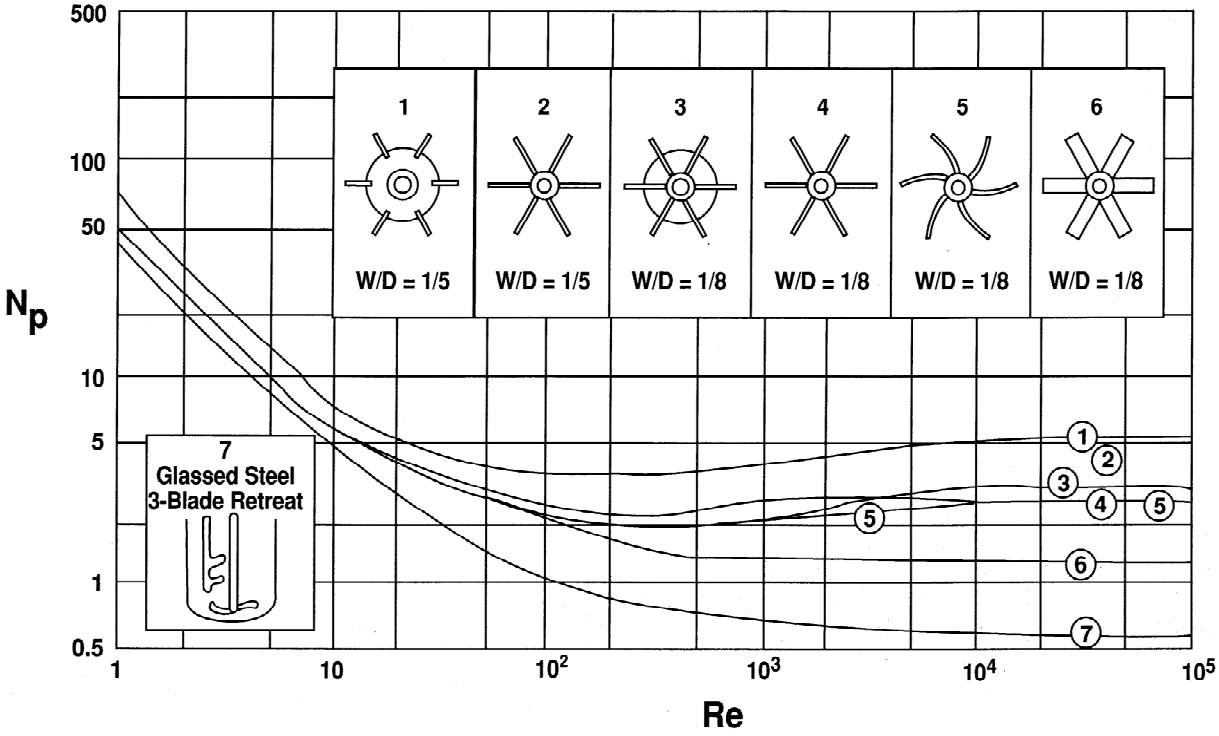

Figure 2.1: Power number versus agitator Reynolds number for seven impellers (from Hemrajani and Tatterson, 2004).

The power curve illustrates three flow regimes which are described by the agitator Reynolds number. For each flow regime, the dependency of Po on Re differs (Hemrajani and Tatterson, 2004):

- Laminar, ($Re \leq 10$)

  $$Po = \frac{k_0}{Re} \tag{2.8}$$

- Transitional, ($10 < Re < 10^4$)

  $$Po = f(Re) \tag{2.9}$$

- Turbulent, ($Re \geq 10^4$)

  $$Po = constant$$

In turbulent flow, power number is independent of Reynolds number, by rearranging Eq. (2.5):

$$P = Po\rho N^3 D^5 \tag{2.10}$$

In the transitional regime the relationship between Po and Re is complex and power draw cannot be easily predicted mathematically. At low Reynolds numbers, the flow is dominated by viscous forces instead of inertial forces. This is known as the laminar regime, where Po is inversely proportional to Re, and the power draw expression is obtained by substituting Eqs. (2.7) and (2.8) into Eq. (2.10):

$$P = k_0 \mu N^2 D^3 \tag{2.11}$$

Power draw for a non-Newtonian fluid in the laminar regime can be related to the Newtonian power draw using a correction based on the Metzner-Otto relationship (Metzner and Otto, 1957; Edwards et al., 1997). This method assumes average shear rate in the impeller region is proportional to the impeller speed:

$$\dot{\gamma} = K_s N \tag{2.12}$$

where K_s is the Metzner-Otto constant. For a power-law fluid, the apparent viscosity is given by:

$$\mu_A = k(\dot{\gamma})^{n-1} \tag{2.13}$$

Eqs. (2.12) and (2.13) can be substituted into Eq. (2.7) for apparent viscosity to give Reynolds number for a power law fluid in the laminar regime (Edwards et al., 1997):

$$Re = \frac{\rho N D^2}{\mu_A} = \frac{\rho N^{2-n} D^2}{k(K_s)^{n-1}} \tag{2.14}$$

The Metzner-Otto constant (K_s) is obtained by measuring the laminar power number and Reynolds number for a Newtonian and non-Newtonian fluid:

$$K_s = \left(\frac{PoRe_{pl}}{PoRe}\right)^{1/(n-1)} \tag{2.15}$$

K_s is a function of the impeller geometry and agitator flow number and varies from 3 to 13 (Wu et al., 2006).

Power draw in stirred vessels has been measured experimentally by several methods. A review of five methods is given by Ascanio et al. (2004); torquemeter, calorimetric measurement, electrical measurement, dynamometer and strain gauge. A review of power draw measurement in rotor-stator mixers is given in the following sections.

2.1.1 Power draw in batch rotor-stator mixers

Open literature on power draw in rotor-stator mixers was practically non-existent until a few years ago, with a review of high shear mixers including power draw given by Zhang et al. (2012). However studies using batch rotor-stator mixers are relatively straightforward as these mixers can be characterised by a single power number in the same way as for agitators in stirred tanks using Eq. (2.5).

Francis (1999) measured turbulent power draw of a Ross ME-100LC radial flow rotor-stator mixer by measuring the electrical power input to the motor and the motor efficiency. He measured power draw of two stator head geometries and two rotor-stator gap widths and found that power scaled with rotor speed with exponents from 2.56 to 2.88, and power numbers varied from 2.7 to 3.2 for the three heads examined.

Developing the work of Francis (1999), one of the most comprehensive studies was undertaken by Padron (2001) who investigated power draw in batch rotor-stator mixers from three different manufacturers; a Ross ME-100LC and Silverson L4RT producing radial flow patterns, and an axial flow Greerco XLR Homomixer. Power draw was measured by the same method used by Francis (1999).

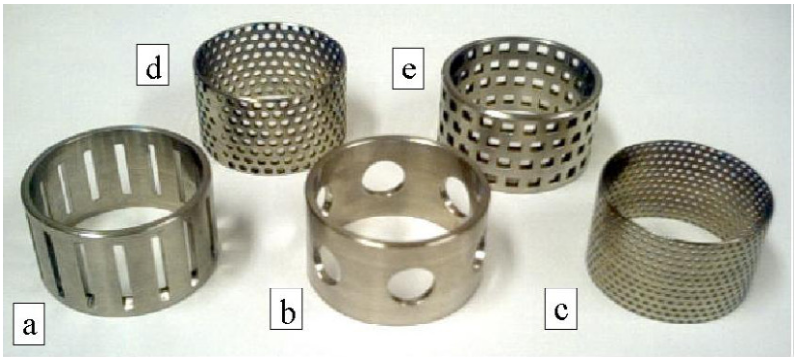

Figure 2.2: Stator geometry investigated by Padron (2001): (a) slotted, (b) disintegrating, (c) fine emulsor, (d) standard emulsor, (e) square hole.

For the radial flow mixers, Padron (2001) found turbulent power draw to scale with rotor speed with an exponent of 2.84 to 3.45, close to the expected value of 3 in Eq. (2.5) for the turbulent regime. He found average turbulent power numbers for the Ross mixer between 2.4 and 3.0, and for the Silverson mixer between 1.7 and 2.3, depending on the type of screen (Figure 2.2). Padron also examined power curves using a range of definitions of Reynolds number based on characteristic length scales of rotor diameter (D), gap width (δ) and hydraulic radius of the stator openings (R_h), and concluded that the conventional definition of Reynolds number (Eq. (2.7)) based on rotor diameter correlated power number most appropriately for rotor-stator mixers. As expected, power number was inversely proportional to Reynolds number in the laminar regime, and roughly constant in the turbulent regime, suggesting rotor-stator mixers can be analysed in a similar way to conventional agitators. Power number was independent of stator geometry in the laminar regime, but dependent upon stator geometry in the turbulent regime (Calabrese and Padron, 2008).

For the axial flow Greerco mixer, the exponents on power draw with rotor speed were slightly lower at 2.71 to 3.13, and power number varied between 1 and 2 depending pumping direction (up or down) and rotor diameter. Padron also established that in the turbulent regime, the effect of the rotor-stator gap width on power draw was not substantial and

suggested that the dominant power dissipation mechanism is turbulent dissipation in the jets from the stator openings. However, in the laminar regime, energy dissipation by viscous shear dominated as power data correlated better with the following definition of Reynolds number:

$$Re_{\delta} = \frac{\rho \delta \pi N D}{\mu} \tag{2.16}$$

Myers et al. (2001) also measured power draw of an axial flow Greerco mixer in the laminar, transitional and turbulent regimes using a strain gauge. Power draw was mainly affected by the pumping mode (up- or down-pumping), followed by the mixer geometry. The up-pumping mode created a radial flow pattern while the flow pattern was axial in the down-pumping mode, with power consumption about 40% greater for the down-pumping mode. A power curve similar to a stirred vessel was obtained, when Po was multiplied by $Fr^{0.1}$, with $PoFr^{0.1}$ values of about 2-3 in the turbulent regime.

Newtonian and non-Newtonian power draw in the turbulent and laminar regimes were investigated by Doucet et al. (2005) using a VMI-Rayneri 4-blade rotor with 72-slotted stator high shear mixer. Power draw was measured for the rotor-stator head, and for the rotor only with the stator removed. For each condition turbulent power number was 3, while in the laminar regime where Po was inversely proportional to Re, the constant k_0 in Eq. (2.8) was three times lower once the stator was removed. They suggested that in laminar flow, power draw depends on the stator, while turbulent power draw depends on the jets from the rotor blades. In laminar flow, caverns formed around the impeller, the shape and magnitude of which scaled with classical Reynolds number (Eq. (2.7)), but the cavern diameter and height could not be predicted using literature correlations for conventional impellers. Doucet et al. (2005) also attempted to create a fluid independent power curve for four non-Newtonian fluids using different definitions of shear rate to shift the non-Newtonian laminar power curve

onto the laminar Newtonian curve. The Metzner-Otto method was the only approach to correlate power draw, but no unique value of the Metzner-Otto constant was obtained.

Khopkar et al. (2007) examined power consumption and mixing time of a batch dual impeller system containing an off-centre rotor-stator and an impeller called Paravisc (Figure 2.3). The rotor-stator did not affect the power drawn by the Paravisc, suggesting a weak pumping capacity of the rotor-stator mixer. Mixing time significantly improved (by 4 times) when operating both the rotor-stator and Paravisc, with the best mixing performance obtained when the Paravisc consumed more power than the rotor-stator.

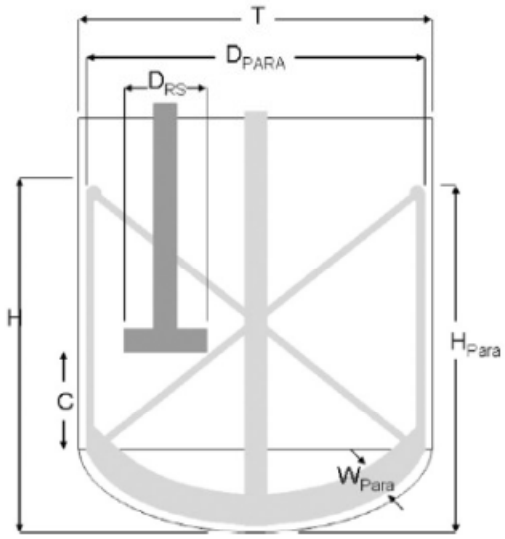

Figure 2.3: The Paravisc mixer studied by Khopkar et al. (2009).

Mortensen et al. (2011) examined the performance of a TPS baffled batch mixer in turbulent flow (Re = 200,000-850,000) by measuring shaft torque and resolving 2D PIV measurements. A transparent Plexiglas stator allowed PIV measurements to be taken inside and outside of the stator. The mean velocities in the flow field and mean strain rate scaled with rotor tip speed while the flow topology remained similar. Hence, they concluded that for

batch rotor-stator mixers, constant rotor tip speed and geometric similarity are the best scaling parameters for mixing processes which depend on macro-scale phenomena. Formation of cavitation bubbles was observed in the low-pressure stator slot vortices, which collapsed outside the stator creating pressure waves and velocity gradients, suggested as being possibly important for emulsification and dispersion performance. The highest mean strain rate was measured in the stator slot jet and near the stator slot vortices, about 3.2 times greater than in the nominal shear rate in the rotor-stator gap. Turbulent power number was 1.2 and flow number was 0.11.

2.1.2 Power draw in in-line rotor-stator mixers

Estimation of power draw in in-line rotor-stator mixers is more complex than batch mixers as the effect of the flow rate needs to be accounted for, which cannot be achieved using Eq. (2.5), for conventional impellers.

One of the early power draw models for turbulent conditions for in-line rotor-stator mixers was proposed by Sparks (1996), who treated rotor-stator mixers as centrifugal pumps, where power draw was likened to a kinetic energy term, proportional to the velocity head in Eq. (2.2):

$$P = Po_I \rho N^2 D^2 Q \tag{2.17}$$

The proportionality constant (Po_I), called power number, was of the order of 10 for all geometries examined. Eq. (2.17) fitted the experimental data rather well at higher power draws but its accuracy deteriorated at low power draws. This expression is similar to the traditional stirred tank approach, therefore the effect of flow rate on power draw was not accounted for separately, thus at zero flow rate the predicted power draw was zero, which is incorrect. Eq. (2.17) does not predict power draw well at low flow rates for the same reason, however at higher flow rates agreement between predicted and experimental results was good.

The inadequacy of Eq. (2.17) led to the development of a multi-term expression for power draw. Baldyga et al. (2007a) and Kowalski (2009) presented an expression for power draw of an in-line rotor-stator mixer consisting of three terms:

$$P = P_T + P_F + P_L \tag{2.18}$$

The first term on the right of Eq. (2.18), corresponds to the power required to rotate the rotor due to the fluid resistance (P_T), the second term is a result of the flow (P_F), while the third term (P_L), accounts for energy losses (for example heat losses, sound, kinetic energy losses) and can be neglected.

The first term (P_T) on the right hand side of Eq. (2.18) is analogous to power consumption in a stirred vessel given by Eq. (2.10) for turbulent flow:

$$P_T = Po_Z \rho N^3 D^5 \tag{2.19}$$

Po_Z is the power number when the flow rate is zero.

The second term (P_F) on the right hand side of Eq. (2.18) accounts for the pumping action of the mixer accelerating the fluid and pumping fluid away (Kowalski, 2009). Centrifugal acceleration of a unit mass is proportional to ND^2, and energy to N^2D^2 (Triton, 1982, in Kowalski, 2009), hence power due to flow is given by:

$$P_F = k_1 M N^2 D^2 \tag{2.20}$$

k_1 is the flow power constant.

The full expression for power draw in turbulent flow is obtained by substituting Eqs. (2.19) and (2.20) into Eq. (2.18), (Baldyga et al., 2007a; Cooke et al., 2008; Kowalski, 2009):

$$P = Po_Z \rho N^3 D^5 + k_1 M N^2 D^2 \tag{2.21}$$

where Po_Z and k_1 are the power constants to be determined.

Ozcan-Taskin et al. (2011) compared measured power draw with power draw predicted from Eqs. (2.10), (2.17) and (2.21), for a Silverson rotor-stator mixer fitted with a

general purpose disintegrating hole (inner) and square hole (outer) stator. They concluded that Eq. (2.21) should be adopted for an in-line rotor-stator mixer.

For laminar flow, Eq. (2.19) can be modified by substitution of the relationship between Po_Z and Re (Kowalski, 2009; Cooke et al., 2012):

$$Po_Z Re = k_0 \tag{2.22}$$

k_0 is the laminar flow power constant. Insertion of Eq. (2.7) and Eq. (2.19) into Eq. (2.22) gives:

$$P_T = k_0 \mu N^2 D^3 \tag{2.23}$$

Assuming P_L is zero, Eq. (2.23) may then be substituted into Eq. (2.18) in place of Eq. (2.19) to give the expression for power draw in laminar flow:

$$P = k_0 \mu N^2 D^3 + k_1 M N^2 D^2 \tag{2.24}$$

where k_0 and k_1 are the experimental power constants to be determined. The full power expression for all regimes is given by (Cooke et al., 2012):

$$P = k_0 \mu N^2 D^3 + Po_Z \rho N^3 D^5 + k_1 M N^2 D^2 \tag{2.25}$$

Kowalski (2009) obtained a slightly different form of Eq. (2.24) based on Reynolds number in the rotor-stator gap in Eq. (2.16):

$$P = \frac{k_0 \mu N^2 D^4}{\delta} + k_1 M N^2 D^2 + P_L \tag{2.26}$$

Kowalski (2009) validated Eq. (2.26) experimentally using a Siefer Trigonal mill rotor-stator device over the range 5-20 kW and found two of the constants, k_1 and P_L appeared to be similar and characteristic of the equipment, while k_0 varied.

Cooke et al. (2012) measured a power curve for an in-line 150/250 mixer with and without the stator present. Values of k_0 of 574 and 276 were obtained with and without the screens, respectively, thus k_0 approximately doubled when the stator was present compared to a three-fold increase found by Doucet et al. (2005) for a batch mixer. The absolute values are

also greater than for a batch mixer since the flow is more restricted by the mixing chamber. Cooke et al. (2012) also measured the Metzner-Otto constant and obtained a value of 46.2 with the screens present, and 6.6 without the screens. These values indicate that average shear rate increased by ~ 7 times when the stator was present.

Additional power draw expressions for in-line rotor-stator mixers were proposed to account for the effect of the mixer geometry. According to Sparks (1996), a Russian paper by Summets (1966) reported for a toothed mixer:

$$P = 0.931N^3D^5\rho\mu^{-0.086}Q^{0.045}H_f^{-0.0787}d^{0.785}Z^{0.068}S^{0.46} \tag{2.27}$$

In addition, a multi-term power draw expression for Greaves and Silverson mixers including the mixer geometry was given by (Middleton, 1984):

$$P = PoN^3D^5\rho + [\frac{\pi^2N^2D^2n_bWx_B\mu}{\delta}] \tag{2.28}$$

Eq. (2.28) appears to be similar to Eq. (2.25) containing both laminar and turbulent power terms, but does not include the flow rate power term.

Kroezen et al. (1988) studied foam generation in an in-line rotor-stator and examined power characteristics of eight rotor-stator configurations. They used the definition of Reynolds number in Eq. (2.16) and redefined power number to account for the rotor-stator geometry:

$$Po = \frac{Pz}{\rho N^3D^4hLq} \tag{2.29}$$

In addition, Hanselmann and Windhab (1999) produced power curves for an in-line rotor-stator mixer and used a similar definition of Po by including the rotor-stator gap:

$$Po = \frac{Pz}{\rho N^3D^3lqh\delta} \tag{2.30}$$

Kroezen et al. (1988) reported that the power curve was similar to a Rushton turbine in the turbulent regime, while Hanselmann and Windhab (1999) obtained similar findings.

However, these different definitions of Po and Re make comparisons between mixers with different geometries in various studies difficult.

2.2 Liquid-liquid dispersion

Liquid-liquid systems consist of two or more immiscible liquids with one liquid, typically in the form of drops, dispersed in the other liquid (Walstra, 2005). These two-phase systems are known as emulsions, with typical droplet diameters of 0.1 to 100 μm. Liquid-liquid systems include water-in-oil (W/O) or oil-in-water (O/W) systems, or more complex systems such as double emulsions (water-in-oil-in-water (W/O/W) and oil-in-water-in-oil (O/W/O) systems), and water-in-water (W/W) dispersions, termed aqueous two-phase systems. The concentration of droplets in an emulsion is described as the dispersed phase volume fraction.

Emulsions are formed from two separate immiscible liquids or by reducing the drop size of an existing emulsion usually by mechanical action called emulsification homogenisation (McClements, 2005). Emulsification is thermodynamically unstable since the two phases will merge or coalesce to reduce the free energy of the system, hence emulsions are stabilised by the addition of an emulsifying agent such as surfactants, proteins and polysaccharides. Emulsifiers are surface-active molecules, generally amphiphilic with polar and non-polar regions, which adsorb onto the droplet surface preventing the droplets from coalescing, and reducing the interfacial tension, facilitating droplet break-up. Texture modifiers such as thickeners may be added to emulsions to increase the continuous phase viscosity to prevent phase separation of droplets due to density differences.

2.2.1 Drop size characterisation

The size of the dispersed phase entity is one of the key parameters used to characterise multiphase systems, as droplet size directly affects the physical properties of the system. Droplets are practically never all of an equal size, as the vast majority of dispersed phases in industry are polydisperse, where a range of drop sizes are formed (Walstra, 2005). Therefore, accurate description of the size of the dispersed phase requires knowledge of the drop size distribution, commonly refered to by a characteristic mean drop diameter.

2.2.1.1 Drop size distributions

Drop size distributions (DSDs) are classified as either discrete or continuous, however all experimentally measured drop size distributions are discrete. Discrete size distributions divide the whole size distribution of a sample into small bins, where the greater the number of bins, the more accurately the distribution is described. In the discrete form, the number frequency of drop of size d_i in the ith bin, is given by the number of drops in the interval n_i, divided by the total number of drops (Seville et al., 1997):

$$f'_N(d_i) = \frac{n_i}{\sum_{j=1}^{m} n_j} = \frac{n_i}{N_T} \tag{2.31}$$

The sum of the number frequencies across all the intervals is one, as $f'_N(d_i)$ in Eq. (2.31) is normalised by the total number of drops:

$$\sum_i f'_N(d_i) = 1 \tag{2.32}$$

Drop size distributions are often described in terms of drop volume instead of drop number, so Eq. (2.31) becomes (Leng and Calabrese, 2004):

$$f'_V(d_i) = \frac{n_i d_i^3}{\sum_{j=1}^{m} n_j d_j^3} \tag{2.33}$$

A comparison between drop size distributions in terms of number and volume is illustrated in Figure 2.4.

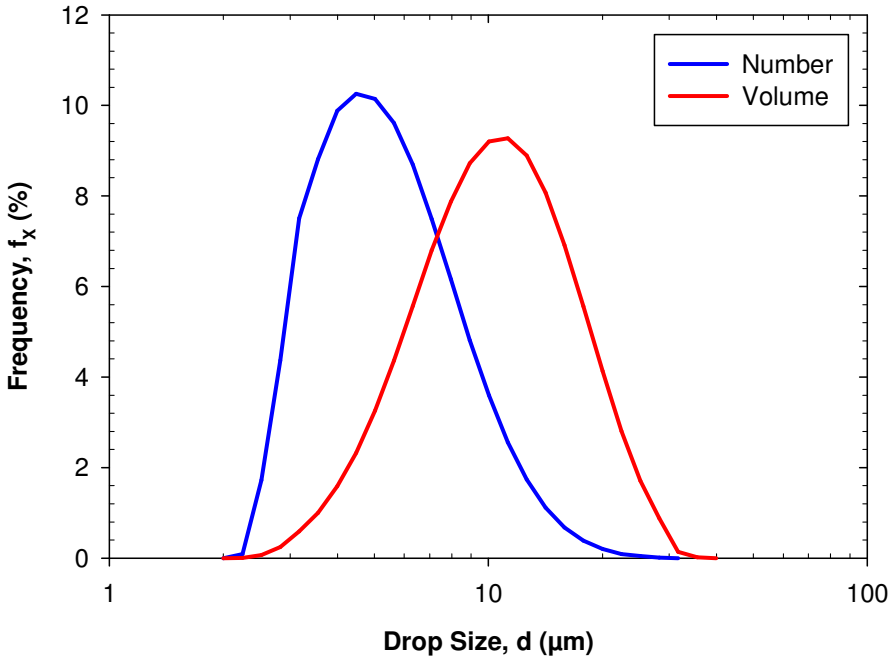

Figure 2.4: A comparison between volume and number drop size distributions.

A useful way of analysing DSDs is in the form of a cumulative frequency distribution which includes all the fractions in bins up to size d_i, given by (Seville et al., 1997):

$$F'_X(d_i) = \sum_{j=1}^{d_i} f_X(d_j) \tag{2.34}$$

Where X means N or V, for number or volume distributions, respectively. An example of discrete and continuous volume distributions as a function of drop size is shown in Figure 2.5. One advantage of cumulative drop size distributions is when they are plotted on linear axis a straight line indicates a normal or Gaussian distribution (Seville et al., 1997), while a straight line on normal probability axis signifies the distribution is log-normal.

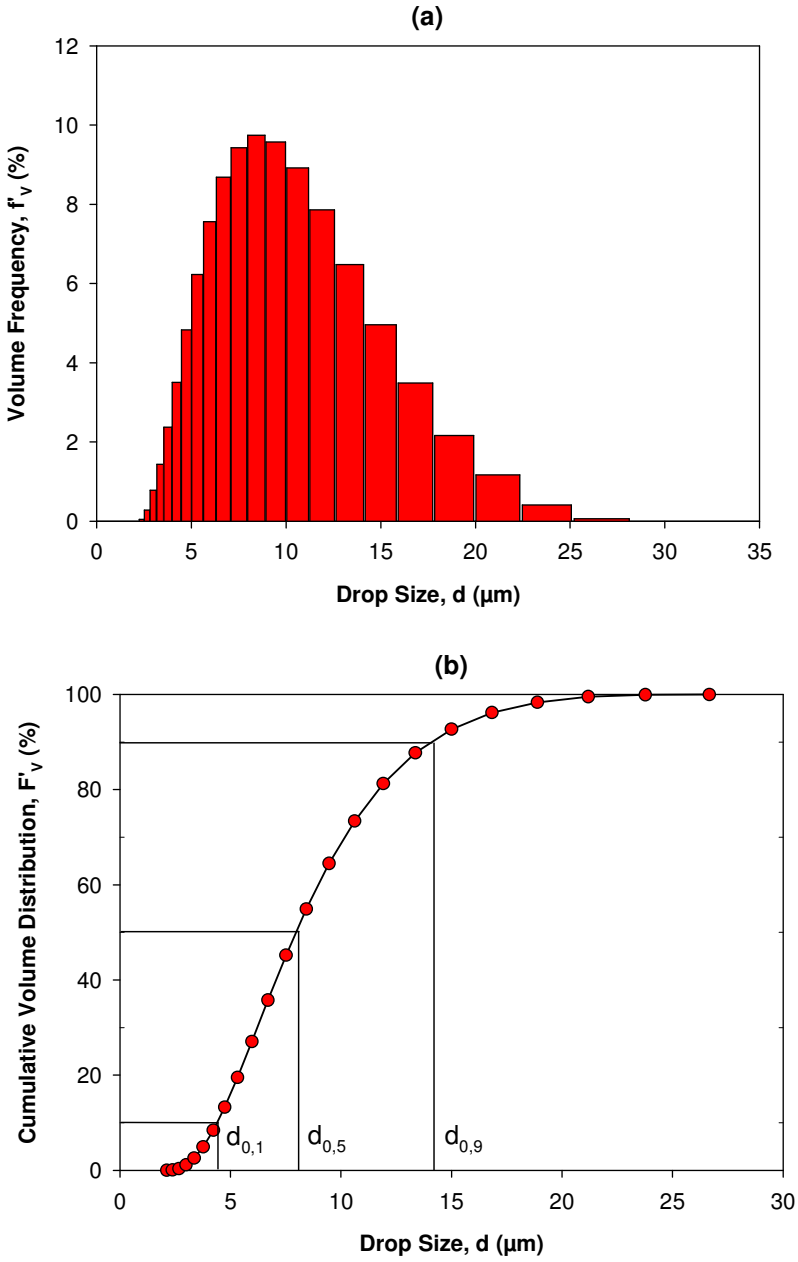

Figure 2.5: Drop size distributions; (a) a discrete volume frequency distribution in classes, and (b) a cumulative volume distribution.

The number median diameter ($d_{0,5}$) is defined as the diameter below which 50% of the population of drops are smaller (Figure 2.5). In addition, $d_{0,1}$ and $d_{0,9}$ correspond to drop diameters below which 10% and 90% of the population of drops are smaller, respectively.

A discrete cumulative distribution may be transformed into a continuous cumulative distribution (Leng and Calabrese, 2004):

$$F_X(d_k) = \int_0^{d_k} P_X(d')\,\mathrm{d}\,d' \tag{2.35}$$

The discrete and continuous distribution functions are related by $f'_X(d_i) = P_X(d_i)\Delta d_i$, where Δd_i is the bin width for class i and $P_X(d)$ is a continuous function, known as the probability density function. A characteristic of probability density functions is that when plotted, the area below the curve is equal to one.

2.2.1.2 Mean drop diameters

In many practical applications, rather than using drop size distributions (functions) to describe the population of drops, a mean drop diameter is often used to characterise the population of drops. Mean drop diameters are defined as the ratio of selected moments of the size distribution (Walstra, 2005):

$$d_{pq} = \left[\frac{\sum_{i=1}^{k} n_i d_i^p}{\sum_{j=1}^{m} n_j d_j^q}\right]^{\frac{1}{p-q}} = \left[\frac{\int_0^\infty d^p f(d)\partial d}{\int_0^\infty d^q f(d)\partial d}\right]^{\frac{1}{p-q}} \tag{2.36}$$

where p and q are integers and $p > q$, and typically p does not exceed 4 (Pacek et al., 1998).

Using Eq. (2.36), the same population of drops are defined by several mean drop diameters which can have completely different values, especially if the drop size distribution is wide. These mean drop diameters have different physical meanings which makes them useful for specific applications.

The most commonly used mean diameter in emulsification/dispersion processes is the surface-volume mean diameter, also known as the Sauter mean diameter (Orr, 1983):

$$d_{32} = \left[\frac{\sum_{i=1}^{m} n_i d_i^3}{\sum_{i=1}^{m} n_i d_i^2}\right]^{\frac{1}{3-2}} = \frac{\int_0^\infty d^3 f(d)\partial d}{\int_0^\infty d^2 f(d)\partial d} \tag{2.37}$$

The Sauter mean diameter is frequently used in dispersion science as it preserves both surface area and population volume, and is related to the specific surface area of the dispersion, a_s, through the dispersed phase volume fraction (Leng and Calabrese, 2004):

$$a_s = \frac{6\Phi}{d_{32}} \tag{2.38}$$

Another mean diameter used in liquid-liquid dispersion processes is the volume-moment mean diameter, also known as the De Brouckere mean diameter (Orr, 1983):

$$d_{43} = \left[\frac{\sum_{i=1}^{m} n_i d_i^4}{\sum_{i=1}^{m} n_i d_i^3}\right]^{\frac{1}{4-3}} = \frac{\int_0^\infty d^4 f(d) \partial d}{\int_0^\infty d^3 f(d) \partial d} \tag{2.39}$$

In this work, Sauter mean diameter (d_{32}) was generally used as this is most appropriate for emulsification.

2.2.1.3 Measurement techniques

Black et al. (1996) divided particle size measurement techniques into three categories; physical, imaging and light scattering, where physical techniques including electrical methods and impaction are more applicable to solids rather than liquids. The most commonly used techniques for measuring drop size distributions are discussed below, with a focus on laser diffraction used in this study.

2.2.1.3.1 Optical microscopy

Optical microscopy is a tool which can provide information on the size, shape and morphology of particles or droplets (Rawle, 1993). Pacek and Nienow (1995) combined this technique with a video camera to acquire images of drops analysed either manually or automatically to determine droplet size distributions.

Image capture by video microscope is an online measurement technique widely applied for measuring DSDs using a camera fitted to a long range microscope for magnification. A strobe light is often placed behind the drops for illumination, where the light

frequency can be synchronised with the frame rate of the camera (Pacek et al., 1994). Droplet size distributions are determined using image analysis software.

This technique was accurate when at least 800 drops were analysed per condition, to measure drops from 20 to 2,000 μm (Pacek et al., 1994). This technique instantaneously measures transient drop size distributions, is non-evasive, and droplets within drops can be analysed. The microscope's zoom can measure rapidly changing drop sizes however this limits the range of drop sizes measured. Disadvantages include slow data treatment and analysis limited to dilute particle dispersions, and if the components have similar refractive indices they can be difficult to distinguish.

Francis (1999) developed a high magnification video probe, similar to the video microscopy technique that can measure particles from 5-150 μm. However this method is only applicable to systems with a large difference in refractive index between the phases since the camera captures the light reflected from particles.

2.2.1.3.2 Electrical sensing zone method

Electrical sensing methods measure particle size by passing particles dispersed in electrolyte through an orifice with an electrical current applied across it (Walstra, 2005). As the drop passes through the electrical field, the current decreases as oil has a lower conductivity than the electrolyte and a peak in the voltage is recorded with amplitude proportional to the particle volume. The measured peaks in voltage are compared against a standard of monodisperse particles; hence this method is not absolute.

There are many drawbacks to this technique for sizing emulsion droplets. Firstly the particle size range is limited as large particles can block the orifice and are less stable in suspension, and small particles < 2 μm are difficult to measure as small orifices are required. Particle sizes of 0.4-1,200 μm can be measured (Padron, 2005), although wide size

distributions are time consuming to measure as multiple orifices are needed. Further problems include more than one particle passing through the orifice at the same time resulting in a voltage pulse equivalent to a single large particle, so the emulsion should be dilute (Walstra, 2005). Flocculation and coalescence of unstable systems can occur, with sedimentation of dense particles, and droplets can be disrupted by shear forces passing through the orifice. This method is also sensitive to calibration which requires standards that are different in electrolyte and distilled water, the dispersed phase must be compatible with the electrolyte, and porous particles can give errors by measurement of the particle envelope (Rawle, 1993).

2.2.1.3.3 Dynamic light scattering

Dynamic light scattering is an off-line technique which applies a laser beam to the emulsion and measures droplet diameter from the diffusion coefficient of droplets. In a dilute emulsion with no particle-particle interactions, drop size can be calculated using the Stokes-Einstein equation (Padron, 2005):

$$R_h = \frac{k_B \theta}{6\pi \mu_c D_{AB}} \tag{2.40}$$

This method, known as Photon Correlation Spectroscopy (PCS), observes variations in the intensity of the scattering pattern with time due to particle movement by Brownian motion. The frequency of particle movement is related to the particle velocity, and therefore its size (McClements, 2005).

This technique is used to measure sub-micron particles (3 nm - 3 μm) (McClements, 2005), so has limited applicability for most emulsions. The emulsion must be dilute as the measured light intensity must be scattered from one particle and the light intensity should be sufficient. PCS is particularly suitable for measuring monodisperse or narrow size distributions, and less applicable for wide size distributions.

2.2.1.3.4 Laser diffraction

Laser diffraction particle size analysis is a light scattering method that uses time-averaged measurements of scattered light flux to measure particle sizes in the range 0.02 to 2,000 μm (Rawle, 1993). The development of computers, low-cost highly stable lasers and detector technologies makes laser diffraction a practical and rapid particle size analysis technique. Several commercial instruments apply this technique, including the Mastersizer 2000 particle size analyser (Malvern Instruments Ltd., Malvern, UK) used in this study.

Typical components of a laser diffraction particle size analyser are shown in Figure 2.6 (Ma et al., 2000). A stable parallel coherent monochrome laser beam is emitted to the fluid flow (Figure 2.6), such as the 9 mm diameter 632.8 nm wavelength helium-neon laser in a Mastersizer 2000.

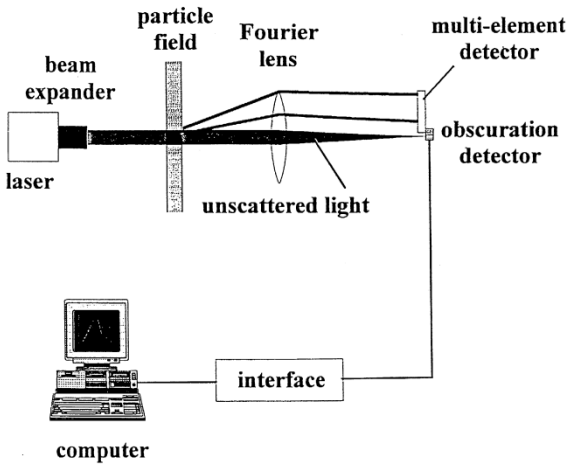

Figure 2.6: Schematic arrangement of a typical laser scattering particle size analyser (from Ma et al., 2000).

A stream of particles or drops suspended in fluid at low concentration is circulated between the glass windows of a transparent sample cell, crossing the laser beam within a focal

distance. A Fourier lens focuses the scattered and diffracted light forward onto a series of photoelectric detectors (Burdin et al., 1999).

The scattered light intensity is measured as a function of the scattering angle, producing a signal proportional to the incident light intensity. The size distribution is obtained from the angle dependent light scattering function by inversion using non-linear least square analysis to find the size distribution which most closely fits the scattering pattern.

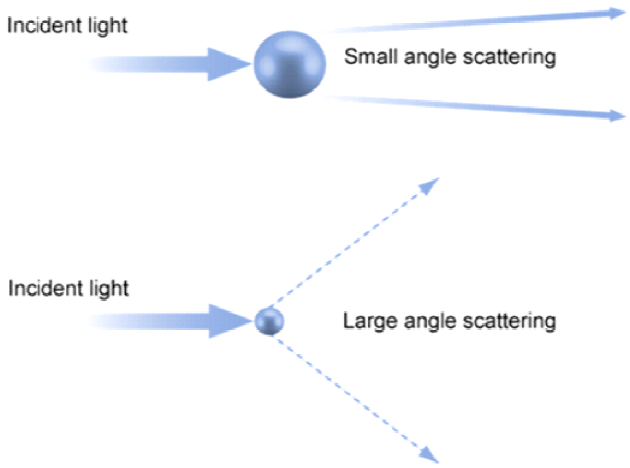

Figure 2.7: Scattering patterns for small and large particles (from Flanagan, 2008).

A basic mathematical model for laser light scattering was developed in 1976 by Swithenbank (Zaidi et al., 1998) based on the Fraunhofer diffraction theory. The Fraunhofer theory predicts that a particle scatters light at an angle inversely proportional to its size, if the particle is larger than the wavelength of light. As particle size decreases, the scattering angle increases logarithmically, while the scattering intensity diminishes according to particle volume (Flanagan, 2008), assuming the particles are spherical, scatter light with equal efficiency and transmit no light. Large particles tend to scatter more light at narrow angles

with high intensities, and smaller particles tend to scatter light at wider angles with low intensities (Figure 2.7).

Particle size and opacity determine the scattering theory; smaller (< 10 μm), transparent particles with lower relative refractive indices are less applicable to the Fraunhofer theory, thus the Mie theory which describes scattering for any particle size is applied (Rawle, 1993). Modern light scattering instruments use both Fraunhofer diffraction and Mie scattering theories to calculate volume-weighted particle size distributions (Rawle, 1993). The Mie theory requires estimation of the particle refractive and absorption indices, and the medium refractive index.

Possible sources of error associated with laser diffraction include detector sensitivity to incident light (Zaidi et al., 1998), and the size distribution can be distorted with the appearance of false particles when the model fails to fit the scattering pattern correctly. Dirt on the cell windows, trapped air bubbles in the circulating flow, irregular particles and inappropriate selection of material properties can all result in erroneous size distributions.

Laser diffraction is based on fundamental scientific principles so the instrument does not require calibration, can measure random particle dimensions and does not depend on fluid velocity (Rawle, 1993). Light scattering requires dilute samples to minimise interactions between particles and reduce secondary scattering which may affect the light angle detected, however, a sufficient sample quantity is required to distinguish the detection signals from background noise (signal-to-noise ratio).

Overall, laser diffraction is a popular method widely used in industry and research to measure particle size, and was chosen in this study due to its speed, convenience and flexibility.

Table 2.1: Advantages and disadvantages of laser diffraction particle sizing (Rawle, 1993).

Advantages	Disadvantages
Wide dynamic working range of measureable particle sizes (0.02 to 2000 μm)	Requires knowledge of the material and medium optical properties
Simple sample preparation	Performance may be instrument related
A volume size distribution is obtained directly	Measurement of particle mixtures are difficult to analyse and differentiate
All orientations of the suspension are presented to the laser beam, preventing over sizing by neglecting a dimension	Large deviations from sphericity lead to detection errors and produce broader or multimodal size distributions, especially for extreme anisotropic shaped particles
Fundamental principles so calibration against a standard is not required	Light diffraction off multiple particles can occur
Does not require highly skilled operators	Fine particle mass fractions are not obtainable
Highly reproducible results	Low particle concentrations may not be measureable
Rapid detection method producing a result in under one minute	Volume distribution curves calculated assuming spherical particles
High resolution with ~ 100 bins	Sample dilution required
Particle mixtures with different densities can be measured together	False particles can appear due to dirt, air bubbles etc.
Entire sample is measured	
Off-line and on-line measurement possible	
Non-destructive and non-intrusive	

2.2.2 Mechanistic models for droplet break-up

Liquid-liquid dispersion has been investigated for many years to attempt to theoretically predict droplet size for different process and formulation conditions. Droplet break-up depends on a number of material and process variables which have been described by authors using various theoretical and empirical models. Droplet coalescence also affects drop size, however in general coalescence is considered negligible for very low phase

volume (dilute) dispersions. Expressions for correlating Sauter mean diameter have been reported for a range of formulations and processing equipment, with most of the previous work summarised by Leng and Calabrese (2004).

Mechanistic models for laminar and turbulent flow conditions typically estimate the maximum stable drop size that can exist in certain hydrodynamic conditions by balancing the disruptive and cohesive forces acting on a drop. The maximum stable drop size depends on the cohesive stresses (τ_c) resisting droplet deformation and disruptive stresses (τ_d) acting on the droplet surface. The cohesive stress depends on the interfacial tension (σ), the dispersed phase viscosity (μ_d) and the drop diameter (d), and for inviscid dispersed phases ($\tau_c = \tau_s$) is given by the stresses due to the surface tension (τ_s) (Leng and Calabrese, 2004):

$$\tau_s \propto \frac{\sigma}{d} \tag{2.41}$$

The disruptive stresses depend on parameters including the continuous phase viscosity (μ_c), the continuous phase density (ρ_c), the drop diameter (d), and the type of flow (laminar or turbulent) and its intensity described either by shear rate ($\dot{\gamma}$) in laminar flow or specific energy dissipation rate (ε) in turbulent flow. The drop is stable if $\tau_d < \tau_c$ and maximum stable drop size is calculated using:

$$\tau_c = \tau_d \tag{2.42}$$

The ratio of disruptive to cohesive stresses ($\tau_d \,/\, \tau_c$) is called the Capillary number (Ca) in laminar flow, and Weber number (We) in turbulent flow, and is commonly used to relate drop size to the hydrodynamic conditions and physical properties of the dispersed and continuous phases. Many correlations for maximum stable drop size published in literature are based on this simple mechanistic model.

2.2.2.1 Laminar droplet break-up

Laminar flow can be defined as flow where fluid moves in separate layers or streamlines, where there is no flow in the direction perpendicular to these streamlines. Fluid motion is dominated by linear, viscous forces due to steady flows, often resulting from low fluid velocities or high viscosity materials, instead of non-linear inertial forces in turbulent flow (Szalai et al., 2004). Laminar flow can be broadly classified as simple shear flow, extensional or elongational flow and plane hyperbolic flow (Walstra, 1983) shown in Figure 2.8. These flow types may occur in certain regions of the processing equipment even when the bulk flow is turbulent due to the complex nature of the equipment geometry.

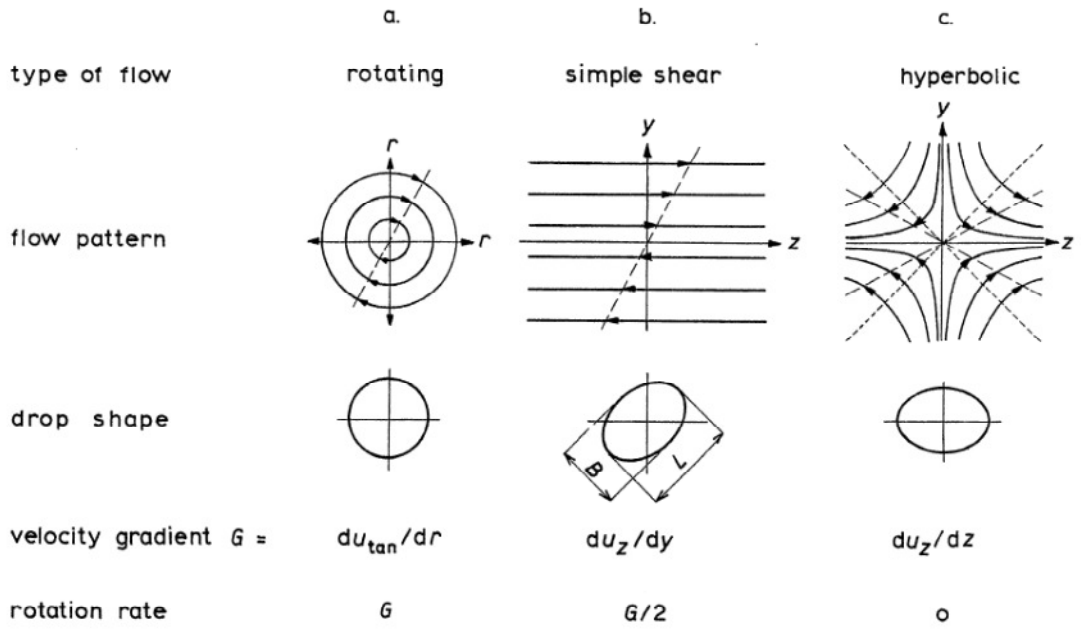

Figure 2.8: Schematic diagram illustrating laminar flows (from Walstra, 1983).

Simple shear flow occurs in the fluid contained between two concentric cylinders separated by a narrow gap with both rotating in opposite directions or with one rotating and one stationary, which may occur in the gap of radial discharge rotor-stator mixers.

Elongational flow occurs when there is a velocity gradient in the direction of flow and may occur in colloid mills when the gap cross-section varies, or in fluid through the stator holes. Hyperbolic flow can be used to approximate a jet of liquid hitting a surface, and could be used to model flow of very viscous emulsions in high pressure homogenisers.

In all flow types, drops are deformed and eventually broken by disruptive shear stresses resulting from velocity gradients across the drop:

$$\tau_d = \mu_c \frac{dU_i}{dx_j} = \mu_c \dot{\gamma} \tag{2.43}$$

The Capillary number $(\tau_d \,/\, \tau_c)$ at which breakage occurs defines the maximum stable drop size and is called the critical Capillary number:

$$Ca_{cr} = \frac{\dot{\gamma}\, \mu_c d_{max}}{\sigma} \tag{2.44}$$

Critical Capillary number in laminar flow depends on the type of flow and viscosity ratio $\mu^* = \frac{\mu_d}{\mu_c}$ and can be determined from experimental stability curves known as Grace curves, shown in Figure 2.9 (Walstra, 1983).

If the viscosities of both phases, interfacial tension and shear rate are known, Grace curves can be used to find the maximum stable drop size:

$$d_{max} = \frac{Ca_{cr}\sigma}{\dot{\gamma}\, \mu_c} \tag{2.45}$$

Figure 2.9 shows that elongational and hyperbolic flows are more effective for droplet breakage than simple shear flow, since very viscous drops with viscosity ratios greater than 4 ($\mu^* > 4$) cannot be broken in simple shear flow even at very high shear rates.

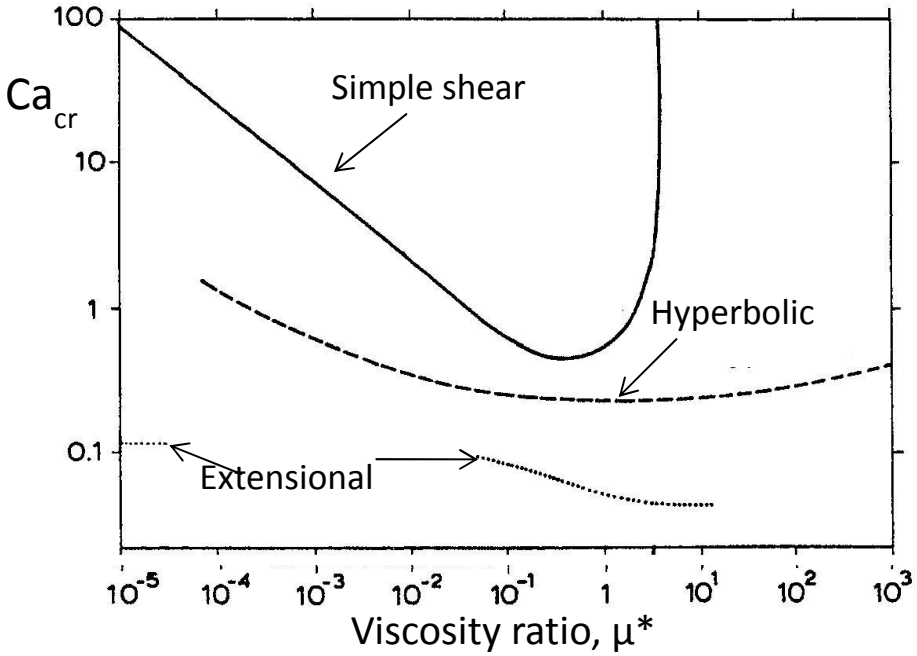

Figure 2.9: Critical Capillary number for different types of laminar flow (adapted from Walstra, 1983).

2.2.2.2 Turbulent droplet break-up

Models developed by Hinze (1955) have often been used as the basis to develop a mechanistic understanding of droplet breakage (Leng and Calabrese, 2004). These models apply the concept of a cascade of turbulent eddies of varying sizes, developed by Kolmogorov, each of which contains a certain amount of energy. The largest eddies are assumed to be comparable to the impeller diameter, which break down and transfer their energy to smaller and smaller eddies, until the energy is eventually dissipated as heat due to viscous friction. This model assumes local homogeneous turbulence, where the Reynolds number is sufficiently high that the flow can be considered isotropic (equal in all directions). Local isotropic turbulence theory divides the flow into three regimes described by the energy spectrum in Figure 2.10. The spectrum shows energy content as a function of wavenumber

(k), and that the largest eddies are most energetic and anisotropic, whilst the smallest eddies have less energy.

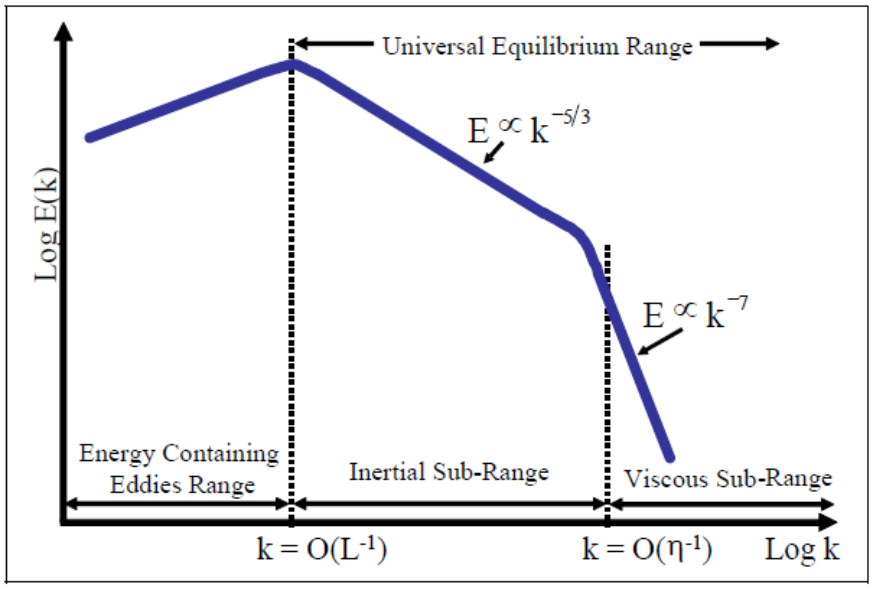

Figure 2.10: Energy spectrum for turbulent flow (from Padron, 2005).

Kolmogorov postulated that in local isotropic turbulence, termed the universal equilibrium range, the nature of the flow depends only on the energy dissipation rate (ε), the kinematic viscosity of the fluid (ν) and the length scale of the smallest eddies which can exist in the flow, known as the Kolmogorov length scale (η_K), given by (Leng and Calabrese, 2004):

$$\eta_K = \left(\frac{\nu^3}{\varepsilon}\right)^{1/4} \tag{2.46}$$

Energy dissipation rate is defined as a function of the swept rotor/impeller volume:

$$\varepsilon = \frac{P}{\rho V_H} \tag{2.47}$$

He also defined a velocity scale (U_K) and a time scale (τ_K) based on these variables:

$$U_K = (\nu\varepsilon)^{1/4} \tag{2.48}$$

$$\tau_K = \left(\frac{\nu}{\varepsilon}\right)^{1/2} \tag{2.49}$$

In local isotropic turbulence two regions are identified, the inertial sub-range, where inertial forces dominate over viscous forces, and the viscous sub-range, where viscous forces dominate and viscous dissipation can occur.

This approach divides mechanisms of turbulent droplet breakage on the basis of whether the drop diameter is greater or smaller than the Kolmogorov length scale (η_K), which defines the boundary between the point where the inertial and viscous stresses acting on the drop are equal. The mechanism of droplet breakage depends on the flow regime since $E \propto k^{-5/3}$ in the inertial sub-range and $E \propto k^{-7}$ in the viscous sub-range due to viscous dissipation (Figure 2.10).

Rotor-stator mixers can produce drops in the order of η_K or smaller (Calabrese et al., 2000), where interactions within the viscous sub-range become important and viscous forces are critical, thus it is difficult to clearly identify the breakage mechanisms.

2.2.2.3 Turbulent inertial sub-range

In the inertial sub-range of isotropic turbulent flow ($E(k) \propto \varepsilon^{2/3}k^{-5/3}$), the disruptive stresses resulting from turbulent eddies in the continuous phase acting on the drop are given by (Leng and Calabrese, 2004):

$$\tau_d \propto \rho_c\, \varepsilon^{2/3} d^{2/3} \tag{2.50}$$

For drop sizes larger than η_K, for dilute low viscosity dispersed phase systems, the drops are inviscid since the internal viscous stresses are negligible and only the interfacial tension surface force contributes to stability. By substituting Eqs. (2.41) and (2.50) into Eq. (2.42), the maximum stable equilibrium drop size can be related to the maximum local energy dissipation rate by the following relationship (Leng and Calabrese, 2004):

$$d_{max} = C_1 \left(\frac{\sigma}{\rho_c}\right)^{3/5} \varepsilon^{-2/5} \tag{2.51}$$

Systems which are geometrically similar have a maximum energy dissipation rate proportional to power draw per unit mass of fluid. If power number remains constant, Weber number (We) may be applied for correlation:

$$\frac{d_{max}}{D} = C_2 We^{-3/5} \tag{2.52}$$

The Weber number is often used as the breakage of a drop depends on the ratio of the external disruptive stresses, to the internal cohesive stresses:

$$We = \frac{\rho_c N^2 D^3}{\sigma} \tag{2.53}$$

The disruptive stresses result from turbulent fluctuations and velocity gradients, while the cohesive stresses depend on the interfacial stresses. Large Weber numbers result in smaller drop sizes and vice versa.

For viscous dispersed phases, according to Hinze (1955), the flow inside the drop is proportional to $(\tau_c/\sigma)^{1/2}$ and the viscous stresses (τ_v) opposing droplet deformation are given by:

$$\tau_v \propto \mu_d \frac{(\tau_c/\sigma)^{1/2}}{d} \tag{2.54}$$

The cohesive stresses are the sum of the viscous and surface components:

$$\tau_c = \tau_s + \tau_v \tag{2.55}$$

For drop sizes larger than η_K, for high viscosity dispersed phase systems, internal viscous stresses resisting droplet deformation become more important than surface forces for resisting droplet deformation and the following expression is obtained by neglecting τ_s (Leng and Calabrese, 2004):

$$d_{max} = C_3(\rho_c \rho_d)^{-3/8} {\mu_d}^{3/4} \varepsilon^{-1/4} \tag{2.56}$$

If power number remains constant, the following may be applied for correlation:

$$\frac{d_{max}}{D} = C_4 \left(\frac{\rho_c}{\rho_d}\right)^{3/8} \left(\frac{\mu_d}{\mu_c}\right)^{3/4} Re^{-3/4} \tag{2.57}$$

Reynolds number is defined by Eq. (2.7).

The effect of viscous stresses due to dispersed phase viscosity on drop size is covered by two similar approaches by Davies (1985) and Calabrese et al. (1986), which may be appropriate for high shear mixers. By considering Eq. (2.50), Eq. (2.54) and Eq. (2.55) in Eq. (2.42), Calabrese et al. (1986) developed:

$$d_{max} = C_5 \left(\frac{\sigma}{\rho_c}\right)^{3/5} \varepsilon^{-2/5} \left[1 + C_6 \frac{\mu_d}{\sigma} \sqrt{\frac{\rho_c}{\rho_d}} \varepsilon^{1/3} {d_{max}}^{1/3}\right]^{3/5} \tag{2.58}$$

For geometrically similar systems with a constant power number, dimensionless Weber number and viscosity group can be introduced:

$$\frac{d_{max}}{D} = C_7 We^{-3/5} \left[1 + C_8 Vi \left(\frac{d_{max}}{D}\right)^{1/3}\right]^{3/5} \tag{2.59}$$

Viscosity group is given by:

$$Vi = \left(\frac{\rho_c}{\rho_d}\right)^{1/2} \frac{\mu_d N D}{\sigma} \tag{2.60}$$

2.2.2.4 Turbulent viscous sub-range

In the viscous sub-range of isotropic turbulent flow, the continuous phase viscosity may also be important for droplet break-up, hence either inertial or viscous stresses may dominate.

2.2.2.4.1 Inertial stresses

The disruptive stresses resulting from inertial stresses in the viscous sub-range acting on the drop are given by ($E(k) \propto \varepsilon^1 \nu^{-1} k^{-3}$) (Shinnar and Church, 1960):

$$\tau_d \propto {\rho_c}^2 \frac{\varepsilon}{\mu_c} d^2 \tag{2.61}$$

Substituting Eqs. (2.41) and (2.61) into Eq. (2.42), for inviscid drops:

$$d_{max} = C_9 \left(\frac{\sigma \mu_c}{{\rho_c}^2}\right)^{1/3} \varepsilon^{-1/3} \tag{2.62}$$

If power number is constant:

$$\frac{d_{max}}{D} = C_{10}(WeRe)^{-1/3} \tag{2.63}$$

The equation for high viscosity drops:

$$d_{max} = C_{11} \left(\frac{{\mu_d}^2 \mu_c}{{\rho_c}^2 \rho_d}\right)^{1/4} \varepsilon^{-1/4} \tag{2.64}$$

Chen and Middleman (1967) proposed a mechanistic model using an alternative definition of $E(k) \propto \varepsilon^2 \nu^{-4} k^{-7}$, for drops far smaller than η_K:

$$d_{max} = C_{12} \left(\frac{\sigma {\mu_c}^4}{{\rho_c}^5}\right)^{1/7} \varepsilon^{-2/7} \tag{2.65}$$

If power number is constant:

$$\frac{d_{max}}{D} = C_{13}(WeRe^4)^{-1/7} \tag{2.66}$$

Both Eqs. (2.63) and (2.66) apply to the viscous sub-range for droplet break-up due to inertial stresses with different dependencies on $E(k)$. Levich (1962) in Padron (2005) stated that below the Kolmogorov length scale, disruptive stresses on the drop must be due to viscous shear and not inertial stresses, hence the applicability of Eqs. (2.63) and (2.66) is questionable. Nevertheless, researchers have continued to fit data to these expressions and found good relationships, including Thapar (2004) for in-line rotor-stator mixers.

2.2.2.4.2 Viscous stresses

Droplet break-up due to viscous stresses in the viscous sub-range can be estimated from (Shinnar, 1961):

$$d_{max} = C_{14} \sigma (\rho_c \mu_c)^{-1/2} \varepsilon^{-1/2} \tag{2.67}$$

For constant power number:

$$\frac{d_{max}}{D} = C_{15} We^{-1} Re^{1/2} \tag{2.68}$$

The expression for highly viscous droplet break-up due to viscous stresses:

$$d_{max} = C_{16} {\rho_d}^{-1/2} \mu_d (\mu_c \rho_c)^{-1/4} \varepsilon^{-1/4} \tag{2.69}$$

For the majority of liquid-liquid systems it is often acceptable to substitute the Sauter mean diameter for the maximum stable drop diameter in the above expressions, as $d_{32} \propto d_{max}$ is valid (Sprow, 1967). A summary of the key theoretical mechanistic models to predict mean droplet size are given in Table 2.2.

2.2.2.5 Dispersed phase volume fraction

The effect of dispersed phase volume fraction on drop size has typically been included in Eq. (2.52), as mean drop size typically increases as dispersed phase volume fraction is increased by enhanced coalescence or turbulence reduction (damping). For inviscid drops in clean systems (Pacek et al., 1999):

$$\frac{d_{32}}{D} = C_{17}(1 + C_{18}\Phi) We^{-3/5} \tag{2.70}$$

The constant C_{17} is geometry dependent, while C_{18} is a measure of the tendency of the system to coalesce and can range from 3-20 for clean systems (Pacek et al., 1999).

2.2.2.6 Surfactants

The majority of mean drop size correlations were developed for non-surfactant systems, however the effect of surfactants has been considered by introducing modified parameters. Modified versions of interfacial tension and dispersed phase viscosity have been proposed by Janssen et al. (1994a,b) and Lucassen-Reynders and Kuijpers (1992), respectively:

$$\sigma_{eff} = \sigma + \beta E_{sd} \tag{2.71}$$

$$\mu_d^{eff} = \mu_d + \frac{E_{sd}}{r_c \propto} \tag{2.72}$$

Janssen et al. (1994a,b) found capillary number to increase (hence d_{max}) with surfactant concentration, corresponding to the surface dilational modulus (E_{sd}) and proposed the use of effective interfacial tension (σ_{eff}). The surface dilational modulus is a system property and relates the change of the interfacial tension resulting from a change in the interfacial area of the drop (Walstra and Smulders, 1998):

$$E_{sd} \approx \frac{E_0}{1+\left(\frac{t_D}{t_{def}}\right)^{-1/2}} \tag{2.73}$$

Where E_0 is the limiting elasticity of the interface:

$$E_0 = \frac{-d(\sigma)}{dln\Gamma} \tag{2.74}$$

The surface excess (Γ) at the oil-water interface depends on the bulk concentration of surfactant in the continuous phase.

Lucassen-Reynders and Kuijpers (1992) found the interfacial viscoelasticity caused by addition of surfactant increased the effective viscosity of the drop (by up to 30 times the μ_d, depending on surfactant concentration), forming larger drops and defined effective dispersed phase viscosity (μ_{eff}).

Table 2.2: A summary of the key theoretical correlations to predict mean droplet size.

Range	Mechanism	Correlation in terms of ε	Correlation in terms of dimensionless groups (constant Po)
$L \gg d \gg \eta_K$	Inertial stresses $\mu_d \to 0$ $\tau_s \gg \tau_v$	$d_{max} \propto \left(\frac{\sigma}{\rho_c}\right)^{3/5} \varepsilon^{-2/5}$	$\frac{d_{max}}{D} \propto We^{-3/5}$
$L \gg d \gg \eta_K$	Inertial stresses $\mu_d \to \infty$ $\tau_v \gg \tau_s$	$d_{max} \propto (\rho_c \rho_d)^{-3/8} {\mu_d}^{3/4} \varepsilon^{-1/4}$	$\frac{d_{max}}{D} \propto \left(\frac{\rho_c}{\rho_d}\right)^{3/8} \left(\frac{\mu_d}{\mu_c}\right)^{3/4} Re^{-3/4}$
$\eta_K > d$	Inertial stresses $\mu_d \to 0$ $\tau_s \gg \tau_v$	$d_{max} \propto \left(\frac{\sigma \mu_c}{{\rho_c}^2}\right)^{1/3} \varepsilon^{-1/3}$	$\frac{d_{max}}{D} \propto (WeRe)^{-1/3}$
$\eta_K \gg d$	Inertial stresses $\mu_d \to 0$ $\tau_s \gg \tau_v$	$d_{max} \propto \left(\frac{\sigma {\mu_c}^4}{{\rho_c}^5}\right)^{1/7} \varepsilon^{-2/7}$	$\frac{d_{max}}{D} \propto (WeRe^4)^{-1/7}$
$\eta_K > d$	Viscous stresses $\mu_d \to 0$ $\tau_s \gg \tau_v$	$d_{max} \propto \sigma (\rho_c \mu_c)^{-1/2} \varepsilon^{-1/2}$	$\frac{d_{max}}{D} \propto We^{-1} Re^{1/2}$

2.2.3 Droplet break-up in rotor-stator mixers

2.2.3.1 Batch rotor-stator mixers

Research on droplet break-up in batch high shear mixers is well established as small scale mixers are widely available in most laboratories, thus, there are several investigations examining the link between processing and formulation parameters and emulsion characteristics.

One of the first studies, by Davies (1985), compared the size of emulsion droplets from various process equipment including Hurrell type colloid mills with energy dissipation

rates up to 440,000 W kg^{-1}. Davies applied the theory of Kolmogorov (1949) and Hinze (1955) for droplet break-up assuming isotropic turbulence, and included a term to account for the effect of dispersed phase viscosity on maximum stable drop size:

$$d_{max} = C_{19}\sigma^{3/5}\left(1 + \frac{C_{20}\mu_d(\varepsilon.d_{max})^{1/3}}{\sigma}\right)^{3/5}\rho_c{}^{-3/5}\varepsilon^{-2/5} \quad (2.75)$$

He found that the turbulent fluctuating velocity is important for drop breakage and droplets are not broken by simple shear. Davies (1987) furthered this work by applying this mechanistic model to emulsions from agitated vessels, static mixers and homogenisers.

Francis (1999) and Calabrese et al. (2000) investigated liquid-liquid dispersion in a batch Ross rotor-stator mixer for three immiscible liquids (anisole, phenetole and chlorobenzene) in water. They found little effect of volume fraction (0.08 to 0.24% by volume), rotor-stator gap width and interfacial tension (27-35 mN m^{-1}) on drop size for dilute liquid-liquid systems. Based on the value of the exponent on energy dissipation rate they concluded that droplet interaction with inertial sub-range eddies and sub-Kolmogorov scale viscous stresses are important for droplet breakage. The following mechanistic model correlated the data well for droplet sizes in turbulent flow, similar to stirred vessels:

$$\frac{d_{32}}{D} = 0.040We^{-0.58} \quad (2.76)$$

Phongikaroon (2001) investigated liquid-liquid dispersion in batch Ross and Silverson rotor-stator mixers at 1,500 rpm to 4,000 rpm. The effect of continuous phase viscosity from 0.98 to 6.32 mPa·s, dispersed phase viscosity from 1 to 500 mPa·s, and interfacial tension from 2 to 38 mN m^{-1}, on drop size distributions were examined. Correlation of mean drop size with models based on energy dissipation rate yielded no definite conclusion about whether drops are broken by inertial sub-range eddies or sub-Kolmogorov inertial stresses. An increase in continuous phase viscosity reduced mean drop size, with less effect at higher rotor

speeds. As expected, mean drop size decreased as interfacial tension decreased with a reduced effect at higher dispersed phase viscosities.

Padron (2005) extended these previous studies by Francis (1999) and Phongikaroon (2001) and examined the effect of dispersed phase viscosity from 10 to 1,000 mPa·s of silicone oils and interfacial tension from 20 to 46 mN m^{-1}, in liquid-liquid systems in a batch Silverson L4R mixer from 2,000 rpm to 7,000 rpm. He also examined silicone oil emulsions stabilised by three different surfactants (Tergitol™ TMN-6, Triton™ X-100, and Triton™ X-165) of varying concentrations and measured droplet size using video microscopy. He found mean droplet size increased and became constant with increasing dispersed phase viscosity, as high viscosity drops may be broken by an extensional flow-like mechanism, and based on fits with mechanistic models, drops were more likely broken by inertial stresses due to turbulent pressure fluctuations.

A specific correlation for a lab scale (0.5 L) batch rotor-stator device using dilute dispersions of organic phase in an aqueous phase with densities of 700 to 900 kg m^{-3}, viscosities of 0.5 to 50 mPa·s, and interfacial tensions of 4.5 to 51 mN m^{-1}, was reported by Puel et al. (2006):

$$\frac{d_{32}}{D} = 0.02We^{-0.6}\left(\frac{\mu_d}{\mu_c}\right)^{0.5} \tag{2.77}$$

Urban et al. (2006) compared emulsification in rotor-stator and high shear disc systems, and found disc systems and rotor-stators to give comparable drop sizes with narrow DSDs for high emulsion viscosities. Khopkar et al. (2009) studied formulation parameters for a batch impeller and rotor-stator device, with a rotor diameter of 90 mm and rotor-stator gap width of 2 mm. They found viscosity ratio did not impact on median droplet size, but the effect of dispersed phase content was more significant for surfactant stabilised emulsions.

2.2.3.2 In-line rotor-stator mixers

Information on drop sizes produced in in-line rotor-stator mixers is extremely limited and many studies are not well explained or analysed. Generally, in-line rotor-stator mixer research is industry specific including the formulations used, as industry is the driver for such studies and has access to the necessary equipment.

The following empirical correlation for mean drop size was given by Koglin et al. (1981) (in German) for a continuous rotor-stator device for flow rates up to 500 kg h^{-1}:

$$\bar{d} = 460 \frac{\mu_c^{1.5}}{\rho^{0.5} \mu_d^{0.6} \tau^{0.3} \varepsilon^{0.4}} \tag{2.78}$$

Averbukh et al. (1988) correlated drop size with various process and formulation parameters such as dispersed phase volume fraction, interfacial tension, flow rate, shear gap, continuous phase viscosity and rotor speed, however details of this study are not given:

$$\bar{d} = C_{21} \Phi^{0.135} \left(\frac{\sigma}{\rho_c}\right)^{0.15} \frac{\nu_c^{0.7}}{\delta^{0.25} N^{0.8} Q^{0.2}} \tag{2.79}$$

Pedrocchi and Widmer (1988) examined a one-stage mixing turbine (BUSS AG, Switzerland) with no details about the emulsion given, where drop size was found to be weakly affected by the size of the shear gap and mainly depend upon energy dissipation rate:

$$d_{32} = C_{22} \varepsilon^b \tag{2.80}$$

Where the exponent b varied between -0.54 and -0.76.

Thapar (2004) investigated the effect of stator geometry, rotor speed and flow rate, and dispersed phase volume fraction on mean drop size in a Silverson mixer, however only two flow rates and one formulation were investigated. He found that rotor speed and dispersed phase volume fraction had the strongest effect on Sauter mean diameter, and the correlation by Chen and Middleman (1967) for inertial stresses in the viscous sub-range gave the best correlation:

$$d_{32} = 2x10^{9}(1 + 20\Phi)(WeRe^{4})^{-1/7} \quad (2.81)$$

Gingras et al. (2005) found for an in-line Silverson rotor-stator mixer processing high phase volume highly viscous bitumen emulsions, the following correlation for droplet size:

$$d_{32} = 0.29\left(\frac{N^{3}}{Q}\right)^{-0.55} \Phi^{4.13}\mu^{*-0.53} \quad (2.82)$$

The results did not follow any of the theroetical models tested and they suggested that this was due to high recoalescence rates between very viscous drops, indicated by the strong dependency on dispersed phase volume fraction.

To evaluate the droplet disruption efficiency for continuous emulsification processes including in-line rotor-stator mixers, Karbstein and Schubert (1995) proposed volumetric specific energy or energy density (E_V):

$$E_V = \varepsilon . t_R = \left(\frac{P}{Q}\right) \quad (2.83)$$

Energy density describes the effect of equipment and process parameters applied to a certain emulsion volume and accounts for the mean residence time acting on the drop assuming no re-coalescence. Mean drop diameter is a function of E_V:

$$d_{32} \propto {E_V}^{b} \quad (2.84)$$

Karbstein and Schubert (1995) stated that if b is of the order -0.4, turbulence is important for droplet disruption and Schubert and Engel (2004) summarised exponents on energy density for rotor-stator mills of ~ -0.35 for turbulent inertial forces and ~ -0.75 for turbulent shear forces.

Kevala et al. (2005) analysed drop size distributions in a single pass in-line rotor-stator mixer by injecting oil directly into the mixing head. For low viscosity dispersed phases the drop size distributions were bimodal, becoming single modal at higher rotor speeds and lower

flow rates. For high viscosity dispersed phases, the drop size distributions were single modal, and became more bimodal when rotor speed was increased, and flow rate decreased.

2.2.3.2.1 Geometry

Bourne and Garcia-Rosas (1986) examined the micromixing performance of an X-20 Ystral mixer between 2,000 and 13,000 rpm using six rotor and two stator designs. Both semi-batch and in-line configurations were investigated, and similar micromixing results were found for several rotor-stator combinations, and this did not change once the stator was removed.

The effect of geometry on liquid-liquid dispersion was examined by Francis (1999), Calabrese et al. (2000) and Calabrese et al. (2002) in batch Ross rotor-stator mixers. They investigated the effect of the rotor-stator gap on emulsification using the same stator design with 0.5 mm and 1 mm gap widths, and found the wide gap stator produced smaller droplets. This was unexpected, and they concluded that droplet break-up does not occur in the rotor-stator gap, and drops are most likely broken by the jets from the slots/holes in the stator. The limited effect of the rotor-stator gap on the resultant droplet size enabled Francis (1999) to invalidate the following correlation, which assumes droplet break-up depends on the mean shear rate in the rotor-stator gap:

$$\frac{d_{max}}{\delta} = C_{23} We^{-1} Re \tag{2.85}$$

Francis (1999) and Phongikaroon (2001) examined two mixing head geometries, and in each case the slotted head stator geometry produced smaller drops than the disintegrating head stator, especially at lower rotor speeds.

Thapar (2004) also investigated rotor-stator gap width for an in-line Silverson mixer and found little effect of the gap on droplet size. Francis (1999) (three stators) and Thapar (2004) (four stators) examined standard stator designs from mixer manufacturers and found

geometry to have an effect on droplet size. However both studies did not extensively investigate geometry parameters to isolate the effect of individual parameters.

Kamiya et al. (2010b) examined the effect of rotor-stator geometry in a Turbo Mixer (SPM-100V) on DSDs using a rapeseed oil-in-water system stabilised with milk protein. They examined five rotor-stator configurations to study the effect of the rotor-stator clearance with 1 and 2 mm gap widths, stator wall thicknesses of 2 and 2.5 mm, stator hole diameters from 1 to 6 mm, and stator opening ratios of 0.11 to 0.31. They found a larger stator opening ratio and a smaller hole size formed smaller mean droplet sizes, while the rotor-stator gap width had little effect on droplet size. The authors proposed an expression to evaluate the performance of rotor-stator configurations called the 'homogenisation coefficient':

$$C_h = A_F \pi^4 n_b (D + 2\delta) D^3 h_s \left(\frac{4t_s}{d_h} + 1\right)\left(\frac{N_P}{N_Q \pi^2} - 1\right) \tag{2.86}$$

The 'homogenisation coefficient' was based on energy dissipation rate in the stator hole, and the shear frequency which expresses the frequency of rotor blades passing the stator holes. Mean droplet size was correlated with total energy dissipation rate based on C_h:

$$\varepsilon_t = C_h \frac{N^4}{V_T} t_m \tag{2.87}$$

Mean droplet size correlated reasonably well with this definition of energy dissipation rate.

2.2.3.2.2 Scale

Typically the scale-up of emulsification processes in turbulent flows in stirred vessels has followed the Hinze model of droplet break-up based on the Kolmogorov theory of isotropic turbulence where drop size was related to average energy dissipation rate. It has been reported that the accuracy of the Hinze model can be improved by accounting for the effect of intermittency on disruptive stresses acting on drops (Baldyga et al., 2001), which may be because average energy dissipation rate oversimplifies irregularities in turbulent flow.

Whilst in the majority of cases, energy dissipation was used as a correlating parameter; Colenbrander (2000) reported that drop size in stirred vessels cannot be correlated with power input. The applicability of average energy dissipation rate as a scaling parameter was also questioned by Okufi et al. (1990) and El-Hamouz et al. (2009), who concluded that tip speed is a better scaling up parameter than energy dissipation rate.

Scaling up rules for rotor-stator mixers in literature is limited. Maa and Hsu (1996) examined emulsification of double emulsions using a Virtishear homogeniser with 1 and 2 cm rotors but a scale-up criterion was not proposed, only that an equilibrium droplet size of ~ 1 μm was achieved above 10,000 rpm at the large scale and above 15,000 rpm at the small scale.

According to the Handbook of Industrial Mixing (Atiemo-Obeng and Calabrese, 2004), manufacturers often design and scale-up rotor-stator mixers based on equal rotor tip speed, since the nominal shear rate in the rotor-stator gap is constant, when the shear gap width remains equal on scale-up:

$$\dot{\gamma} = \frac{\pi ND}{\delta} \tag{2.88}$$

For turbulent flow the actual shear rate in the rotor-stator gap varies substantially from Eq. (2.88), however Atiemo-Obeng and Calabrese (2004) state "*tip speed may control turbulence characteristics, especially if the spacing between stator elements (teeth or stator openings) as well as the shear gap width do not change on scale-up*". Findings by Francis (1999) and Thapar (2004) invalidating the effect of the rotor-stator gap width on drop size in turbulent flow suggests that tip speed, rather than nominal shear rate in the rotor-stator gap is the more important scale-up criterion.

Kamiya et al. (2010a,c) are two of the few studies undertaken using mixers at different scales. Kamiya et al. (2010a) examined a small mixer (D = 0.030 m) and a large mixer (D =

0.057 m) with 0.25 mm rotor-stator gaps, using the formulation described by Kamiya et al. (2010b) in Section 2.2.3.2.1. A 'homogenisation index' was suggested as applicable for estimating mean droplet diameter for different product volumes, rotor speeds, and mixer geometry configurations. The 'homogenisation index' (HI) is based on the local energy dissipation rate and the 'circulation number' (N_c):

$$HI = \left(\frac{P}{\rho V_h}\right).N_c \tag{2.89}$$

$$N_c = \left(\frac{Q}{V_T}\right).t_m \tag{2.90}$$

Mean droplet size correlated reasonably well ($R^2 = 0.926$) with HI:

$$d_{0,5} = HI^{-0.328} \tag{2.91}$$

These mixers were situated in vessels with external recirculation loops so this scaling parameter may also be applicable to in-line rotor-stator mixers.

Kamiya et al. (2010c) also examined a pilot plant scale mixer (D = 0.198 m) with a rotor-stator gap width of 0.001 m and opening ratio of 0.26, and a production scale mixer (D = 0.396 m), with rotor-stator gap width of 0.002 m and opening ratio of 0.18. Compared to the study of Kamiya et al. (2010a), this work investigated rotor-stator mixers without recirculation loops. Kamiya et al. (2010c) correlated mean droplet size with an expression for total energy dissipation rate and stated that this expression means scale-up does not require geometric similarity, constant tip speed or constant gap width.

Utomo et al. (2008) undertook three-dimensional computational fluid dynamics simulations of a batch Silverson rotor-stator mixer and suggested that scale-up should be based upon constant energy dissipation rate per unit mass and geometrical similarity.

However Mortensen et al. (2011) applied two-dimensional PIV to obtain the flow pattern in a batch rotor-stator mixer and suggested that constant rotor tip speed and geometric

similarity should be used as the scale-up criterion for mixing processes which depend on macro-scale phenomena, which may be the case for non-equilibrium drop size distributions in rotor-stator mixers. Yang (2011) simulated different scales of in-line Silverson rotor-stator mixer from batch and in-line bench scale mixers to pilot plant and factory scale mixers. The study concluded that tip speed may be a reasonable scaling up parameter for macroscopic velocity and shear fields in similar geometry devices, from pilot plant to factory scale, but not for mixers with vastly differing geometry, or from bench scale to the pilot plant or factory scale mixers. Yang (2011) suggested maintaining a constant flow rate per stator slot is required for scale-up.

2.2.3.2.3 Multiple passes

Emulsification using multiple passes requires knowledge of additional parameters such as the number of passes and processing time, and this operating mode also forms droplets closer to 'equilibrium'.

Baker (1993) investigated the effect of number of passes on droplet size distributions in a vessel with an in-line mixer placed in a recirculation loop, where some components of the emulsion would not have passed through the mixer at all, while others elements would have passed once, twice, thrice, etc. Hence it was useful to determine the fraction of material (C_i) in the vessel which had passed through the mixer i number of times. Baker (1993) applied a mass balance assuming that the stirred vessel was well mixed and the recycle loop volume was negligible compared to the batch volume:

$$C = 1 - e^{-\frac{Qt}{V_T}} = 1 - e^{-B} \tag{2.92}$$

Where $B = \frac{Qt}{V_T}$, is the number of batch vessel turnovers. The mass balance to predict the fraction of material circulated i times:

$$\frac{dC_i}{dt} = \frac{Q}{V_T}(C_{i-1} - C_i) \tag{2.93}$$

The solution of Eq. (2.93) (Baker, 1993):

$$C_i = \frac{e^{-B}(B)^i}{i!} \tag{2.94}$$

This function gives a Poisson distribution and enables the fraction of material in the vessel that has circulated through the mixer as a function of the number of batch turnovers (B) to be obtained. Drop size distributions in the vessel can then be predicted:

$$d(B) = \sum_0^\infty d_i C_i(N) = \sum_0^\infty d_i \frac{e^{-B}(B)^i}{i!} \tag{2.95}$$

This model was validated with experimental data for a low viscosity emulsion.

Brocart et al. (2002) examined the effect of recycling on emulsification of water-in-diesel oil emulsions. The mixers investigated were colloid mills, toothed rotor-stators and slotted rotor-stators at scales of 20 to 40,000 L at tip speeds of 9 to 60 m s^{-1}. The authors show power density in the stator holes can classify different mixer scales and designs, and proposed the following expression:

$$\varepsilon = \frac{\rho(U_T)^3}{4d_h} \tag{2.96}$$

2.3 Modelling flow and drop/particle break-up

Over the past decade, simulations of flow and modelling of droplet break-up and coalescence in rotor-stator mixers has grown, partly from an improvement in computational processing power and available software, coupled with a desire for industry to reduce labour intensive and time consuming experiments.

The hydrodynamics of the rotor-stator mixing head are simulated using computational fluid dynamics (CFD) to calculate velocity, kinetic energy and energy dissipation rate

profiles. Numerical simulations resolve continuity, momentum and turbulence models over a discrete domain with appropriate boundary conditions.

The continuity equation is essentially a mass balance equation which states that the sum of the mass flowing through all faces of an element must be zero for mass to be conserved (Fluent Inc., 2006; Utomo, 2009):

$$\frac{\partial \rho}{\partial t} + \frac{\partial}{\partial x_i}(\rho U_i) = 0 \tag{2.97}$$

The momentum balance equation is based on Newton's second law of motion which states that the rate of change of momentum in a control volume is equal to the sum of the forces acting upon it (Marden Marshall and Bakker, 2004):

$$\frac{\partial (\rho U_i)}{\partial t} + U_j \frac{\partial}{\partial x_j}(\rho U_i) = -\frac{\partial p}{\partial x_i} + \nu \frac{\partial^2 U_i}{\partial x_i \partial x_j} \tag{2.98}$$

Eq. (2.98) includes momentum transport by convection terms on the left, and diffusion terms on the right of the equation.

The continuity and momentum equations are solved by various methods including Direct Numerical Simulations (DES), and Large Eddy Simulations (LES) (Marden Marshall and Bakker, 2004). However, currently the most widely used approach for industrial flows is to solve Reynolds-Averaged Navier-Stokes (RANS) momentum equations, which are time-averaged and less computationally intensive than DES or LES models.

RANS models include a Reynolds stress tensor which means the models are not closed, however closure can be achieved using Reynolds stress models, or more commonly used eddy viscosity models (Utomo, 2009). The eddy viscosity model is a function of the turbulent viscosity (ν_t) which is not a fluid property and depends on the structure of the flow. ν_t can be calculated using models such as the standard $k-\varepsilon$ model, renormalised group (RNG) $k-\varepsilon$ model and realisable $k-\varepsilon$ model. The standard $k-\varepsilon$ model is one of the most widely used in engineering since it is robust and reasonably accurate (Fluent Inc., 2006). The

complete set of balance equations including the standard $k-\varepsilon$ turbulence model are (Fluent Inc., 2006; Utomo, 2009):

$$\frac{\partial U_i}{\partial x_j} = 0 \tag{2.99}$$

$$\frac{\partial U_i}{\partial t} + U_j \frac{\partial U_i}{\partial x_j} = -\frac{1}{\rho}\frac{\partial p}{\partial x_i} - \frac{2}{3}\frac{\partial k}{\partial x_i} + (\nu + \nu_t)\frac{\partial}{\partial x_j}\left(\frac{\partial U_i}{\partial x_j} + \frac{\partial U_j}{\partial x_i}\right) \tag{2.100}$$

$$\frac{\partial k}{\partial t} + U_j \frac{\partial k}{\partial x_j} = \frac{\partial}{\partial x_j}\left(\nu + \frac{\nu_t}{\sigma_k}\frac{\partial k}{\partial x_j}\right) + \nu_t\left[\left(\frac{\partial U_i}{\partial x_j} + \frac{\partial U_j}{\partial x_i}\right)\frac{\partial U_i}{\partial x_j}\right] - \varepsilon \tag{2.101}$$

$$\frac{\partial \varepsilon}{\partial t} + U_j \frac{\partial \varepsilon}{\partial x_j} = \frac{\partial}{\partial x_j}\left(\nu + \frac{\nu_t}{\sigma_\varepsilon}\frac{\partial \varepsilon}{\partial x_j}\right) + C_{\varepsilon 1}\nu_t \frac{\varepsilon}{k}\left[\left(\frac{\partial U_i}{\partial x_j} + \frac{\partial U_j}{\partial x_i}\right)\frac{\partial U_i}{\partial x_j}\right] - C_{\varepsilon 2}\frac{\varepsilon^2}{k} \tag{2.102}$$

$$\nu_t = C_\mu \frac{k^2}{\varepsilon} \tag{2.103}$$

and $C_\mu = 0.09, \sigma_k = 1, \sigma_\varepsilon = 1.3, C_{\varepsilon 1} = 1.44, C_{\varepsilon 2} = 1.92$ (Fluent Inc., 2006).

Eq. (2.99) is the reduced version of the continuity equation for incompressible fluids and Eq. (2.100) is the RANS momentum equation that describes the fluid velocity vectors. Resolution of the transport equations in Eqs. (2.100) to (2.103) enable calculation of local kinetic energy and energy dissipation rate.

2.3.1 Flow simulation in rotor-stator mixers

The numerical simulation of flow in rotor-stator mixers is less widely available in literature than for stirred vessels, partly due to the complexity of the geometry. For example, spatial resolution of the flow is required at very small length scales around hundreds of microns in the rotor-stator gap, and high rotor speeds require short time steps in transient simulations.

One of the earliest published works using CFD in rotor-stator mixers was given by Sparks (1996). He examined the effect of the rotor-stator gap width from 2.1 to 0.23 mm to increase ε_{max} from 45,000 to 10×10^6 W kg^{-1}, respectively, although Sparks did concede that non-convergence of the solution may result in inaccurate values.

Calabrese et al. (2002) undertook 2D single phase numerical simulations of an in-line IKA Works rotor-stator mixer, to compare the effect of gap widths of 0.5 mm and 4 mm on the flow fields. For turbulent flow, they found mechanical forces in the shear gap were not principally responsible for emulsification and dispersion processes; instead the predominant dispersion mechanism resulted from impingement on the stator and wall jets radiating from the stator. For the enlarged gap stator (4 mm), impingement of the leading edge of the stator teeth was reduced, resulting in lower levels of turbulent kinetic energy at the hole edges. Therefore, for efficient mixing and dispersion it was necessary to have a narrow shear gap even if the gap is not a major contributor in the dispersion process.

Barailler et al. (2006) investigated the laminar flow of viscous fluids in rotor-stator mixers using 3D CFD geometry, using a VMI-Rayneri 4-blade rotor with 72-slotted stator. The authors found the maximum shear stress occurred in the clearance between the rotor blade tip and the stator. It was also shown that pseudo-cavern size scaled with classical Reynolds number (Eq. (2.7)).

Utomo et al. (2008) simulated a batch Silverson L4R rotor-stator mixer using sliding mesh and standard $k-\varepsilon$ turbulence models, with LDA experimental validation. They established that about 70% of the energy was dissipated close to the mixing head and that energy dissipation rate scaled with N^3. They found jet velocity and flow rate through the stator holes to be directly proportional to the rotor speed, with maximum energy dissipation rates occurring in stagnant points at the hole edges. Agreement between simulated and experimental results was good, with a calculated power number of 1.55 and an experimental value of 1.7. Utomo et al. (2009) extended this work and investigated the effect of stator geometry on the flow pattern and energy distribution rate profiles (Figure 2.11) and found predicted power number values were 10-20% lower than experimental Po for all geometry,

and power number was proportional to total flow rate. Energy dissipation rate distributions were more uniform from smaller hole stators, therefore it was concluded that narrower hole stators may produce dispersions with narrower DSDs.

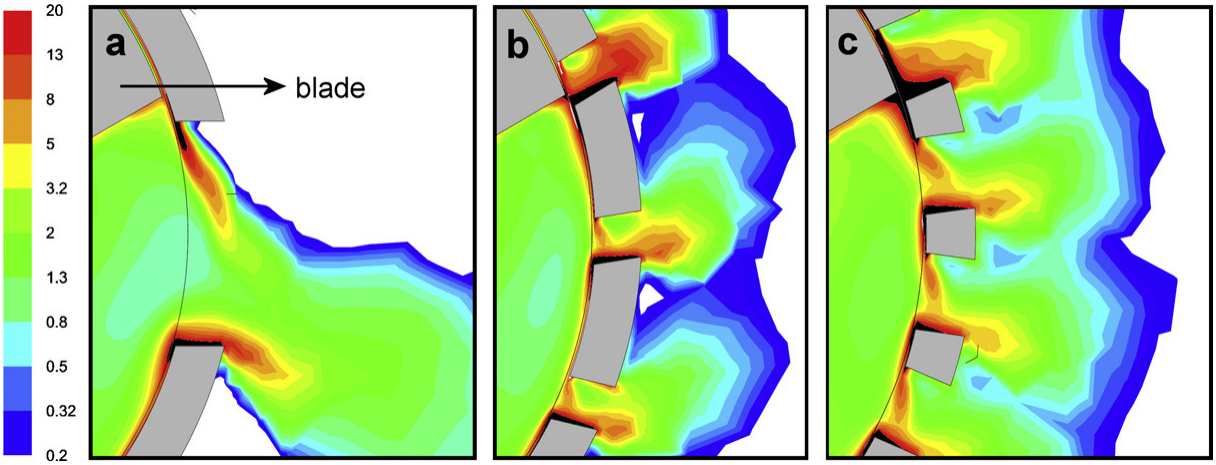

Figure 2.11: Normalised energy dissipation rate contours by Utomo et al. (2009) in a L4R batch rotor-stator mixer for (a) disintegrating, (b) slotted head and (c) square hole stators.

Baldyga et al. (2007a) conducted a micromixing and CFD study of an in-line Silverson mixer. Using a standard $k-\varepsilon$ turbulence moving reference frame model, the rotor-stator geometry was simulated in 2D to calculate power number constants. Based on energy dissipation, they stated that for low values of flow number, power can be expressed by a single power term, and a two-term expression for high flow numbers:

$$P = 0.42\rho N^3 D^5 \qquad N_Q < 0.013 \tag{2.104}$$

$$P = 0.10\rho N^3 D^5 + 18.4 Q N^2 D^2 \qquad N_Q > 0.013 \tag{2.105}$$

Power draw was predicted by torque on the rotor shaft:

$$P = 2\pi NT \tag{2.106}$$

And by integrating energy dissipation rate across the mixer volume:

$$P = \rho h_s \int_{A_s} \varepsilon dA_s \tag{2.107}$$

Calculated values of power draw from torque and energy dissipation rate were only slightly higher than experimental values.

Ozcan-Taskin et al. (2011) undertook 3D simulations in two in-line rotor-stator mixers; a 150/250 Silverson fitted with two stator geometry and an Ytron Z unit (Ytron-Quadro). The flow fields were simulated using the realisable $k-\varepsilon$ turbulence model coupled with a steady state multiple reference frame model. As expected, the velocity profile for the Ytron was greatly different compared to the Silverson mixer investigated. In particular, recirculation of flow back into the rotor region was not observed for the Ytron mixer, while for the Silverson mixer the fluid returned to the zones of highest energy dissipation rate several times. CFD predictions of power draw based on the torque method from Eq. (2.106) gave good agreement with experimental power values, however CFD vastly underpredicted power draw based on integration of energy dissipation rate, for both types of mixer and all geometries investigated.

Yang (2011) also solved 3D simulations in a batch Silverson L4R rotor-stator mixer, and three in-line rotor-stator mixers; an inline L4R, a 450 LS and a 600 LS. Yang (2011) employed the realisable $k-\varepsilon$ turbulence model with non-equilibrium wall functions. A hybrid RANS simulation was developed to reduce computational time by applying the sliding mesh method to the region where interactions between the rotor and the stator walls are important, and the multiple reference frame method in the region where time periodicity is not important (far from the mixing head). The vessel flow field of the batch L4R bench Silverson was also validated using Particle Image Velocimetry. Yang (2011) concluded that velocity, turbulence and deformation rate fields of the pilot plant and factory mixers were similar but significantly different compared to the batch mixer.

2.3.2 Population balance modelling

Drop size distributions in multiphase liquid-liquid systems depend on the rate of droplet breakage and coalescence, which occur simultaneously in non-surfactant systems. Droplet breakage and coalescence models have been used within the framework of population balances to calculate drop size distributions, which can be solved in conjunction with CFD using local flow conditions (Jaworski et al., 2007). The population balance model is basically a mass balance on the dispersed phase in the system (Ramkrishna, 2000):

$$\frac{\partial n(v,t)}{\partial t} + \nabla\left[\vec{U} n(v,t)\right] + \nabla[G_V n(v,t)] = B_d - D_d \tag{2.108}$$

The first term on the left describes the time change of a number of drops of size v, the second term describes the change of number of drops of size v by convection and the third term describes the net change of drops of size v due to continuous growth by mass transfer. The terms on the right describe disappearance of drops (death, D_d) and appearance of drops (birth, B_d) which result from coalescence and breakage. This general version of the population balance can be simplified by neglecting coalescence, which is reasonable for low dispersed phase volume fractions in the presence of excess surfactant, for perfectly mixed systems (Raikar et al., 2009):

$$\frac{\partial n(v,t)}{\partial t} = -g(v)n(v,t) + \int_v^\infty \beta(v,v')\nu(v')g(v')n(v',t)dv' \tag{2.109}$$

Where $n(v,t)$ is the number of drops with size v per unit volume, $\beta(v,v')$ is the size distribution of daughter droplets (probability density function), $g(v)$ is the breakage rate of drops of size v discussed above and $\nu(v')$ is the number of daughter drops formed by breakage of a drop of size v'.

In literature, many theoretical breakage and coalescence models have been developed, the majority of which were reviewed by Liao and Lucas (2009, 2010). However, in the

majority of emulsification processes, coalescence is highly undesirable and is prevented by the selection of appropriate surfactants; hence details of coalescence are not discussed further.

The kinetics of droplet breakage is described in terms of breakage frequency and the number of droplets (daughter drops) the large drop (mother drop) is broken into, as described by Coulaloglou and Tavlarides (1977):

$$g(d) = \left(\frac{1}{breakage\ time}\right)\left(\begin{matrix} fraction\ of \\ drops\ breaking \end{matrix}\right) = \frac{1}{t_b}\frac{N_b}{N_T} \tag{2.110}$$

This model assumes $g(d)$ is a product of the fraction of drops breaking, and the reciprocal time for breakage to occur. One of the first models was developed by Coulaloglou and Tavlarides (1977), based on the fact that an oscillating drop will deform and break once the kinetic energy due to pressure fluctuations equals the droplets' surface energy, assuming the kinetic energy is normally distributed:

$$g(d) = K_1 \frac{\varepsilon^{1/3}}{d^{2/3}(1+\Phi)} exp\left(-\frac{K_2\sigma(1+\Phi)^2}{\rho_d \varepsilon^{2/3} d^{5/3}}\right) \tag{2.111}$$

This model has two unknown constants K_1 and K_2, which are calculated from experimental data. Many other expressions for droplet breakage frequency were developed (Liao and Lucas, 2009).

In addition to selection of the droplet breakage frequency, description of the daughter drop distribution function is required. A model describing the method by which the drops fragment, known as a probability density function (PDF), defines the daughter size distribution, for example the symmetric fragmentation distribution (Jaworski et al., 2007):

$$b(L|L_i) = 2\delta(L - L_i/2) \tag{2.112}$$

This fragment distribution function assumes binary droplet breakage into two equal daughter droplets. A range of fragmentation distributions are summarised by Marchisio et al. (2003) and Liao and Lucas (2009).

2.3.3 Population balance modelling in rotor-stator mixers

Solving both momentum balance equations for turbulent flow and population balance equations is not straightforward, especially for rotor-stator mixers where complex geometry creates high tip speeds and wide kinetic energy distributions. Relatively recently Baldyga et al. (2008) used this approach to analyse aggregate breakage formed from nano-particles. Population balance equations describing the kinetics of breakage of aggregates were solved using the quadrature methods of moments (QMOM) (Marchisio et al., 2003) linked with the solver of momentum balance equations within Fluent. Population balance equations can be solved by two main methods in Fluent, either by the discrete model which divides the whole distribution into bins, or by the method of moments which summarises the drop size distribution in terms of moments. Baldyga et al. (2008) found calculated transient size distributions during breakage were in good agreement with experimental data using the QMOM method.

The QMOM method simplifies the DSDs by describing them in terms of moments, which means some information about the distribution is lost, however QMOM is less computationally intensive, with relatively small errors. QMOM employs a quadrature approximation (Marchisio et al., 2003):

$$m_k(x,t) \approx \sum_{i=1}^{N} w_i L_i^k \tag{2.113}$$

The weights and abscissas are determined by the product-difference algorithm from the input of lower-order moments, see Marchisio et al. (2003). Once the general population balance equation is written in terms of moments, the following closed transport equation can be derived for moments for breakage only (Jaworski et al., 2007; Baldyga et al., 2007b):

$$\frac{\partial m_k(x,t)}{\partial t} + \langle U_{id} \rangle \frac{\partial m_k(x,t)}{\partial x_i} - \frac{\partial}{\partial x_i}\left[D_{\mathrm{T}} \frac{\partial m_k(x,t)}{\partial x_i}\right] = \sum_{i=1}^{N} a_i b_i^{-(k)} w_i - \sum_{i=1}^{N} a_i L_i^k w_i \tag{2.114}$$

Where $a_i = a(L_i)$ and $b_i^{-(k)} = \int_0^\infty L^k b(L|L_i) dL$.

Mean drop diameters can be calculated from the moments using Eq. (2.36), and drop size distributions can be reconstructed from the moments (John et al., 2007).

2.4 Summary

Theory and literature relating to power draw measurement, droplet break-up, characterisation of drop size distributions, and numerical simulations and population balance modelling were described. Particular emphasis focused on the application of these topics to rotor-stator mixing, and the subsequent chapters aim to extend research in these areas to in-line rotor-stator mixers.

CHAPTER 3. MATERIALS AND EXPERIMENTAL METHODS

3.1 Equipment and experimental assembly

3.1.1 Equipment

The Silverson rotor-stator mixers (Silverson Machines Ltd., Chesham, UK) investigated in this study were three scales of in-line devices; the 088/150 UHS, 150/250 MS and 450/600 UHS models (Figure 3.1 and Table 3.1). 'MS' is the abbreviation for 'multiscreen' and 'UHS' means 'ultra hygienic screen'. The design of each mixer was identical except for the position of the outlet which is placed at the bottom of the mixing chamber for the 'UHS' mixers, so they are self draining.

(a) 088/150	**(b) 150/250**	**(c) 450/600**
	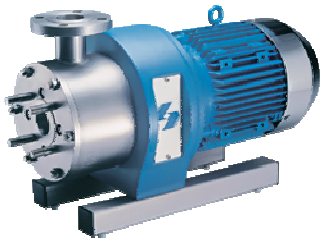	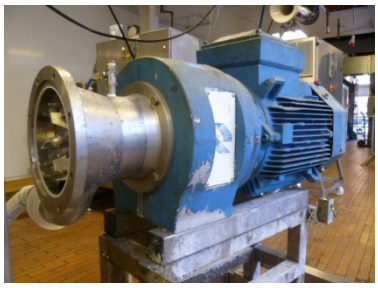

Figure 3.1: Images of the (a) Laboratory scale (088/150), (b) Pilot plant scale (150/250) and (c) Factory scale (450/600) in-line Silverson rotor-stator mixers (from Silverson, 2012).

Table 3.1: Dimensions of the laboratory scale, pilot plant scale and factory scale in-line Silverson rotor-stator mixers fitted with double standard emulsor stators.

Mixer scale	**Laboratory scale 088/150**	**Pilot plant scale 150/250**	**Factory scale 450/600**
Inner rotor diameter, $D_{r,i}$ (mm)	22.4	38.1	114.3
Outer rotor diameter, $D_{r,o}$ (mm)	38.1	63.5	152.4
Inner rotor blades	4	4	4
Outer rotor blades	4	8	12
Rotor height, h_r (mm)	11.10	11.91	31.75
Swept rotor volume, V_H (mm^3)	12,655	37,726	579,167
Inner stator diameter, $D_{s,i}$ (mm)	22.71	38.58	114.6
Outer stator diameter, $D_{s,o}$ (mm)	38.58	63.98	152.7
Outer stator height, h_s (mm)	14.33	16.66	32.56
Inner stator			
○ *Number of holes,* n_h	*180*	*300*	*2,016*
○ *Rows,* n_r	*6*	*6*	*14*
○ *Holes per row,* n_{hr}	*30*	*50*	*144*
Outer stator			
○ *Number of holes,* n_h	*240*	*560*	*2,496*
○ *Rows,* n_r	*5*	*7*	*13*
○ *Holes per row,* n_{hr}	*48*	*80*	*192*
Outer stator perimeter of openings, P_h (mm)	1,197	2,793	12,448
Outer stator screen area, A_s (mm^2)	12,655	37,726	579,167
Outer stator open area, A_h (mm^2)	1,736	3,349	15,620
Fraction of outer stator open area, A_F (%)	27.4	33.1	31.6
Maximum rotor speed, N (rpm)	10,000	12,000	3,600
Maximum flow rate investigated, M (kg h^{-1})	1,500	6,200	6,200

The main mixer used in investigations was the pilot plant scale Silverson 150/250 MS rotor-stator mixer, specially commissioned for research. This mixer has a 22 kW motor controlled by a frequency inverter with a maximum rotor speed of 12,000 rpm (200 Hz), compared to 6,000 rpm for standard machines, which allowed a wide range of processing

conditions to be investigated. The 088/150 and 450/600 mixers are capable of achieving maximum speeds of 10,000 rpm and 3,600 rpm, respectively. The main details and dimensions of these mixers are given in Table 3.1.

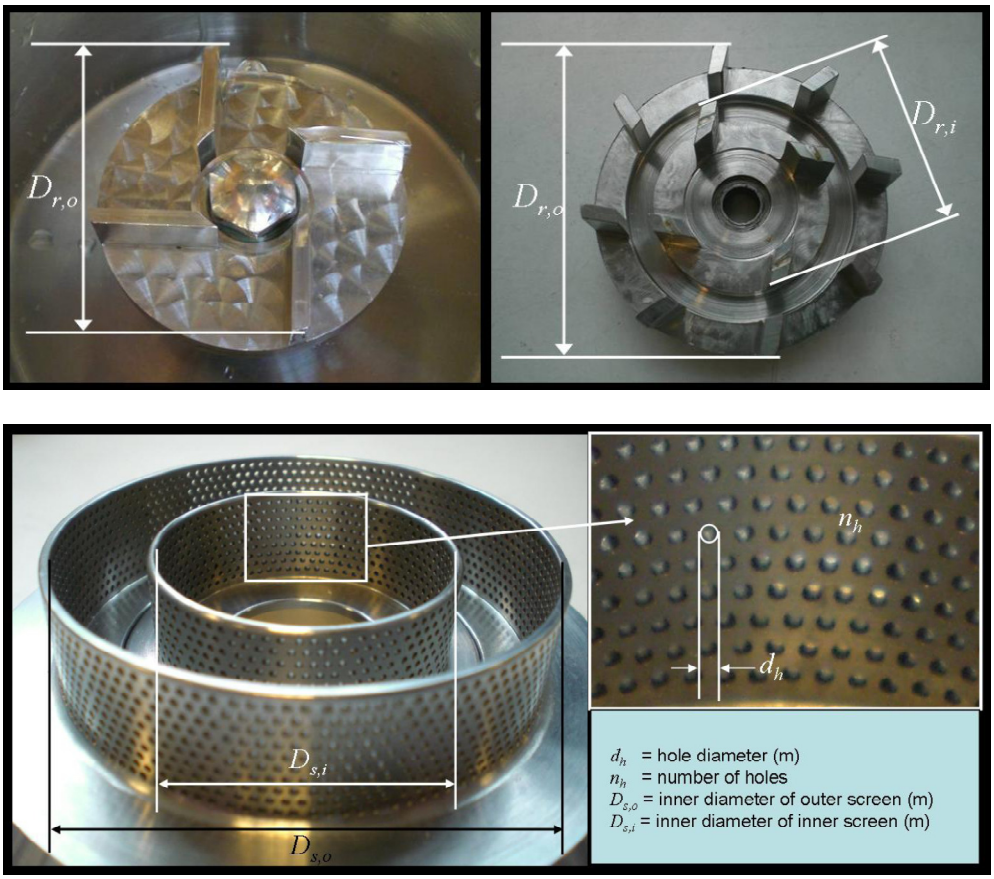

Figure 3.2: Rotor and stator dimension nomenclature.

All of the mixer scales comprised of double rotors, which sit within standard double Silverson emulsor screens (Figure 3.3). The rotor-stator gap width (δ) was 0.24 mm, the stator thickness (t_s) was 2.0 mm, and the stators contain 1.59 mm diameter holes (d_h) on a triangular pitch at all scales.

088/150	150/250	450/600
		
		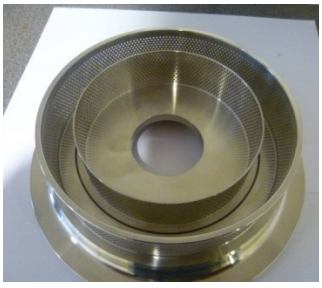

Figure 3.3: Images of double rotors and standard Silverson double emulsor stators used in the 088/150,150/250 and 450/600 mixers.

The pilot plant scale 150/250 mixer was used in the majority of this work (Figure 3.4) to investigate the effect of formulation variables, and in total, thirteen rotor-stator configurations. Two rotor designs were examined; single and double rotors, as well as six stator designs, see Table 3.2 and Figure 3.5. The stator heights (h_s) were 16.7 mm.

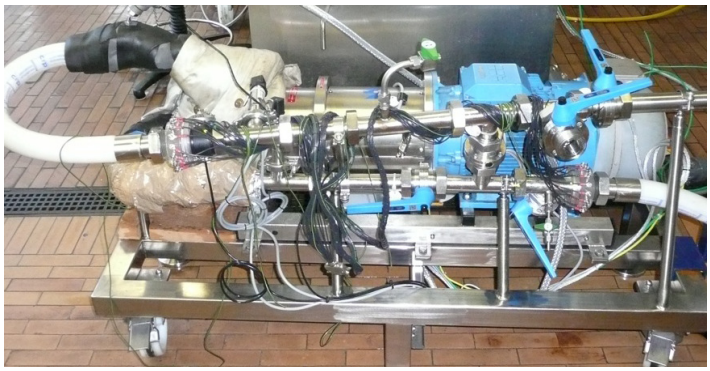

Figure 3.4: The in-line Silverson 150/250 mixer rig.

Table 3.2: Details and dimensions of the rotor-stator configurations investigated.

Configuration	Rotors	Stators	Stator design	d_h (mm)	n_r (-)	n_{hr} (-)	n_h (-)	δ (mm)	t_s (mm)	A_s (mm^2)	P_h (mm)	P_F (mm^{-1})	A_h (mm^2)	A_F (-)
A	2	0	No stator	-	-	-	-	-	-	-	-	-	-	-
B	1	1	Fine emulsor	0.794	10	125	1250	0.169	2.0	3342	3117	0.933	618.5	0.185
C	1	1	Square hole	2.381	3	48	144	0.127	2.0	3337	1372	0.411	816.5	0.245
D	1	1	Standard emulsor	1.588	7	80	560	0.119	2.0	3337	2793	0.837	1108	0.332
E	2	1	Blank	-	-	-	-	0.152	2.0	3340	-	-	-	-
F	2	1	Small 3 row	1.588	3	24	72	0.178	2.0	3343	359.1	0.107	142.5	0.426
G	2	1	Standard emulsor	1.588	7	80	560	0.119	2.0	3337	2793	0.837	1108	0.332
H	2	1	Large 3 row	4.753	3	24	72	0.178	2.0	3343	1077	0.322	1283	0.384
I	2	1	Large 3 row wide gap	4.753	3	24	72	1.016	2.0	3430	1077	0.314	1283	0.374
J	2	1	Large 3 row thick	4.753	3	24	72	0.152	8.0	3340	1077	0.384	1283	0.384
K	2	2	Fine emulsor	0.794	9	75	675	0.169	2.0	1822	1683	0.924	334.0	0.183
					10	125	1250			3342	3117	0.933	618.5	0.185
L	2	2	Standard emulsor	1.588	6	50	300	0.241	2.0	1829	1496	0.818	593.8	0.325
					7	80	560			3349	2793	0.834	1108	0.331
M	2	2	Standard emulsor wide gap	1.588	6	50	300	0.483	2.0	1852	1496	0.808	593.8	0.321
					7	80	560			3375	2793	0.828	1108	0.329

For details on the double rotor, see Table 3.1 for the 150/250 mixer. The single rotor has exactly the same dimensions but with no inner rotor blades and only four outer rotor blades (Figure 3.5).

	
Single 4 bladed rotor – used in config. B, C, D	Double 8 bladed rotor – used in config. A, E, F, G, H, I, J, K, L, M
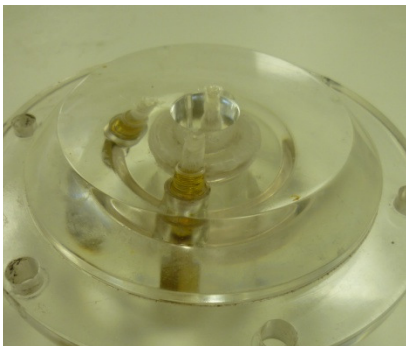	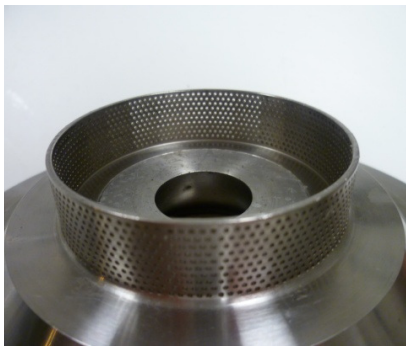
No stator – used in config. A	Single fine emulsor stator – used in config. B
	
Single square hole stator – used in config. C	Single standard emulsor stator – used in config. D and G
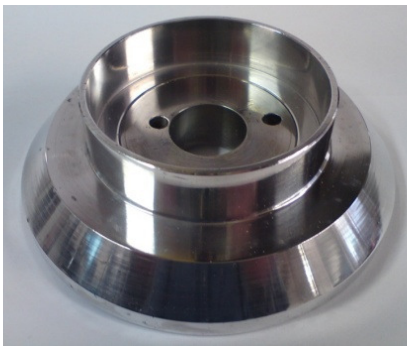	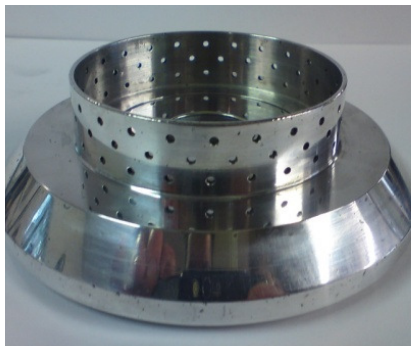
Blank stator – used in config. E	Small 3 row stator – used in config. F

	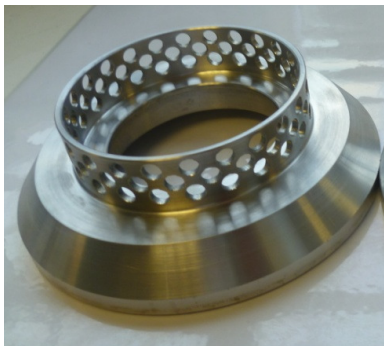
Large 3 row stator – used in config. H	Large 3 row wide gap stator – used in config. I
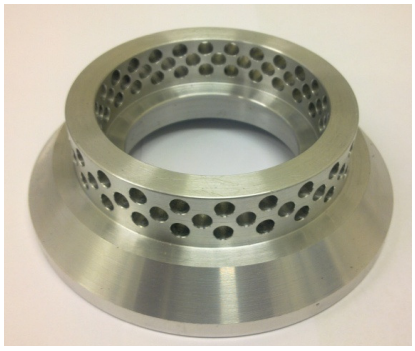	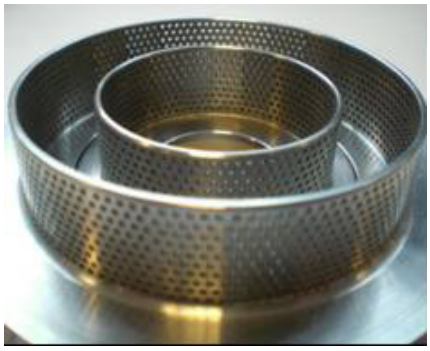
Large 3 row thick stator – used in config. J	Double fine emulsor stator – used in config. K
	
Double standard emulsor stator – used in config. L	Double standard emulsor stator wide gap – used in config. M

Figure 3.5: Images of the rotors and stators used in the various rotor-stator configurations given in Table 3.2.

3.1.2 Experimental arrangement

The experimental rig (Figure 3.6) primarily consisted of the Silverson mixer and agitated mixing vessels to store water for power measurements and prepare coarse emulsions for emulsification experiments. This rig was situated in the Morton Laboratory at The University of Manchester's Chemical Engineering and Analytical Sciences Department.

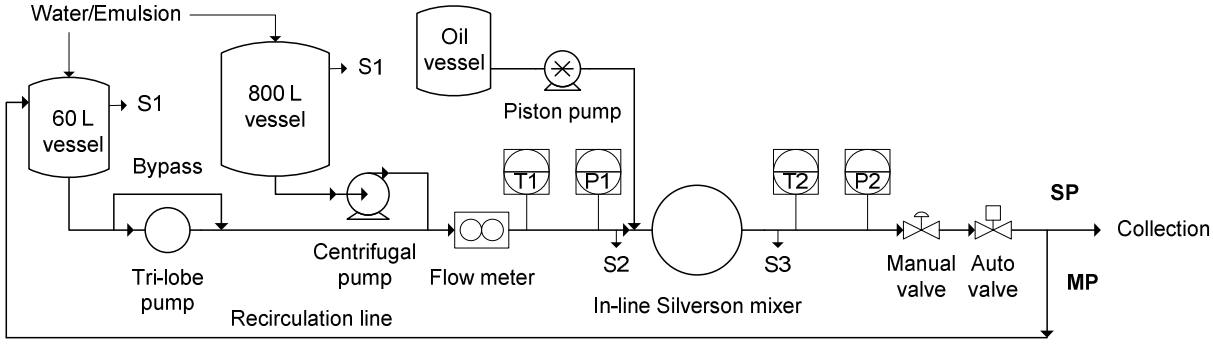

Figure 3.6: Experimental rig arrangement; 'SP' and 'MP' denotes single pass and multiple pass routes, respectively. Sampling points: S1 - 'tank', S2 - 'mixer inlet' and S3 - 'mixer outlet'.

The experimental rig (Figure 3.6) comprised of two mixing vessels of 60 L and 800 L capacity. The 800 L mixing vessel (Figure 3.7a) included a 0.305 m diameter Cowles Disc impeller (Figure 3.8), while the 60 L vessel contained a 0.126 m diameter high shear dissolver disk (similar to the Cowles Disc). The 60 L vessel included an anchor, which was ideal for keeping the emulsion homogenous.

The 800 L mixing vessel was used for power measurements and preparation of coarse emulsions for the larger flow rate experiments, while the 60 L vessel was used in experiments with smaller flows (< 1,500 kg h^{-1}), and for multiple pass operation. Each vessel was jacketed to enable temperature control.

(a) 800 L vessel	(b) 60 L vessel
	

Figure 3.7: Mixing vessels.

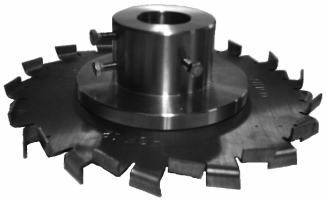

Figure 3.8: Sawtooth Cowles Disc agitator in the 800 L vessel.

All in-line mixers have considerable self-pumping ability, although they are typically employed with a pump in industry. Fluid from each vessel was either pumped or gravity-fed to the mixer (via a 38.1 mm pipeline), with a centrifugal pump connected from the 800 L vessel. A speed adjustable rotary tri-lobe pump was connected in-line from the 60 L vessel, which could be bypassed.

Flow rates were measured using a Coriolis mass flow meter (Micro Motion R-Series, Emerson Process Management), and pressure drop (up to 10 barg) and temperature using transducers (PT100) at the mixer inlet and outlet. All instrumentation was connected to the

DeltaV digital automatic control system (Emerson Process Management) which automatically records pressures, temperatures, flow rate, rotor speed, density, and vessel impeller speeds. Downstream of the mixer, a manual diaphragm valve, and an automatic proportional valve (custom-built) in conjunction with the flow meter, controlled the flow rate. Sampling points were situated at the mixer inlet and outlet, and in the vessels.

3.2 Power draw measurement

Power draw for a mixing device is a sum of (King et al., 1988, in Padron, 2001):

$$P_{Total} = P_{Motor} + P_{Bearings} + P_{Fluid} \tag{3.1}$$

Total power consumed can be measured via the motor (Ascanio et al., 2004):

$$P = \sqrt{3}VIF \tag{3.2}$$

Where $\sqrt{3}$ indicates a three phase power supply. The power factor (F) is a function of the power load, and calculation of F for different loads is difficult, therefore significant inaccuracy in the total power draw measurement can occur if Eq. (3.2) is used (Ascanio et al., 2004). Consequently, power draw measurement through the electrical motor was not used; instead power was measured by torque and calorimetry methods. These techniques measure the power imparted to the fluid (P_{Fluid}) and the power consumed due to friction in the bearings ($P_{Bearings}$), however as only P_{Fluid} is important for calculations, $P_{Bearings}$ was measured and subtracted from the total power draw. Kowalski (2009) provides an expression for power draw of an in-line rotor-stator mixer in turbulent flow.

3.2.1 Characterisation methods

Two techniques for measuring power draw were applied; the calorimetry and torque methods. The torque method is generally more accurate but requires a specially adapted Silverson with an extended rotor shaft for a torque meter, while calorimetry only requires

flow rate, pressure and temperature measurements, thus can be applied in any pilot plant or factory environment. Hence, the 150/250 Silverson was the only mixer where torque was employed to measure power draw. Power measurements by each technique were used to obtain the power draw constants in Eq. (2.21) (Cooke et al., 2012).

3.2.1.1 Torque method

For turbulent power draw measurement, the 800 L tank (Figure 3.7a) was filled with water at ambient temperature and overflowed to maintain a constant head. Water was then fed into the Silverson mixer at rotor speeds from 3,000 rpm to 11,000 rpm in steps of 1,000 rpm. Torque was measured over a series of flow rates from 0 kg h^{-1} to the maximum possible using the rig configuration (~ 6,200 kg h^{-1} at 11,000 rpm). This procedure was used to measure power of thirteen rotor-stator configurations in the 150/250 mixer.

At steady state conditions, when flow rate/pressure, rotor speed and temperature were constant, a torque measurement was taken for 30 seconds. The torque meter (Torqsense RWT 321, Sensor Technology Ltd.) (0-20 N m) took ~ 100 torque readings per second, so ~ 3,000 readings were taken per measurement and averaged. Power was calculated from:

$$P_{Torque} = 2\pi NT \tag{3.3}$$

The torque meter (Figure 3.9a) also measured the bending moments on the rotor shaft in addition to the torque. This meant the torque meter gave different torque readings at 0 rpm before and after the experimental condition measurement was taken, depending on the shaft position when it became stationary. In addition, at 0 rpm, measured torque should be zero (Eq. (3.3)), however in reality torque readings at 0 rpm drifted from 0 N m with time. To account for this, a 'running' zero was taken before and after each experimental condition. This was achieved by running the Silverson at a low speed (50 rpm) with the outlet valve closed (zero flow rate) where measured torque is very low. Values of 'running zero' torque before and

after the experimental condition were averaged and subtracted from the torque measurement at the experimental condition.

(a) Torque meter	(b) Temperature probes
	

Figure 3.9: Power measurement methods: (a) Torque meter on the rotor shaft and (b) Temperature probes at the mixer inlet and outlet with lagging.

Power required to overcome friction in the shaft bearings ($P_{Bearings}$) was determined with the rotor removed, and replaced with a disc without blades (bladeless rotor) to minimise fluid resistance. Torque was then measured over the same range of rotor speeds (3,000-11,000 rpm) at a constant low flow rate of 500 kg h^{-1}. $P_{Bearings}$ was roughly constant with flow rate as the resistance in the bearings is mainly a function of the rotor speed. In addition, power draw measurement with the rotor removed meant the mixer could not pump fluid to any degree. Total power draw was obtained by subtracting the 'bearing losses' value from the measurement condition value:

$$P_{Torque} = 2\pi N(T - T_Z) - 2\pi N\left(T_B - T_{B,Z}\right) \tag{3.4}$$

3.2.1.2 Calorimetry method

Power draw was determined using the calorimetry method from an energy balance across the Silverson mixing head. Figure 3.10 shows a diagram of the in-line rotor-stator mixer including the parameters used in the energy balance.

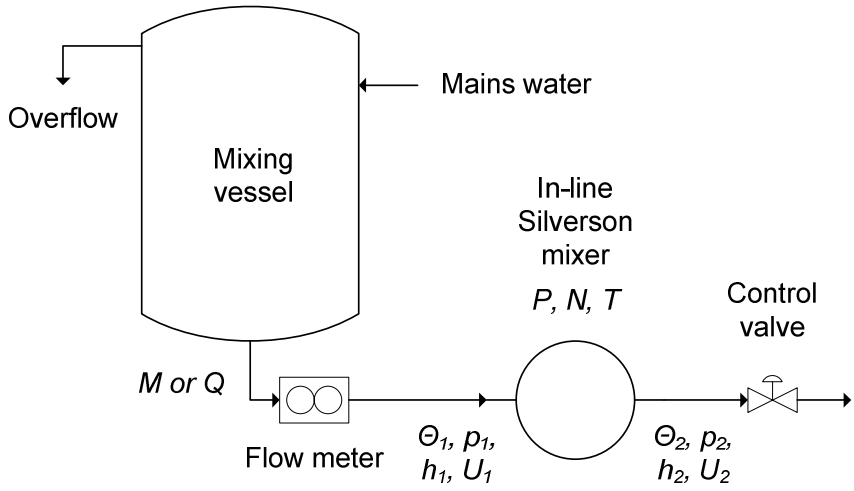

Figure 3.10: Energy balance diagram for the in-line rotor-stator mixer.

Power consumed due to fluid movement was calculated from (Ascanio et al., 2004):

$$P_{Energy} = MC_P \frac{d\theta}{dt} \tag{3.5}$$

Power consumed due to pumping was calculated from Bernoulli's steady flow energy equation:

$$P_{Flow} = Q\left(\frac{1}{2}\rho\left({U_2}^2 - {U_1}^2\right) + \rho g(h_2 - h_1) + (p_2 - p_1)\right) \tag{3.6}$$

Each of the terms on the right hand side of Eq. (3.6) contributes to power draw. The first term is a kinetic energy term, which is zero as the inlet and outlet pipe diameters are equal, so the flow velocity at the inlet and outlet are equal. The second term is a potential energy term which accounts for the difference in fluid height between the mixer inlet and outlet, which is ~ 0.2 m for the 150/250 MS Silverson. This corresponds to ~ 0.1% of the power draw at

higher rotor speeds, and ~ 1% at the lower rotor speeds, so was considered negligible. The third term is a pressure drop term, which is greater at higher rotor speeds and flow rates, and ranges from 5-15%, so was included in the measurement of power draw.

The calorimetry measurement procedure was the same as for the torque method described in Section 3.2.1.1. One of the main differences is the lowest flow rate measured was 300 kg h^{-1} as opposed to 0 kg h^{-1} for the torque method, since it was not possible to measure temperature difference without a flow. This method was used to measure power of all three mixer scales, and the experimental conditions are detailed in Table 3.5 (Section 3.3.2.2).

In addition, for calorimetry the Silverson head and pipe work at the outlet were well lagged so that heat losses to the surroundings were negligible and the system was considered to be adiabatic. The outlet thermocouple was placed close to the mixing head to minimise heat losses from the pipe work between the probe and the mixer, while the inlet thermocouple was unlagged to ensure it did not measure heat transferred from the mixer. This was also overcome by fitting a plastic section into the inlet pipeline.

For each experimental condition, 2 minutes were allowed for the system to reach steady state conditions. Then flow rate, temperature and pressure measurements were recorded automatically for > 5 minutes. The DeltaV operating system was configured to take 6 readings per minute, so at least 30 readings were taken per measurement condition and averaged. Data not at thermal equilibrium was discarded, so at least 5 minutes of data were recorded to allow for conditions that took longer to achieve equilibrium. Assuming steady state conditions, power draw was calculated using Eq. (3.5), from the temperature difference between the mixer inlet and outlet ($\Delta\theta$).

Systematic temperature differences between the thermocouples were accounted for, since each thermocouple gave different temperature values for the same fluid temperature,

thus a temperature correction between the thermocouples (θ_c) was required. The correction between temperature probes ranged from 0.11 to 0.17°C, however as the temperature differences were also very small and difficult to measure accurately, even a small systematic error could lead to an overall error of ~ 15%. The temperature correction was determined by feeding water under gravity at a low flow rate (~ 300 kg h^{-1}), at constant temperature through the system, with the mixer switched off. The temperature correction was taken once the temperature readings at the mixer inlet and outlet reached constant values, which took a couple of minutes if the mixer had been running previously, to ensure the metal in the mixer/pipelines was not inputting heat to the fluid.

Power draw due to heat generation from friction in the bearings was measured in the same way as for torque, using a bladeless rotor to minimise fluid resistance. The temperature rise due to friction in the bearings (θ_b), and the temperature correction between the thermocouples (θ_c), was subtracted from the total temperature difference ($\Delta\theta = \theta_o - \theta_i$):

$$P_{Heat} = MC_P(\Delta\theta - \theta_c) - MC_P(\Delta\theta_b - \theta_c) + Q(p_2 - p_1) \tag{3.7}$$

3.2.2 Determination of power draw constants

The turbulent power constants in Eq. (2.21) were obtained by two main methods, plus a third alternative method known as the 'fast' method (Cooke et al., 2012).

The first method applied regression analysis to obtain the power constants, Po_Z, k_1 and P_L. Multi-linear regression was undertaken to fit the raw data calculated using Eq. (3.4) and Eq. (3.7) to obtain the constants and the standard error associated with the fitting procedure. The 'Regression' function available in the 'Data Analysis Tools' in Microsoft Excel 2007 was employed, with measured power as the dependent variable $\rho N^3 D^5$ and MN^2D^2 as the independent variables (the inputs). The outputs were the constants Po_Z, k_1 and

P_L, shown in Figure 3.11. Careful measurement should produce a low value of P_L (intercept), so the regression can be repeated with P_L set as zero (no losses).

SUMMARY OUTPUT						
Regression Statistics						
Multiple F	0.998654					
R Square	0.99731					
Adjusted	0.997157					
Standard I	38.03786					
Observati	38					
ANOVA						
	df	*SS*	*MS*	*F*	*gnificance F*	
Regressio	2	18777846	9388923	6489.087	1.05E-45	
Residual	35	50640.76	1446.879			
Total	37	18828487				
	Coefficients	*tandard Err*	*t Stat*	*P-value*	*Lower 95%*	*Upper 95%*
P_L	-16.2865	11.00396	-1.48006	0.147803	-38.6258	6.052705
Po_z	0.128485	0.003392	37.87603	5.33E-30	0.121598	0.135371
k_1	11.12521	0.159724	69.65282	3.91E-39	10.80095	11.44947

SUMMARY OUTPUT						
Regression Statistics						
Multiple F	0.999465					
R Square	0.99893					
Adjusted	0.971123					
Standard I	38.66173					
Observati	38					
ANOVA						
	df	*SS*	*MS*	*F*	*gnificance F*	
Regressio	2	50255694	25127847	16810.96	6.27E-53	
Residual	36	53810.27	1494.73			
Total	38	50309504				
	Coefficients	*tandard Err*	*t Stat*	*P-value*	*Lower 95%*	*Upper 95%*
P_L	0	#N/A	#N/A	#N/A	#N/A	#N/A
Po_z	0.125484	0.002764	45.39831	2.23E-33	0.119878	0.131089
k_1	11.08822	0.160344	69.15288	6.98E-40	10.76303	11.41341

Figure 3.11: An example of the multi-linear regression output from Microsoft Excel, showing the effect of setting P_L to zero on the constants Po_Z and k_1.

The second method was a graphical method which may be used for both torque and calorimetry methods. Assuming P_L is zero, Eq. (2.21) can be divided through by $\rho N^3 D^5$:

$$\frac{P}{\rho N^3 D^5} = Po_Z + \frac{k_1 M}{\rho N D^3} \tag{3.8}$$

$$Po = Po_Z + k_1 N_Q \tag{3.9}$$

This gives dimensionless power draw $\frac{P}{\rho N^3 D^5}$ or power number (Po), as a function of dimensionless flow rate $\frac{M}{\rho N D^3}$, or flow number (N_Q). Flow number is a constant for stirred vessels, but is variable for in-line rotor-stator mixers, except for unrestricted (maximum) flow conditions. With the outlet value fully open, the full pumping capability of the mixer was utilised. A plot of power number against flow rate number produces a linear relationship with a gradient of k_1 and intercept of Po_Z, see Section 4.2.

The power draw constants Po_Z and k_1 were also determined by a third method, by measuring power draw both at zero flow rate and at unrestricted flow rate (Cooke et al., 2012). Firstly, power draw at zero flow was measured (outlet value closed) when the second term (P_F) in Eq. (2.21) is zero:

$$P = Po_Z \rho N^3 D^5 \tag{3.10}$$

Secondly, power draw for unrestricted flow was measured (outlet value fully open). Assuming flow rate is proportional to the swept rotor volume:

$$M = N_Q \rho N D^3 \tag{3.11}$$

When Eq. (3.11) is substituted into Eq. (2.21), both P_T and P_F terms have the same dependency on N and D:

$$P_{max} = Po_Z \rho N^3 D^5 + k_1 N_Q \rho N^3 D^5 = (Po_Z + k_1 N_Q) \rho N^3 D^5 = Po_U \rho N^3 D^5 \tag{3.12}$$

The unrestricted flow power constant (Po_U) from Eq. (3.12) is the maximum power number, and is comparable to the traditional power number for stirred tanks. By rearranging Eq. (3.12):

$$k_1 = \frac{(Po_U - Po_Z)}{N_Q} \tag{3.13}$$

This procedure can only be undertaken using the torque method as it is necessary to measure power draw when the flow rate is zero. The power draw measurement results are given in Chapter 4.

3.3 Emulsification experiments

3.3.1 Materials

The dispersed phase used in this study was a range of silicone oils. In total, silicone oils (Table 3.3) were investigated with kinematic viscosities of 2, 10, 20, 50, 100, 350, 1,000 and 10,000 cSt. These oils, called 200® Fluids, are poly-dimethyl siloxanes manufactured by

Dow Corning. The 2 cSt oil was a blend of 0.65 and 10 cSt silicone oil, while 20 cSt oil was a blend of 10 and 50 cSt silicone oil. The advantage of using silicone oil is that a wide range of viscosities are obtained with similar physical properties; in particular surface tension and interfacial tension are almost constant (Padron, 2005), and silicone oil is a Newtonian fluid.

Table 3.3: Silicone oil physical properties at 25 ºC.

Material	**Density, ρ (kg m^{-3})**	**Dynamic viscosity, μ (mPa·s)**	**Surface tension, σ (mN m^{-1})**	**Refractive index, n_{ri} (-)**
2 cSt silicone oil	870	1.7	17.4	1.390
10 cSt silicone oil	937	9.4	20.1	1.399
20 cSt silicone oil	947	19	20.6	1.400
50 cSt silicone oil	957	48	20.8	1.402
100 cSt silicone oil	965	97	20.9	1.403
350 cSt silicone oil	969	339	21.1	1.403
1,000 cSt silicone oil	969	969	21.2	1.404
10,000 cSt silicone oil	970	9,701	21.5	1.404

The continuous phase materials used were water, ethanol, sodium carboxyl methyl cellulose and sodium laureth sulfate. Deionised water was used in the emulsions manufactured using the 60 L vessel, and for measurement of the material physical properties. Emulsions created in the 800 L vessel used mains water as large volumes of deionised water were not available.

Absolute ethanol was obtained from VMR International Ltd. with a minimum purity of 99.8% and used without further purification and treatment.

Sodium laureth sulfate (SLES), 'Texapon N701', manufactured by Cognis UK Ltd., Hertfordshire, is a mixed alkyl ether sulphate ($C_{12}.2nH_{25}.4nNaO_4.nS$) anionic surfactant added to the majority of the continuous phases, supplied as viscous yellow liquid with 70

wt.% active ingredient at a commercial grade containing impurities. SLES has a molecular weight of 420 g mol^{-1} (El-Hamouz, 2007) and is a highly effective emulsifier. Impure SLES is cheap and was selected as it is widely used in many household and personal care products.

Sodium carboxyl methyl cellulose (CMC), Hercules powder grade 7H4C, was used to thicken the continuous phase. CMC solutions were used to increase the continuous phase viscosity to investigate viscosity ratio, and their shear thinning nature is comparable to that of many multiphase products (Figure 3.12).

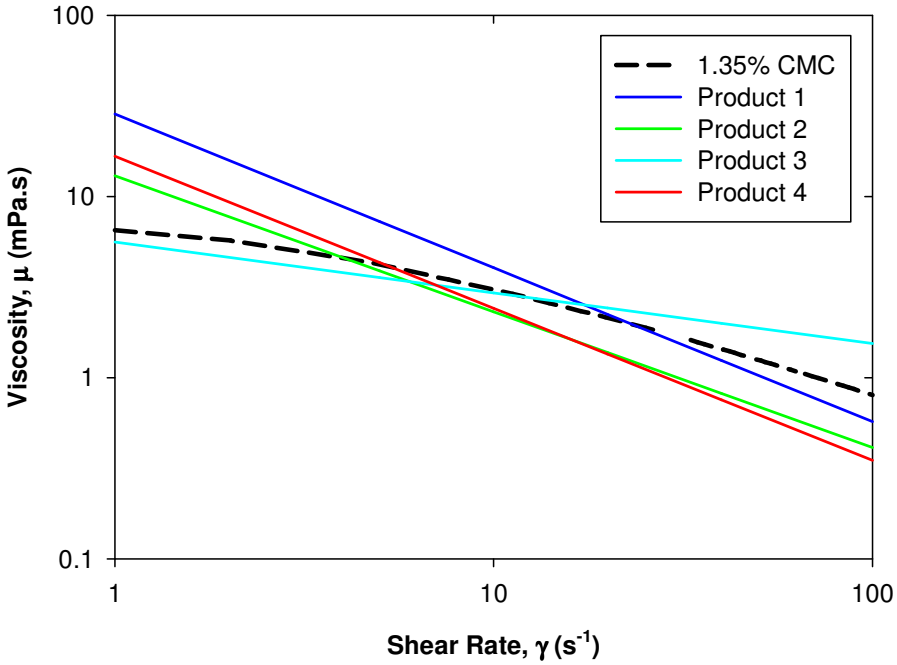

Figure 3.12: Comparison of flow curve for 1.35 wt.% CMC solution and emulsion-based products.

3.3.2 Experimental procedure

The general procedure for liquid-liquid dispersion experiments was divided into two sections; coarse emulsion preparation and rotor-stator emulsification.

3.3.2.1 Coarse emulsion preparation

Initially, the experimental arrangement was cleaned by circulating hot water and SLES surfactant solution through the rig, before rinsing with cold water and draining all remaining water. The mixing vessel was then charged with the required quantity of water, heated via the jacket to maintain a constant temperature of 25 ±1 °C, and agitated to improve heat transfer.

For the aqueous ethanol continuous phases, ethanol was added slowly to the water in the 60 L vessel, as alcohol and water form non-ideal solutions which react exothermically (Padron, 2005). Ethanol was added to the water surface with no agitation, then the solutions were mixed throughly at 25°C. Ethanol is flammable so an air extraction unit was positioned above the vessel to remove any ethanol vapour, especially during ethanol addition. Aqueous phases containing 0, 10 and 20 wt.% ethanol were examined.

The majority of experiments contained SLES, which was added in the required quantity, mixed and allowed to completely dissolve in the water. Roughly 10 minutes of agitation in the 60 L vessel, and > 20 minutes in the 800 L tank were required. Continuous phases containing 0.05, 0.5 and 5 wt.% SLES were investigated. All SLES concentrations were above the critical micelle concentration of 0.2 mmol dm^{-3} (El-Hamouz, 2007), by roughly 6, 60 and 600 times for 0.05, 0.5 and 5 wt.% SLES, respectively, assuming the CMC of oil-SLES solution is a similar order of magnitude to air-SLES solution.

For the thickened continuous phases, CMC was added after the SLES dispersion. CMC in powder form was added to the vessel surface quickly to ensure CMC was not added after the fluid had thickened. The fluid was mixed well to ensure the CMC was completely dissolved, which took several hours in the 800 L vessel, depending on concentration. CMC concentrations of 0.05, 0.15, 0.4, 0.8 and 1.35 wt.% were investigated. The continuous phase properties are given in Table 3.4, and CMC physical properties in Table 3.7.

Table 3.4: Continuous phase physical properties at 25 ºC.

Material	**Density, ρ (kg m^{-3})**	**Dynamic viscosity, μ (mPa·s)**
Water	997	0.89
10% EtOH solution	980	~ 0.9
20% EtOH solution	966	~ 0.9
0.05% SLES solution	997	~ 0.9
0.5% SLES solution	998	~ 0.9
5% SLES solution	1,005	1.15

Once the continuous phase was prepared, silicone oil was added to the mixing tank. Oil phase volumes of 1, 5, 25 and 50 wt.% were examined. For the majority of cases, oil was added to the vessel surface, except for high viscosity oils (10,000 cSt) in the 800 L vessel. This was either injected into the impeller region using a peristaltic pump which was time consuming (2-3 hours), or added to the fluid surface whilst water was being added, so the fluid surface was closer to the impeller and the oil could be more easily dispersed. Bulk mixing was slower for the CMC thickened aqueous phases so the oil was also injected directly into the impeller region so the target drop size distribution could be obtained sooner.

The dispersed phase was always added under agitation using the high shear dissolver discs to form a crude dispersion. The impeller speed and agitation time were selected to form a target inlet droplet size (20 to 70 µm). Coarse emulsions were prepared for 5 minutes at tip speeds between 4.0 and 5.2 m s^{-1}, depending on the oil viscosity. Then, the high shear disc impeller in the 800 L vessel, or the anchor in the 60 L vessel, were rotated at low speed to maintain a well-mixed dispersion and prevent creaming during the experimental trials. Creaming still occurred in the 800 L vessel once the emulsion level fell below the impeller, so a high flow rate experiment was performed to limit the impact of creaming.

3.3.2.2 Rotor-stator emulsification

The effect of process and formulation parameters on drop size distributions were investigated for both single and multiple pass emulsification.

3.3.2.2.1 Single pass

Coarse emulsion was fed to the Silverson in a single pass at a series of flow rates and rotor speeds. For the 150/250 mixer, rotor speeds from 3,000-11,000 rpm (in steps of 1,000 rpm) at a primary flow rate of 300 kg h^{-1}, and rotor speeds of 6,000 rpm and 11,000 rpm for flow rates between 150 and ~ 6,200 kg h^{-1} were examined. All single pass investigations with dilute emulsions (1-5 wt.%) including the effect of rotor-stator geometry, were taken using these conditions in the 150/250 mixer. For the concentrated emulsions (> 5 wt.%), high CMC concentrations (> 1.35 wt.%), and ethanol continuous phase emulsions, samples were only taken at 3,000-11,000 rpm (in steps of 2,000 rpm) at 300 kg h^{-1}.

Table 3.5 summarises the processing conditions examined at each scale in Chapter 7. The primary flow rates for the 088/150 and 450/600 mixers were roughly 100 kg h^{-1} and 4,600 kg h^{-1} respectively, to match the residence time in the 150/250 mixer of τ = 0.45 s.

Flow rate was controlled by a diaphragm valve downstream of the mixer (Figure 3.6), with a neutral or slightly positive pressure maintained at the mixer inlet by adjusting the speed of the in-line tri-lobe pump (for the 60 L vessel). For the 800 L vessel, positive pressure was achieved using the fluid pressure head in the vessel alone, except for very high flow rates (> 2,400 kg h^{-1}), when the centrifugal pump was employed. The Silverson cannot easily pump these high flow rates as negative pressure drops were formed, increasing the risk of cavitation, due to the location of the 800 L tank some distance from the mixer, and restrictions through the connecting pipeline.

Table 3.5: Single pass processing conditions.

Mixer scale	Laboratory scale (088/150)	Pilot plant scale (150/250)	Factory scale (450/600)
Rotor speed, N (rpm)	4,000-10,000	3,000-11,000	1,200-3,600
Flow rate, M (kg h^{-1})	50-1,500	150-6,200	1,200-6,200

Drop size distributions measured in the mixing tanks and at the Silverson inlet after passing through the tri-lobe pump were practically identical. The centrifugal pump did reduce the inlet droplet size, but no appreciable effect on the outlet drop size from the mixer was measured, for samples taken with and without the pump.

The dispersed phase was also injected into the continuous phase in a single pass in Section 8.6. The continuous phase was prepared in the 800 L mixing vessel and oil was added from a separate vessel at a flow rate to form a 1 wt.% emulsion, i.e. a 1 wt.% dispersion at 300 kg h^{-1} required 3 kg h^{-1} of oil and 297 kg h^{-1} of continuous phase. Oil injection was achieved using a piston pump, the speed of which could be adjusted automatically to dose the required oil quantity.

Once steady state conditions of rotor speed, pressures/flow rates and temperatures were achieved (indicated by real-time displays by the automatic control system), an emulsion sample was taken directly from sampling points at the inlet and outlet of the Silverson.

3.3.2.2.2 Multiple passes

The effect of multiple passes on droplet size distributions was investigated by three methods; ‘single condition’ recirculation, ‘complete pass’ recirculation and ‘step-wise’ recirculation methods, all using the 60 L rig.

In the ‘single condition’ method, coarse emulsion was fed to the Silverson mixer in a recycle loop between the mixing tank and the mixer. Flow rate and rotor speed were kept

constant to investigate the effect of number of batch turnovers on the drop size distributions. Samples were taken from the Silverson outlet and from the mixing vessel at regular time intervals corresponding to a given number of batch turnovers, for example at 1, 2, 5, 10, 20 etc. Sixty batch turnovers were examined for the 2,350 kg h^{-1} experiments, and at least 20 batch turnovers for the 600 kg h^{-1} experiments.

Initially, coarse emulsion was circulated around the system at a low flow rate (300 kg h^{-1}) to remove air from the pipelines, then the Silverson was turned to the required rotor speed, and the flow rate was controlled through a combination of the tri-lobe pump and the valve at the mixer outlet. Experimental details are given in Table 3.6.

Table 3.6: Multiple pass processing conditions.

Mixer scale	**Laboratory scale (088/150)**	**Pilot plant scale (150/250)**				**Factory scale (450/600)**
Single condition						
Rotor speed (rpm)	10,000	6,000	11,000	11,000	-	2,500
Flow rate (kg h^{-1})	600	2,350	600	2,350	-	2,400
Complete pass						
Rotor speed (rpm)	-	6,000	11,000	-	-	-
Flow rate (kg h^{-1})	-	600	600	-	-	-
Step-wise						
Rotor speed (rpm)	6,000-10,000	3,000-11,000	3,000-11,000	3,000-11,000	3,000-11,000	1,200-3,600
Flow rate (kg h^{-1})	805	300	1,000	1,700	2,400	2,400

The second method, ‘complete pass’ recirculation, was similar to the first method in that only one rotor speed and flow rate was investigated per experiment. The key difference is that the entire emulsion batch was collected in buckets from the mixer outlet after each pass and returned to the vessel with a sample taken, for a total of 10 passes. This ensured all of the

fluid had passed through the mixer so that the effect of each pass was decoupled from mixing in the vessel. Emulsion was returned to the vessel and agitated to form a well mixed dispersion at 25ºC before processing the subsequent pass, aided by the pump, with the first > 3 L of emulsion disposed of while rotor speed, flow rate and temperature reached the required conditions. Experiments were undertaken using the 150/250 mixer at 6,000 and 11,000 rpm at 600 kg h^{-1}.

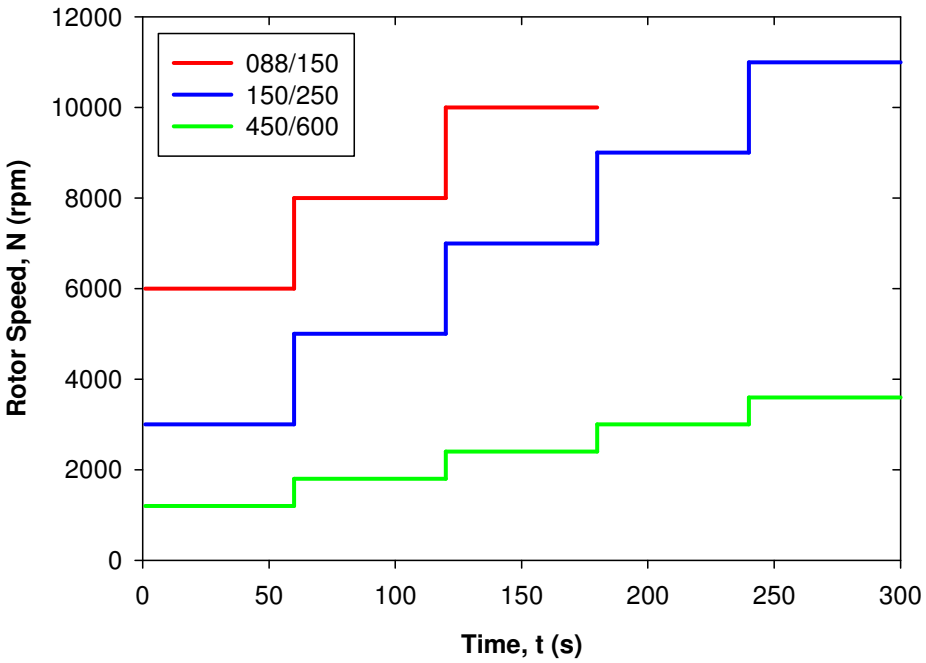

Figure 3.13: Step-wise recirculation method for each mixer scale.

In the third method, 'step-wise' recirculation, coarse emulsion was recycled for a fixed time of 1 hour to obtain an 'equilibrium' droplet size distribution. For an experimental run, flow rate was constant and rotor speed increased in steps, see Table 3.6 and Figure 3.13. Samples were taken from the Silverson outlet and the mixing vessel at regular time intervals of 5, 15, 30, 45 and 60 minutes for each rotor speed investigated (corresponding to 5 to 40

batch turnovers depending on flow rate). This method examined the effect of processing at long times, although in reality droplet size never reached an 'equilibrium', but a time of 1 hour was selected as this was considerably longer than manufacturing timescales.

3.3.3 Sample analysis

Droplet size distributions were measured by laser diffraction using a Mastersizer particle analyser (Malvern Instruments, Malvern, UK), described in Section 2.2.1.3.4. Two types of particle analyser were used; a Mastersizer X long bed and a Mastersizer 2000. Key details are given in Appendix B.2, along with a comparison of results obtained with each machine. For the Mastersizer X, a lens of focal length 300 mm was employed as this provided the most suitable range of drop size measurement of 1.2-600 μm.

The Hydro SM small volume dispersion unit was employed for all measurements. Emulsion samples were diluted in a weak aqueous SLES solution (~ 0.1 wt.%) to ensure the oil droplets were dispersed in a medium similar to the continuous phase, and to prevent coalescence and oil deposition on the optical windows of the sample cell. A sufficient number of drops were added to the dispersion unit to achieve an obscuration of 5-10%, and an impeller speed of ~ 1,500 rpm was selected to circulate the droplets.

The relative refractive indices (n_{ri}) used were 1.33 for the continuous water phase, and 1.42 for the silicone oil dispersed phase, see Appendix B.1 for details. The imaginary component of the absorption index for silicone oil was taken as 0.001 for emulsions (Thapar, 2004). A general purpose, spherical model was used to describe the droplets.

In general, samples were measured < 48 hours after the experiment was completed, although the samples were stable long-term (Appendix B.3).

3.3.4 Drop size analysis

In the majority of cases, the coefficient of determination (R^2) was used as the quality of fit indicator in correlations. Adjustable parameters in correlations were determined in Microsoft Excel by minimising the root mean squared difference (σ_{rms}) between experimental and predicted d_{32} or d_{32}/D values:

$$\sigma_{rms} = 100\sqrt{\frac{\sum\left(\frac{d_{32,exp.}-d_{32,calc.}}{d_{32,exp.}}\right)^2}{N_s}} \tag{3.14}$$

σ_{rms} was also used to compare drop size correlations.

3.4 Material property measurements

3.4.1 Interfacial tension

Equilibrium interfacial tensions between the oil and continuous phases were measured by three methods; the drop volume, pendant drop and Wilhelmy plate methods.

The drop volume method calculates interfacial tension from the balance between the gravity force and surface force at equilibrium (Davies and Rideal, 1961). This method required the injection of one phase from a vertically mounted syringe into the second phase. The syringe, with tip inner diameter of 800 µm, was fitted with a micrometer to determine the liquid volume excluded and the droplet was recorded using a microscope (Olympus SZ11) and video camera (Allied Vision Technologies Dolphin F145B) to detect droplet detachment. By forming the drop extremely slowly, the interfacial tension force was calculated from the droplet mass force at the moment of drop separation from the syringe and the surface force (Davies and Rideal, 1961; El-Hamouz, 2007):

$$\sigma = \frac{\phi_F V_d(\rho_c-\rho_d)g}{2\pi r_s} \tag{3.15}$$

A correction factor (ϕ_F) was necessary in Eq. (3.15) because the liquid does not completely leave the tip, the interfacial tension force does not act exactly vertically (Schramm, 2005) and a pressure difference occurs across the curved surface. However, ϕ_F of ~ 1.0 was found from empirical data (Davies and Rideal, 1961). The syringe tip must be completely wetted and the last 10% of the drop must form and detach slowly (Shaw, 2003).

The pendant drop method also calculates interfacial tension from the balance between the gravity force and interfacial force at equilibrium; however unlike the drop volume method which requires droplet detachment, the pendant drop technique calculates interfacial tension from the droplet shape (Schramm, 2005). The principle of this technique is based upon the fact that droplets form a sphere in zero gravity, hence interfacial tension can be calculated from the equilibrium between gravitational and surface forces which are related to the shape of a hanging (or rising) drop. Pendant drop measurements were undertaken using a Kruss Easydrop (VI-03) Drop Shape Analysis System, which performed the above calculations in the accompanying software. All measurements were undertaken at ambient temperature (~ 22 ºC) and allowed 30 minutes to achieve equilibrium for systems containing surfactant.

The Wilhelmy plate method is a force method which is advantageous as it does not require knowledge of the material densities. In this method, a very clean thin platinum plate was used to ensure the contact angle made with the phases was zero (Shaw, 2003). The plate was immersed across the interface between the phases where it measures the change in force required to maintain a constant immersion depth. These measurements were also undertaken using the Kruss Easydrop (VI-03) Drop Shape Analysis System at (~ 22 ºC) for 30 minutes.

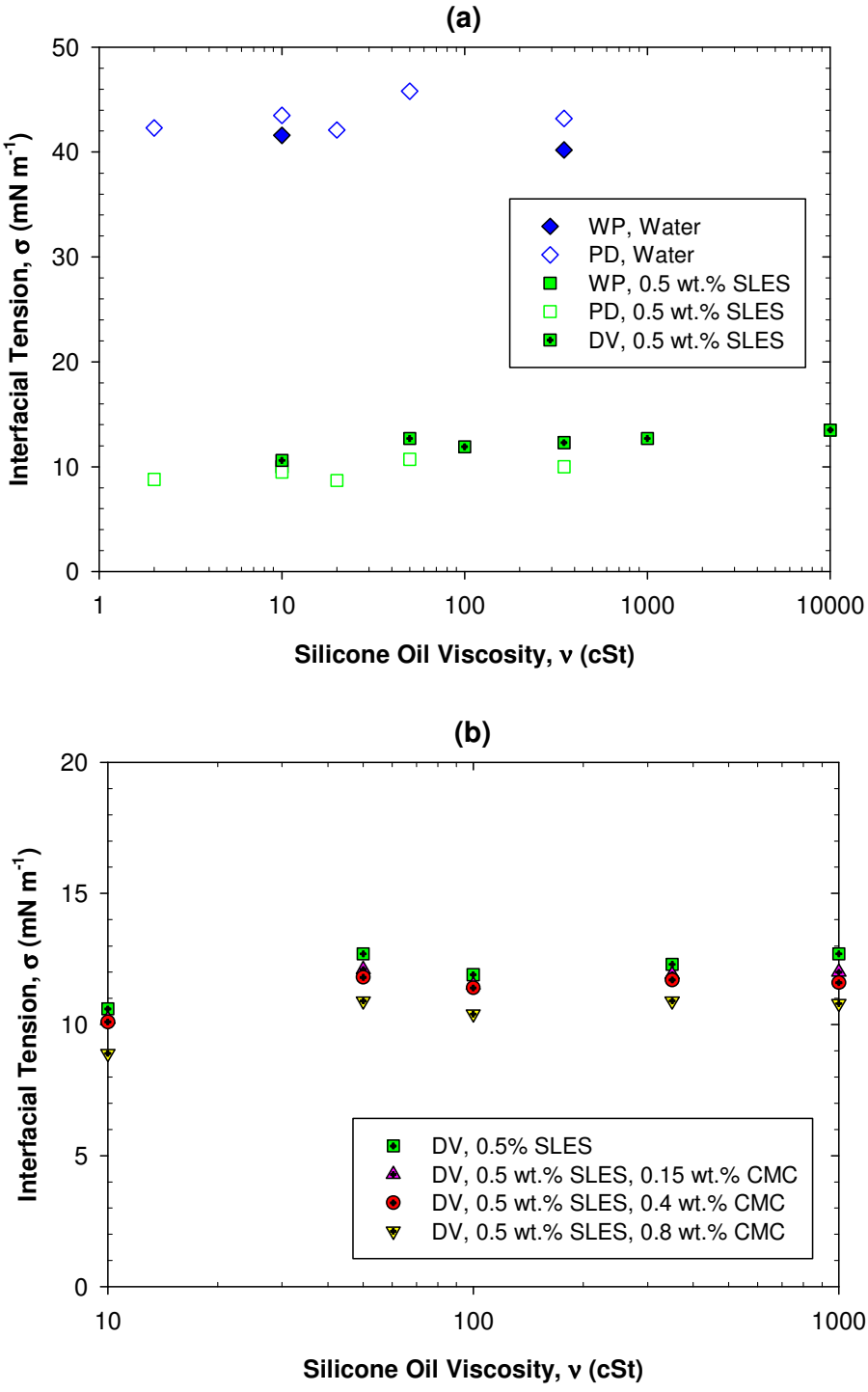

Figure 3.14: Equilibrium interfacial tensions for silicone oil and (a) water and SLES solutions and (b) SLES and CMC solutions. 'WP' – Wilhelmy Plate, 'PD' – Pendant Drop and 'DV' – Drop Volume.

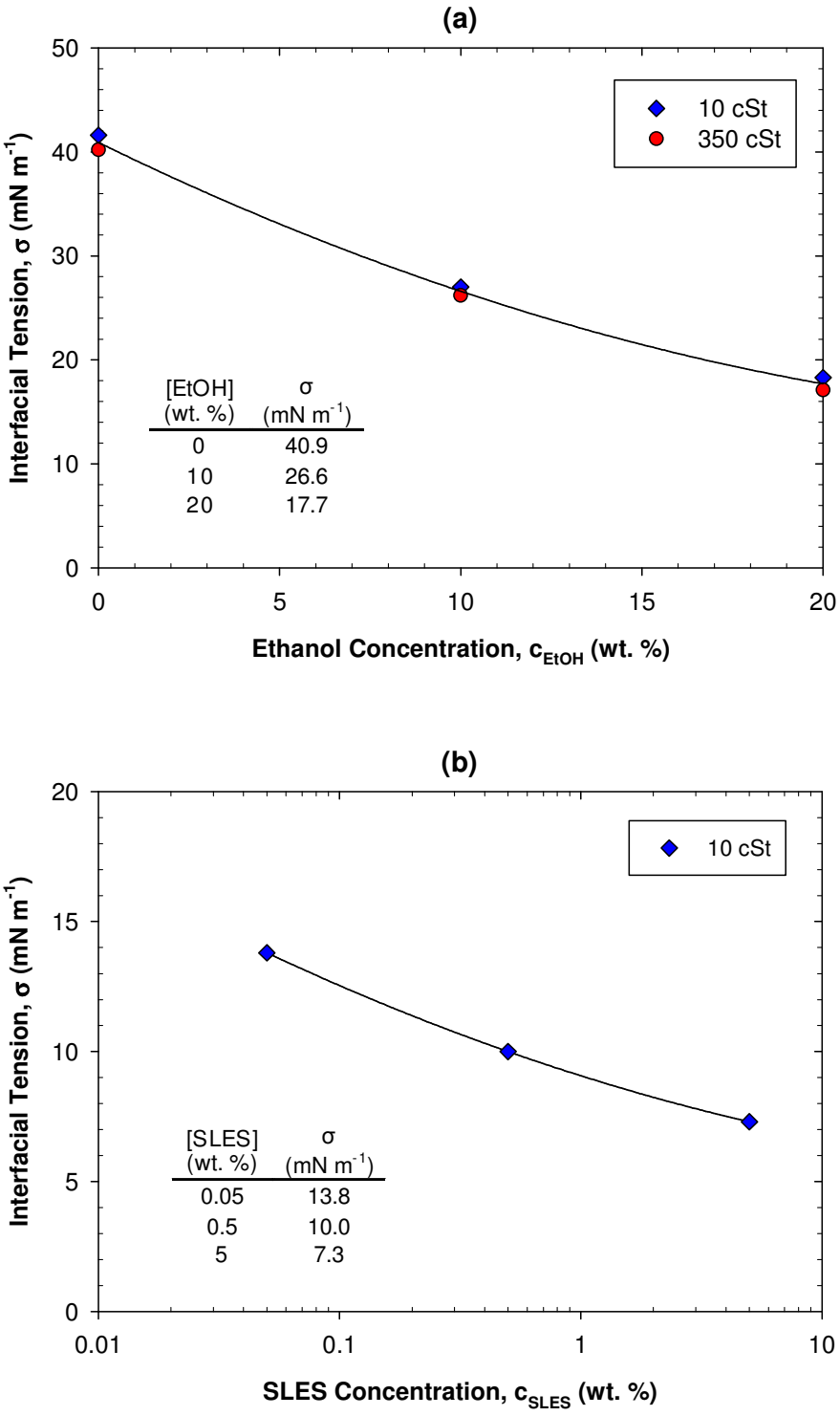

Figure 3.15: Equilibrium interfacial tensions for silicone oil and (a) ethanol and (b) SLES solutions by Wilhelmy Plate.

Values of equilibrium interfacial tension for silicone oil and water/SLES systems (Figure 3.14a) show equilibrium interfacial tension is independent of silicone oil viscosity (~ 43 mN m^{-1} for water and ~ 10 mN m^{-1} for 0.5 wt.% SLES systems), as confirmed by Padron (2005) by the pendant drop method. Figure 3.14a also shows little difference between the three techniques used, however for calculations, values from a single technique were used. Figure 3.14b shows higher CMC concentrations systematically reduced interfacial tension slightly, by ~ 15% from 0 to 0.8 wt.% CMC.

Figure 3.15a shows the effect of ethanol concentration on silicone oil-ethanol interfacial tensions by the Wilhelmy plate method. Again there is a negligible effect of silicone oil viscosity, and interfacial tension falls from 40.9 to 17.7 mN m^{-1} over the range of 0-20 wt.% ethanol. Figure 3.15b reveals a two-fold increase of SLES concentration from 0.05 to 5 wt.% reduced interfacial tension from 13.8 to 7.3 mN m^{-1}.

3.4.2 Viscosity

The apparent viscosity of the aqueous SLES/CMC continuous phases and high phase volume emulsions were measured.

Continuous phases containing CMC were measured at 25 ºC using a Haake RV20 viscometer which is a standard cup and bob configuration. The rheometer was fitted with a MV1 rotor for lower viscosities or a MV2 rotor for higher viscosities. The shear profile was increased over the range from 2 to 450 s^{-1}, before decreasing again over the same range. The rheology of CMC solutions are shear thinning and follow the power law viscosity relationship:

$$\mu_A = k\dot{\gamma}^{n-1} \tag{3.16}$$

The power law constants for the CMC solutions are given in Table 3.7. Jaworski (2010) observed CMC solutions to exhibit viscoelastic properties, hence the estimation of viscosity from a power law model may not be applicable at high shear rates in rotor-stator mixers.

Table 3.7: Physical properties and rheological constants in Eq. (3.16) for CMC solutions at 25 ºC.

CMC concentration, c_{CMC} (wt. %)	**Density, ρ (kg m^{-3})**	**Interfacial tension, σ with 10 cSt silicone oil (mN m^{-1})**	**Power law index, n (-)**	**Constant, k (Pa·s)^n**
0.05	997	10.5	0.7971	0.0146
0.15	998	10.2	0.7648	0.0483
0.4	999	10.1	0.5970	0.4614
0.8	1,002	8.9	0.4605	3.2192
1.35	1,004	7.3	0.3320	17.065

High phase volume emulsions were measured using a Haake RheoStress 1 (Thermo Electron) using concentric cylinder geometry with a gap width of 0.5 mm. Measurements were taken at 25 ºC over an increasing and decreasing shear profile of 0 to 1,500 s^{-1}.

3.5 Summary

The equipment, experimental rig, and power draw measurement by torque and calorimetry methods were described. In addition, the liquid-liquid dispersion experiments for single and multiple passes were detailed including emulsion preparation, emulsification procedure and sample analysis. Finally, the measurement of interfacial tension and rheological properties were detailed, together with results used in subsequent chapters.

CHAPTER 4. POWER DRAW IN IN-LINE SILVERSON ROTOR-STATOR MIXERS

4.1 Introduction

Power draw is an important variable to calculate energy dissipation rate, a commonly used scale-up term in industrial processes such as liquid-liquid dispersion. Power consumption of a Silverson high shear mixer was measured by both torque and calorimetry methods, and fitted to a two-term expression for turbulent power draw for in-line rotor-stator mixers, to determine two power draw constants. The turbulent power data was compared with previous work to produce a power curve, including Newtonian and non-Newtonian fluids. Then, power draw constants at three scales of geometrically similar in-line Silverson mixer were measured and the effect of various rotor-stator configurations on the turbulent power draw constants was studied. Finally, power draw was calculated from numerical simulations and compared with experimental values. Part of this work has been published in:

- Kowalski, A. J., Cooke, M., and Hall, S., (2011). "Expression for turbulent power draw of an in-line Silverson high shear mixer", *Chemical Engineering Science*, **66(3)**, 241-249.

4.2 The effect of process parameters on power draw

Figure 4.1 illustrates the strong relationship between power draw and rotor speed, and that power draw increases with flow rate (for the 150/250 mixer). The data fits a power law relationship with exponents from 2.26 to 2.67, thus the exponent for each flow rate has an

index of ~ 2.5 which is consistent with earlier findings by Bourne and Studer (1992). This results from the combined effects of power consumption due to fluid resistance, the first term ($P_T = Po_Z \rho N^3 D^5$) of Eq. (2.21) where power is proportional to rotor speed cubed, and the fluid acceleration, the second term ($P_F = k_1 M N^2 D^2$) where power draw is related to the rotor speed squared. In fact, at higher flow rates the exponent on power draw is lowest, reflecting the impact of the squared flow rate term on the total power draw. At low flow rates (< 500 kg h^{-1}), there is an anomalous increase in power draw, not shown in Figure 4.1. These flow rates are not industrially relevant; hence the low flow rate power data was removed from the subsequent analysis, but is discussed in Section 4.4.

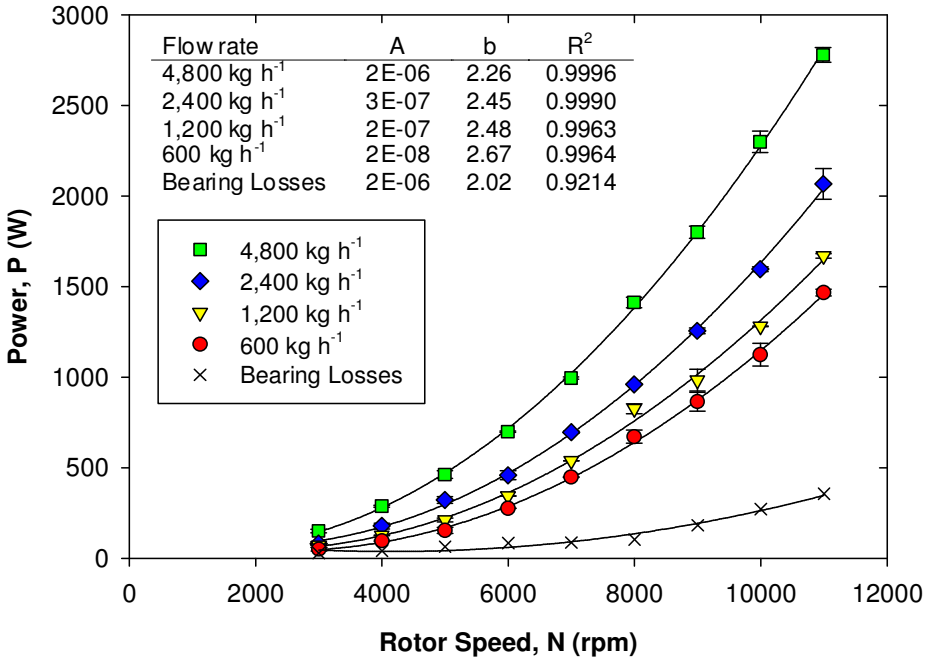

Figure 4.1: The effect of rotor speed on power draw for various flow rates and for frictional bearing losses measured by torque (average of two data sets), with standard deviation error bars.

Power draw due to friction created by the bearings ($P_{Bearings}$) in the shaft (Figure 4.1) increased with increasing rotor speed. Power due to friction as a proportion of the total power draw was lower at higher rotor speeds, ~ 20% at 11,000 rpm, compared to 50% at 3,000 rpm, however, $P_{Bearings}$ is not a constant and depends on the age of the seals and bearings.

Figure 4.2 presents the data in Figure 4.1 in terms of power number (Po) defined by Eq. (2.5), as function of rotor Reynolds number (Re) defined by Eq. (2.7), for various flow rates. This figure shows that power number is a strong function of flow rate, especially at lower Re (or rotor speeds). At higher Re, Po begins to reach an asymptote between 0.2 and 0.5, depending on flow rate.

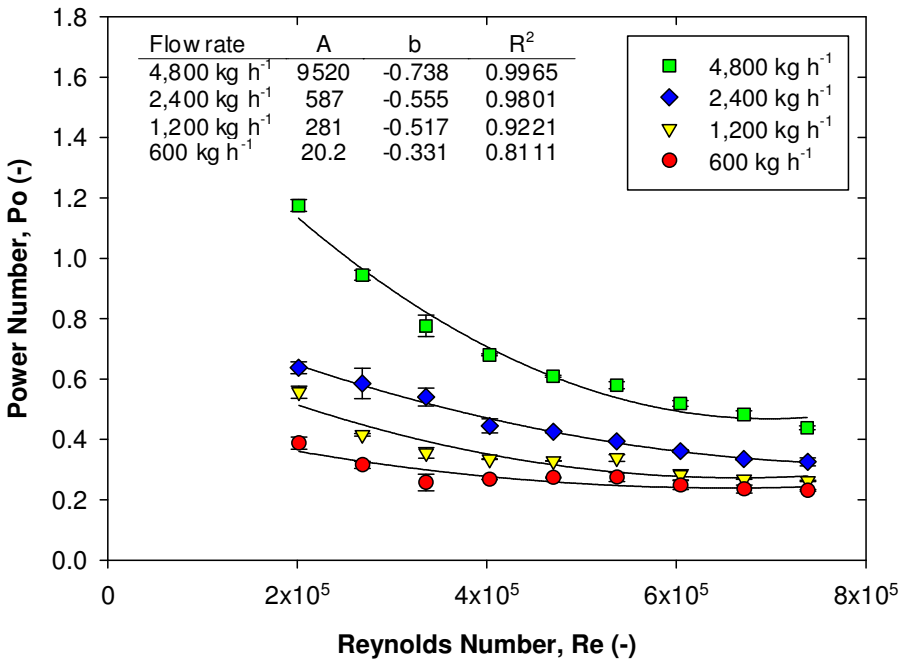

Figure 4.2: The effect of Reynolds number on power number for various flow rates measured by torque (average of two data sets) with standard deviation error bars.

For a stirred tank impeller, Po remains constant with increasing Re in the turbulent flow regime, however Figure 4.2 shows this is not the case for an in-line rotor-stator mixer. At 3,000 rpm, Po varies significantly from 0.4 to 1.2 depending on flow rate, thus Eq. (2.10) cannot be used to calculate power draw. Accordingly, a two-term expression for power draw is required to account for flow rate separately (Kowalski, 2009). At higher rotor speeds or lower flow rates, the first term of Eq. (2.21) ($P_T = Po_Z \rho N^3 D^5$) dominates and at lower rotor speeds or higher flow rates the second term, ($P_F = k_1 M N^2 D^2$) has a stronger effect on power draw.

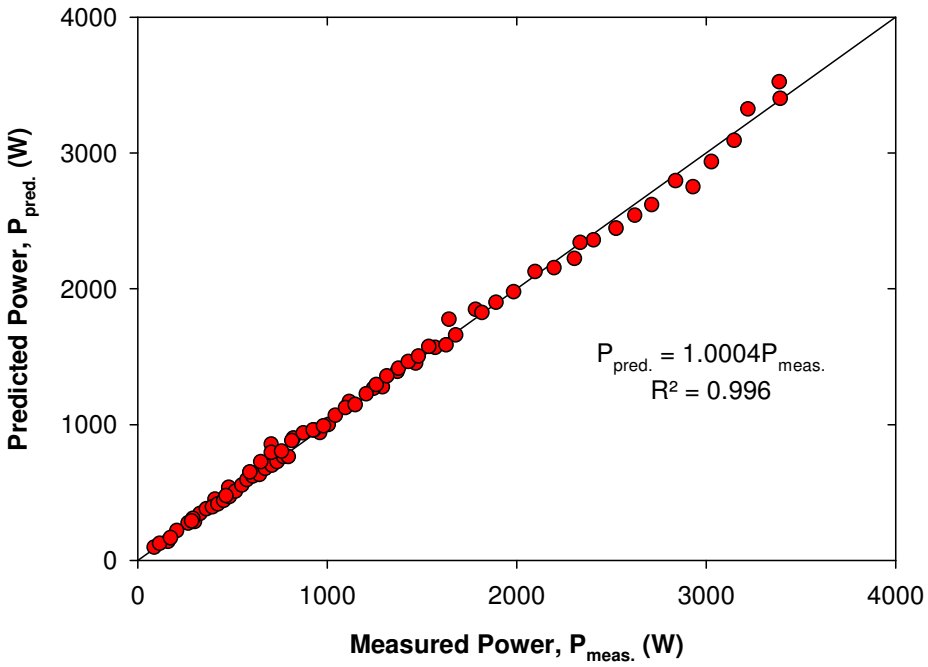

Figure 4.3: A comparison of power draw measured by torque with power predicted using Eq. (2.21), with power constants from the regression of the torque data.

The power draw constants in Eq. (2.21) were determined by multi-linear regression, described in Section 3.2.2, to give Po_Z = 0.197 and k_1 = 9.35. Figure 4.3 shows the fit

between experimental power draw values from torque measurement, and power draw predicted from Eq. (2.21) using the constants obtained from a regression of the torque data. The fit is excellent with R^2 = 0.996, indicating the model fits the experimental values accurately.

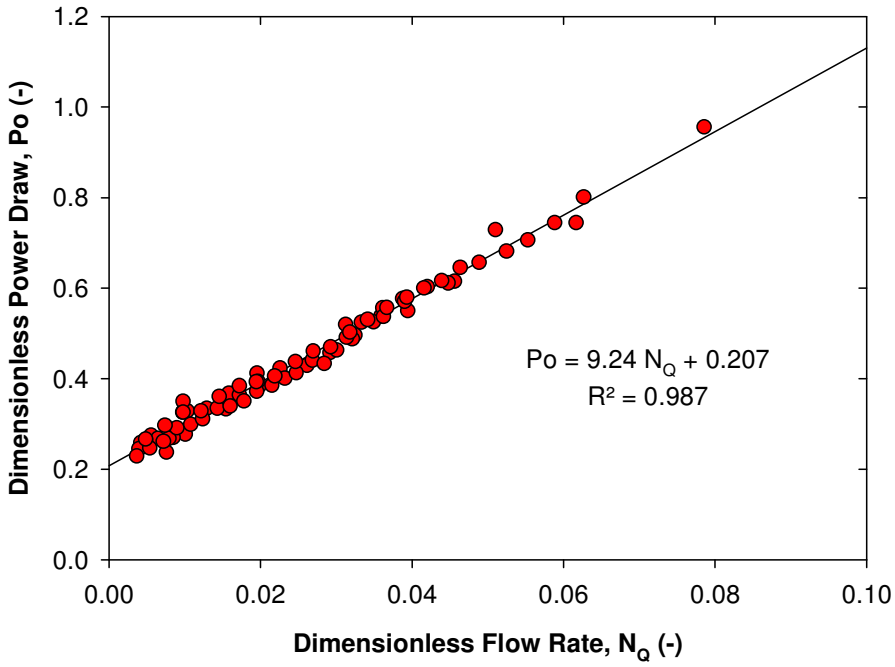

Figure 4.4: Dimensionless power draw from torque measurement as a function of dimensionless flow rate.

The power draw constants were also obtained graphically from a plot of dimensionless power draw (Eq. (2.5)) as a function of dimensionless flow rate (Eq. (2.3)), see Figure 4.4. The constants obtained, Po_Z = 0.207 and k_1= 9.24, are in good agreement with values obtained from multi-linear regression. A plot of Po against N_Q is also useful for assessing the reliability of the experimental data as significant scatter from a linear relationship would either indicate difficulty in measuring power draw accurately, or that some effects have not

been taken into account in the power draw expression (losses are not zero), however Figure 4.4 suggests that this is not the case. For consistency, the multi-linear regression method was the primary method used to determine the power draw constants.

4.3 Comparison between measurement techniques

As described in Section 3.2, power draw was measured experimentally by the torque and calorimetry methods. The calorimetry power measurements showed similar trends to those in Figure 4.1 and Figure 4.2, specifically that power increased with both rotor speed and flow rate (Figure 4.5a). One of the main differences between the techniques is that calormetry cannot measure power draw at zero flow rate.

Table 4.1 summarises the power draw constants determined from multi-linear regression. The constants from each method are similar, with torque giving slightly lower Po_Z values but higher k_1 values than calorimetry. A comparison of measured and predicted power draw by calorimetry gave a similar correlation to the torque method in Figure 4.3, with $R^2 = 0.9989$ (not shown).

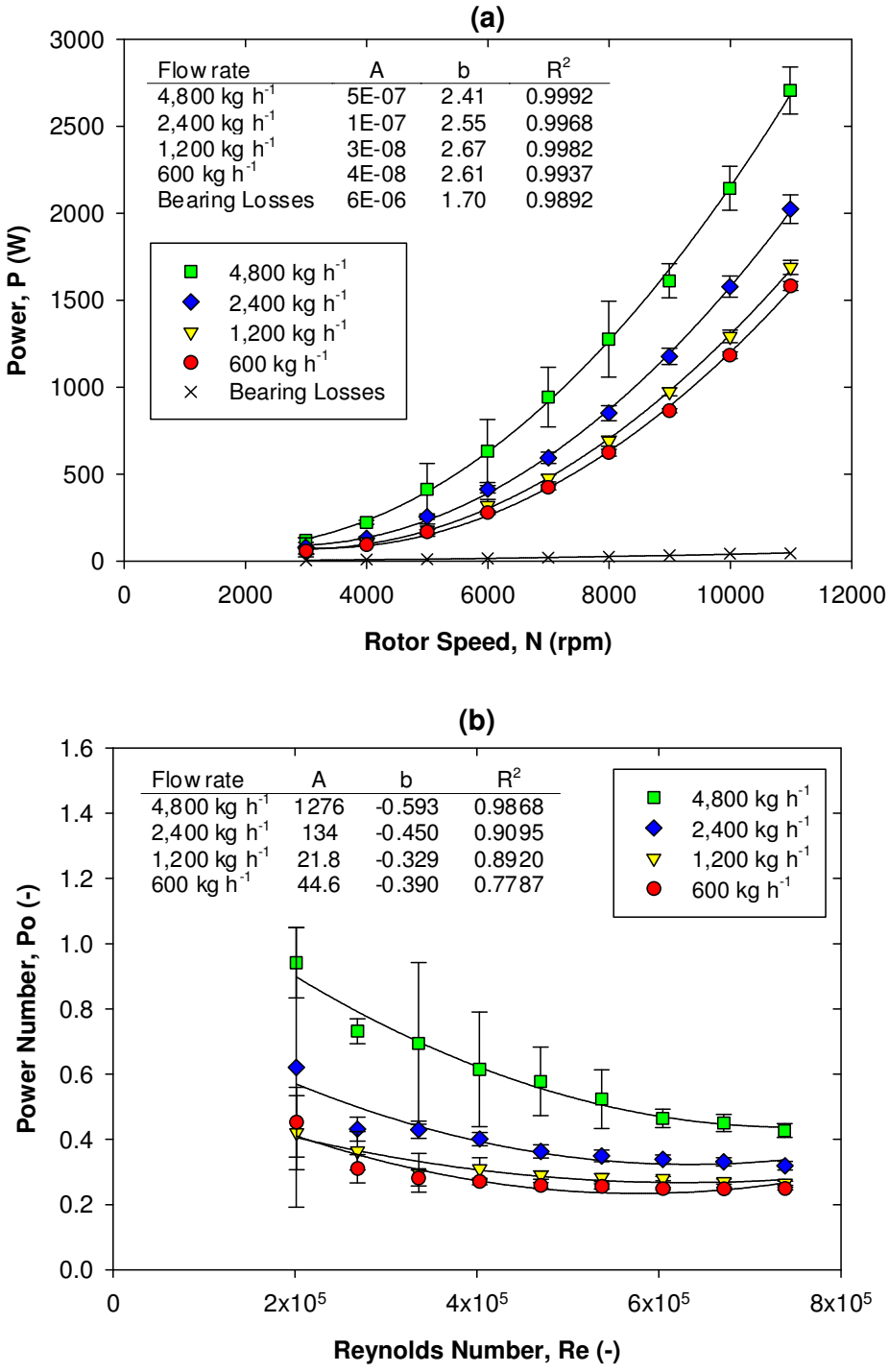

Figure 4.5: (a) The effect of rotor speed on power draw for various flow rates and for frictional bearing losses, and (b) the effect of Reynolds number on power number for various flow rates measured by calorimetry (average of five data sets) with standard deviation error bars.

Table 4.1: Power draw constants in Eq. (2.21) (Po_Z and k_1) obtained from torque and calorimetry methods with 95% confidence intervals.

Power draw constants	**Regression results**			
	Value	***Standard Error***	***Lower 95% CIs***	***Upper 95% CIs***
Torque				
Zero flow power constant, Po_Z	0.197	0.003	0.190	0.204
Flow power constant, k_1	9.35	0.14	9.07	9.63
Calorimetry				
Zero flow power constant, Po_Z	0.229	0.004	0.222	0.237
Flow power constant, k_1	7.46	0.16	7.13	7.78

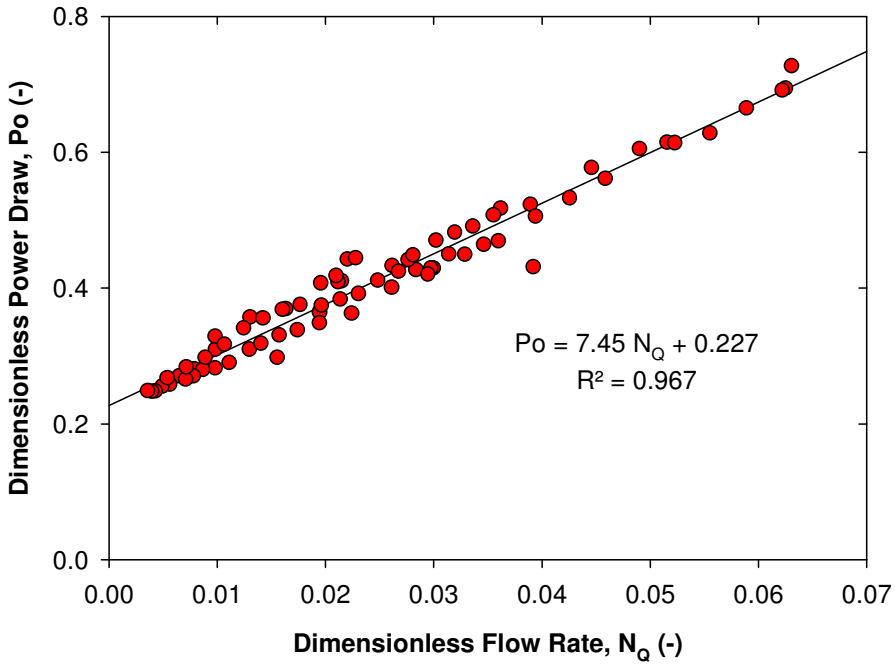

Figure 4.6: Dimensionless power draw from calorimetry measurement as a function of dimensionless flow rate.

Figure 4.6 presents the equivalent Po vs. N_Q plot of Figure 4.4 for calorimetry, and shows a good relationship. A comparison between the coefficients of determination (R^2 = 0.987 for torque and R^2 = 0.967 for calorimetry) in Figure 4.4 and Figure 4.6, reveals a better fit for torque, and the error bars in Figure 4.1, Figure 4.2 and Figure 4.5, indicate that the torque method is more reliable. The poorer fit for calorimetry is due to greater variability in the measured power values, particularly at low rotor speeds when temperature differences are low. This is clearly illustrated in Figure 4.5b, where there is more variability in Po for $Re < 4\times10^5$.

Figure 4.7 presents a comparison of power measured by calorimetry and torque, which indicates each method gives a reasonable estimation of power draw, and validates the calorimetry method for use at other scales.

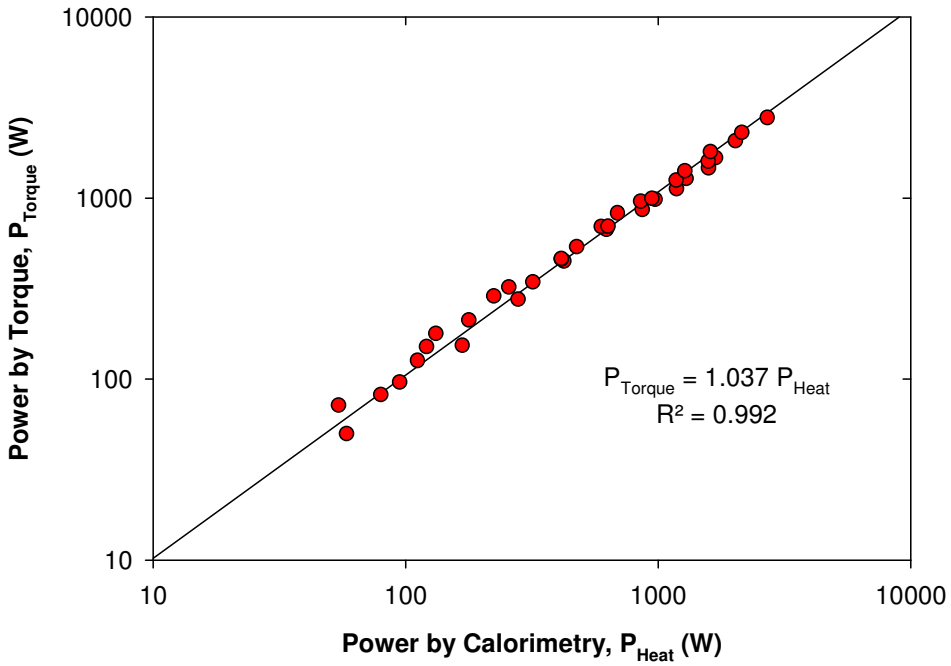

Figure 4.7: A comparison of experimental power draw obtained from the calorimetry and torque methods.

Power number readings for each technique are shown with time in Figure A.1 in Appendix A.1, for selected rotor speeds and flow rates, together with temperature differences. The measurement data obtained by each method is more reliable at higher rotor speeds as the deviation of power number is less. However, the torque method gave more consistent readings at higher flow rates due to larger torque readings, while calorimetry produced more reliable readings at lower flow rates where temperature differences are greatest.

4.4 Power draw at low flow rates

As discussed in Section 4.2, an unexpected increase of power draw at low flow rates was observed, as shown in Figure 4.8, which is unlikely to result from measurement error as this effect was observed by both techniques. The expression for power draw in an in-line rotor-stator mixer in Eq. (2.21) does not account for this effect as it assumes power draw increases linearly with flow rate. This effect may result from increased power draw due to fluid recirculation when fluid is expelled through the stator holes at the leading edge of the rotor blade, then sucked back through the stator holes due to the wake caused by the trailing edge of the rotor blade, see Figure 4.22a (Section 4.9). As a consequence, the value of Po_Z of 0.197 from regression is lower than the true value of Po_Z for this geometry of 0.24, see Section 4.6 for more details.

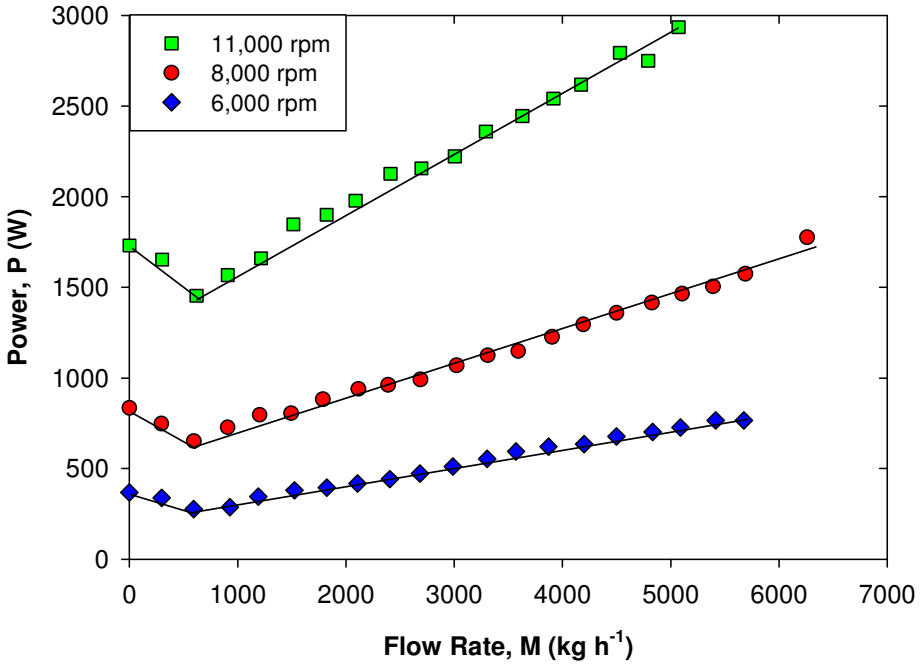

Figure 4.8: The effect of flow rate on power draw measured by torque for a range of rotor speeds (average of two data sets), including flow rates below 500 kg h^{-1}.

To assess the pumping efficiency of the mixer the following expression was used:

$$P = \frac{P_P}{\eta} = \frac{Q\Delta p}{\eta} \tag{4.1}$$

Pumping power (P_P), is the fraction of the total power imparted to the fluid used for pumping. If this is compared to the total power drawn, an efficiency term (η) is obtained for each process condition with a value between 0 and 1, where a value closer to 1 indicates more of the power drawn is used for pumping. Figure 4.9 shows that the efficiency values are low, and appear virtually independent of rotor speed, and depend solely on flow rate. The figure shows that η increases as flow rate increases, as more pumping power of the Silverson is used, until a plateau is reached at higher flow rates.

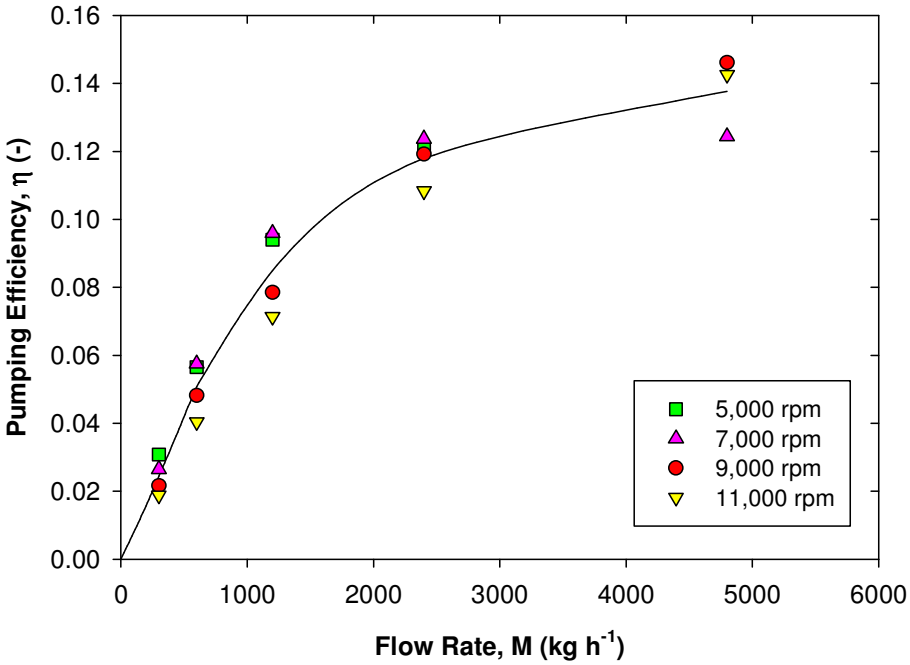

Figure 4.9: Effect of rotor speed and flow rate on the Silverson pumping efficiency.

4.5 Zero and unrestricted flow power draw

Figure 4.10 shows rotor speed as a function of unrestricted flow rate, with the outlet value fully open, and no external pumping aids. The relationship is linear (Eq. (3.11)) so the flow number (N_Q) can be determined from the gradient. If the relationship is non-linear, this suggests that the flow is restricted at the mixer inlet resulting in cavitation. It is important that Po_U is only measured when the relationship between N and M is linear and flow number is constant. The calculated N_Q value of 0.054 is much smaller than for an impeller in a stirred vessel, such as 0.7 for a Rushton turbine (Hemrajani and Tatterson, 2004), as the flow is restricted in in-line devices due to the presence of the mixing chamber and upstream/downstream pipework.

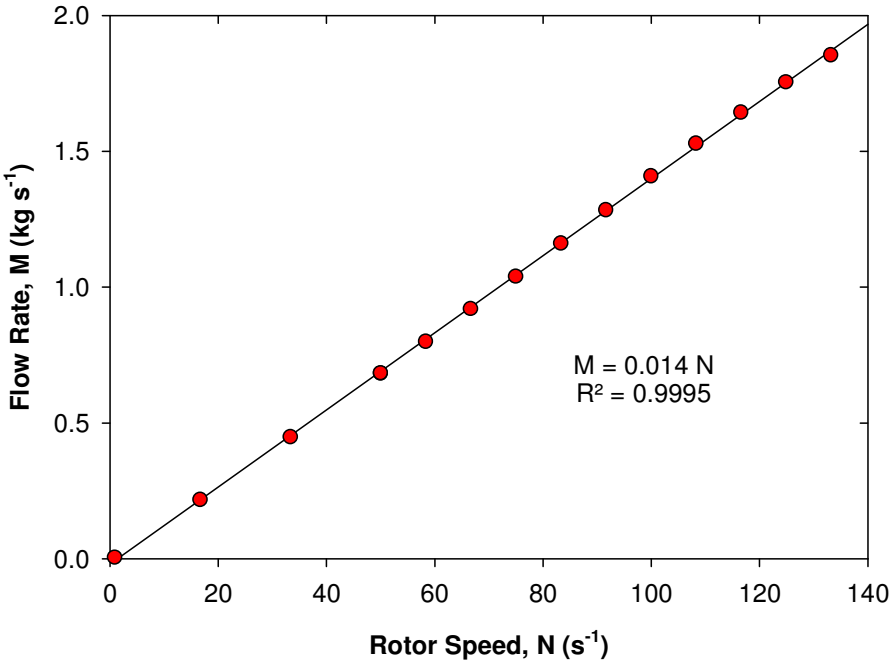

Figure 4.10: Rotor speed as a function of unrestricted flow rate through the Silverson mixer.

Power was measured at zero flow rate and at full flow rate as described in Section 3.2.2. Assuming $P_L = 0$, the zero flow power constant (Po_Z) was obtained from Eq. (3.10), since Po_Z is constant with Re in turbulent flow (Figure 4.11), and flow number (N_Q) is constant. The flow power constant (k_1) was then obtained from Eq. (3.13) using N_Q calculated from Eq. (3.11) using Figure 4.10, and unrestricted power number from Eq. (3.12).

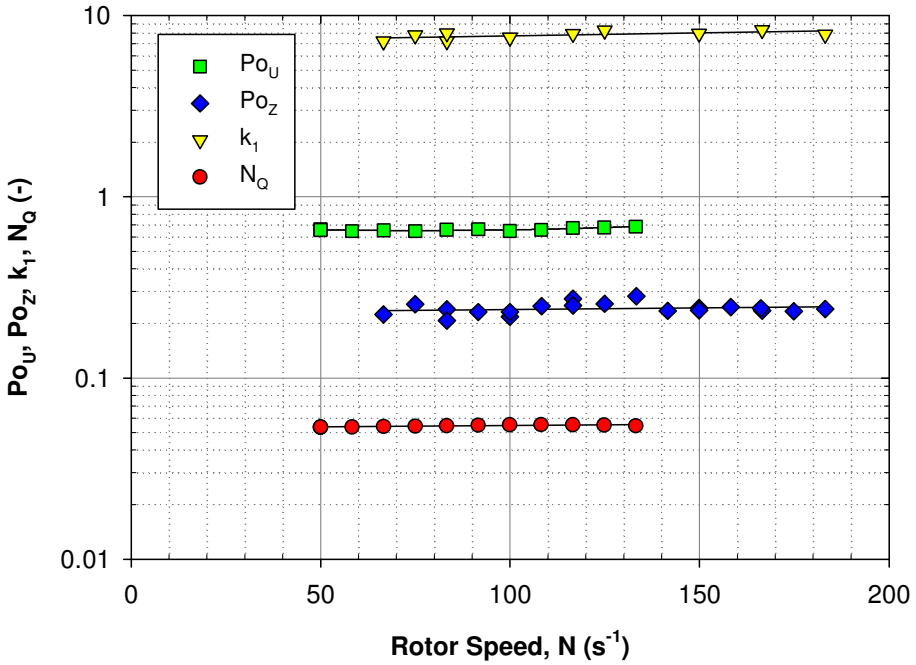

Figure 4.11: The effect of rotor speed on the power constants Po_U, k_1, Po_Z and the flow number, N_Q for the 150/250 mixer with standard double emulsor stators.

The value of Po_Z by this method is too high at 0.24 compared to 0.20 by regression (Table 4.1), due to the increase in power draw at low flow rates (Figure 4.8), see Section 4.4. Po_U is useful for power measurement when the mixer is operated in unrestricted flow conditions, and Po_U is better for comparison with Po for stirred tank impellers, which normally operate without restriction. Po_U is approximately 0.6, which as for flow number, is roughly an order of magnitude lower than for a Rushton turbine where Po = 5 (Edwards et al., 1997), which is similar in design to the rotor. Po_U is also lower than Po for a batch rotor-stator mixer where Po = 1.7-3.0 (Padron, 2001).

4.6 Power curve

Figure 4.12 presents the power curve for the 150/250 Silverson mixer, combining the turbulent power measurements in Section 4.2 with laminar and transitional power

measurements from The University of Manchester, reported by Cooke et al. (2012). Figure 4.12 shows that the power curve is similar to an unbaffled stirred tank impeller power curve (Hemrajani and Tatterson, 2004), and the position of these regimes is similar to a batch rotor-stator mixer (Padron, 2001).

The main difference between a power curve for a conventional agitator and the in-line rotor-stator mixer is the presence of unrestricted flow and zero flow curves in the turbulent regime. Since the mixer can operate at varying flow rates (valve fully closed to fully open), a range of power measurements were obtained at a given Re, depending on flow rate. This results in the concept of two turbulent power numbers, the zero flow power constant (Po_Z), and the unrestricted flow power constant (Po_U), see Section 4.5. The power curve shows that for double emulsor stators, Po_Z is roughly 0.24 and Po_U is ~ 0.66.

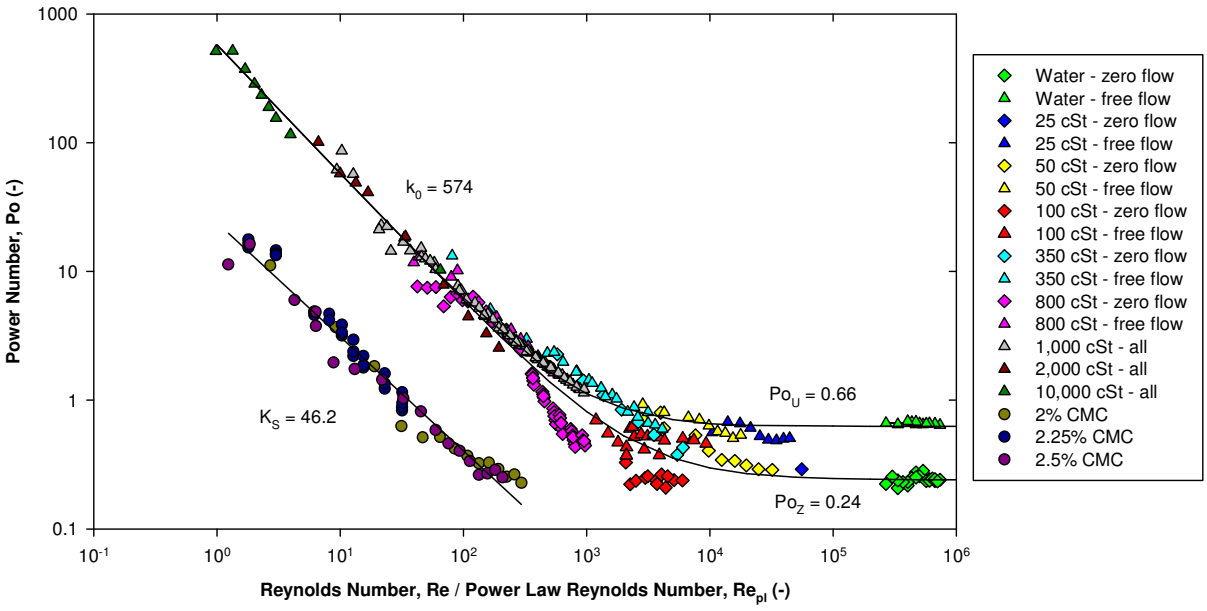

Figure 4.12: Power number as a function of Reynolds number and power law Reynolds number for Newtonian and non-Newtonian fluids for the 150/250 Silverson mixer with standard double Silverson emulsor screens. Data taken from Cooke et al. (2012) for 2 to 2.5 wt.% CMC non-Newtonian fluids and for 25 to 10,000 cSt Newtonian silicone oils.

In the laminar regime, the laminar power constant (k_0) is 574, which is a function of the rotor geometry. Doucet et al. (2005) found a value of 314 for a batch rotor-stator device, which is greater than for a stirred tank impeller, due to the presence of the stator.

Applying the Metzner-Otto approach to the non-Newtonian power data using Eq. (2.15), Cooke et al. (2012) obtained a Metzner-Otto shear rate constant (K_S) of 46.2, which is significantly greater than typical values of K_S (~ 11.5) for a Rushton turbine (Wu et al., 2006). The Metzner-Otto shear rate constant suggests that for the Silverson mixer with double stators, the average shear rate is much higher than for a stirred vessel agitator.

4.7 Power draw at different scales

The power constants for three scales of in-line Silverson rotor-stator mixer obtained from multi-linear regression are summarised in Table 4.2. Values of Po_Z are roughly constant at ~ 0.24 at each scale, which suggests that Po_Z is practically scale independent when the mixer geometry is similar. Other findings suggest that Po_Z is geometry dependent which is discussed in Section 4.8. The flow power constant (k_1) varies more with scale than Po_Z, from 7.5 to 11.8. Figure 4.13 illustrates that Eq. (2.21) can accurately predict power draw from the lab scale to the factory scale.

Table 4.2: Power draw constants in Eq. (2.21) (Po_Z and k_1) with 95% confidence intervals (CIs) and Po_U and N_Q constants by calorimetry.

Power draw constants	**Regression results**				N_Q	Po_U **Eq. (3.12)**
	Value	***Standard Error***	***Lower 95% CIs***	***Upper 95% CIs***		
088/150						
Po_Z	0.254	0.034	0.176	0.332	0.047	0.70
k_1	9.59	1.60	5.89	13.30		
150/250						
Po_Z	0.229	0.004	0.222	0.237	0.054	0.66
k_1	7.46	0.16	7.13	7.78		
450/600						
Po_Z	0.231	0.006	0.219	0.243	-	-
k_1	11.80	1.15	9.45	14.15		

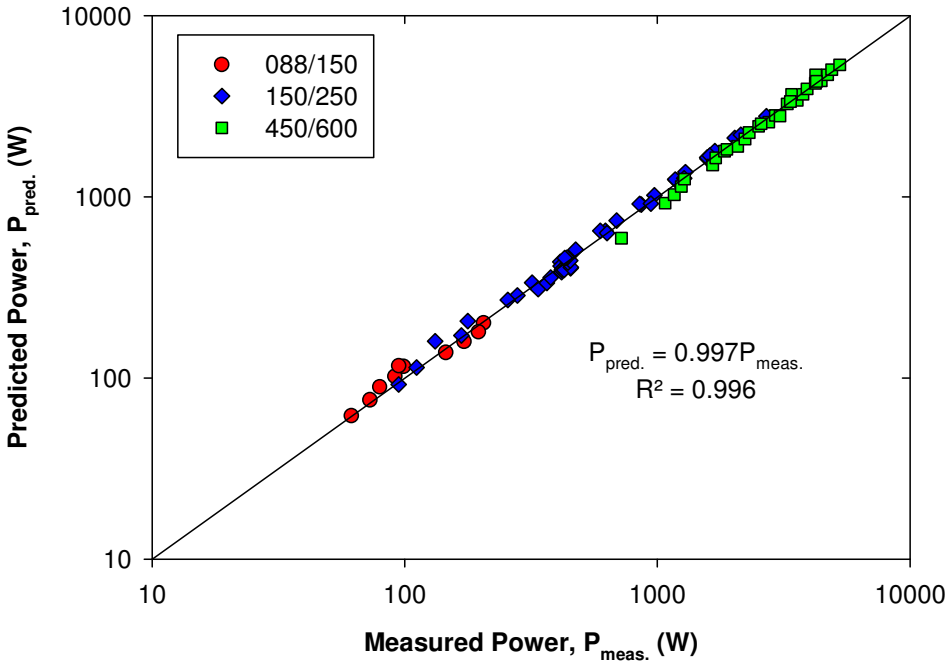

Figure 4.13: Predicted power draw from Eq. (2.21) versus measured power draw by calorimetry for three scales of in-line Silverson mixer, fitted with standard double Silverson emulsor screens.

Since both Po_Z and k_1 are similar at each scale, this confirms that the modified expression for power draw can be used for scale-up of in-line Silverson mixers. The confidence intervals for the smaller scale 088/150 mixer are wider, due to the difficulty in measuring small temperature differences as the temperatures are of a similar order to the systematic difference in the readings between the thermocouples, hence experimental error as a percentage is higher.

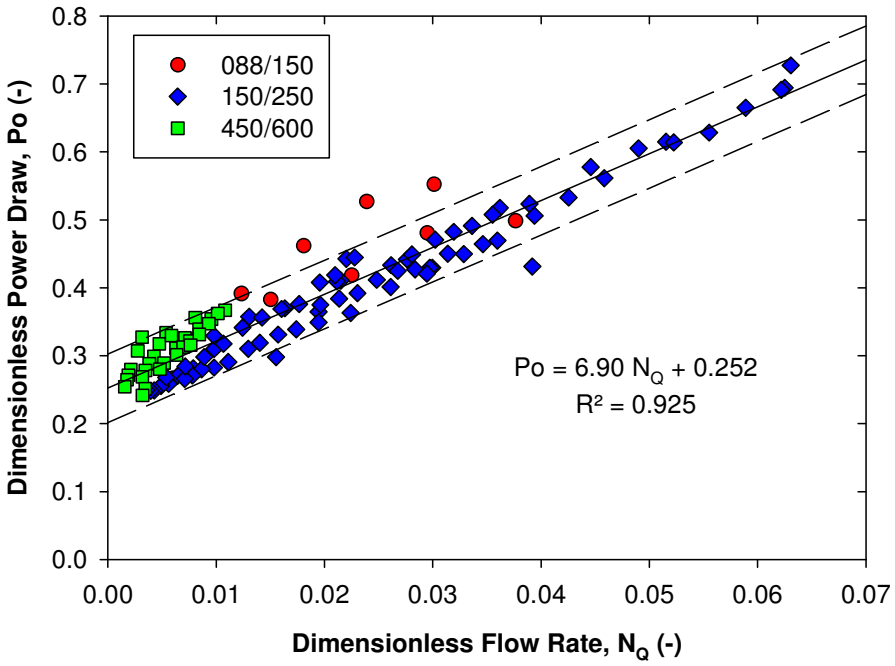

Figure 4.14: Dimensionless power draw as a function of dimensionless flow rate for three scales of in-line Silverson mixer, with 20% error lines.

Figure 4.14 clearly shows the variability in power draw measurements for the small scale mixer. When power draw was normalised and data from three scales compared, power values for the pilot plant scale 150/250 mixer lay slightly below the other scales, which is a

reflection of the slightly lower values of Po_Z and k_1 obtained at this scale. Figure 4.14 shows that Po_Z and k_1 are not linearly dependent on scale.

4.8 Effect of rotor-stator geometry on power draw

The effect of rotor-stator geometry on power draw was investigated in the 150/250 mixer. Measured power draw as a function of flow rate at 11,000 rpm is presented in Figure 4.15. This figure shows the trends in power draw are similar for seven rotor-stator geometry as linear fits give gradients from 0.23 to 0.30, with no systematic differences based on geometry.

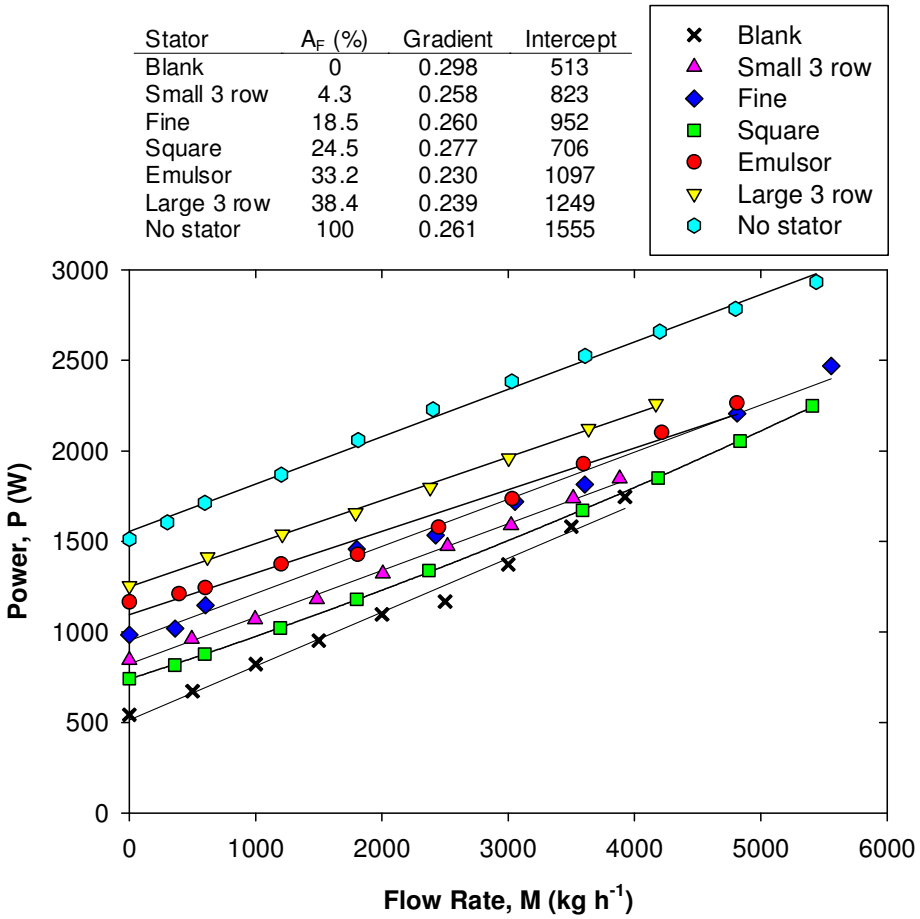

Figure 4.15: The effect of flow rate on power draw measured by torque in the 150/250 mixer for a rotor speed of 11,000 rpm, for seven rotor-stator configurations (single stators) with open area fractions (A_F) from 0 to 100%.

However, the absolute value of power consumption from the intercepts appears to be strongly related to the geometry, in particular power draw when the stator was removed is about three times greater than for the blank stator when the holes were blocked.

In Section 4.4, power draw was observed to increase at low flow rates (< 500 kg h^{-1}) for double standard emulsor screens (config. L). This may result from internal recirculation due to the expulsion of fluid through the stator openings, that is drawn back through the openings by negative pressure caused by the rotor blade (Figure 4.22a in Section 4.9). However, Figure 4.15 does not show a pronounced increase in power draw at low flow rates, for a range of single stators. This may imply that the effect described in Section 4.4 for double standard emulsor screens may be an artefact of the design of this particular rotor-stator configuration, where factors are such that recirculation flow fields are reinforced and power draw increases.

The power draw constants Po_Z and k_1 in Eq. (2.21), along with selected unrestricted flow power numbers (Po_U) are given in Table 4.3 for various rotor-stator configurations, (A-M) investigated.

Table 4.3: Power draw constants for various rotor-stator configurations in the 150/250 mixer with error values based on 95% confidence intervals.

Configurations	Rotors	Stators	Stator design	Po_Z	k_1	Po_U	η
A	2	0	No stator	**0.252** ±0.004	**6.64** ±0.18	0.735	0.27
B	1	1	Fine emulsor	**0.144** ±0.013	**7.52** ±0.58	0.588	0.17
C	1	1	Square hole	**0.104** ±0.004	**7.70** ±0.16	0.556	0.25
D	1	1	Standard emulsor	**0.166** ±0.007	**6.12** ±0.39	0.541	0.26
E	2	1	Blank	**0.079** ±0.008	**8.00** ±0.52	-	-
F	2	1	Small 3 row	**0.114** ±0.004	**7.09** ±0.25	-	-
G	2	1	Standard emulsor	**0.162** ±0.008	**6.81** ±0.43	0.510	0.21
H	2	1	Large 3 row	**0.195** ±0.003	**6.40** ±0.20	-	-
I	2	1	Large 3 row wide gap	**0.241** ±0.008	**6.20** ±0.39	-	-
J	2	1	Large 3 row thick	**0.165** ±0.006	**8.21** ±0.29	-	-
K	2	2	Fine emulsor	**0.141** ±0.003	**9.76** ±0.16	0.590	0.14
L	2	2	Standard emulsor	**0.197** ±0.007	**9.35** ±0.28	0.595	0.13
M	2	2	Standard emulsor wide gap	**0.205** ±0.004	**8.05** ±0.20	-	-

Overall, Table 4.3 shows that Po_Z averages at about 0.17 for all rotor-stator configurations investigated, ranging from 0.079 when the stator holes were blocked, to 0.252 when the stator was removed. These are the extreme conditions which together with Figure 4.15 suggest that stator open area strongly effects power draw.

Values of k_1 average at 7.5 and range from 6 to 10. The power numbers for unrestricted flow (Po_U) are roughly 0.5-0.6 for an in-line rotor-stator mixer, with a notable rise to 0.74 for config. (A) with no stator present.

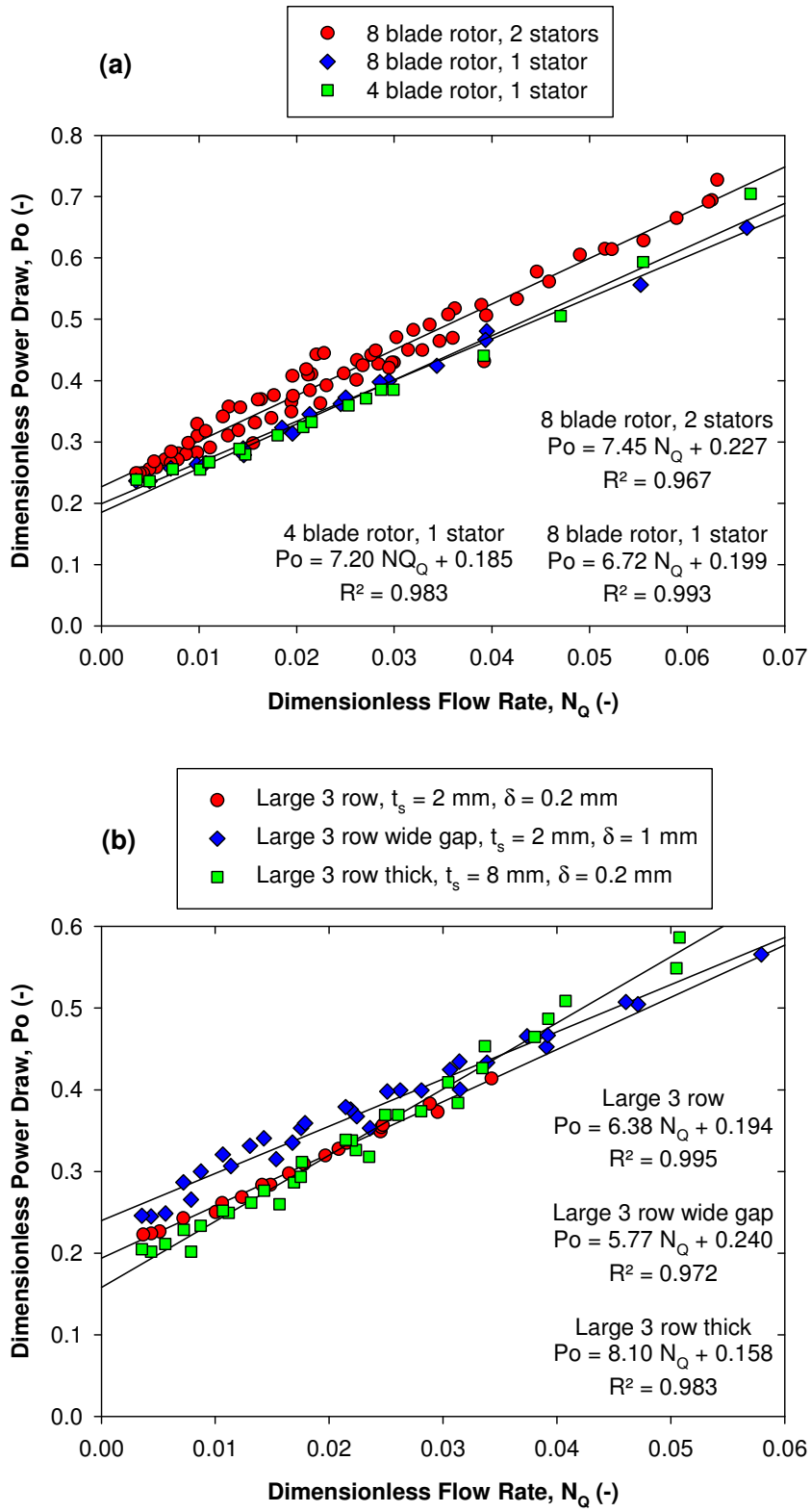

Figure 4.16: Dimensionless power draw as a function of dimensionless flow rate for (a) three stators examining the effect of number of rotor blades and number of stators on power draw and for (b) three stators examining the effect of stator thickness and rotor-stator gap width on power draw in the 150/250 mixer.

The effect of various rotor-stator geometry parameters on power number are shown in Figure 4.16. Since power draw depends on rotor speed and flow rate, both operating conditions need to be considered, hence Table 4.4 shows the effect of power draw averaged across various operating conditions. A summary of the effect of geometry on power draw:

- Number of rotor blades – Increasing the number of blades on the outer rotor from 4 to 8 blades had little effect on power consumption (Figure 4.16a).
- Number of stators – Figure 4.16a shows power draw clearly increased by ~ 30% once a double emulsor stator was used compared to a single emulsor stator, as expected, since the flow resistance is greater for two stators. Power draw also increased by 15% for the double fine emulsor stator (Table 4.4). This is manifested through an increase in k_1 for double stators, which are approximately 9.5 for double stators, and 7 for single stators.
- Hole diameter – Increasing the hole diameter increased power consumption in both cases investigated (Table 4.4). However once the open area was kept roughly constant, the effect of hole diameter diminished, suggesting that the effect of the stator open area is more important, indicated by Figure 4.15.
- Stator thickness – Power draw was not greatly affected by a four-fold increase in the stator thickness, see Figure 4.16b and Table 4.4.
- Rotor-stator gap width – Increasing the rotor-stator gap width by five times increased power draw by 12% for the large 3 row stator design, especially at lower flow rates (Figure 4.16b), which suggests internal recirculation is increased for a wider δ. However, for the double standard emulsor design, power draw actually decreased once δ was doubled. Higher power consumption for a wider gap stator intuitively makes

sense as a wider gap would allow easier flow recirculation back into the rotor region, but other parameters such as the hole diameter and open area may also have an effect. In addition, a very wide gap stator equals the no stator case, where power draw was greatest. Padron (2001) found power draw decreased by 10% for a 100% increase in rotor-stator gap width, while Thapar (2004) reported a four-fold difference in δ had a minimal effect on the power characteristics, and concluded that the effect of the gap width on drop size is insignificant.

Table 4.4: Effect of geometry parameters on power draw constants and power draw for a range of operating conditions in the 150/250 mixer.

Geometry parameter	**Geometry change**	**Effect on Po_Z**	**Effect on k_1**	**Effect on average power consumption**
Number of rotor blades	4 to 8 blades	-2%	+11%	+4%
Number of stators – emulsor	1 stator (outer) to 2 stators (inner and outer)	-13%	+37%	+29%
Number of stators – fine emulsor	1 stator (outer) to 2 stators (inner and outer)	-2%	+30%	+15%
Hole diameter – equal number of holes (n_h: 72)	1.6 to 4.8 mm (A_h: 140 to 1,200 mm^2)	+71%	-10%	+23%
Hole diameter – equal open area (A_h: 1,200 mm^2)	1.6 to 4.8 mm (n_h: 560 to 72)	+20%	-6%	+7%
Stator thickness	2 to 8 mm	-15%	+28%	+4%
Rotor-stator gap width – large 3 row	0.18 mm to 1.02 mm	+24%	-3%	+12%
Rotor-stator gap width – double emulsor	0.24 mm to 0.48 mm	+4%	-14%	-5%

An attempt to determine the key factors of the geometry which affect the power draw constants, Po_Z and k_1, is given below.

4.8.1 Zero flow power constant

The zero flow power constant (Po_Z) (from regression) is a measure of the power required to rotate the rotor against the fluid resistance, and provide internal fluid recirculation across the screens. Therefore, it may be expected that Po_Z would correlate well with stator open area (A_h), as a greater open area enables more flow to be recirculated across the screens.

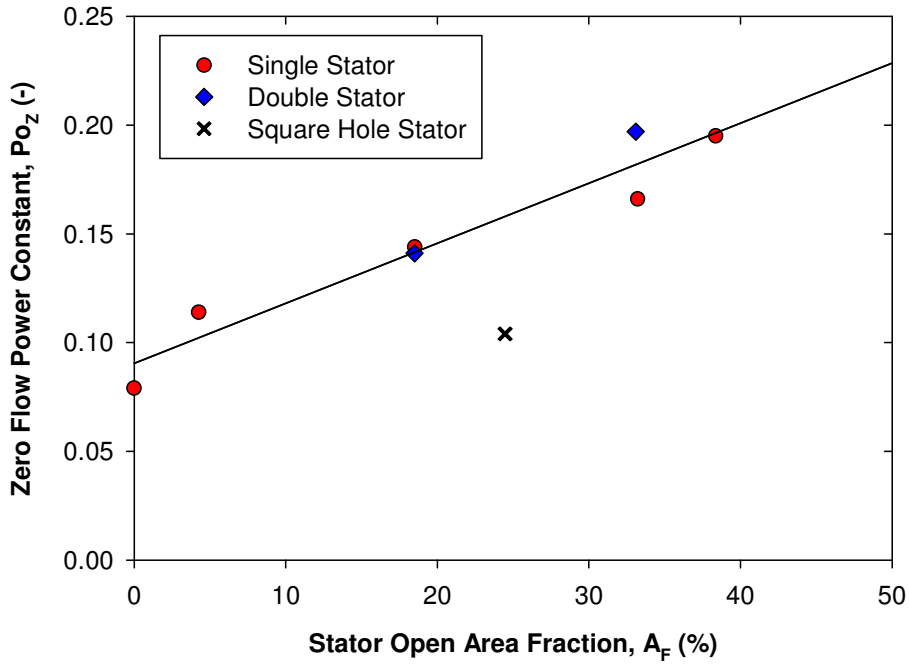

Figure 4.17: The effect of the stator open area fraction (area of openings as a fraction of the total stator area) on the zero flow power constant (Po_Z) for single and double stators in the 150/250 mixer.

Figure 4.17 shows Po_Z is proportional to the stator open area fraction ($A_F = A_h/A_s$), for single and double stators. This is despite the fact that the stator designs are different in

other respects, which indicates that Po_Z is strongly influenced by A_F. Utomo et al. (2009) found using numerical simulations that Po was proportional to both stator open area and flow rate through the stator holes for three geometry configurations.

The data point furthest from the trend line is for the square hole stator (config. C), which is the only screen investigated with non-circular openings, thus it may be more difficult for the flow to be recirculated when the openings are angular, and a lower Po_Z is obtained. The application of CFD may provide an insight into this effect. Figure 4.17 shows no effect of the number of stators on Po_Z since the addition of a second stator generally resulted in an increase in k_1. To determine the effect of the geometric parameters, only single stator results were included in the analysis below.

Further geometry variables that may affect power draw include the perimeter of the stator holes (P_h) and rotor-stator gap width (δ). A speculative expression for Po_Z is presented as a function of δ, the area of the holes per unit area of the stator, $A_F = (A_h/A_s)$, and perimeter of holes per unit area of the stator, $P_F = (P_h/A_s)$, for six single stator configurations:

$$Po_Z = 0.29{A_F}^{0.29}{P_F}^{-0.08}\delta^{0.13} \quad (4.2)$$

This correlation gives an excellent fit (R^2 = 0.999), when the data point for the square hole stator is omitted, and indicates that Po_Z depends less on δ and P_F, than A_F.

A common way of characterising a stator is by using hydraulic radius, defined as the cross-sectional area of the hole divided by the hole perimeter (Padron, 2001):

$$R_h = \frac{A_c}{P_w} \quad (4.3)$$

Figure 4.18 shows that hydraulic radius does not readily correlate Po_Z for single and double stators, and cannot be used to compare the rotor-stator configurations with no openings.

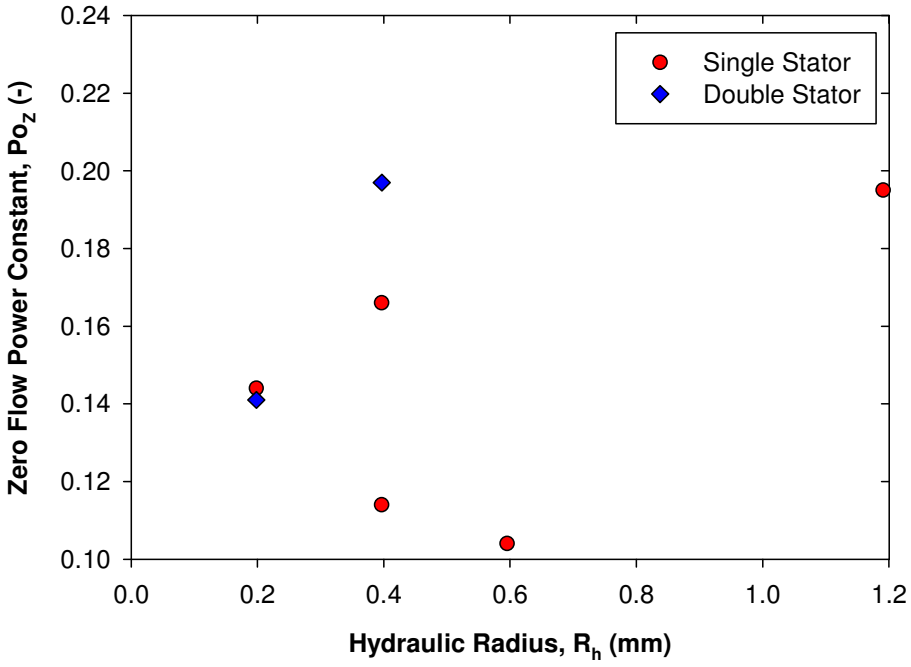

Figure 4.18: Correlation between measured (Po_Z) values and hydraulic radius for single and double stators in the 150/250 mixer.

4.8.2 Flow power constant

The flow power constant (k_1), is a measure of the power required to accelerate and pump fluid (Kowalski, 2009), and is related to factors that increase the pressure drop across the screens. Using the variables in Eq. (4.2), the correlation for k_1 is:

$$k_1 = 6.19{A_F}^{-0.12}{P_F}^{0.08}\delta^{-0.02} \tag{4.4}$$

This relationship is much poorer than Eq. (4.2) with a R^2 of 0.641, which suggests that k_1 is not strongly related to the stator geometry, and further conclusions cannot be drawn about the dependency of k_1 on geometric variables.

The efficiency term in Eq. (4.1) is constant at high flow rates, given in Table 4.3 for different rotor-stator designs, show η is smaller for double stators where fluid flow experiences more resistance. Figure 4.19 shows that k_1 is inversely related to η which confirms that power required for pumping (k_1) is greater when the fluid resistance is greater (η is smaller). The same relationship also holds across different scales, where the high k_1 for the factory scale 450/600 mixer translates into poor pumping efficiency, most likely due to rig restrictions (feeding the mixer with a 1.5" pipeline instead of a 3" pipeline).

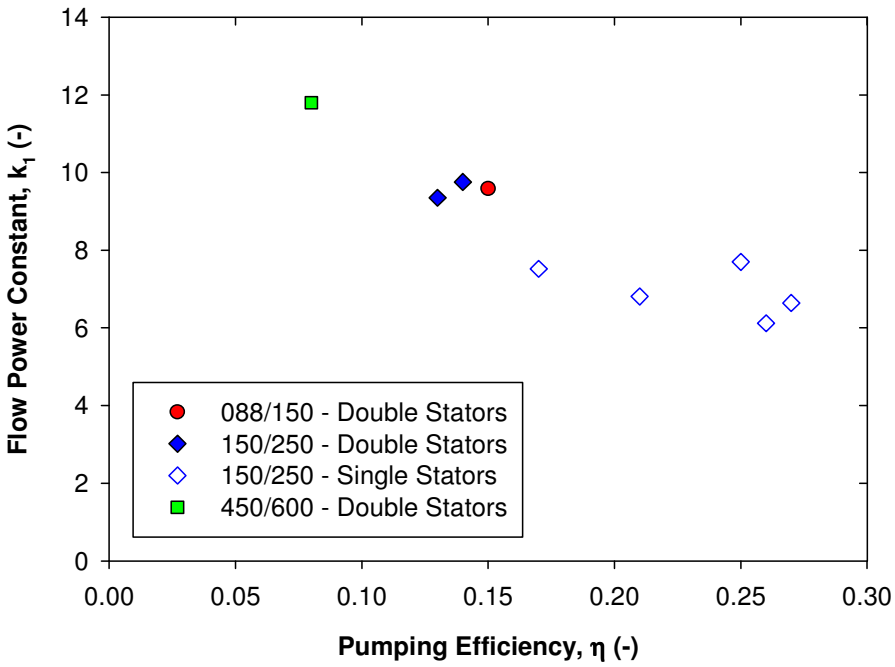

Figure 4.19: The effect of pumping efficiency (η) in Eq. (4.1) on the flow power constant (k_1). The 088/150 and 450/600 data are from calorimetry.

4.9 Theoretical calculation of power draw

The measurement of power draw in the sections above is often applied to design and analyse emulsification processes to predict average energy dissipation rate in Eq. (2.47). This

approach is simple as it assumes that the intensity of flow determining drop size (energy dissipation rate or shear rate) is constant in the mixing head.

Flow fields in the in-line 150/250 rotor-stator mixer were simulated using a 2D model geometry created in Gambit 6.3 and run in Fluent 12.0 (ANSYS). The model contained about 200,000 cells (tetrahedral and hexahedral) and 180,000 nodes (Figure 4.20). The rotor-stator gap and the stator holes were divided into 8 hexahedral cells, with the interface between the rotating and stationary frames located in the centre of the rotor-stator region. Mass flow rate was used as the inlet boundary condition and outflow as the outlet boundary condition, with no slip velocity conditions at the rotor and stator walls. Details regarding the 2D geometry are given in Appendix C.1.

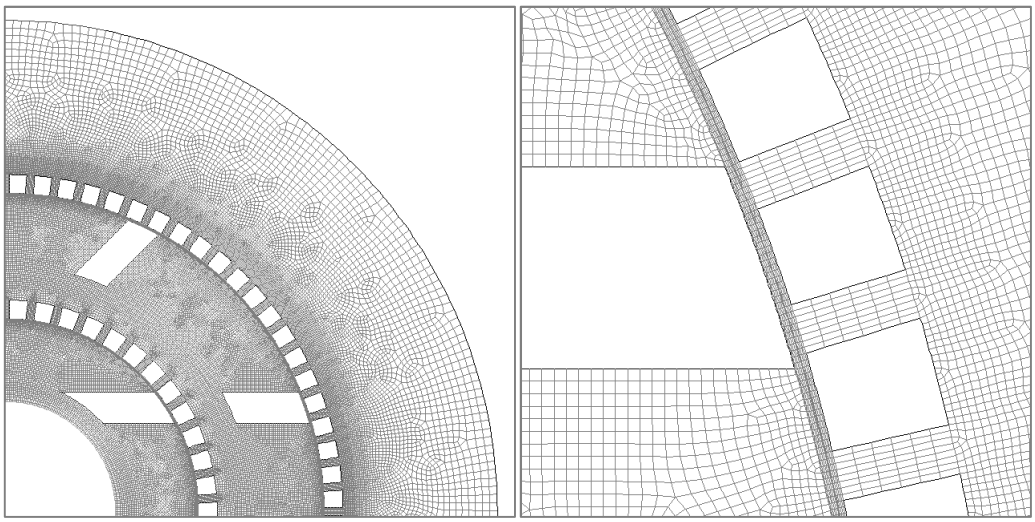

Figure 4.20: The 2D rotor-stator mesh.

Simulations were run using steady state standard multiple reference frames. The standard $k-\varepsilon$ turbulence model was employed with standard wall functions to describe the boundary layer. The solution was obtained using second order discretisation schemes, and

was considered converged when residuals fell below 10^{-3}. Rotor speed was varied from 3,000 to 11,000 rpm and flow rate from 0 to 2,400 kg h^{-1}.

Velocity and energy dissipation rate profiles inside an in-line 150/250 Silverson rotor-stator mixer fitted with double standard emulsor screens are shown in Figure 4.21, and in detail in Figure 4.22. It is obvious from Figure 4.21a, that both the intensity and nature of flow varies greatly across the mixing head, with velocity reaching a maximum at the leading and trailing edges near the tips of the outer rotor. This suggests that the outer rotor and stator play a stronger role in emulsification than the inner rotor and stator. Details of the flow around the holes show high velocity jets emerging from the holes at the leading edge of the rotor blade, with some fluid forced back into the stator in the form of recirculation loops through the holes at the trailing edge of the rotor blade (Figure 4.22a).

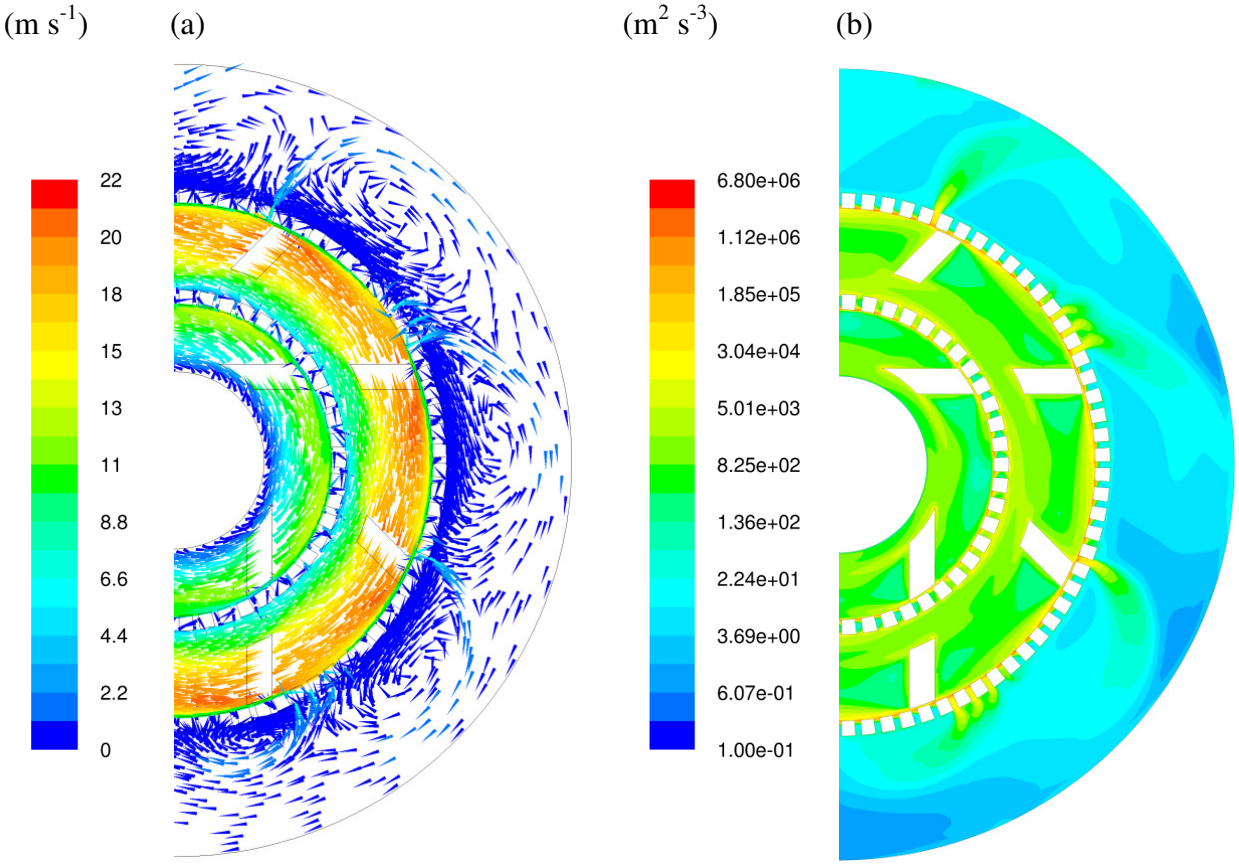

Figure 4.21: (a) Velocity vectors and (b) contours of energy dissipation rate for the 150/250 Silverson mixer fitted with standard double emulsor screens at 6,000 rpm and 600 kg h^{-1}.

The energy is mainly dissipated relatively uniformly in the region between the inlet and the outer screen (Figure 4.21b), while the maximum levels of energy dissipation occur in the relatively small volume at the leading edges of the holes and in the gap between the outer rotor and the outer stator (Figure 4.22b).

(a) (b)

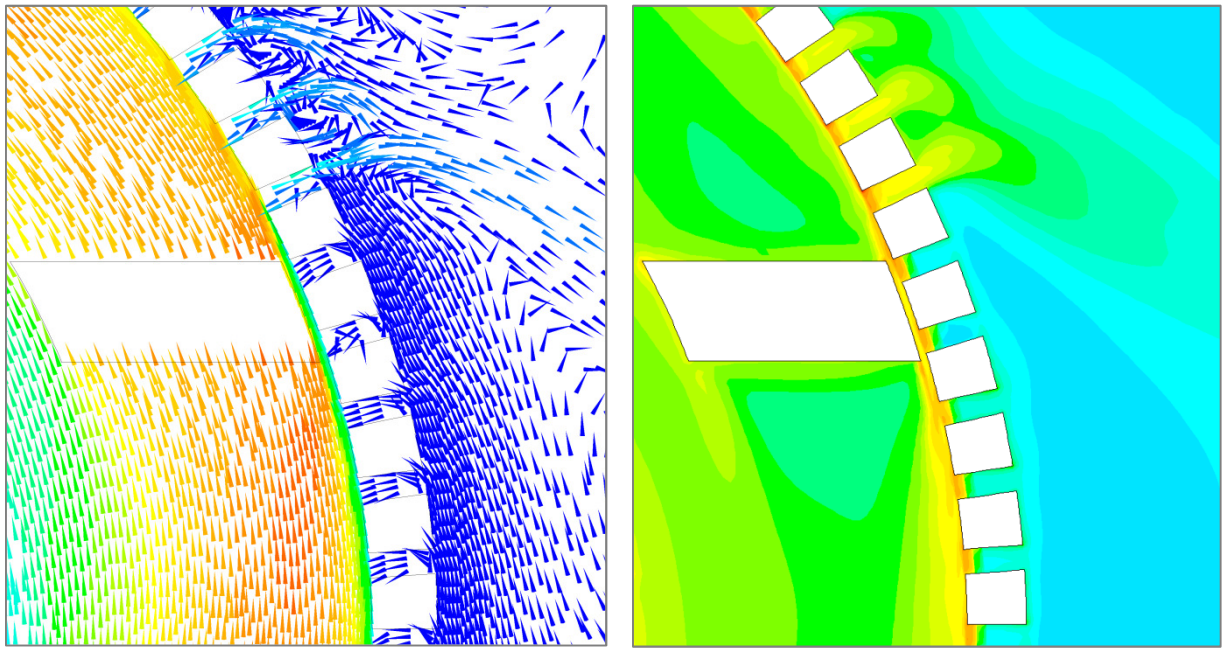

Figure 4.22: Details of (a) velocity vectors and (b) contours of energy dissipation rate in Figure 4.21. For key, see Figure 4.21.

Figure 4.23 shows the distribution of energy dissipated in the rotor-stator mixer corresponding to the case in Figure 4.21b. The distribution of energy is practically bimodal with a high level of energy dissipated inside the stator between the inlet and the outer screen, and a relatively low level of energy dissipated outside the outer screen. There are a few regions of very high energy dissipation (~ 10^6 W kg^{-1}) in close proximity to the screens, but these occupy a very small volume of the mixer, therefore their contribution to emulsification is negligible. The ratio of the maximum to mean energy dissipation rates $\left({}^{\varepsilon_{max}}/_{\varepsilon}\right)$ is approximately 1,000, roughly an order of magnitude greater than for stirred vessels (Zhou and Kresta, 1998).

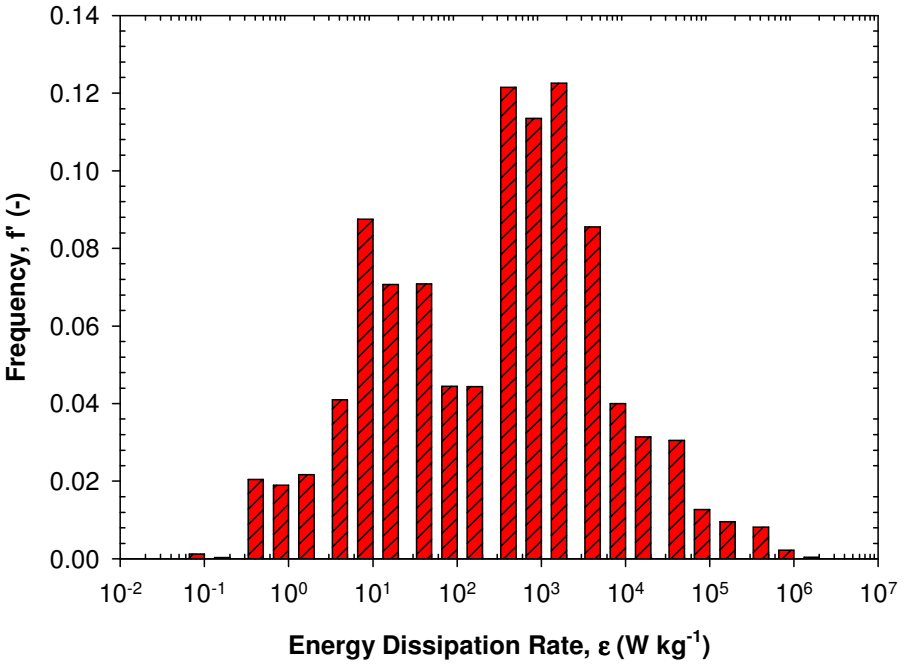

Figure 4.23: Distribution of energy dissipation rate in the 150/250 rotor-stator mixer, at 6,000 rpm and 600 kg h^{-1}.

Simulations enable estimation of the recirculating flow rates observed in Figure 4.22a as a function of the total mixer flow rate. Figure 4.24 defines the flow rate of fluid exiting the outer stator (Q_{os}) (positive radial flow), the flow rate of fluid returning to the outer stator (Q_{is}) (negative radial flow) and total mixer flow rate ($Q_{out} = Q_{in}$).

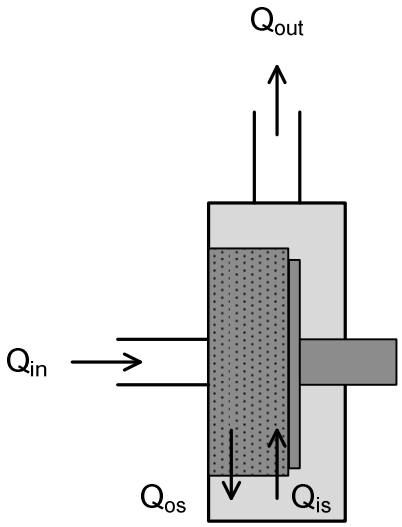

Figure 4.24: The stator flow rates in the mixing head.

Figure 4.25 shows that the inward flow is always rather considerable and means outward flow through the stator always exceeds the total flow rate measured through the mixing head. The inward flow rate was highest, when $Q_{is} = Q_{os}$, when flow rate through the mixer was zero, falling as a function of mixer flow rate to ~ 20% of the outward flow at 2,400 kg h^{-1}. The significance of inward flow (Q_{is}) is important at low mixer flow rates as this characteristic of rotor-stator mixers allows more fluid to return to the rotor region during each pass. In addition, the minimum in flow rate at 300 kg h^{-1} is the same as measured experimentally in Section 4.4.

The calculated values of stator flow rate are lower than in reality, partly because 2D simulations do not simulate the flow perfectly, and as the flow rate in each stator hole was averaged to find the net inward and outward flow, an underestimate arises since in some stator holes, inward and outward flow occur simultaneously.

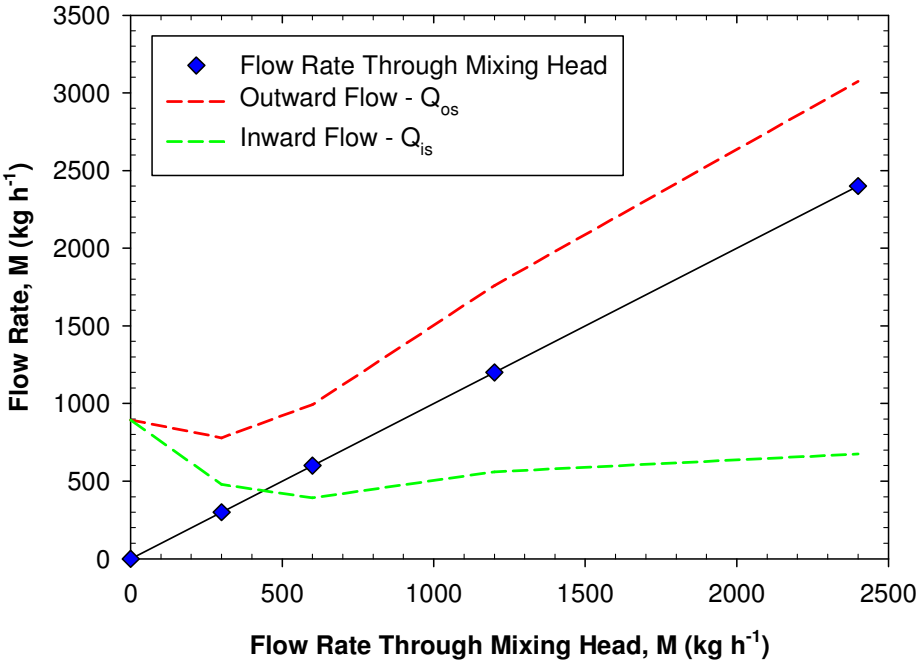

Figure 4.25: Calculated outward and inward flows through the outer stator of the 150/250 mixer at 6,000 rpm.

Figure 4.26 compares power draw measured experimentally by torque and power draw predicted from simulations from torque on the rotor shaft and the integral of energy dissipated across the mixing head. Good agreement between experimental and calculated power values were obtained at lower rotor speeds, while at higher rotor speeds experimental values exceeded simulated values by ~ 30%. Under prediction of power from simulations was reported by Utomo et al. (2009) for a batch rotor-stator mixer and Ozcan-Taskin et al. (2011) for an in-line rotor-stator mixer, despite both studies undertaking full 3D simulations. Ozcan-Taskin et al. (2011) also compared calculated power from torque and energy dissipated, and similar to this study (Figure 4.26), established that torque gave a better approximation of measured power.

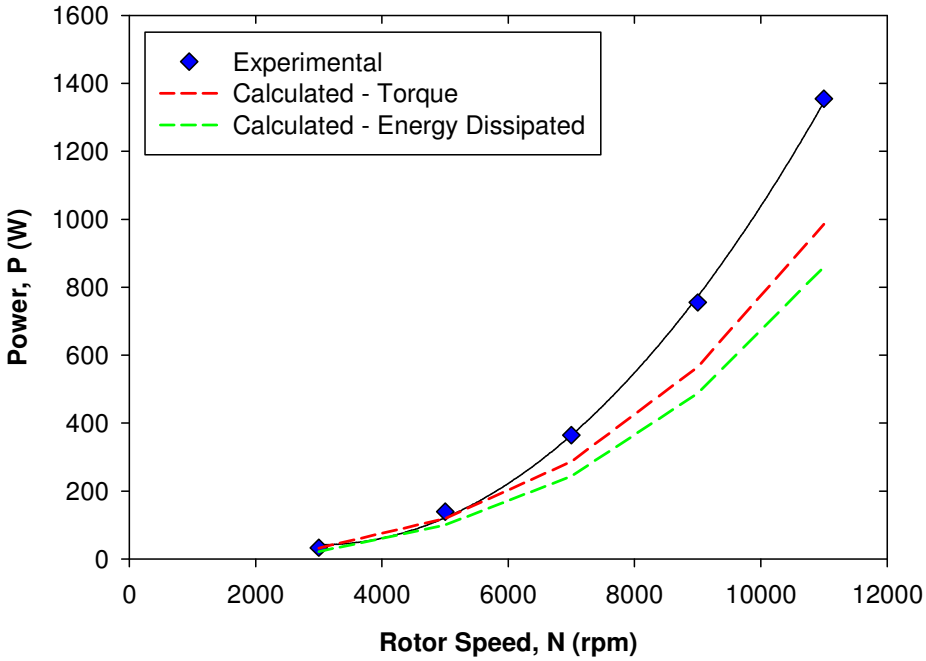

Figure 4.26: The effect of rotor speed on experimental (by torque) power draw and calculated power draw by torque and energy dissipated at 300 kg h^{-1} in the 150/250 mixer.

4.10 Summary

Power draw was measured as function of rotor speed and flow rate at three mixer scales and for thirteen rotor-stator configurations. Turbulent power draw fitted well to a two-term expression containing two power constants (Po_Z and k_1) using both torque and calorimetry methods. The 'zero flow power constant' (Po_Z) remained constant at different scales, however Po_Z was geometry dependent, especially depending on the stator open area. Power draw calculated theoretically from CFD simulations gave reasonable agreement with experimental measurements.

CHAPTER 5. DROPLET BREAK-UP BY IN-LINE SILVERSON ROTOR-STATOR MIXERS

5.1 Introduction

Literature on emulsification using in-line rotor-stator mixers is limited, hence this study aims to increase the understanding of emulsification in these devices and examine possible literature correlations and droplet breakage mechanisms. The effect of process parameters including rotor speed and flow rate, and formulation variables such as dispersed phase volume fraction, dispersed phase viscosity and continuous phase viscosity on drop size distributions (DSDs) for a single pass through the mixer were investigated. Mean droplet size was correlated with commonly used parameters including energy dissipation rate to gain a fundamental understanding and obtain expressions that could be applied to other systems. All DSDs were formed by a single pass through the 150/250 mixer using standard double Silverson emulsor screens and measured using the Mastersizer X particle analyser. Part of this work has been published in:

- Hall, S., Cooke, M., El-Hamouz, A., and Kowalski, A. J., (2011). "Droplet break-up by in-line Silverson rotor-stator mixer", *Chemical Engineering Science*, **66(10)**, 2068-2079.

5.2 Effect of inlet droplet size on outlet drop size

The coarse emulsions prepared in the batch stirred vessels inevitably show a degree of variation in droplet size over the experiments so the effect of the inlet drop size (Sauter mean diameter) on the outlet drop size from the Silverson mixer was investigated.

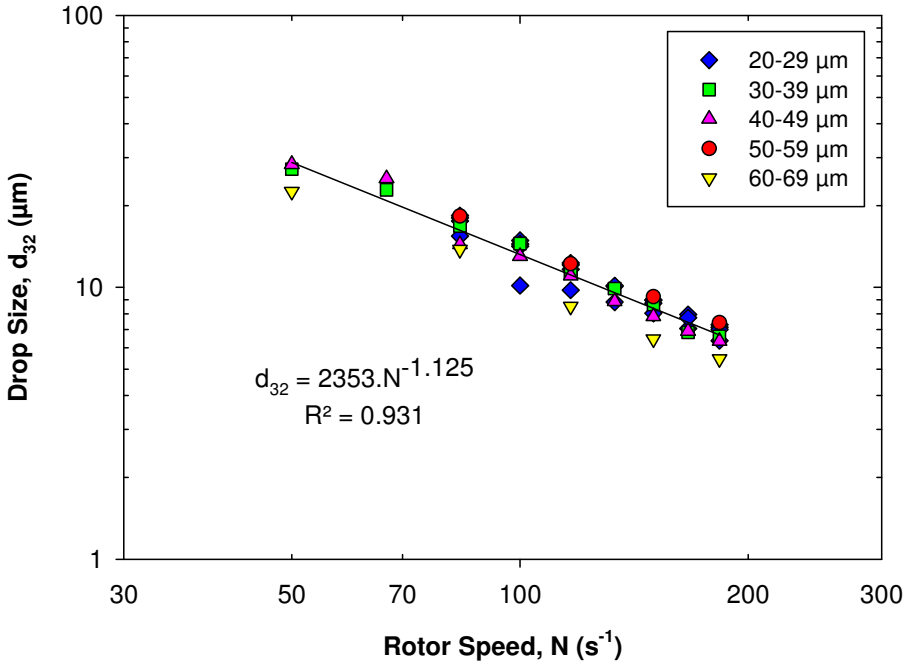

Figure 5.1: Effect of rotor speed on mean drop size of silicone oil emulsions for a range of inlet drop sizes for a flow rate of 300 kg h^{-1} and dispersed phase viscosity of 339 mPa·s.

Outlet mean drop size for 1 to 50 wt.% 339 mPa·s silicone oil emulsions as a function of rotor speed (N) for a range of inlet drop sizes from 23 to 62 µm are shown in Figure 5.1. As expected, the outlet Sauter mean diameter is inversely related to the rotor speed, but there do not appear to be any systematic trends between the outlet and the inlet droplet sizes. A single power law relationship fit to the data in Figure 5.1 gave a regression value (R^2) of 0.931. Therefore, it seems that the Silverson emulsification performance does not strongly depend on variations in the inlet drop size that may arise from upstream process unit operations. This result suggests that outlet drop size is dependant mainly on the operating conditions of the Silverson, possibly due to a combination of very high shear rates and the containing effect of the stator which helps to concentrate the flow.

5.3 The relationship between mean and maximum drop size

The relationship between Sauter mean diameter (d_{32}) and maximum droplet diameter, where $d_{max} = d_{0,9}$, for 1 wt.% silicone oil emulsions with viscosities from 9.4 to 9,701 mPa·s is presented in Figure 5.2. This figure shows a good linear relationship between d_{32} and d_{max} when the intercept is forced through the origin, which confirms the assumption of $d_{max} \propto d_{32}$ is acceptable and d_{32} can be applied in drop size correlations.

Figure 5.2 shows the gradient in the correlation $d_{32} = A.d_{max}$ is a strong function of dispersed phase viscosity, falling steadily from 0.5 for 9.4 mPa·s oil to 0.08 for 9,701 mPa·s oil. Typical values of the gradient reported for stirred vessels include 0.64 (Chen and Middleman, 1967), 0.72 (Brown and Pitt, 1972) and 0.61 (Calabrese et al., 1986), and Thapar (2004) and Francis (1999) obtained 0.13 and 0.44 for rotor-stator mixers, respectively. For a range of silicone oils, Padron (2005) presented values of 0.42-0.45 for low viscosity oils (10-100 cSt), falling to 0.31 for 10,000 cSt oil. The relatively low values indicate that rotor-stator mixers form wide distributions with a relatively large proportion of smaller droplets.

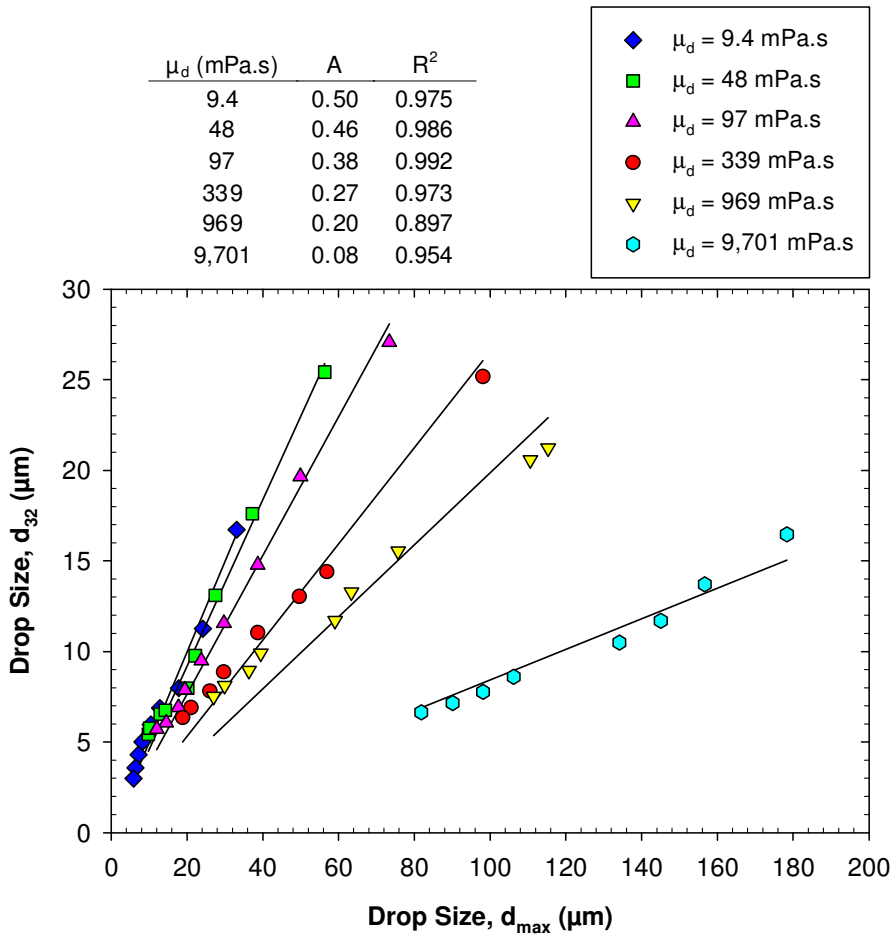

Figure 5.2: Correlation between mean drop size and maximum drop size for emulsions of six silicone oil viscosities for a flow rate of 300 kg h^{-1}.

5.4 Effect of rotor speed on drop size

Figure 5.3 shows the effect of rotor speed on drop size for 1 wt.% silicone oil emulsions at 300 kg h^{-1} for viscosities of 9.4 to 9,701 mPa·s. These results indicate that rotor speed has a strong effect on the emulsion drop size, with Sauter mean drop diameter proportional to N^b, where b = -1.14 to -1.29 for all viscosities except the most viscous oils where b ~ -0.86.

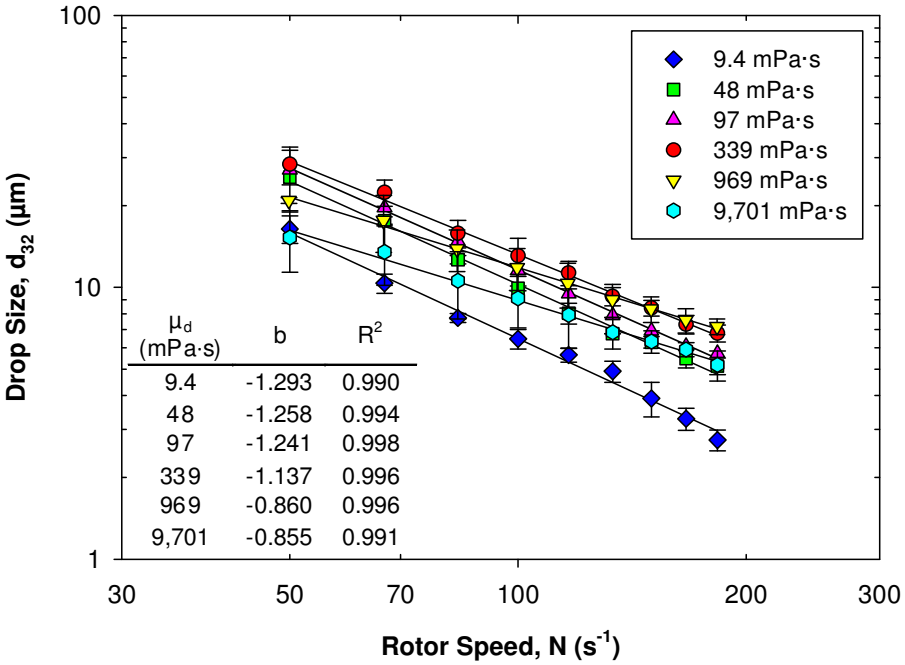

Figure 5.3: Effect of rotor speed on mean drop size of silicone oil emulsions for a range of dispersed phase viscosities for a flow rate of 300 kg h^{-1} and dispersed phase fraction of 1 wt.% with standard deviation error bars. The inlet drop sizes range from 28 to 54 µm.

The models in Eqs. (2.51), (2.62) and (2.67) are based on energy dissipation rate which is proportional to power draw, which for a fixed low flow rate is approximately proportional to N^3. For turbulent inertial break-up, b should equal -1.2 for drop sizes larger than η_K, while for drops below the Kolmogorov length scale, Shinnar (1961) suggested b = -1. For drop sizes smaller than η_K when viscous stresses are important for breakage, b should equal -1.5 (Shinnar, 1961). The results from this investigation cover a range of exponents; however turbulent inertial break-up is more likely since the majority of the drops are above the Kolmogorov length scale, calculated to be of the order of 2-5 µm, comparable to the size of the smallest drops produced (Table 5.1 in Section 5.8). Applying the Kolmogorov theory to this data suggests that drop breakage is due to turbulent inertial stresses, with a transition in

breakage mechanism when the cohesive viscous stresses become significant for the highest viscosity oils used.

For viscous dispersed phases, b should equal -0.75 when viscous forces are important for stabilising the drop (Leng and Calabrese, 2004), and b reduces to -0.86 for the highest viscosity oils. However the models in Eqs. (2.51), (2.62) and (2.67) are for inviscid drops when the effect of dispersed phase viscosity is negligible, but Figure 5.3 shows that there is a viscosity effect over the range 9.4 to 339 mPa·s, when b is > -1.14, since mean drop size increases for a given rotor speed. This discrepancy may be due to the complex flow regimes and shorter timescales in rotor-stator mixers compared to stirred vessels. Furthermore, the flow in the Silverson is highly irregular with regions of high energy dissipation rate near the rotor and regions where turbulent flow may not fully develop at short residence times, hence simple shear flow may be important.

Arai et al. (1977) found for emulsions of polystyrene-o-xylene in aqueous polyvinyl alcohol solutions dispersed using a disc turbine, that the higher viscosity data (> 520 mPa·s) fitted closer to a slope of -0.75, while the lower viscosities (< 34 mPa·s) fitted more appropriately to a -1.2 gradient. This is seemingly because the drop size was larger than the Kolmogorov length scale. This trend is similar to the results of this study where a lower gradient of -0.86 was found for the highest viscosities of 969 and 9,701 mPa·s.

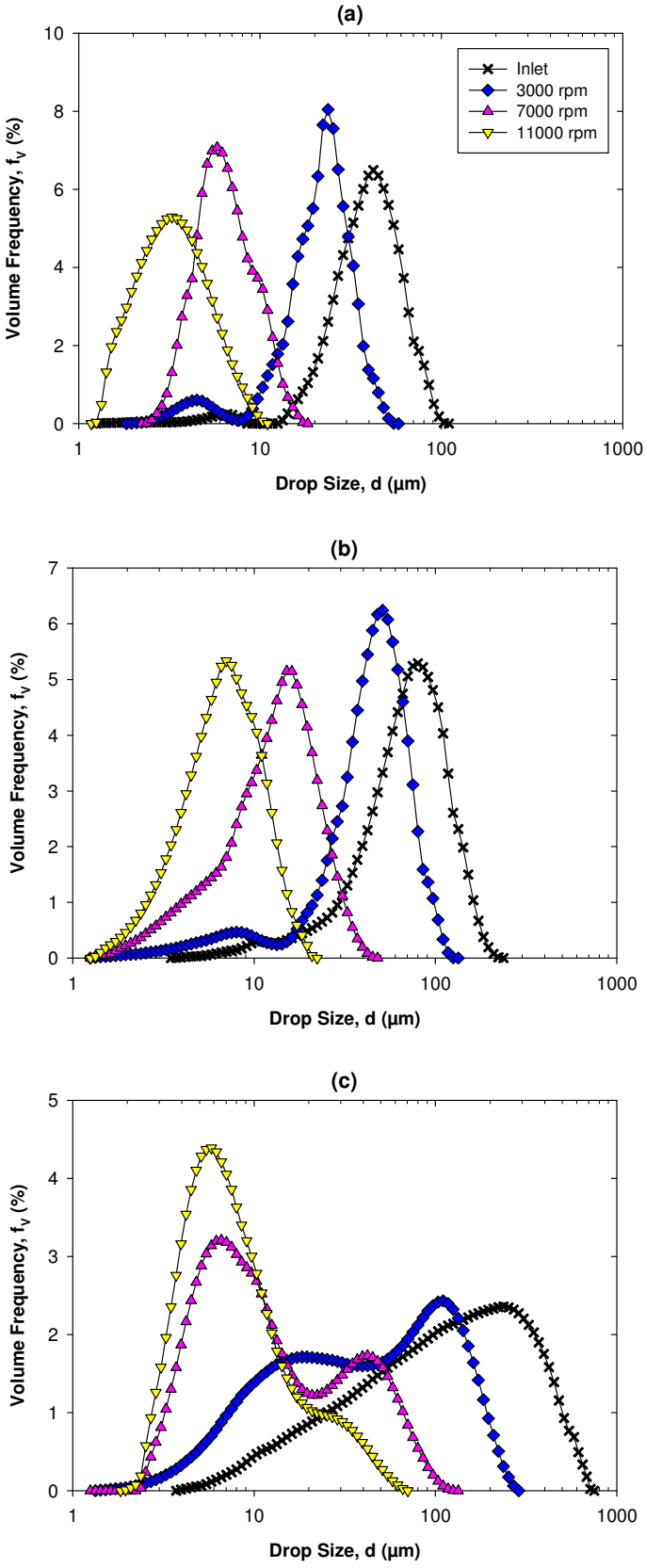

Figure 5.4: Effect of rotor speed on the volume drop size distributions for 1 wt.% emulsion of (a) 9.4 mPa·s, (b) 97 mPa·s and (c) 969 mPa·s silicone oils at a flow rate of 300 kg h^{-1}.

Figure 5.3 also shows a marked difference between drop sizes for 9.4 mPa·s oil and the higher oil viscosities (48 to 9,701 mPa·s), where the 9.4 mPa·s experiments consistently produced smaller droplets over a range of rotor speeds. In Figure 5.4, the volume DSDs as function of rotor speed for the 9.4, 97 and 969 mPa·s silicone oil emulsions are given. The distributions for the two lower viscosity oils are all predominantly monomodal and the whole size distribution shifts to smaller droplet sizes with increasing rotor speed. This trend in drop size reduction is consistent with the findings of Calabrese et al. (2000), Padron (2005) and Thapar (2004) for rotor-stator devices.

The DSDs for the 969 mPa·s silicone oil emulsion are greatly different to the other viscosities as all the rotor speeds show a pronounced bimodal distribution with the emergence of a peak at smaller drop sizes (< 20 μm) at the expense of a peak at larger drop sizes. However both the smaller and larger drop size peaks shift to a smaller drop size as observed for the lower viscosity oils. The formation of a bimodal distribution for high viscosities at higher rotor speeds was observed by Kevala et al. (2005) for a rotor-stator mixer.

Theoretical models of droplet breakage assume that an equilibrium Sauter mean diameter has been achieved, which was not the case for drop sizes formed after a single pass through the mixer. However theoretical models have only been applied to drop sizes produced at a constant flow rate, thus the mean time drops are exposed to shear forces was equal. Single pass emulsification is the focus of this chapter as this experimental arrangement easily allows many processing conditions to be examined, and single pass processing is important for many industrial processes. Multiple pass emulsification is examined in Chapter 6.

5.5 Effect of flow rate on drop size

Figure 5.5 presents mean drop size as a function of flow rate for two rotor speeds of 11,000 rpm and for selected viscosities at 6,000 rpm. In general droplet size is almost

independent of flow rate. At 6,000 rpm, the three dispersed phase viscosities examined show that droplet size is almost identical for a range of flow rates, and there is little flow rate dependency. At 11,000 rpm the drop sizes are of course smaller, but there appears to be a slight dependence on flow rate for the lower flow rates, which is extremely weak. This may suggest that the role of the stator becomes increasingly important for droplet breakage as flow rate is increased, as the flow velocity through the stator increases. Figure 5.6, the DSDs for 97 mPa·s silicone oil, illustrates the small effect of flow rate on the whole volume distribution.

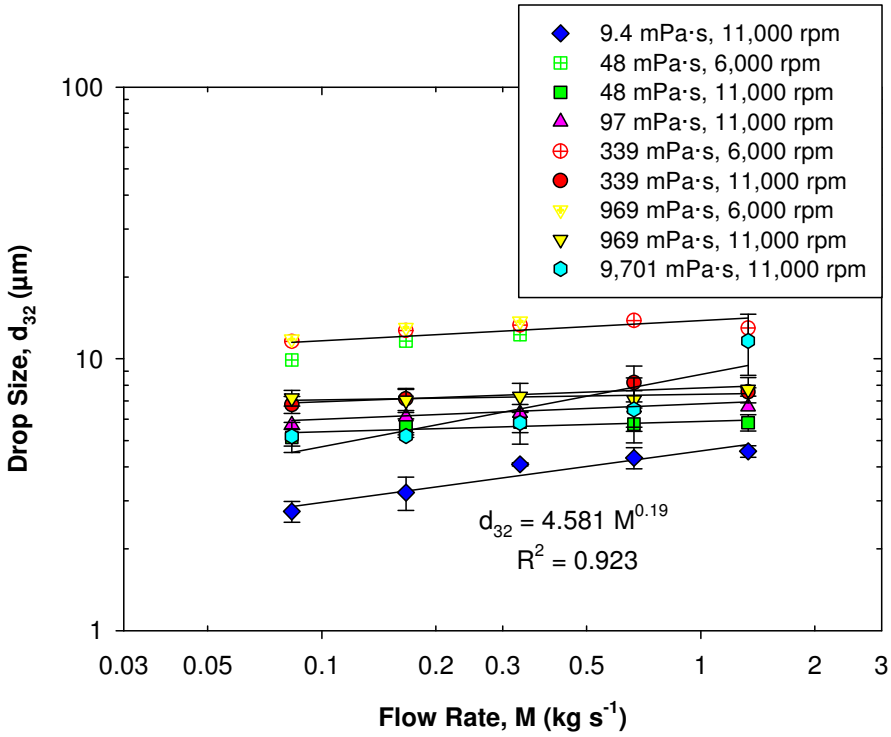

Figure 5.5: Effect of flow rate on mean drop size of 1 wt.% silicone oil emulsions at rotor speeds of 6,000 rpm and 11,000 rpm for a range of dispersed phase viscosities with standard deviation error bars.

The 9.4 mPa·s oil emulsions are the exception where there appears to be a fairly strong relationship between drop size and flow rate with a power law index of 0.19 and R^2 = 0.923. This could result from a change in breakage mechanism as observed in the DSDs in

Figure 5.4. The formation of a small peak of daughter drops at smaller droplet sizes for higher oil viscosities may suggest that droplet breakage is more dependent upon extensional flow than simple shear flow as dispersed phase viscosity increases (Padron, 2005).

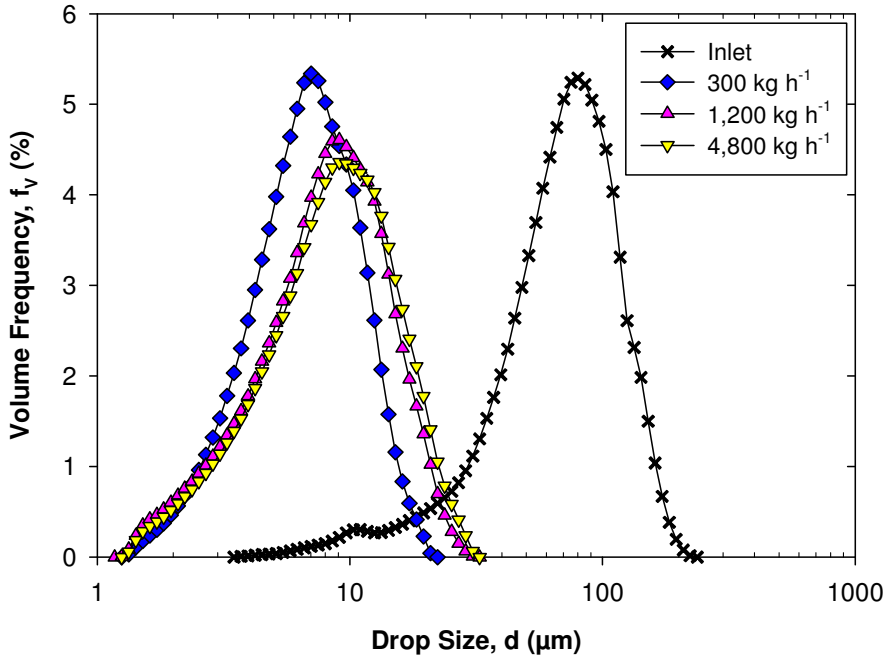

Figure 5.6: Effect of flow rate on the volume drop size distributions for 1 wt.% 97 mPa·s silicone oil emulsion for a rotor speed of 11,000 rpm.

Furthermore, breakage of high viscosity drops requires a longer deformation time than low viscosity drops. Larger high viscosity drops are easier to deform but once they are broken down to a critical droplet size, the droplet deformation time of the smaller drops seemingly exceeds the residence time in the high shear regions and further breakage cannot occur for all flow rates and drop size remains roughly independent of flow rate. Low viscosity droplets deform in a shorter time, and have a lower viscosity ratio so may be broken to a greater extent by simple shear flow, thus lower viscosity drops are broken further by an increase in

residence time. The effect of dispersed phase viscosity is discussed further in Section 5.7 and droplet deformation times in Section 8.6.3.

At the highest flow rate examined of 4,800 kg h^{-1} (1.33 kg s^{-1}), drop size began to fall slightly, for all viscosities except 9,701 mPa·s oil. To achieve these flow rates the centrifugal pump was required which did not affect the inlet drop size to any significant degree but is likely to cause cavitation. Despite the pressure head created by the pump, the inlet pressure to the Silverson was very negative (-0.9 bar) which was found to reduce the outlet drop size by ~ 0.5 μm at the highest rotor speed studied, at a constant flow rate. For 9,701 mPa·s oil, it appears that the residence time in the mixer is a limiting factor at 1.33 kg s^{-1}, resulting in larger droplet sizes.

For a rotor-stator mixer using bitumen emulsions, Gingras et al. (2005) also found no clear effect of flow rate. Ludwig et al. (1997) found the drop size to be slightly higher for higher flow rates, while Thapar (2004) obtained smaller drop sizes at higher flow rates, however both effects were diminished at higher rotor speeds.

5.6 Effect of dispersed phase volume fraction on drop size

Figure 5.7 shows that the effect of the dispersed phase volume fraction on mean droplet size is not significant up to ~ 50%. At both rotor speeds of 5,000 and 11,000 rpm there appears to be no trend with oil viscosity. These results are expected as the presence of excess surfactant aids the prevention of coalescence as phase volume is increased. These findings are consistent with much of the literature which finds either no or a weak relationship of drop size with dispersed phase volume for non-coalescing systems. However at 11,000 rpm, the drop size for 969 mPa·s and 9,701 mPa·s oil began to decrease slightly as phase volume increased, which supports the possibility of the beginning of droplet breakage where viscous stresses dominate as the emulsion viscosity increases. Vankova et al. (2007) studied Φ up to 80%

within a narrow-gap homogeniser, and confirmed a sharp decrease in d_{32} for $\Phi > 50\%$ which was more pronounced for highly viscous oils. The authors proposed that the emulsification regime changed from turbulent inertial to turbulent viscous at very high volume fractions resulting in a reduction in droplet size.

At high dispersed phase volumes, the emulsion viscosity increased slightly, from ~ 1 mPa·s for 1 wt.% oil, to ~ 20 mPa·s for 50 wt.% oil ($\dot{\gamma}$ = 1,500 s^{-1}). Moreover, since SLES was added in a fixed quantity per emulsion batch, the continuous phase SLES concentration increased at higher Φ, resulting in a slight decrease in interfacial tension, by ~ 15% from 1 to 50 wt.% oil. These factors contribute to drop size remaining small.

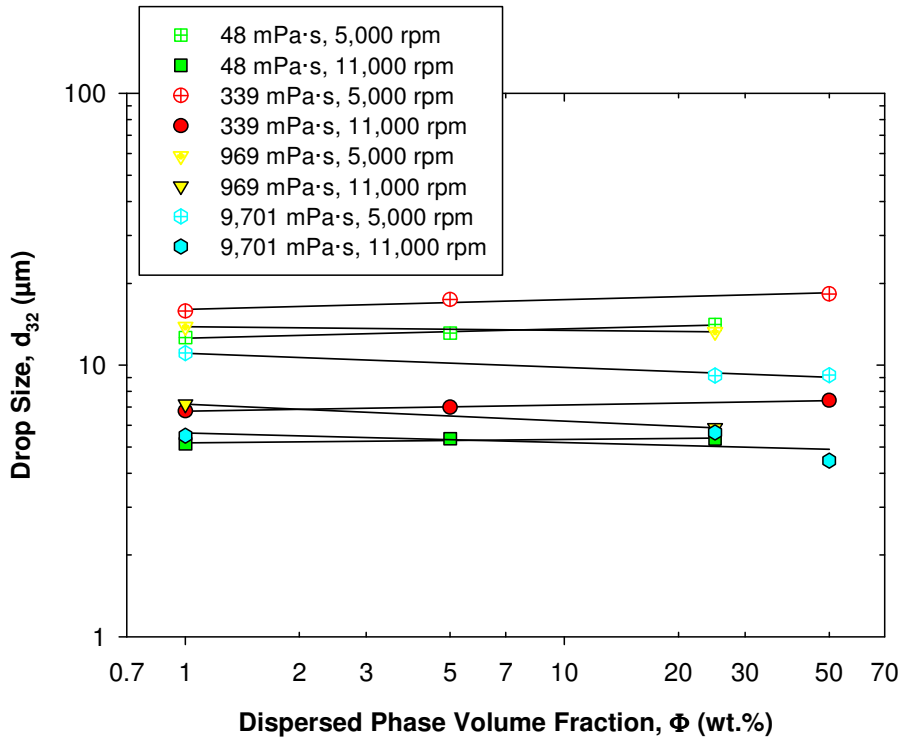

Figure 5.7: Effect of dispersed phase volume fraction on mean drop size of silicone oil emulsions for a range of dispersed phase viscosities at rotor speeds of 5,000 rpm and 11,000 rpm for a flow rate of 300 kg h^{-1}. The inlet drop sizes range from 29 to 48 µm.

The amount of surfactant required for full surface coverage of oil droplets was estimated as 1.2 mg m^{-2}, assuming all the drops have the same d_{32}, and are completely covered by surfactant with a head group size of ~ 0.6 nm^2 per molecule (Goloub and Pugh, 2003). The surfactant quantity required to cover the smallest drops of a 50 wt.% emulsion represents ~ 13% of the total available surfactant.

To correlate Sauter mean diameter with dispersed phase volume fraction, a modified version of Eq. (2.52), given by Eq. (2.70) is often used for inviscid drops (Leng and Calabrese, 2004). Oil viscosities of 48 to 969 mPa·s fit the correlation in Eq. (5.1) with a regression coefficient, R^2 = 0.964 (Figure 5.8):

$$\frac{d_{32}}{D} = 0.250(1 + 0.459\Phi)We^{-0.58} \tag{5.1}$$

The low value of C_{18} (0.46) indicates that coalescence is minimal. Thapar (2004) found droplet size to decrease with a reduction of dispersed phase volume, although he suggested this was not due to coalescence but a result of the oil being injected into the continuous phase upstream of the Silverson mixer and large globules of oil bypassing the mixing head. For a batch mixer, Calabrese et al. (2000) found droplet size to be independent of phase volume for a range of Φ, from 0.08 to 0.24% by volume.

Khopkar et al. (2009) varied phase volume from 10% to 50% in a rotor-stator mixer inserted into a batch vessel using 60 mPa·s oil. They found drop size to increase as phase volume increased, and the DSDs to become wider and bimodal. The results in this study indicate that d_{32} and the DSDs remain relatively constant for a range of dispersed phase volumes, and bimodality does not develop as Φ increases. Figure 5.9 presents the DSDs for 339 mPa·s silicone oil emulsions at phase volumes up to 50 wt.%, and indicates that bimodality does not develop and the distribution width remains practically the same. Figure

5.9 also shows that increasing phase volume reduced the fraction of drop sizes < 5 µm, possibly due to coalescence of the very smallest drops.

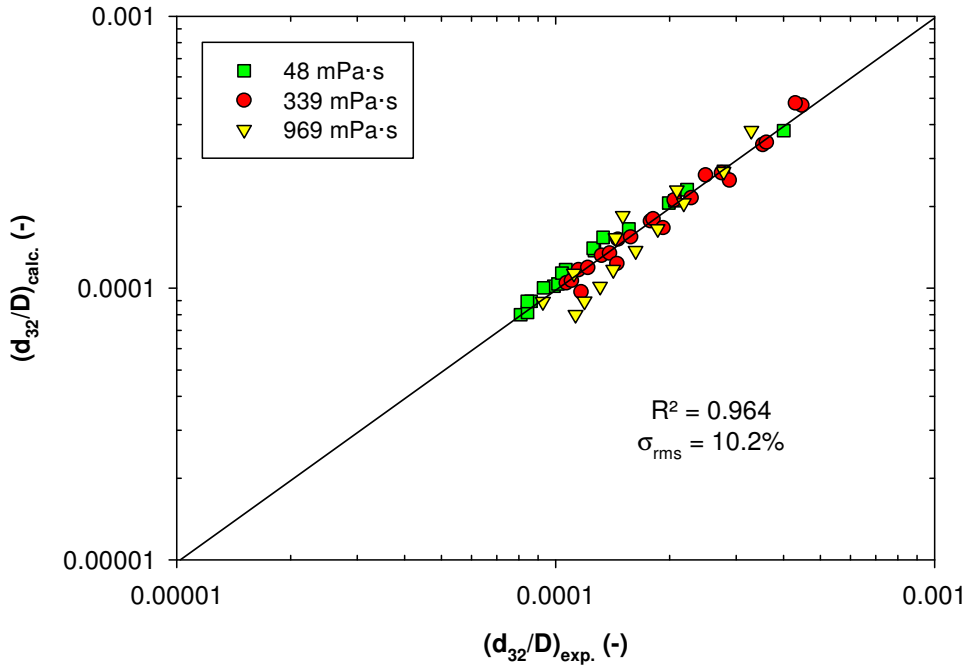

Figure 5.8: Quality of fit between dimensionless mean drop size from the correlation presented by Eq. (5.1) with experimental dimensionless mean drop size, for a flow rate of 300 kg h^{-1} and dispersed phase fraction of 1 wt.%.

For a screw loop reactor, Ludwig et al. (1997) found larger drop sizes for an increase in volume fraction, up to 50%, but at higher rotational speeds (U_T = 13.2 m s^{-1}), the change in drop size was minimal. This tip speed is close to the 150/250 Silverson at 4,000 rpm (U_T = 13.3 m s^{-1}), thus their finding is consistent with rotor-stator mixers.

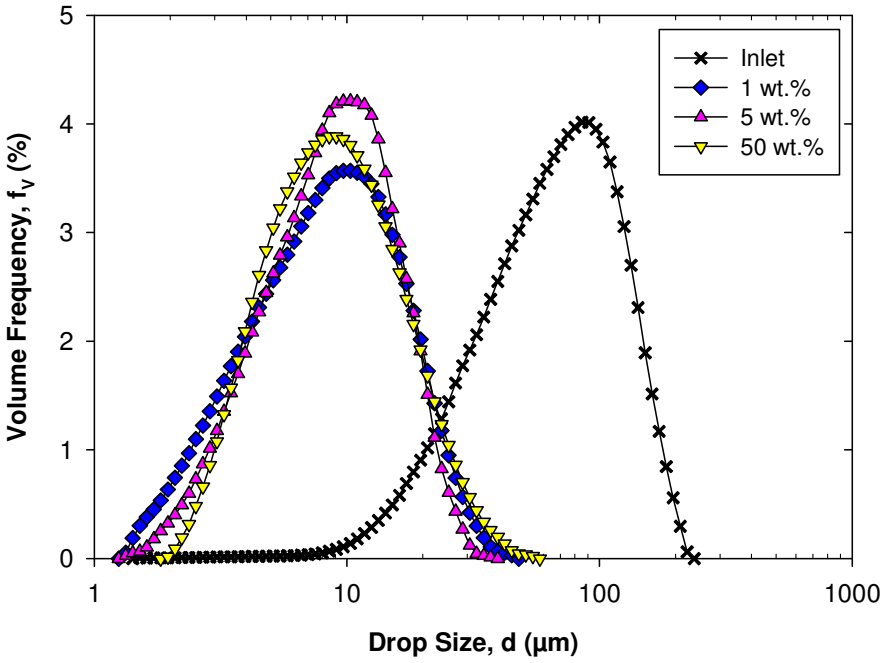

Figure 5.9: Effect of dispersed phase volume fraction on the volume drop size distributions for 339 mPa·s silicone oil emulsions, at a flow rate of 300 kg h^{-1} and rotor speed of 11,000 rpm.

5.7 Effect of dispersed phase viscosity on drop size

Figure 5.10 shows the effect of dispersed phase viscosity on droplet size for various rotor speeds, and shows Sauter mean diameter gradually increases with dispersed phase viscosity before it reaches a maximum and decreases slightly. This figure also clearly supports the differences in the trends observed for 9.4 mPa·s oil in Figure 5.3 and Figure 5.5. Padron (2005) found a similar effect for a non-surfactant emulsion in a batch Silverson where drop size increased with μ_d for 10 to 1,000 mPa·s, followed by a roughly constant droplet size. He suggested that the maximum was reached due to a shift towards an extensional flow breakage mechanism which favours the breakage of high viscosity droplets. This mechanism slowly deforms highly viscous drops by stretching them into long threads which break down over time resulting in the formation of two daughter drops with a number of smaller satellite

drops. As oil viscosity increases, drop stability rises creating longer threads prior to break-up (Janssen and Meijer, 1993), and the production of a larger population of smaller satellite drops during extensional breakage, which accounts for the bimodal distributions in Figure 5.4 for the highest viscosity oils.

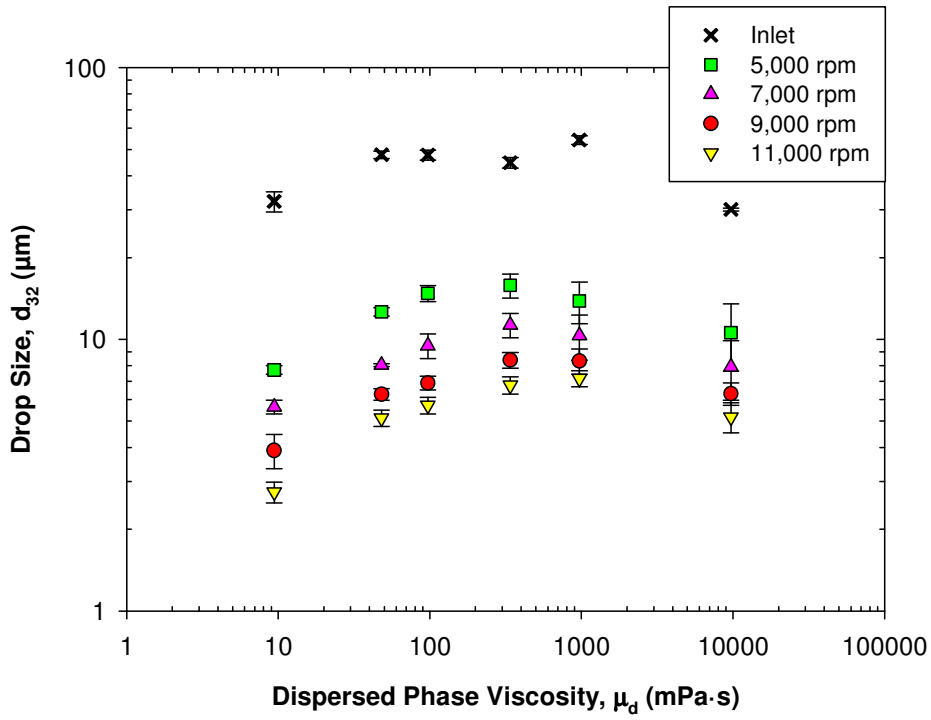

Figure 5.10: Effect of dispersed phase viscosity on mean drop size of emulsions for a range of rotor speeds for a flow rate of 300 kg h^{-1} and dispersed phase fraction of 1 wt.%, with standard deviation error bars. The inlet drop sizes range from 28 to 54 µm.

In Figure 5.10, mean drop size decreased at the highest oil viscosities, also observed by Padron (2005), and may be due to a possible shift in breakage mechanism. Higher oil viscosities stretch more under the applied velocity gradients, resulting in a larger population of smaller droplets, increased bimodality and a reduced mean droplet size. The other possibility for the observed bimodality is due to an increase in droplet deformation times for larger viscosity drops, resulting in incomplete droplet break-up, discussed in Section 8.6.3.

The standard deviation error bars for the high viscosity drop sizes are large and overlap for different rotor speeds, due in part to the bimodality of the distribution as it is harder to measure a wide range of droplets accurately using the same measuring technique. In addition, Sauter mean diameter is not an ideal parameter for describing bimodal size distributions, discussed in Section 5.10. Figure 5.10 also suggests that the inlet droplet size can be important for the final droplet size of highly viscous oils.

Figure 5.11 shows the effect of viscosity on the cumulative volume distributions at 11,000 rpm. This figure shows the previously discussed shift in droplet size to larger sizes with dispersed phase viscosity, and indicates that the volume distributions for 9.4 mPa·s oil are more distinct than the other viscosities. In terms of volume, both 9.4 and 97 mPa·s distributions are similar in shape, are both monomodal and more log-normally distributed, while the 969 mPa·s oil curve bends more at larger drop sizes, as the distribution is bimodal with a higher proportion of larger sized droplets. The highest viscosity oil distribution also has a significantly larger maximum droplet size of ~ 100 μm, however the smallest droplet sizes for all oil viscosities are close at 1-2 μm.

The volume DSDs (Figure 5.11) are log-normal as observed by Padron (2005) for a batch Silverson. This differs from stirred tanks where normal or Gaussian distributions are formed for low μ_d systems, and log-normal distributions for high μ_d oils (Wang and Calabrese, 1986). Calabrese et al. (1986) examined silicone oil emulsions in stirred tanks and established that the DSD broadened as μ_d increased, with the size of the largest and smallest drops both increasing and decreasing respectively. This study found the size of the largest drop to rise with μ_d, but the size of the smallest drop did not decrease as viscosity increased (Figure 5.11).

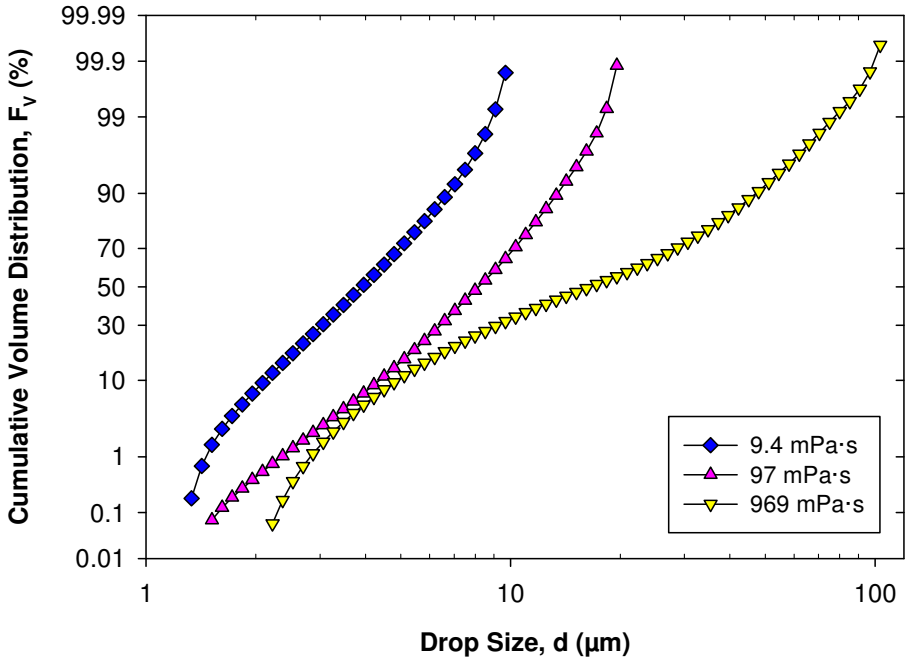

Figure 5.11: Effect of dispersed phase viscosity on the cumulative volume drop size distributions for 1 wt.% emulsions of 9.4 mPa·s, 97 mPa·s and 969 mPa·s silicone oils at a rotor speed of 11,000 rpm and flow rate of 300 kg h^{-1}.

Arai et al. (1977) found drop size remained constant when plotted against viscosity for μ_d < 10 mPa·s. Drop size then increased until a gradient of 0.75 was reached for μ_d > 200 mPa·s, as given by Eq. (2.56). However, for μ_d > 1,500 mPa·s, the slope began to level off as viscosity increased, as is the case for this study for higher oil viscosities. They stated that possibly the reason for this observation at high μ_d could be a result of more viscous droplets taking a longer time to return to a spherical shape between turbulent fluctuation time intervals. Hence, subsequent turbulent fluctuations act upon a drop which becomes steadily more deformed and more prone to forming smaller drops (Arai et al., 1977). Wang and Calabrese (1986) examined silicone oil emulsions with viscosities of 1 to 1,000 mPa·s, dispersed in water using a Rushton turbine and obtained similar findings to Arai et al. (1977), where the relationship between drop size and dispersed phase viscosity was constant < 10 mPa·s, rising

to a gradient of 0.75, before levelling off at 1,000 mPa·s. Ludwig et al. (1997) investigated viscosities of 32 to 190 mPa·s for a flow rate of 50 l h^{-1} and produced similar results to Arai et al. (1977), but with an increase in drop size above 50 mPa·s and a plateau at ~ 200 mPa·s.

Dimensionless Sauter mean diameter did not correlate well (R^2 = 0.827) with the viscosity group correlation in Eq. (2.59), which accounts for dispersed phase viscosity, see Figure 5.12, excluding 9,701 mPa·s oil:

$$\frac{d_{32}}{D} = 0.210We^{-3/5}\left[1 + 0.035Vi\left(\frac{d_{32}}{D}\right)^{1/3}\right]^{3/5} \tag{5.2}$$

Essentially, Eq. (5.2) does not provide a good relationship because in this study, drop size increases as viscosity increases, but above a critical value of viscosity, drop size begins to fall at higher μ_d (Figure 5.10), which was not observed for stirred vessels. Furthermore, this correlation is for equilibrium drop sizes and is based on mean energy dissipation rate (at constant power number), both of which are not true. In addition for rotor-stator mixers, droplet breakage is likely to occur by a combination of breakage mechanisms, while Eq. (5.2) is for inertial stresses in the inertial sub-range of turbulence. For a range of dispersed phase viscosities in surfactant systems in a batch rotor-stator mixer, Padron (2005) found C_7 and C_8 values of 0.08 and 0.09, respectively, compared to 0.20 and 0.04 in Eq. (5.2) in this study.

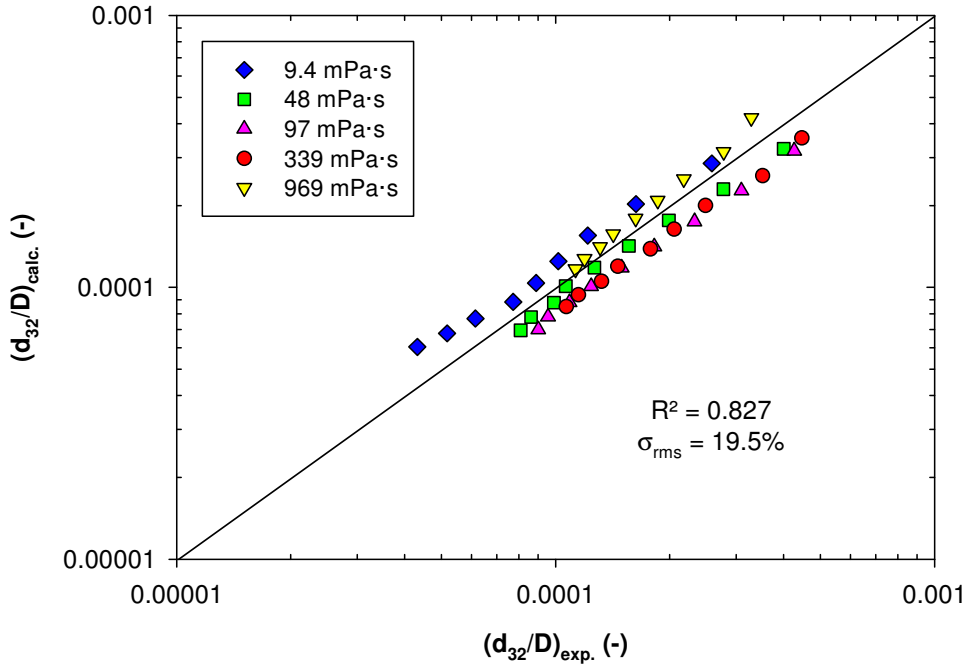

Figure 5.12: Quality of fit between dimensionless mean drop size from the correlation presented by Eq. (5.2) with experimental dimensionless mean drop size, for a flow rate of 300 kg h^{-1} and dispersed phase fraction of 1 wt.%.

The span of the DSD provides information about the spread of the data values. Span is a measure of the width of the distribution:

$$span = \frac{d_{0.9} - d_{0.1}}{d_{0.5}} \tag{5.3}$$

Span did not correlate strongly with the rotor speed, flow rate and dispersed phase volume fraction, however μ_d does influence span significantly. Span increased linearly with dispersed phase viscosity, and is well correlated with R^2 of 0.949 (Figure 5.13). For 9.4 mPa·s oil, span averaged at 1.08 over a range of rotor speeds, rising to 3.18 for 969 mPa·s oil. A broadening of the drop size distribution was also found by Ludwig et al. (1997) for increasing μ_d oil. The width of the distribution increased greatly as the size of the largest droplet increased with a growing proportion of smaller droplets observed with increasing oil viscosity (Figure 5.11).

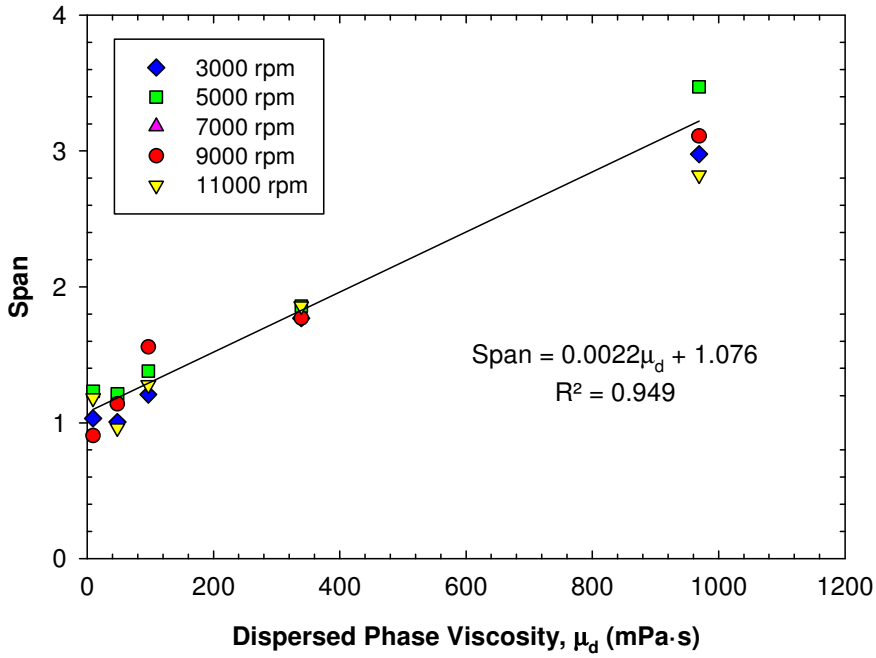

Figure 5.13: Effect of dispersed phase viscosity on span for a range of rotor speeds, at a flow rate of 300 kg h^{-1}.

5.8 Effect of continuous phase viscosity on drop size

Figure 5.14 shows the effect of the continuous phase viscosity on droplet size, with the apparent viscosity of the continuous phase calculated using Eq. (2.13), with shear rate calculated from Eq. (2.12) and a Metzner-Otto constant of 46.2. This figure indicates that decreasing the viscosity ratio reduces the droplet size for all viscosities examined, except for the lowest viscosity oil of 9.4 mPa·s, where the drop size increased slightly then decreased again. The result for the higher oil viscosities is expected since a more viscous continuous phase can transmit the shear stress to the droplet interface more effectively (Ludwig et al., 1997), however the result for the 9.4 mPa·s oil is unforeseen. The drop size curves for this oil viscosity appear to go through a maximum around a continuous phase viscosity of ~ 5 mPa·s.

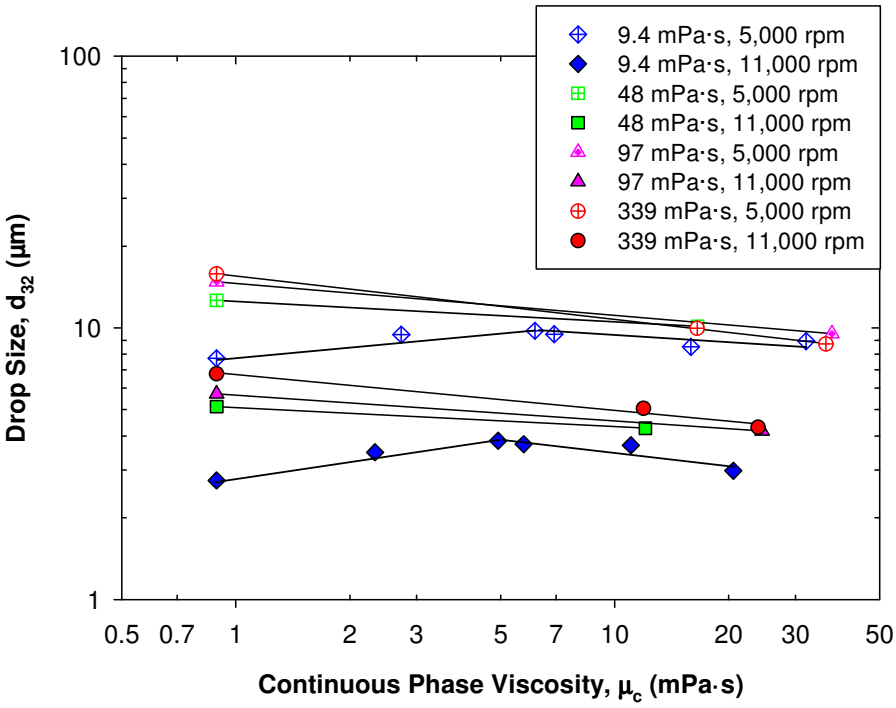

Figure 5.14: Effect of continuous phase viscosity on mean drop size of silicone oil emulsions for a range of dispersed phase viscosities at rotor speeds of 5,000 rpm and 11,000 rpm, for a flow rate of 300 kg h^{-1} and dispersed phase fraction of 1 wt.%.

For nearly all cases when the continuous phase was thickened, the Kolmogorov length scale increased so that all the droplets formed were below η_K (Table 5.1). For drops below η_K, Shinnar's (1961) model in Eq. (2.62) for the viscous sub-range where inertial stress are important gives an exponent on μ_c of 0.33, and Eq. (2.67) for viscous stress gives -0.5. Figure 5.14 suggests that for viscosities of 48 to 339 mPa·s, viscous stresses are more important for droplet breakage. For 9.4 mPa·s oil there appears to be a transition from where inertial stresses are dominant, to where viscous stresses play a greater role in droplet breakage. The importance of both inertial stresses for drops above η_K and viscous stresses for drops below η_K was also concluded by Calabrese et al. (2000) for a batch rotor-stator mixer. However, the exponents on μ_c for the data in Figure 5.14 are all less steep (< 0.16), than indicated by the

models in Eqs. (2.62) and (2.67), which suggests that neither model can exclusively describe droplet breakage.

Table 5.1: Apparent continuous phase viscosities, viscosity ratios, Reynolds numbers and Kolmogorov length scales for various CMC concentrations.

CMC conc., c_{CMC} (wt. %)	**Apparent continuous phase viscosity, μ_A (mPa·s)**		**Viscosity ratio with 9.4 mPa·s silicone oil, μ^* (-)**		**Reynolds number, Re (-)**		**Kolmogorov length scale, η_K (μm)**	
	3,000 rpm	**11,000 rpm**	**3,000 rpm**	**11,000 rpm**	**3,000 rpm**	**11,000 rpm**	**3,000 rpm**	**11,000 rpm**
0	0.89	0.89	10.6	10.6	225,851	828,122	5.2	2.0
0.05	3.03	2.33	3.10	4.04	66,339	316,321	13.1	4.2
0.15	7.12	5.75	1.32	1.63	28,260	128,307	26.6	8.3
0.4	20.34	12.05	0.46	0.78	9,902	61,287	54.2	13.5
0.8	42.63	24.46	0.22	0.38	4,739	30,283	94.9	21.4

Eq. (2.52) can correlate mean drop size using Weber number, modified by adding viscosity ratio:

$$\frac{d_{32}}{D} = 0.201 \left(\frac{\mu_d}{\mu_c}\right)^{0.066} We^{-0.6} \tag{5.4}$$

This expression gives a power law fit to the data with $R^2 = 0.971$ for all droplet sizes formed where drop size decreased with increasing viscosity ratio, where drop breakage is dominated by viscous stresses (Figure 5.15). This correlation indicates that for droplets primarily broken by viscous stresses, the effect of viscosity ratio on droplet size is relatively weak, which was also found by Calabrese et al. (2002) for a batch rotor-stator using glycerol solutions.

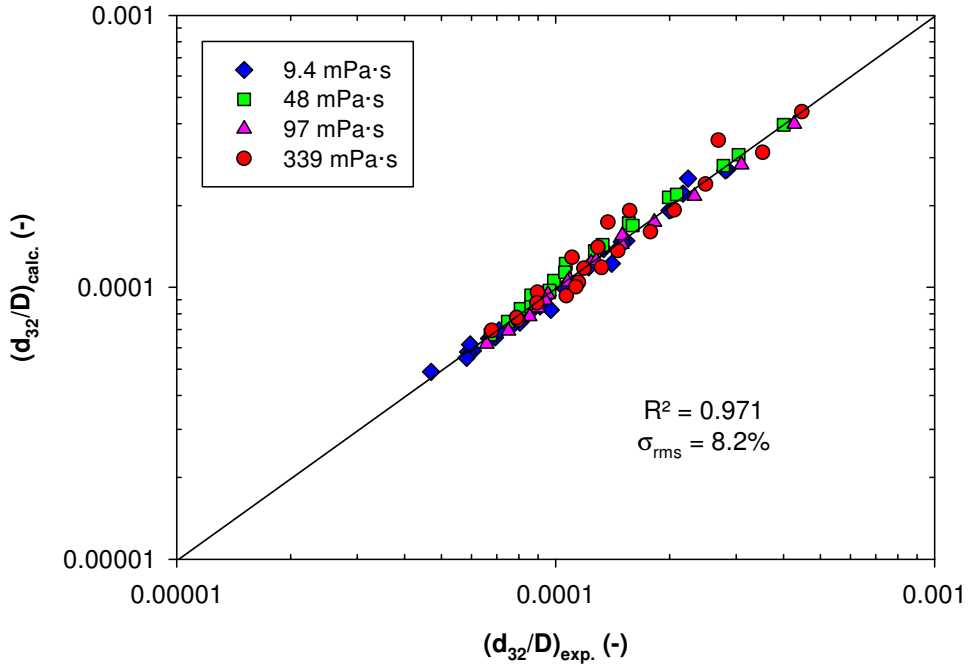

Figure 5.15: Quality of fit between dimensionless mean drop size from the correlation presented by Eq. (5.4) with experimental dimensionless mean drop size, for a flow rate of 300 kg h^{-1} and dispersed phase fraction of 1 wt.%.

Mean drop size as a function of rotor speed for viscosities of 9.4-97 mPa·s oil (Figure 5.16a), at a viscosity ratio of 4.0, showed that the gradient reduced in magnitude from -1.20 to -1.03 as dispersed phase viscosity increased. Similar trends were found with energy dissipation rate (the effect of continuous phase viscosity on power draw was measured for each experiment). The exponent on N for viscous stresses in Eq. (2.67) is -1.5, therefore the reduction in the exponent with increasing μ_c suggests that drops are still broken by a combination of inertial and viscous stresses as the exponents are between -1 and -1.5.

Therefore, the experimental data does not follow all of the energy dissipation rate trends described by the theoretical models in Eqs. (2.62) and (2.67) for increasing μ_c. The Mastersizer X particle size analyser used in this chapter was restricted to a minimum droplet size of 1.2 µm, hence small droplets may not be measured (Figure 5.16b), resulting in less

steep gradients. In addition, the Reynolds number (Re) for the highest continuous phase viscosities is < 10,000 (Table 5.1), which from the power curve for the in-line Silverson 150/250 mixer is at the point where the flow becomes transitional (Section 4.6). The theoretical models are developed for turbulent flows, thus at larger continuous phase viscosities the models may not accurately describe droplet break-up in transitional flow, and in some areas of the mixing head where the flow has little time to develop, laminar flow breakage may have an impact on droplet break-up.

Ludwig et al. (1997) found drop size reduced when continuous phase viscosity was increased from 1 to 200 mPa·s. Drop size remained roughly constant up to a viscosity of around 10 mPa·s, before decreasing as μ_c was reduced further. Khopkar et al. (2009) also found droplet size decreased with viscosity ratio for a given energy density.

In general, the DSDs broaden at lower viscosity ratios. For a dispersed phase viscosity of 97 mPa·s (μ^* = 109), the span averaged at 1.39 over a range of N, while for a μ^* of 4.0, span increased slightly to 1.95. This finding is consistent with results by Noro (1978) for emulsions in stirred vessels, who also obtained broadening drop size distributions with decreasing viscosity ratio.

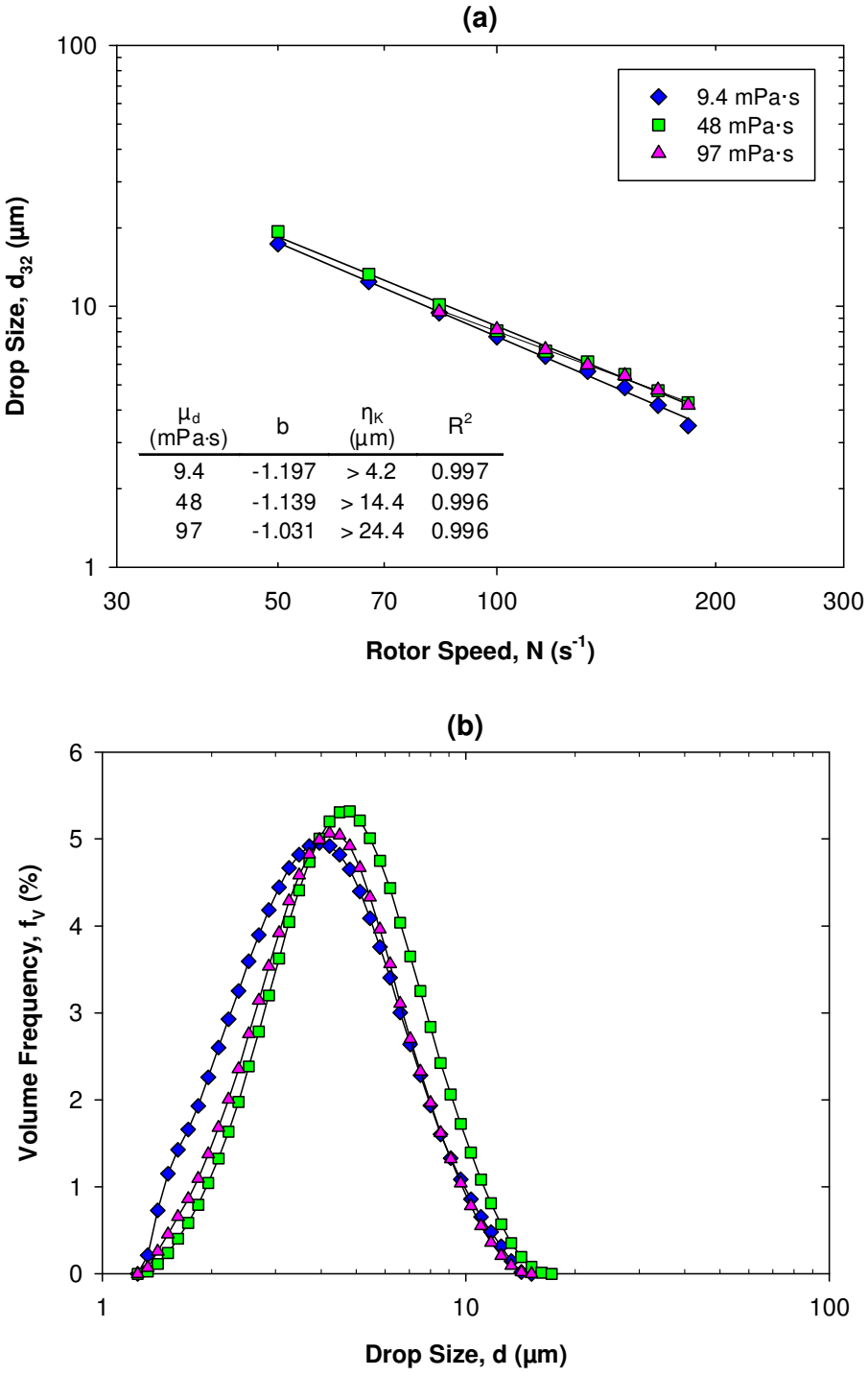

Figure 5.16: (a) The effect of rotor speed on mean drop size for selected 1 wt.% silicone oil emulsions at a constant viscosity ratio of 4.0, at 300 kg h^{-1}, and (b) the effect of dispersed phase viscosity on the volume drop size distributions for 1 wt.% silicone oil emulsion at a constant viscosity ratio of 4.0, at 300 kg h^{-1} and 11,000 rpm.

Vankova et al. (2007) examined the effect of continuous phase viscosity on a 1% 95 mPa·s silicone oil emulsion, using glycerol for continuous phase viscosities up to ~ 18 mPa·s. Vankova et al. (2007) found a three-fold reduction of drop size over the viscosity ratio range of 95 to 5.3, compared to a reduction from 5.7 to 4.2 μm for a similar range of μ^* in this investigation, and they concluded that the droplet breakage mechanism changed as the regime transformed from turbulent inertial to turbulent viscous.

5.9 Energy dissipation rate and energy density

Figure 5.17 presents two commonly used parameters for scale-up, namely energy dissipation rate based on the swept volume of the rotor, and energy density in Eqs. (2.47) and (2.83). Both of these parameters are calculated from the mixer power draw, measured in Chapter 4. Figure 5.17a is very similar to Figure 5.3 since at a fixed flow rate and a single mixer scale, power draw is entirely dependent on the rotor speed. The exponents of -0.39 to -0.45 for viscosities of 9.4-339 mPa·s are close to the value of -0.48 found by Calabrese et al. (2000) for a batch Ross rotor-stator mixer. At the highest rotor speed of 11,000 rpm where a range of flow rates were investigated, as power draw increased there was a slight increase in drop size (Figure 5.5). However, energy dissipation rate is not sufficient to describe the behaviour for continuous processes; hence energy density is more appropriate as it accounts for mean residence time.

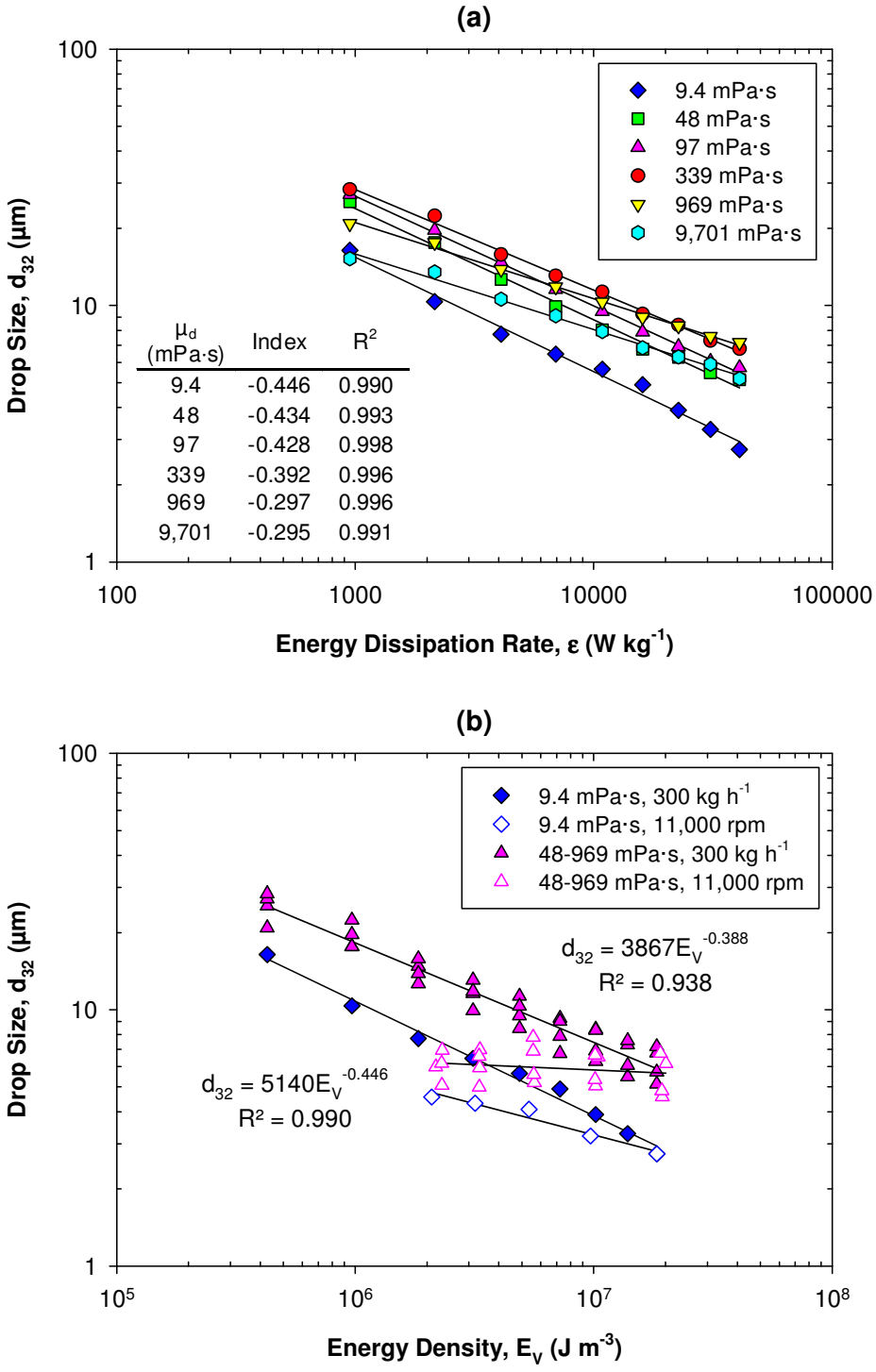

Figure 5.17: Mean drop size of silicone oil emulsions presented as a function of (a) energy dissipation rate and (b) energy density for a range of dispersed phase viscosities. In (b), closed symbols are a flow rate of 300 kg h^{-1} and rotor speeds of 3,000-11,000 rpm, and open symbols are a rotor speed of 11,000 rpm and flow rates of 300-4,800 kg h^{-1}. Dispersed phase fraction is 1 wt.%.

Figure 5.17b presents drop size in terms of energy density. At a fixed flow rate (M = 300 kg h^{-1}), increasing the rotor speed (closed symbols) increased the energy used per unit volume of fluid, and smaller drop sizes are formed as expected. The exponents are -0.45 and -0.39 for 9.4 and 48-969 mPa·s oil respectively, which are similar to those obtained for turbulent inertial forces for rotor-stator systems when b is -0.4 (Karbstein and Schubert, 1995). At a fixed rotor speed (N = 11,000 rpm), increasing the flow rate (open symbols) had a much weaker effect on drop size as seen in Figure 5.5, and the exponents on energy density are 0.24 and 0.04 for 9.4 and 48-969 mPa·s oil respectively. Hence, Figure 5.17b indicates that increasing the flow rate at a constant rotor speed increases the power drawn, but this is marginal compared to the additional fluid processed, which overall reduces energy density.

Consequently, to obtain a given droplet size it is more energy efficient to operate the mixer at as high a flow rate as possible. Increasing the flow rate is efficient as more of the pumping capability of the Silverson is utilised, see Figure 4.9, as restricting the flow rate results in energy wastage through generation of large pressure gradients, and increased outlet temperatures at reduced residence times.

5.10 High dispersed phase viscosity

The onset of bimodal drop size distributions at high dispersed phase viscosities (Figure 5.4) was investigated further using 1 wt.% 9,701 mPa·s silicone oil. Figure 5.18 presents the effect of a range of rotor speeds and flow rates on the DSDs. Figure 5.18a shows that increasing rotor speed increases the volume of oil contained in small drops (peak 1) while the volume of oil in large drops is reduced (peak 2). Meanwhile, Figure 5.18b presents the converse effect with increasing flow rate, namely that increasing flow rate reduced the volume of oil in small drops. Higher rotor speeds also resulted in both d_{max} and d_{min} to shift to small drop sizes, while the effect of flow rate on d_{max} and d_{min} was less clear.

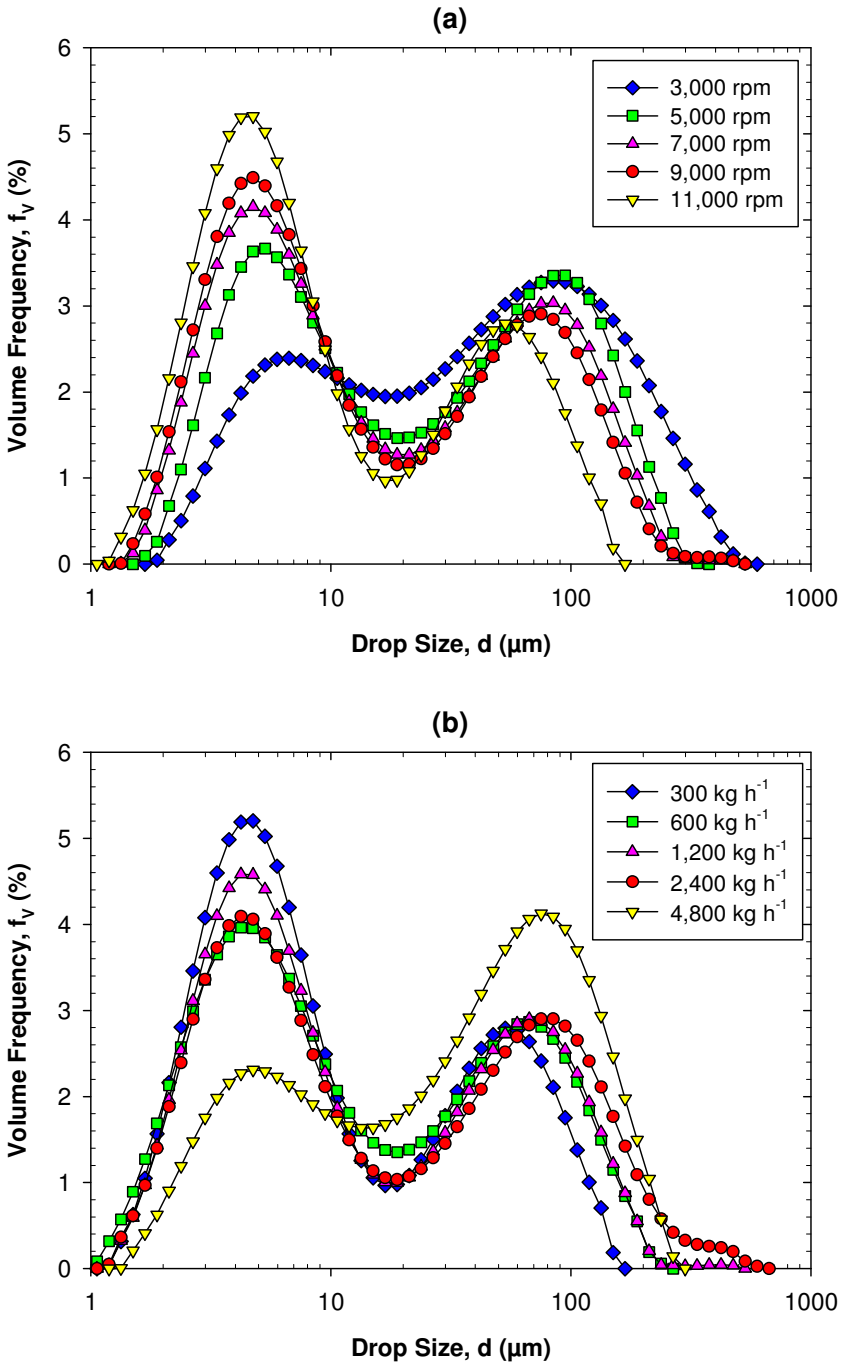

Figure 5.18: Volume drop size distributions of 1 wt.% 9,701 mPa·s silicone oil emulsions as a function of (a) five rotor speeds at a flow rate of 300 kg h^{-1} and (b) five flow rates at a rotor speed of 11,000 rpm.

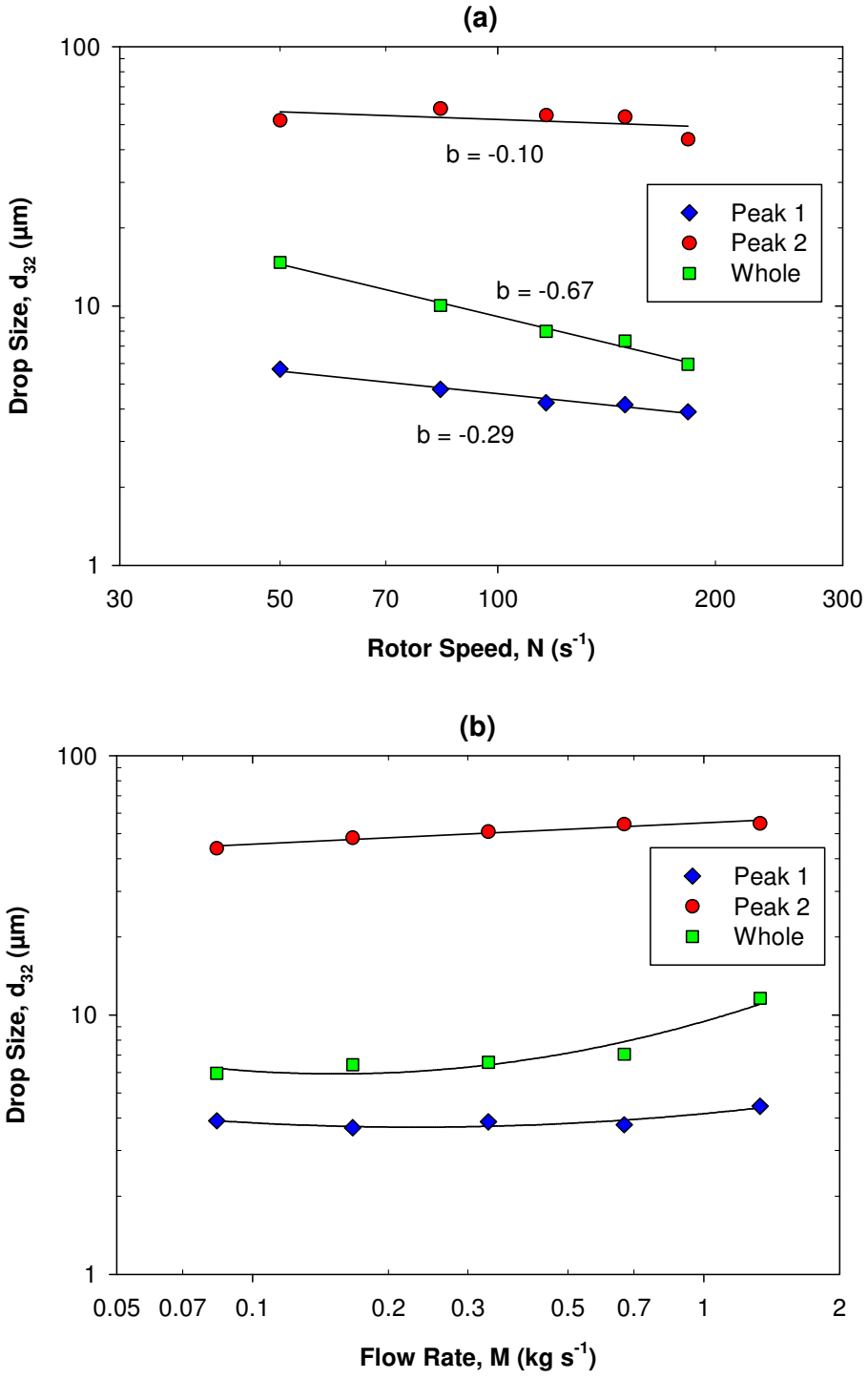

Figure 5.19: Mean drop sizes of peak 1, peak 2 and the whole distribution of 1 wt.% 9,701 mPa·s silicone oil emulsions as a function of (a) five rotor speeds at a flow rate of 300 kg h^{-1} and (b) five flow rates at a rotor speed of 11,000 rpm.

For a bimodal system, average drop size defined by d_{32} or d_{43} is fairly meaningless since the mean value may fall between the bimodal peaks. Thus it is of more interest to determine the d_{32} or d_{43} of the two peaks separately.

The bimodal high viscosity DSDs were analysed separately to calculate d_{32}, d_{43} and volume fraction for each peak, see Appendix B.5 for details. The d_{32} of peak 1, peak 2 and the whole distribution are shown in Figure 5.19. The d_{32} of peak 1 decreased with rotor speed from 5.7 to 3.9 µm, while the d_{32} of peak 2 fluctuated between 44 and 62 µm, and remained roughly constant with rotor speed (Figure 5.19a). This is consistent with Phongikaroon (2001) who found bimodal distributions to occur for highly viscous (500 mPa·s) silicone oil dispersions in a batch rotor-stator mixer.

Figure 5.19b shows that the effect of flow rate on the d_{32} of peak 1 is minimal at low flow rates (3.7 to 3.9 µm), before increasing to 4.4 µm at 4,800 kg h^{-1} (1.33 kg s^{-1}), leading to a simultaneous increase in d_{32} of the entire distribution. The d_{32} of peak 2 rose slightly from 44 to 54 µm as flow rate increased. The abrupt increase of d_{32} at the highest flow rate suggests that the effect of residence time may become important for creating a large proportion of small drops, at a critical flow rate. Highly viscous drops take longer to deform so it may be expected that very short residence times may result in incomplete droplet break-up, hence droplet deformation times are considered below.

In the turbulent inertial regime, the droplet deformation time is defined as (Padron, 2005):

$$t_{def} = \frac{\mu_d}{\varepsilon^{2/3} d^{2/3} \rho_c} \tag{5.5}$$

The effect of droplet deformation times on the volume fraction of oil in peak 1 and peak 2 are illustrated in Figure 5.20. This figure shows that as expected, for drops that take longer to deform (for a single pass above t_{def} ~ 0.025 s), a higher proportion of the droplet volume

resides in peak 2 of the DSD. This suggests that larger residence times are necessary to effectively stretch and break high viscosity drops into smaller droplets.

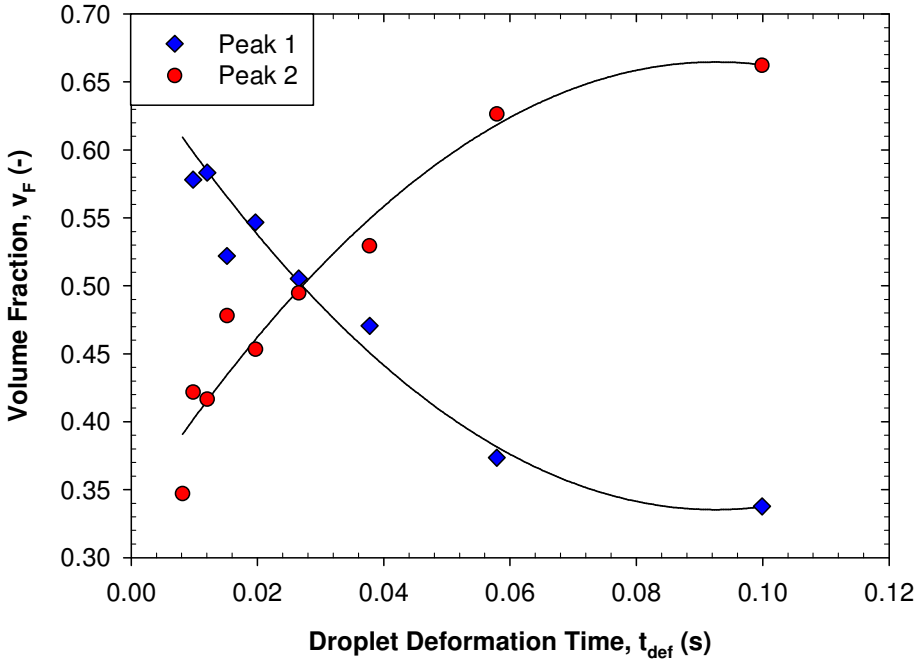

Figure 5.20: Volume fractions of peak 1 and peak 2 as a function of droplet deformation times of 1 wt.% 9,701 mPa·s silicone oil at a flow rate of 300 kg h^{-1}.

5.11 Summary

Drop size distributions measured for a range of processing and formulation conditions showed that DSDs are strongly dependent on rotor speed and dispersed phase viscosity, but weakly dependent upon flow rate, continuous phase viscosity, inlet droplet size and dispersed phase volume fraction for surfactant systems. The exponents correlating mean drop size with energy dissipation rate suggest turbulent inertial forces are most important for droplet break-up. Mean droplet size increased with dispersed phase viscosity to a point where bimodal DSDs were formed and mean drop size became roughly constant.

CHAPTER 6. SINGLE AND MULTIPLE PASS EMULSIFICATION IN IN-LINE SILVERSON ROTOR-STATOR MIXERS: EXPERIMENTS AND MODELLING

6.1 Introduction

In Chapter 5, liquid-liquid dispersion in a single pass was investigated, however in many industrial applications it is necessary to produce smaller drops. Furthermore, many correlations for droplet break-up in literature are based upon equilibrium droplet sizes which are not achieved using a single pass, hence the effect of number of passes on droplet break-up is required under different processing conditions. The effect of process and formulation variables on DSDs for multiple passes was examined, including the effect of number of passes on the characteristics of DSDs using the 150/250 mixer. A comparison between single and multiple pass DSDs was investigated, along with prediction of DSDs in a stirred vessel placed in a recycle loop with a rotor-stator mixer. Finally, population balance equations were solved using calculated flow fields to theoretically predict DSDs.

6.2 In-line mixers in recirculation loops

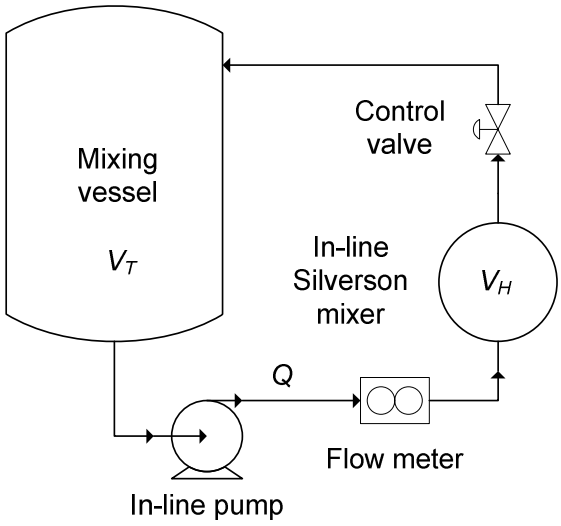

Figure 6.1: In-line Silverson mixer in a recirculation loop.

The effect of number of passes on the mean drop size of the emulsion can either be analysed in terms of the number of passes or residence time in the mixing head. Concepts commonly used in industry depend on the flow rate, the emulsion batch volume (V_T) and the mixing head volume (V_H) (Figure 6.1). The number of batch vessel turnovers pumped (B) (mean number of passes) (Baker, 1996):

$$B = \frac{Q}{V_T} t \tag{6.1}$$

And residence time (τ) in the mixing head for a single pass (Gingras et al., 2005):

$$\tau = \frac{V_H}{Q} \tag{6.2}$$

To compare emulsification for both single and multiple passes at different flow rates, residence time was modified to estimate the total amount of time the emulsion spends inside the mixing head, total residence time:

$$t_R = \frac{V_H}{Q} B \tag{6.3}$$

For a single pass system, $B = 1$. The following expression may then by applied to compare process conditions and formulations:

$$d_{32} \propto {t_R}^b \tag{6.4}$$

Droplet size at the mixer outlet partly depends upon the initial droplet size, so the exponent b may not be transferable to vastly different initial droplet sizes, but b is used in this study to compare droplet break-up when coarse emulsions were prepared in the same way.

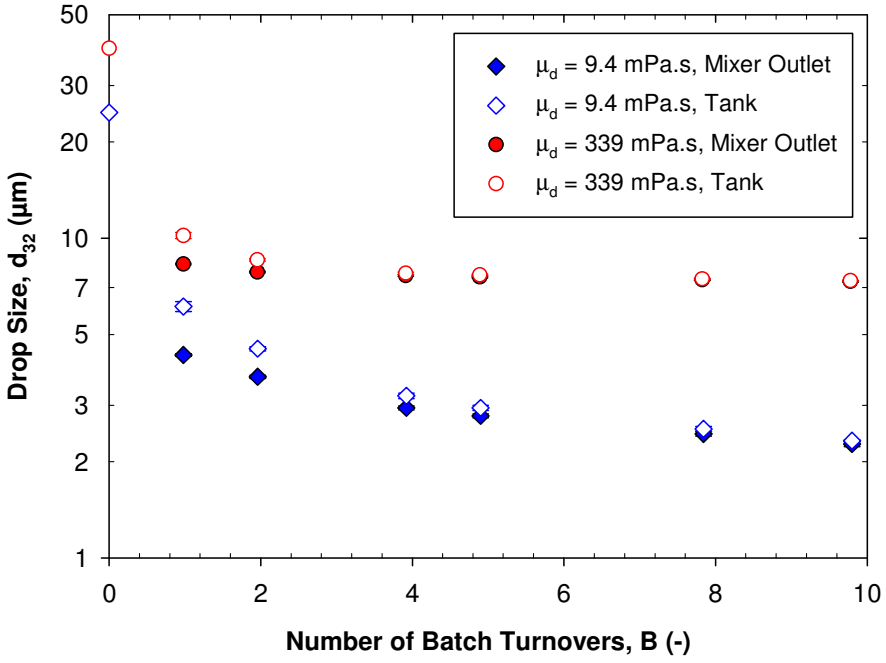

Figure 6.2: Effect of number of batch turnovers on mean drop sizes in the stirred tank and at the mixer outlet for 1% 9.4 and 339 mPa·s silicone oils emulsions at a constant rotor speed of 11,000 rpm and flow rate of 2,350 kg h^{-1}.

Figure 6.2 presents a comparison between mean drop sizes of emulsions in the mixing tank and at the mixer outlet, as a function of number of batch turnovers pumped. At initial times, mean drop size in the tank is larger than mean drop size at the mixer outlet, since not all of the emulsion will have passed through the mixer. Figure 6.2 shows that after 5 batch

turnovers, mean drop size in the tank and at the mixer outlet are roughly equal, and after 8-10 turnovers the drop sizes completely converge for two oil viscosities. The DSDs in the mixing tank are predicted in Section 6.9. In Sections 6.3 to 6.7, samples from the mixer outlet and not the mixing tank are used, to remove the effect of the initial droplet size on the trends.

6.3 Flow rate and number of batch turnovers

Figure 6.3a presents the effect of dispersed phase viscosity, number of batch turnovers (Eq. (6.1)) and recirculation flow rate on Sauter mean diameter, while Figure 6.3b shows the effect of total residence time from Eq. (6.3) on d_{32}. These results were obtained using the 'single condition' recirculation method. The recirculation flow rate does not have a significant effect on mean droplet size since both flow rates resulted in roughly the same degree of droplet size reduction with number of batch turnovers or total residence time, with exponents of -0.25 for 9.4 mPa·s oil and -0.05 for 339 mPa·s oil.

For an equal number of batch turnovers (Figure 6.3a), a similar droplet size was obtained for the high viscosity oil at both flow rates, while the lower flow rate produced smaller drops at the same B for low viscosity oil. At constant total residence time (Figure 6.3b), a slightly lower droplet size was produced for both oil viscosities when the emulsion was recirculated at a higher flow rate. This suggests that when droplet break-up is not limited by residence time, increasing the flow rate is advantageous to produce smaller drops and reduce manufacturing timescales.

Figure 6.4 shows the effect of number of batch turnovers on drop size distributions for 9.4 mPa·s and 339 mPa·s oils. For the higher viscosity oil (Figure 6.4a), after the initial pass the effect of number of passes on the DSDs is minimal. This proves that a single pass is most energy efficient and may be all that is necessary to form the emulsion of the desired drop size. Additionally, d_{min} appears to be roughly independent of the number of passes while d_{max}

continues to decrease with each pass, until an equilibrium is reached at $t \to \infty$, where $d_{max} = d_{min}$.

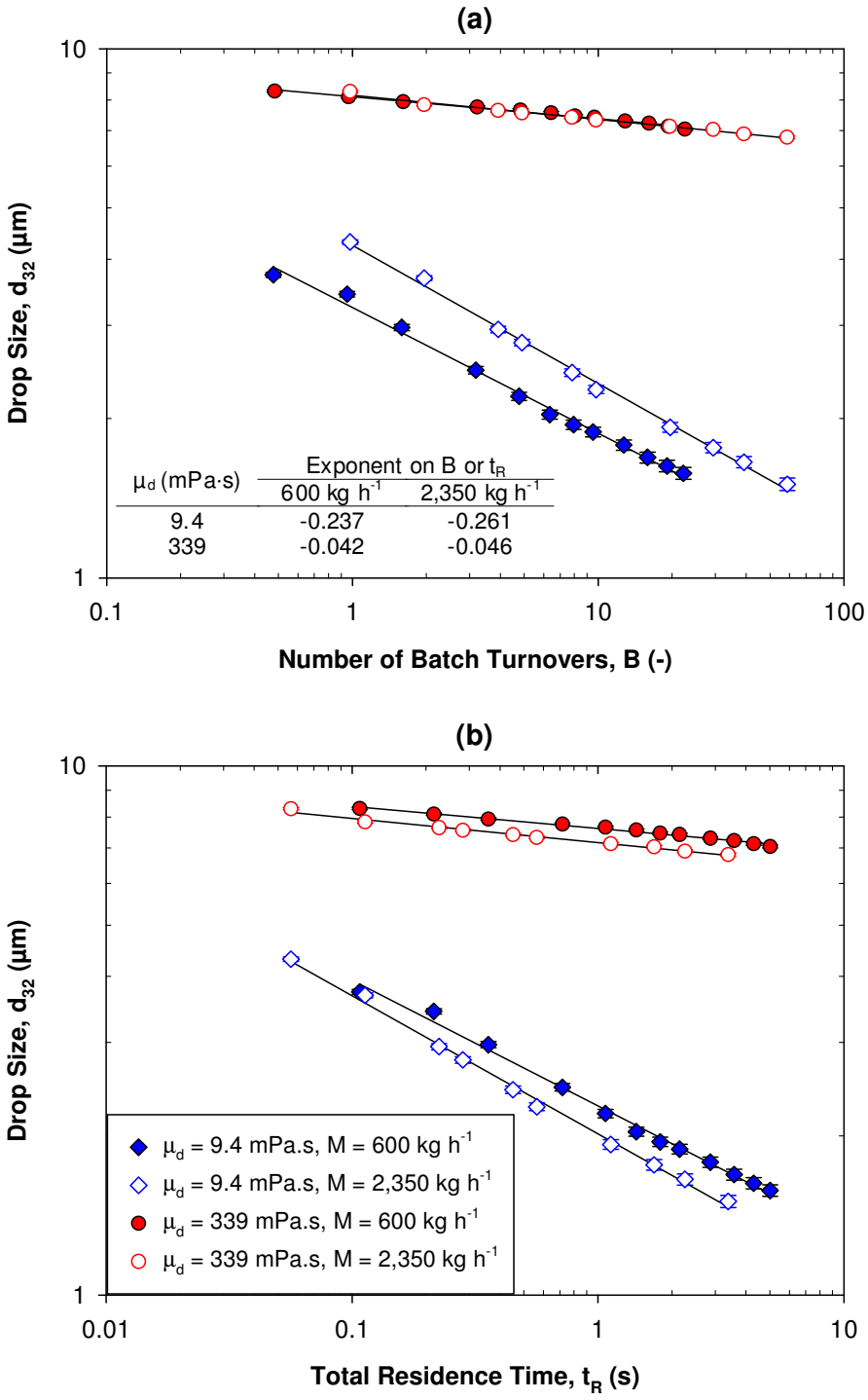

Figure 6.3: Mean drop size as a function of (a) number of batch turnovers and (b) total residence time for 1% 9.4 mPa·s and 339 mPa·s silicone oil emulsions recirculated at 11,000 rpm, with standard deviation error bars.

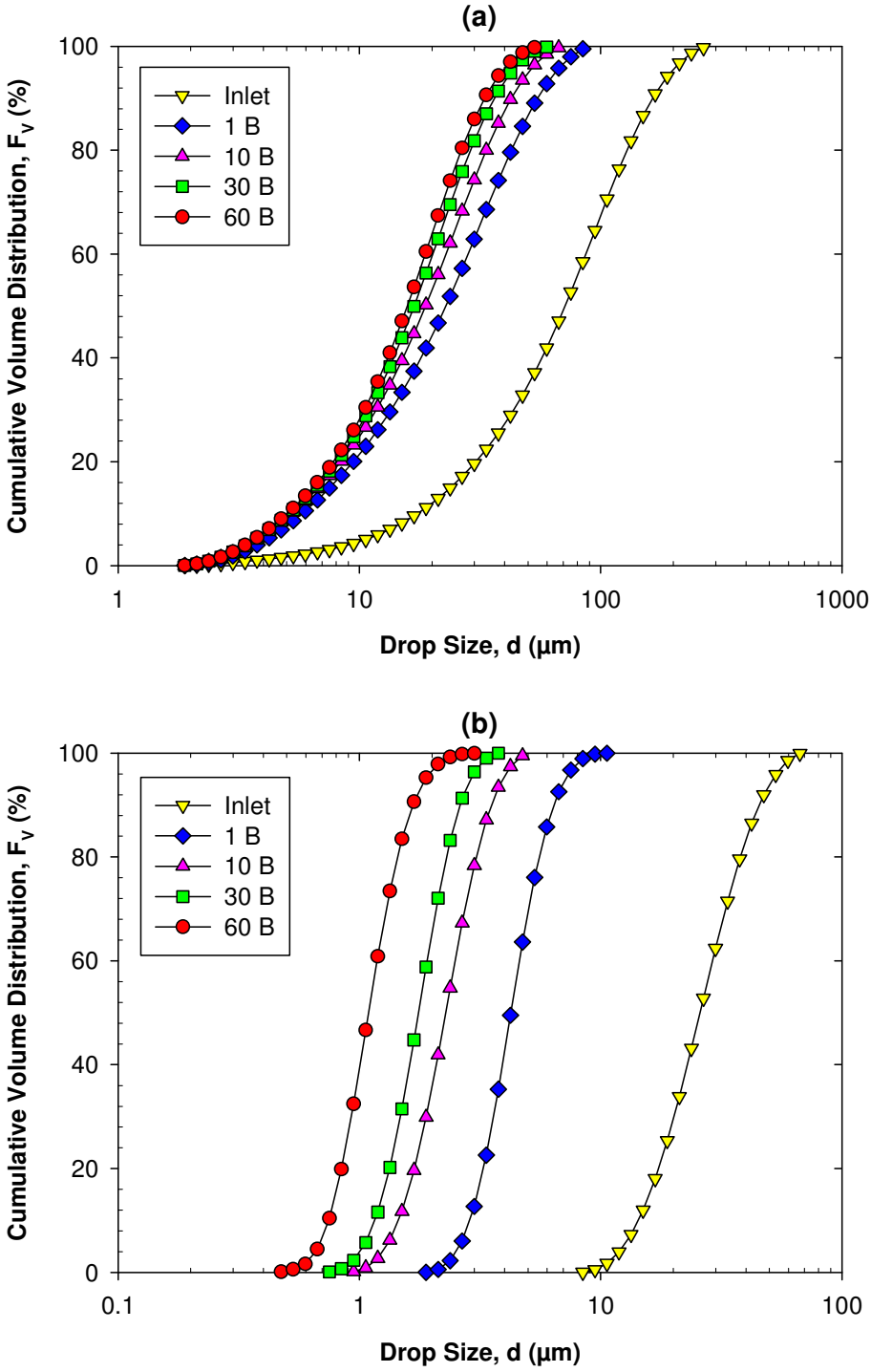

Figure 6.4: Cumulative volume drop size distributions for 1% silicone oil emulsions showing the effect of number of batch turnovers for (a) 339 mPa·s and (b) 9.4 mPa·s silicone oil at a constant rotor speed of 11,000 rpm and flow rate of 2,350 kg h^{-1}.

For the low viscosity oil, it is clear from Figure 6.4b that the effect of the number of batch turnovers on the DSDs is more pronounced than for higher viscosity oils. All DSDs are of a similar shape and both d_{max} and d_{min} reduce as the number of batch turnovers is increased. This implies that small droplets (< 1 μm) are only formed once the very largest drops have been broken, and very long processing times are needed for an 'equilibrium' DSD to be achieved.

6.4 Rotor speed and energy density

Figure 6.5 shows the effect of dispersed phase viscosity, total residence time and rotor speed on the Sauter mean diameter at a constant flow rate of 2,350 kg h^{-1}. Figure 6.5 shows that the effect of total residence time on mean drop size is reduced at lower rotor speeds for 9.4 mPa·s oil, while for 339 mPa·s oil the gradients are similar with rotor speed. Kamiya et al. (2010a) also observed a steeper decrease in drop size with increasing number of mixer passes at higher rotor speeds.

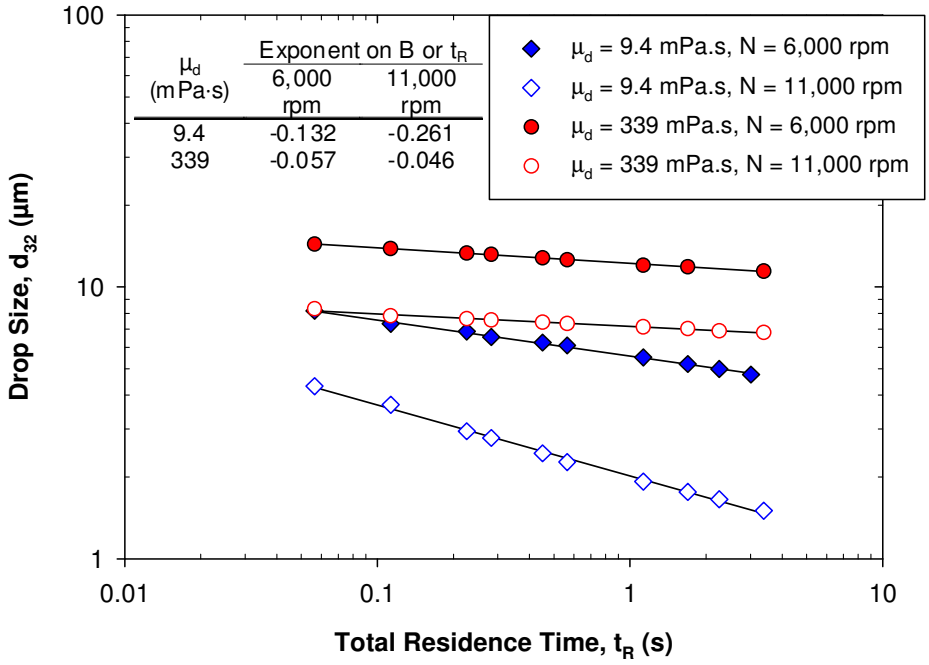

Figure 6.5: Mean drop size as a function of total residence time for 1% 9.4 mPa·s and 339 mPa·s silicone oil emulsions at 2,350 kg h^{-1}.

Figure 6.6 presents mean drop size in terms of energy density defined for multiple passes (Pacek et al., 2007):

$$E_V = \rho.\varepsilon.t_R = \frac{P}{V_H}t_R = \frac{P}{V_T}t \tag{6.5}$$

Figure 6.6 indicates that energy density correlates drop sizes formed at different flow rates, but does not correlate drop sizes formed at different rotor speeds. Nevertheless, energy density is useful for determining how much energy is consumed per unit volume of emulsion, and Figure 6.6 indicates that to form small droplets, higher rotor speeds are necessary and they are more efficient.

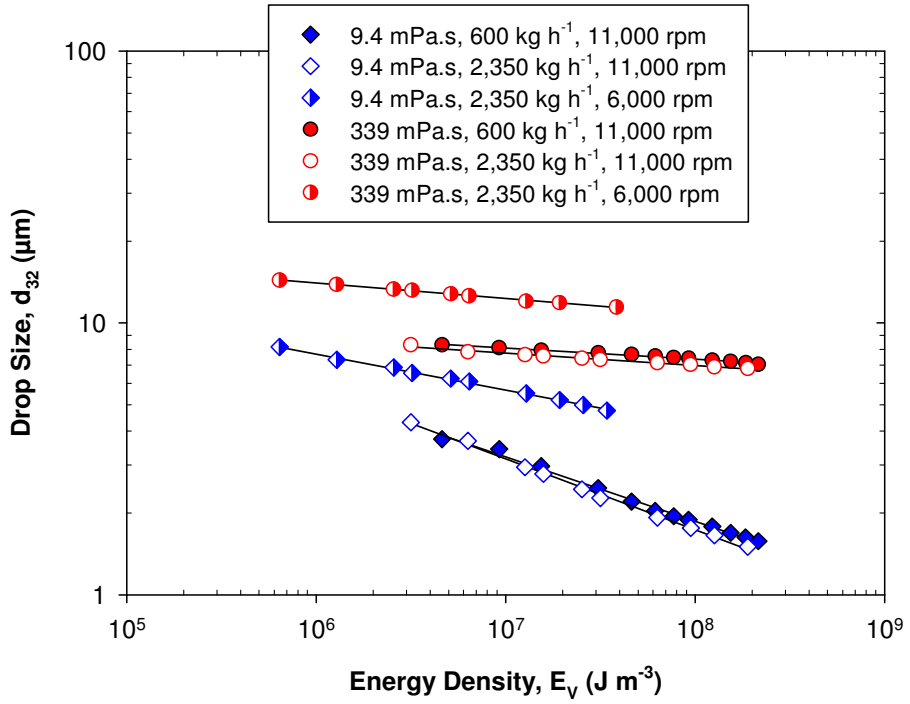

Figure 6.6: Mean drop size as a function of energy density for 1% 9.4 mPa·s and 339 mPa·s silicone oil emulsions at rotor speeds of 6,000 and 11,000 rpm, and flow rates of 600 and 2,350 kg h^{-1}.

6.5 Dispersed phase viscosity

The effect of dispersed phase viscosity on Sauter mean diameter of silicone oil emulsions is shown in Figure 6.7. At the highest viscosity (339 mPa·s), increasing t_R had practically no effect on mean drop size with an exponent of ~ -0.05, however the gradient decreased to -0.33 for the lowest viscosity (1.7 mPa·s). These findings show that multiple passes only have a notable effect on drop size distributions for lower viscosity oils, and the probability of droplets breaking partly depends on the droplet size and the oil viscosity. It appears that for highly viscous oils, the probability of further drop break-up is limited by the increase in the droplet deformation times of small drops, see Section 8.6.3.

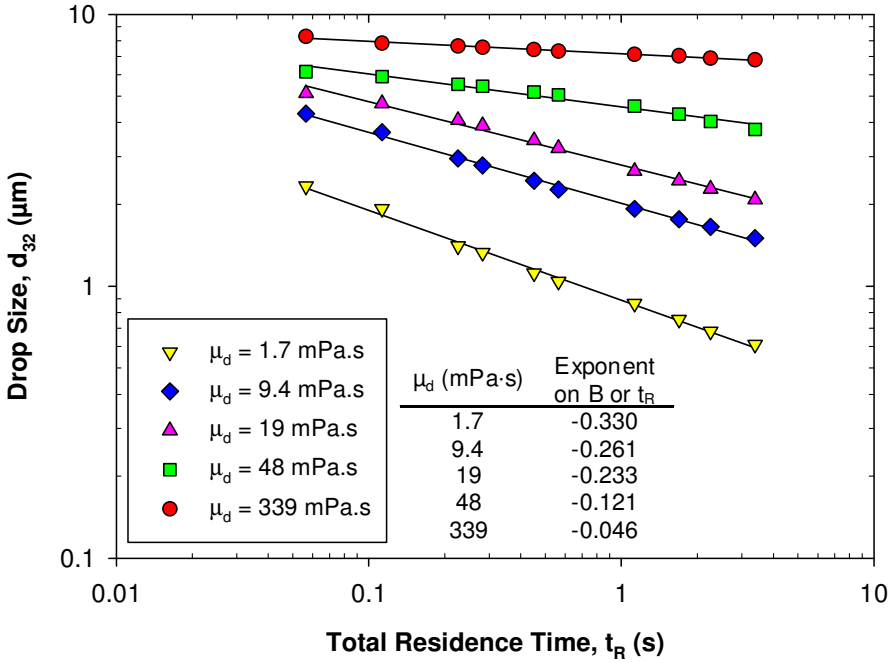

Figure 6.7: Mean drop size as a function of total residence time for 1% silicone oil emulsions with dispersed phase viscosities from 1.7 to 339 mPa·s, at a constant rotor speed of 11,000 rpm and flow rate of 2,350 kg h^{-1}.

For lower μ_d oil (Figure 6.7), mean drop size is a stronger function of number of batch turnovers (Figure 6.8). For example for 339 mPa·s oil, d_{32} falls 18% from 1 to 60 batch turnovers, compared to 74% for 1.7 mPa·s oil. This figure clearly indicates that breakage of lower viscosity drops depends more on number of passes, and lower μ_d oils are more dependent upon the initial droplet size. As a consequence, droplet break-up is both a strong function of the processing time and the dispersed phase viscosity.

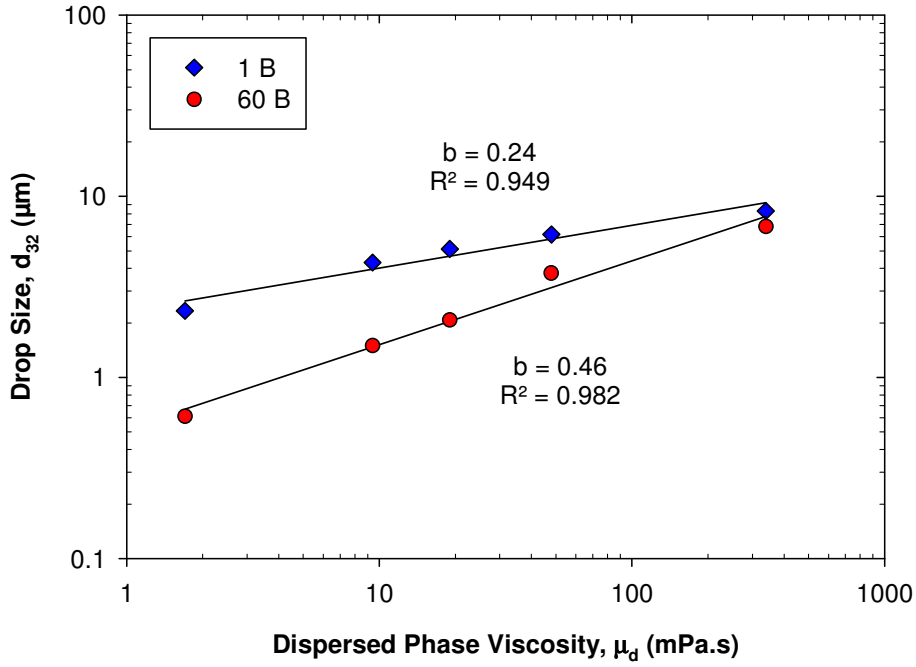

Figure 6.8: Mean drop size as a function of dispersed phase viscosity for 1% silicone oil emulsions with dispersed phase viscosities from 1.7 to 339 mPa·s after 1 and 60 batch turnovers, at a rotor speed of 11,000 rpm and flow rates of 2,350 kg h^{-1}.

Figure 6.8 shows that droplet sizes formed after 60 mixer passes tends to $\mu_d{}^{0.46}$. For a stirred vessel, equilibrium droplet size correlates with $\mu_d{}^{0.75}$ (Eq. (2.56)) (Leng and Calabrese 2004), which may be where the trend for this study is approaching at long times. However for a continuous screw loop reactor, Ludwig et al. (1997) reported an exponent of 0.53 on μ_d, while Schultz et al. (2004) stated a value > 0.5 for non-toothed rotor-stator systems, which are both close to 0.46 (Figure 6.8). The key difference between droplet break-up in stirred vessels and rotor-stator mixers is the effect of μ_d on DSDs shifts to lower viscosities for rotor-stator mixers, from > 100 mPa·s (stirred vessels) to < 350 mPa·s (rotor-stator mixers), discussed in Section 5.7.

6.5.1 Drop size distributions

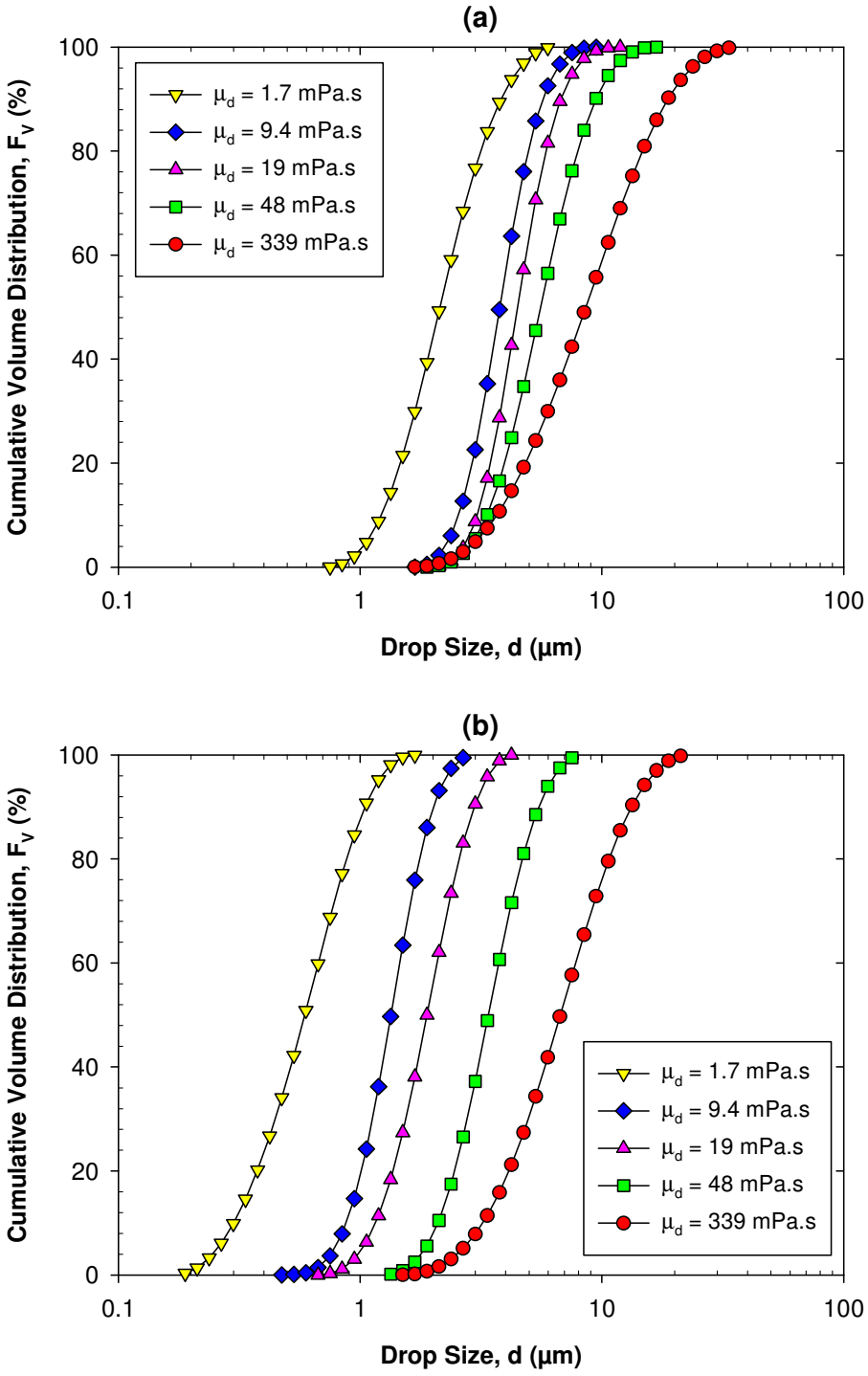

Figure 6.9: Cumulative volume drop size distributions for 1% silicone oil emulsions with dispersed phase viscosities from 1.7 to 339 mPa·s, after (a) one and (b) 60 batch turnovers, at a constant rotor speed of 11,000 rpm and flow rate of 2,350 kg h^{-1}.

Volume DSDs after a single batch turnover and 60 batch turnovers for μ_d oils from 1.7 to 339 mPa·s are presented in Figure 6.9. Both Figure 6.9a and Figure 6.9b show the DSD for 9.4 mPa·s oil is close to log-normal, and for μ_d oils above 9.4 mPa·s, the DSDs became skewed towards smaller drops, see Section 5.7, while the DSD for 1.7 mPa·s oil has a large population of small drops.

Figure 6.9b shows that d_{min} for each oil viscosity are different, compared to Figure 6.9a where d_{min} is practically the same for all oil viscosities except 1.7 mPa·s oil. This implies that highly viscous small droplets formed initially cannot be broken with further processing, while less viscous small droplets can be broken further after initial formation.

Table 6.1: Span and skewness of the drop size distributions of emulsions at five dispersed phase viscosities, for 1 and 60 batch turnovers at 11,000 rpm and 2,350 kg h^{-1}.

Dispersed phase viscosity, μ_d (mPa·s)	**Span, w (-)**		**Skewness, s (-)**	
	1 B	**60 B**	**1 B**	**60 B**
1.7	1.77	1.87	0.021	-0.085
9.4	1.49	1.53	0.021	-0.051
19	1.49	1.60	0.036	-0.042
48	1.68	1.61	0.016	-0.004
339	2.26	2.03	-0.041	-0.044

The span of log-normal distributions may be defined using the ratio of large to small drop sizes, similar to geometric standard deviation (Seville et al., 1997):

$$w = \sqrt{\frac{d_{0,9}}{d_{0,1}}} \tag{6.6}$$

This term describes the width of the distribution, where a larger value indicates a wider spread. The skewness of log-normal DSDs (based on $d_{0,9}$ and $d_{0,1}$) is described by (Vanoni, 2006):

$$s = \frac{ln\left(\frac{\sqrt{d_{0,9}.d_{0,1}}}{d_{0,5}}\right)}{ln(w)} \tag{6.7}$$

Eq. (6.7) describes the ratio of the number of droplets on the left hand side of the DSD to the number of droplets on the right hand side of the DSD, normalised by the span. A value of zero indicates a perfect log-normal distribution, while a positive value means the DSD is skewed towards the right of the DSD (larger drops) and a negative value means the DSD is skewed towards the left of the DSD (smaller drops).

Figure 6.10a shows the span of the DSDs are similar from 1.5 to 2.5 with increasing number of batch turnovers, with slightly higher values for 1.7 and 339 mPa·s oils due to a tail of small droplets, see Figure 6.9. Figure 6.10b shows the skewness of these DSDs are symmetrically log-normal with a value near zero that changes little with number of batch turnovers. For 1.7 mPa·s oil, the distribution skewness becomes very negative, due to a high proportion of small drops, especially near 20 batch turnovers. These results suggest that multiple pass processing does not particularly result in narrower, more uniform DSDs, which may have been expected.

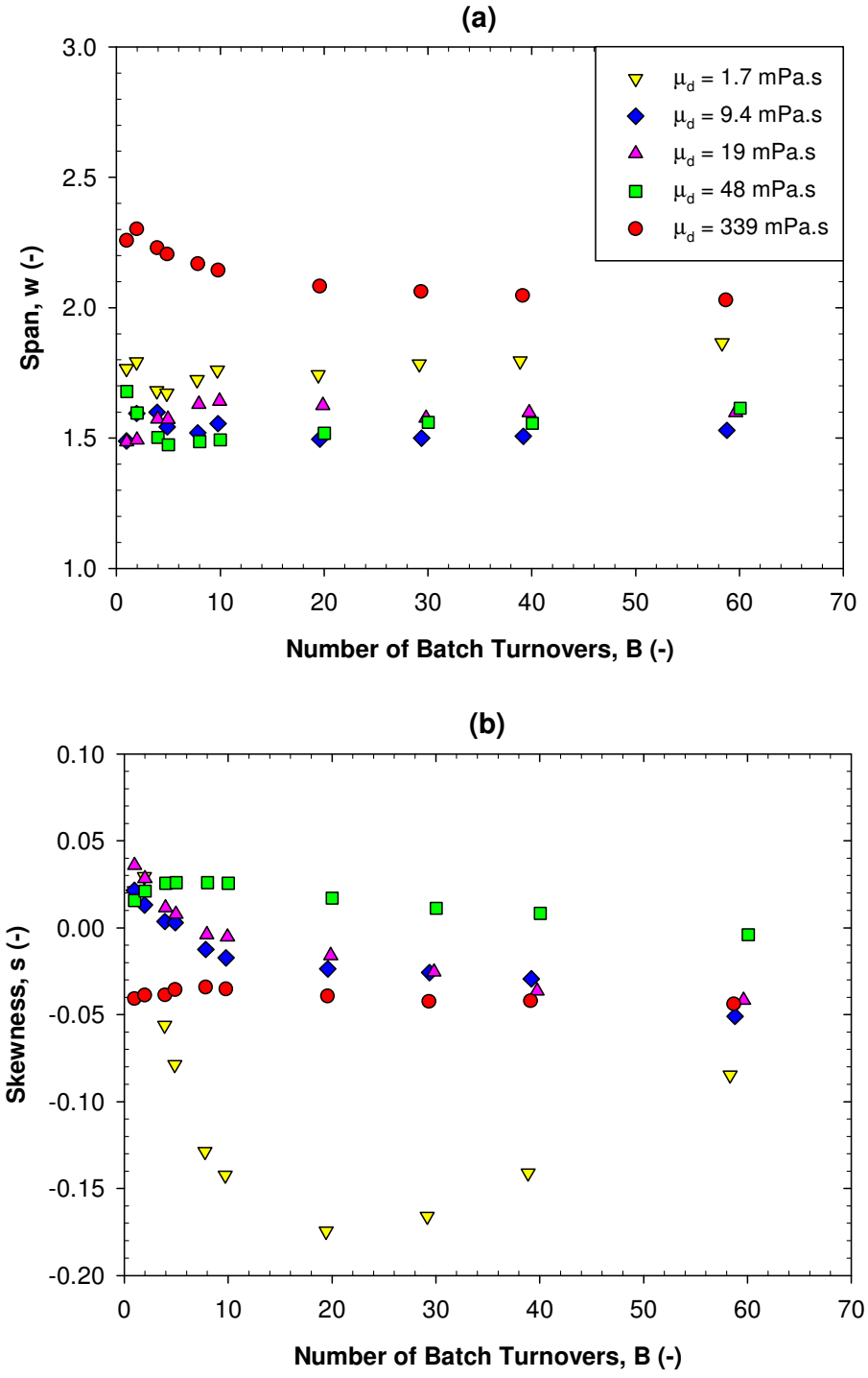

Figure 6.10: (a) Span and (b) skewness of the DSDs as a function of mean drop size for 1% silicone oil emulsions with dispersed phase viscosities from 1.7 to 339 mPa·s at a rotor speed of 11,000 rpm and flow rate of 2,350 kg h^{-1}.

6.6 High dispersed phase viscosity

The effect of number of passes on highly viscous dispersed phases (9,701 mPa·s) form bimodal DSDs, as for single passes in Section 5.10. The peaks of these distributions were analysed separately using the same method described in Appendix B.5 to calculate d_{32} for each peak.

Figure 6.11 compares the effect of number of batch turnovers on d_{32} for the entire distribution, and for fitted peaks 1 and 2. This figure shows all measures of d_{32} are not greatly affected by number of passes, with all gradients varying from 0 to -0.05, confirming the findings from Figure 6.3 for 339 mPa·s oil emulsions, that viscous forces limit further droplet break-up. This implies that 9,701 mPa·s oil should be processed in a single pass, since once the drops are broken they are too small to be broken further under the hydrodynamic stresses exerted by the system. Figure 6.11 also indicates there is little difference in d_{32} for peak 1 with rotor speed, with values of 4.3 µm and 3.9 µm at 6,000 rpm and 11,000 rpm, respectively.

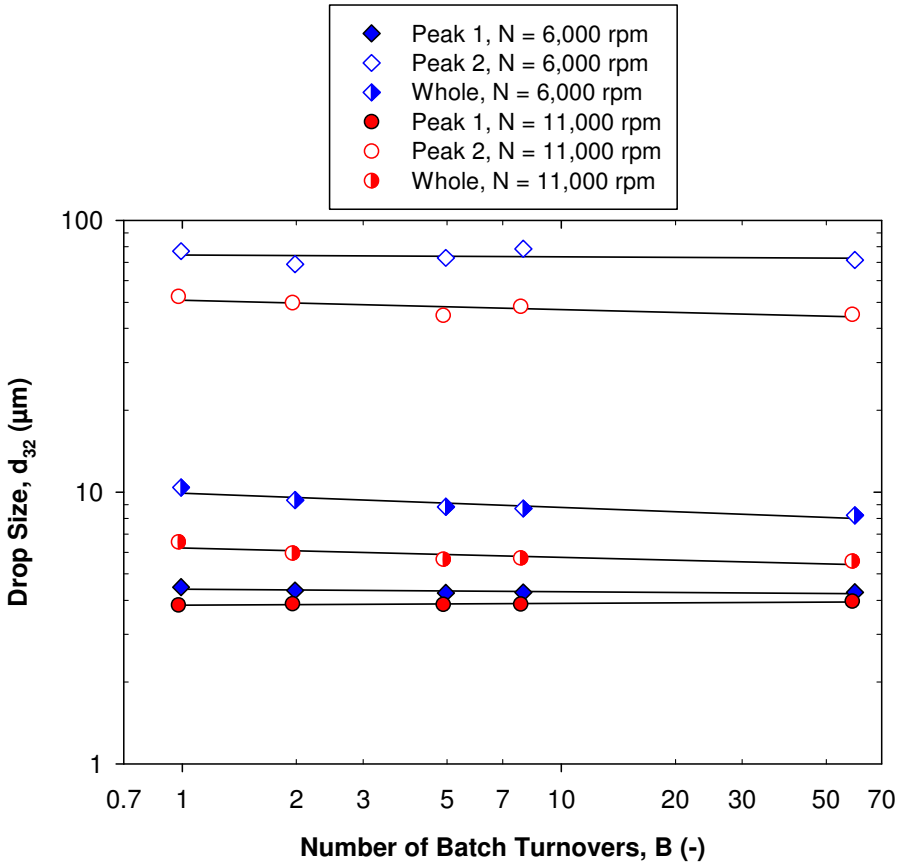

Figure 6.11: Mean drop size for the whole DSD, peak 1 and peak 2 for 1% 9,701 mPa·s silicone oil emulsions as a function of number of batch turnovers, at rotor speeds of 6,000 rpm and 11,000 rpm for a flow rate of 2,350 kg h^{-1}.

6.7 Dispersed phase volume fraction

Figure 6.12 shows that the trends in drop size reduction for volume fractions of 1 wt.% and 25 wt.% are practically the same, due to the presence of surfactant. In fact, slightly smaller droplets were formed at 25 wt.% phase volume, due to a slight increase in emulsion viscosity. This suggests that together with the results from Figure 5.7, the trends for 1 wt.% oil can be extended to higher dispersed phase volume fractions of at least 50 wt.%.

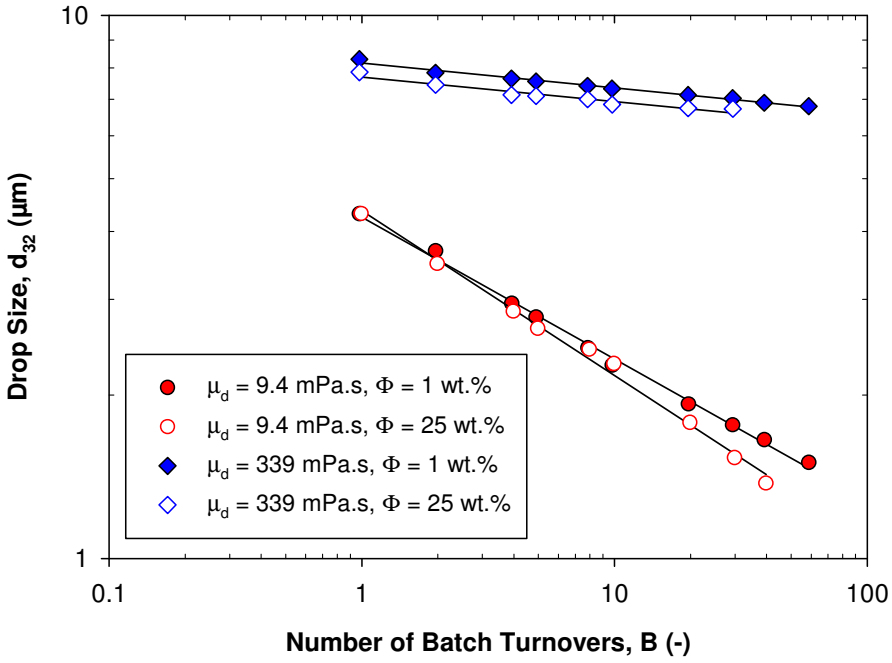

Figure 6.12: Mean drop size as a function of number of batch turnovers for 1 wt.% and 25 wt.% 9.4 mPa·s and 339 mPa·s silicone oil emulsions at 11,000 rpm and 2,350 kg h^{-1}.

6.8 Single and multiple pass comparison

For 9.4 mPa·s oil emulsions, mean drop size for single passes ('SP') and for multiple passes ('MP') in the mixing vessel as a function of total residence time is shown in Figure 6.13. For a given total residence time, slightly smaller drops were obtained for multiple passes since the drops have been broken down by previous passes, however, this is only true when the emulsion has passed through the mixer ~ 5 times (Figure 6.2).

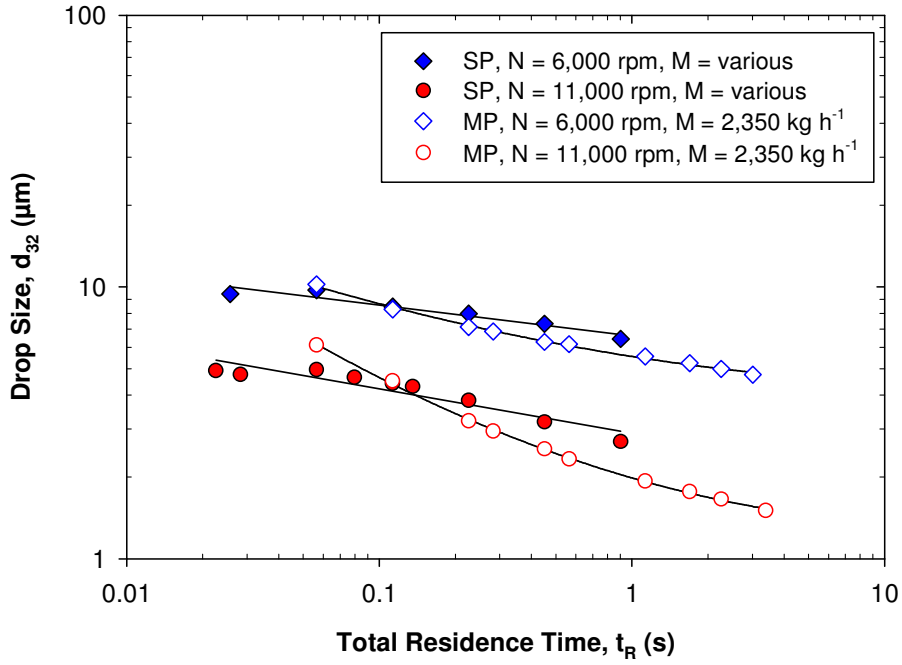

Figure 6.13: Mean drop size for single passes (SP) at various flow rates (150-6,200 kg h^{-1}) and for multiple passes (MP) at 2,350 kg h^{-1} in the mixing vessel as a function of total residence time for 1% 9.4 mPa·s silicone oil emulsions, at rotor speeds of 6,000 and 11,000 rpm.

Figure 6.13 shows that if small droplets are required then multiple passes should be utilised. Multiple passes are advantageous, especially for low viscosity oils, as they increase the probability of further droplet break-up, however this mode of operation is more energy intensive as > 5 passes are required (Figure 6.2). Single passes are recommended for high viscosity oils and systems where control of droplet size is less critical, as flexibility is increased for multiple pass systems, which may be desirable.

6.8.1 Correlations

In the following section, single and multiple passes are compared by correlation with energy dissipation rate. The results were obtained using the 'step-wise' recirculation method whereby the rotor speed is increased in steps to form DSDs close to 'equilibrium'.

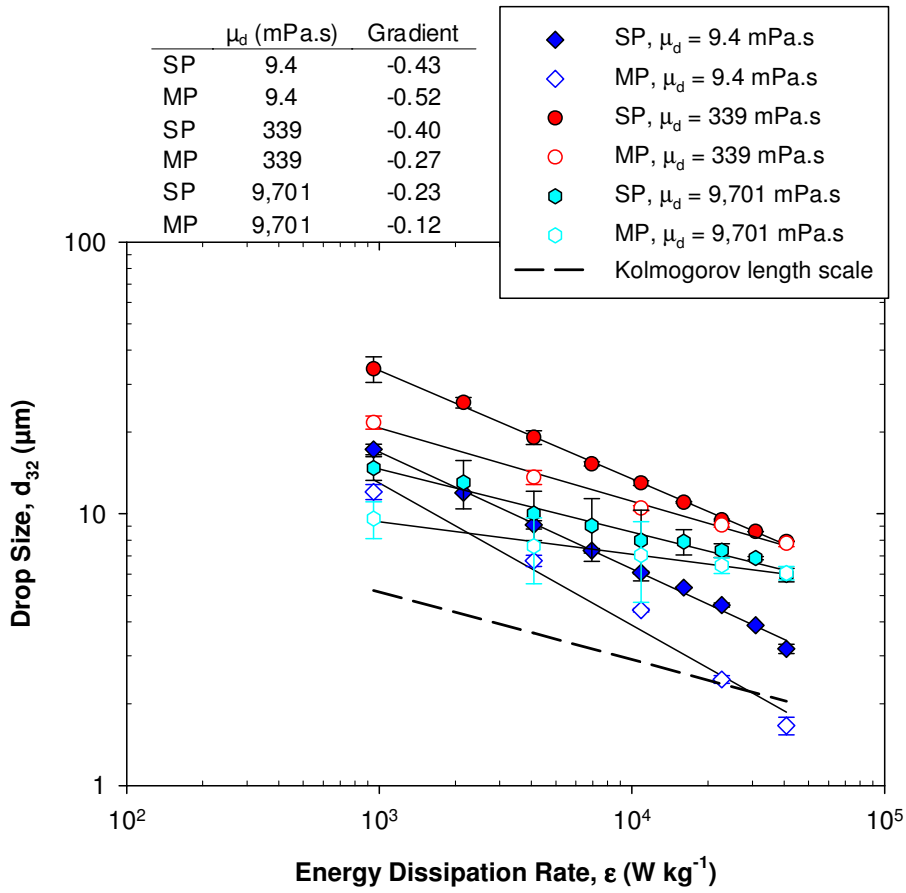

Figure 6.14: Mean drop size as a function of energy dissipation rate for 1% silicone oil emulsions, at three dispersed phase viscosities, for a single pass (SP) and for multiple passes (MP) after 5 batch turnovers, at rotor speeds from 3,000 rpm to 11,000 rpm at a flow rate of 300 kg h^{-1} with standard deviation error bars.

Figure 6.14 compares single and multiple pass mean drop sizes of emulsions with μ_d oils of 9.4, 339 and 9,701 mPa·s. For higher μ_d oils, single pass and multiple pass drop sizes converge at higher energy dissipation rates, hence only single passes should be used at high rotor speeds. This suggests that an 'equilibrium' drop size has practically been achieved in a single pass for high viscosity oils, and the probability of further droplet break-up is limited. For lower μ_d oils, there is a clear distinction between single and multiple pass drop sizes at all ε, confirming the findings of Figure 6.5.

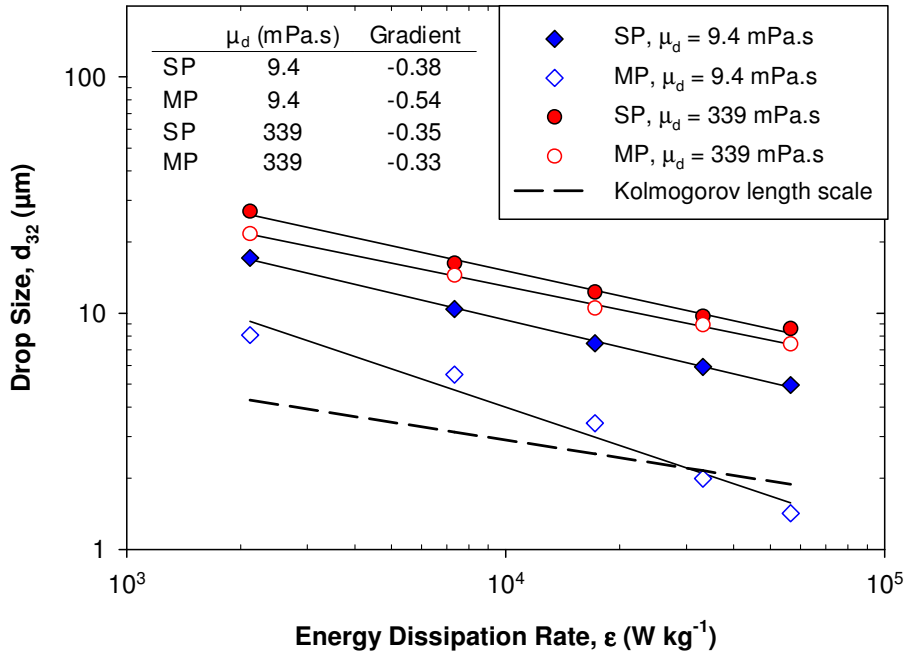

Figure 6.15: Mean drop size as a function of energy dissipation rate for 1% silicone oil emulsions, at two dispersed phase viscosities, for a single pass (SP) and for multiple passes (MP) after 40 batch turnovers, at rotor speeds from 3,000 rpm to 11,000 rpm at a flow rate of 2,400 kg h^{-1}. Data for 339 mPa·s oil from Rodgers and Cooke (2011).

Figure 6.14 and Figure 6.15 present mean drop size of emulsions at equal t_R, with differing flow rates and number of passes; 5 B at 300 kg h^{-1}, and 40 B at 2,400 kg h^{-1}, respectively. The exponents on ε for single passes and 339 mPa·s oil emulsions, range from -0.35 to -0.40, falling to -0.27 to -0.33 after multiple passes. Applying the Hinze theory to these correlations, it may be deduced that turbulent inertial forces are important for droplet break-up, where the fall in the exponent is due to break-up approaching the viscous limit with an exponent of -0.25 in Eq. (2.56).

For lower μ_d oils (9.4 mPa·s), mean drop sizes fall below η_K at the two highest energy dissipation rates for multiple passes, and the exponent shifts from -0.40 (single pass), to -0.53

(multiple passes), which supports a change in droplet breakage mechanism at higher ε, once $d_{32} < \eta_K$. Schubert and Engel (2004) reported an exponent of -0.35 in rotor-stator devices, indicating that droplet break-up depends on turbulent inertial forces, while an exponent of -0.75 suggests turbulent viscous forces are important.

6.8.2 Drop size distributions

Volume DSDs comparing single pass and multiple passes ($5B$) (Figure 6.16) at a constant rotor speed and flow rate, shift slightly to smaller drop sizes after $5B$ as expected, for various viscosities. The main difference is the size of the largest droplet which increased greatly as μ_d oil increased, and increased for single passes.

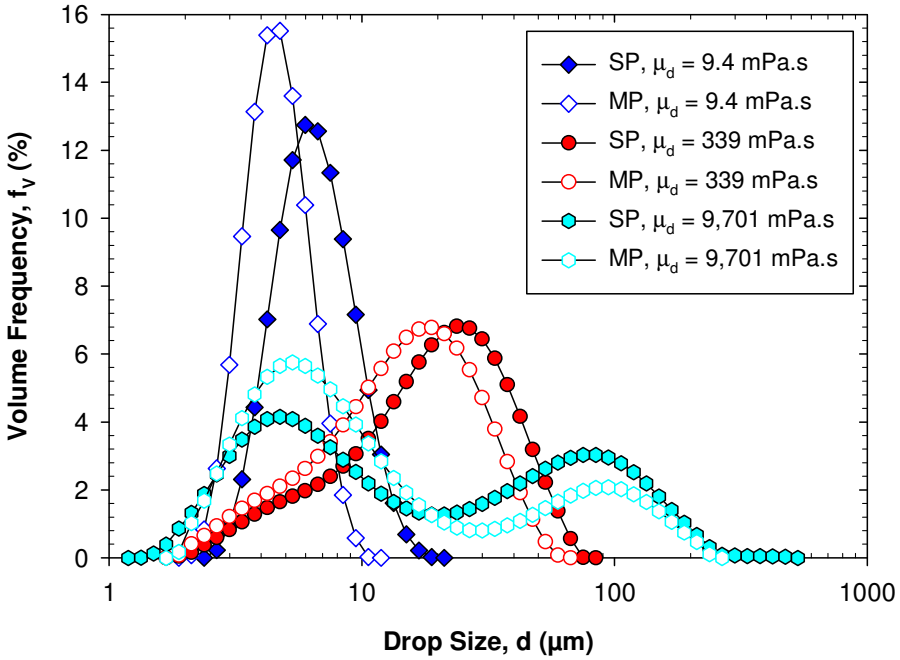

Figure 6.16: Volume drop size distributions for 1% silicone oil emulsions for three dispersed phase viscosities, for a single pass (SP) and for multiple passes (MP) after 5 batch turnovers, at a constant rotor speed of 7,000 rpm and flow rate of 300 kg h^{-1}.

As discussed in Section 6.5, for low and intermediate viscosity oils there is little variation in the span of the emulsion DSDs with rotor speed, as span ranged from 1.4 to 1.9 (9.4 mPa·s oil), increasing to 2.0 to 2.9 for 339 mPa·s oil (Figure 6.17a). For the highest viscosity oil (9,701 mPa·s), span increased further, however unlike the lower oil viscosities, span decreased with increasing rotor speed, especially for multiple passes. This indicates that multiple passes may affect the spread of the distribution for highly viscous oils.

The skewness for both single and multiple pass low viscosity oil emulsions are generally close to zero suggesting a perfect log-normal shape, while for 339 mPa·s oil the skewness becomes increasingly negative at lower rotor speeds (Figure 6.17b), where the tail of small drops on the left of the DSD becomes more pronounced. Skewness at the highest viscosity oil switched from negative to positive as rotor speed increased (for a single pass), since the DSDs have a larger volume of small drops on the left of the DSD at lower rotor speeds. However at higher rotor speeds, a larger population of small drops on the right of the DSD are formed, particularly for multiple passes (Figure 6.16), which results in positive skewness.

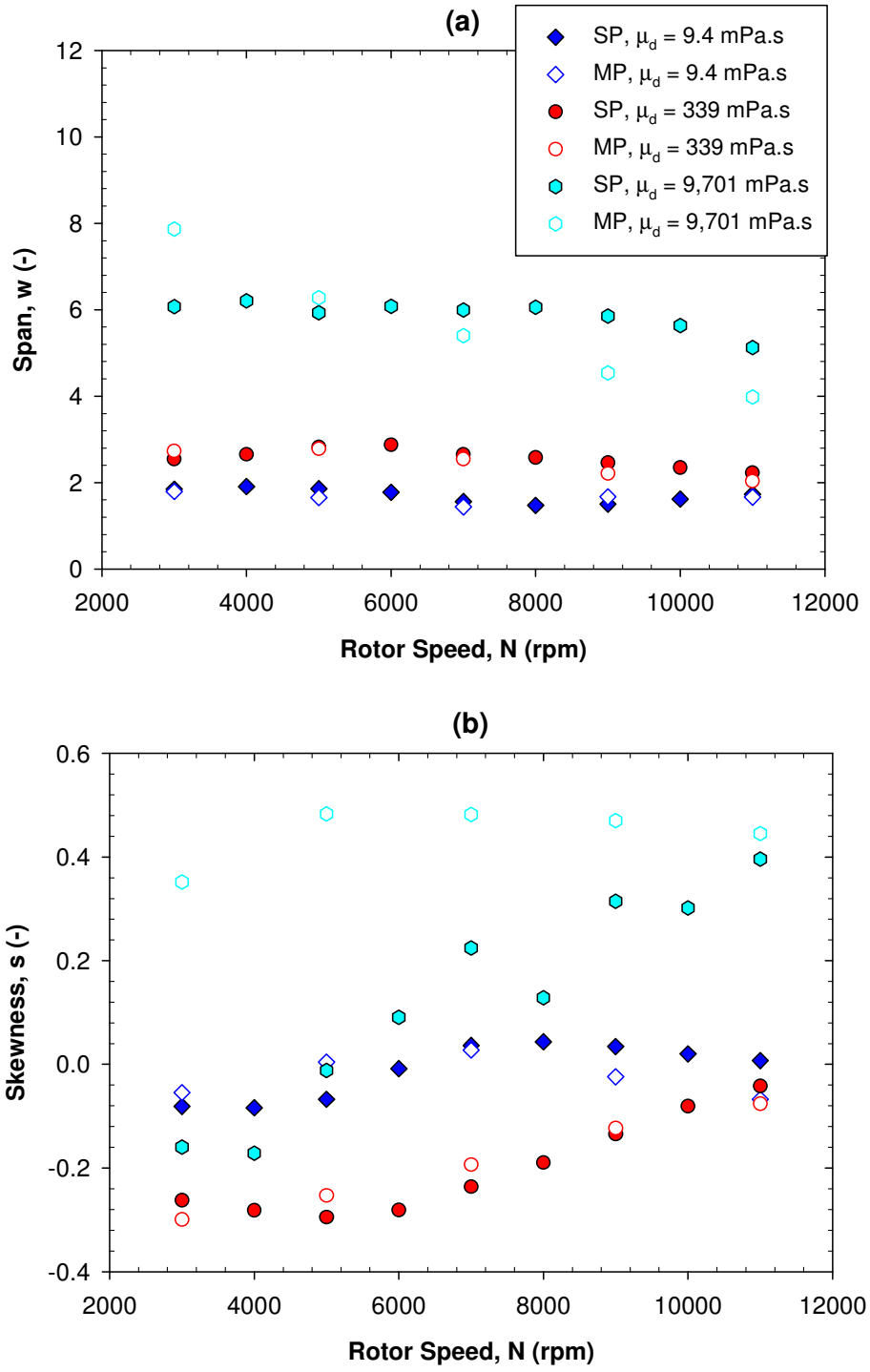

Figure 6.17: (a) Span and (b) skewness of the DSDs as a function of mean drop size for 1% silicone oil emulsions for a single pass (SP) and for multiple passes (MP) after 5 batch turnovers, at a constant flow rate of 300 kg h^{-1}.

6.9 Modelling multiple passes in recirculation loops

The effect of number of passes is shown in Figure 6.18 for three oil viscosities and two rotor speeds using the 'complete pass' recirculation method. Figure 6.18 shows that the majority of drop break-up occurs after the first mixer pass, with substantially less break-up after subsequent passes, as reported by Baker (1993), and the continual decrease of droplet size with increasing number of passes suggests that the probability of drops breaking remains. From Figure 6.18, the probability of droplet break-up increased at higher rotor speeds and lower μ_d oils. Figure 6.18 is useful for modelling to isolate the effect of each mixer pass on drop size, and remove the effect of mixing in the vessel to model the effect of the recirculation loop.

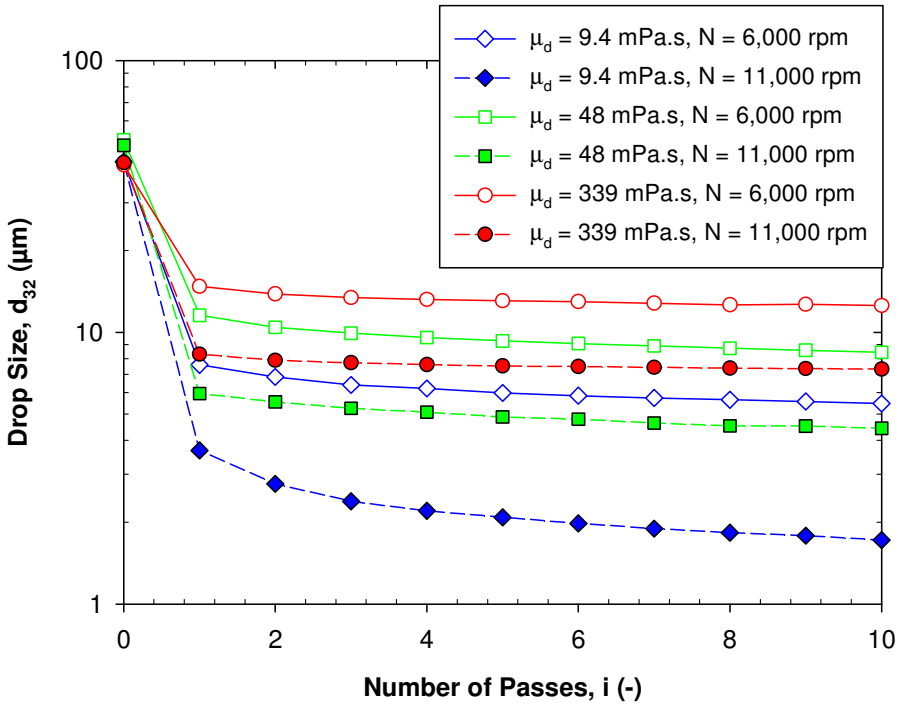

Figure 6.18: Mean drop size as a function of number of passes for 1% silicone oil emulsions, at three dispersed phase viscosities and rotor speeds of 6,000 and 11,000 rpm. Results for multiple passes (after 10 passes) at a flow rate of 600 kg h^{-1} undertaken by the 'complete pass' recirculation method.

Operation of the in-line Silverson mixer in a recirculation loop results in a range of DSDs in the stirred vessel (Figure 6.2), depending on the number of times the components of the emulsion have passed through the mixer, which can be predicted using the expression by Baker (1993) in Eq. (2.95) and the experimental data for each mixer pass from Figure 6.18.

A comparison between experimental and calculated mean drop sizes as a function of the number of batch turnovers is shown in Figure 6.19. The curves for two μ_d oils provide good fits which confirms the model is applicable for predicting mean drop size in the mixing vessel.

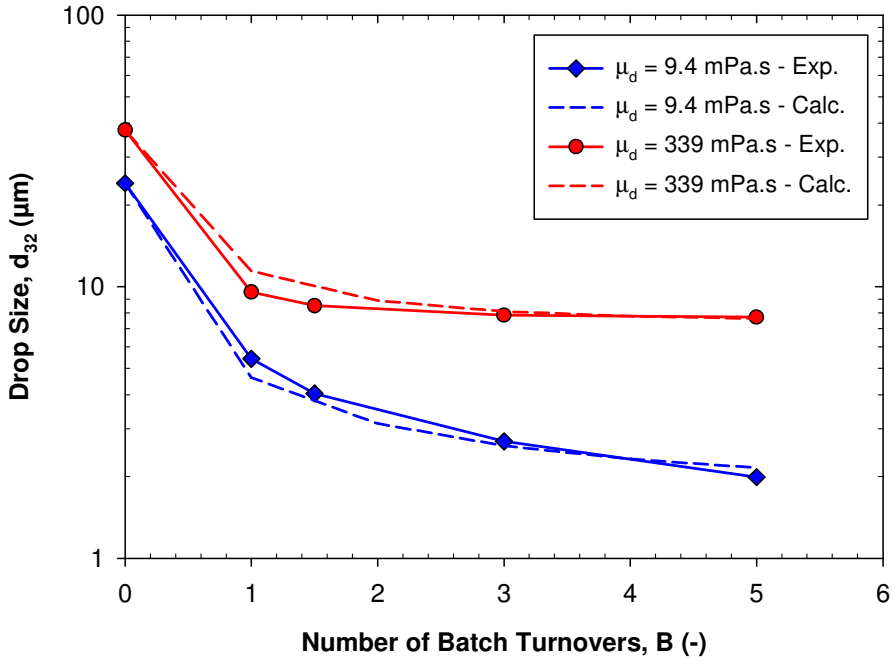

Figure 6.19: Calculated and experimental mean drop sizes in the mixing vessel for 1% 9.4 and 339 mPa·s silicone oil emulsions, at a rotor speed of 11,000 rpm and flow rate of 600 kg h^{-1}.

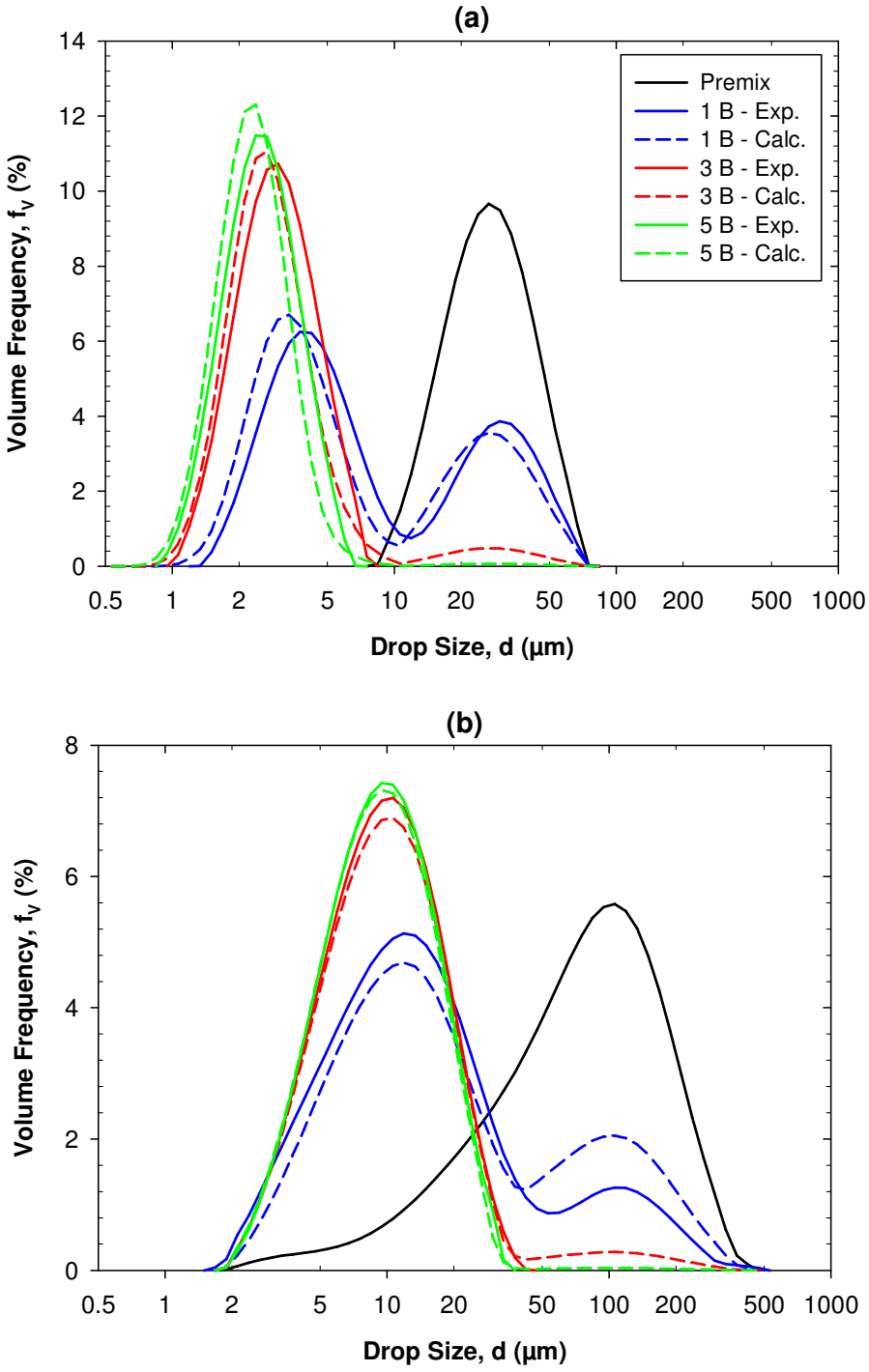

Figure 6.20: Calculated and experimental volume drop size distributions for 1% (a) 9.4 mPa·s and (b) 339 mPa·s silicone oil emulsions, at a rotor speed of 11,000 rpm and flow rate of 600 kg h^{-1}.

A comparison between the experimental and calculated DSDs using Eq. (2.95), (Figure 6.20) also gave good agreement for 1 to 5 batch turnovers. The agreement improved as number of passes increased, since the distribution became single model, as for $B > 4.6$, at least 99% of the drops have passed through the mixer at least once (Baker, 1993). For lower batch turnovers such as $B = 3$, the model slightly over predicted the volume of large drops present.

6.10 Population balance modelling

Population balance equations were solved using the 2D rotor-stator geometry described in Section 4.9. The model equations were solved in Fluent 12.0 from 3,000 rpm to 11,000 rpm at 300 kg h^{-1}, using the 'Population Balance Module'. The model equations were solved by applying the quadrature methods of moments (QMOM), see Section 2.3.3 (Marchisio et al., 2003), in collaboration with Prof. Baldyga's group in Warsaw University of Technology, Poland.

A mixture model was used in Fluent to describe the multiphase flow containing 1% 9.4 mPa·s oil dispersed in 0.5 wt.% SLES solution. The silicone oil density was 937 kg m^{-3}, the continuous phase density was 998.2 kg m^{-3} and the interfacial tension was 10 mN m^{-1}. Values of the first four moments (m_o to m_3) were calculated using QMOM, with the moments at the mixer inlet (initial conditions) determined experimentally (Table 6.2).

Table 6.2: Moments used as initial conditions.

Zero moment, m_o (m^{-3})	**First moment, m_1 ($m\ m^{-3}$)**	**Second moment, m_2 ($m^2\ m^{-3}$)**	**Third moment, m_3 ($m^3\ m^{-3}$)**
4.27×10^{11}	1.35×10^{7}	4.87×10^{2}	2.04×10^{-2}

Population balance equations were solved using a second order discretisation scheme until the residuals of all moments converged with values < 10^{-5}. Moments at the mixer outlet were compared with experimental results.

6.10.1 Breakage kernels

Two droplet breakage kernels were examined; the first a simple model developed by Coulaloglou and Tavlarides (1977) in Eq. (2.111), and the second a multi-fractal breakage kernel. The model in Eq. (2.111) was developed for inviscid dispersed phases, so the calculated results are most applicable for low viscosity oil emulsions. However the advantage of the multi-fractal breakage kernel is that it can account for the effect of higher dispersed phase viscosities in addition to intermittency in turbulent flow. Initial work was undertaken using the breakage kernel in Eq. (2.111) as this was computationally less demanding, however the ultimate aim was to employ the multi-fractal breakage kernel. The multi-fractal turbulence breakage kernel (Baldyga and Podgorska, 1998):

$$g(d) = C_g\sqrt{\ln\left(\frac{L}{d}\right)}\,\varepsilon^{1/3}d^{-2/3}\int_{0.12}^{\alpha_X}\left(\frac{d}{L}\right)^{\frac{\alpha+2-3f(\alpha)}{3}}d\alpha \tag{6.8}$$

Where (Baldyga and Bourne, 1999), $f(\alpha) = a + b\alpha + c\alpha^2 + d\alpha^3 + e\alpha^4 + f\alpha^5 + g\alpha^6 + h\alpha^7 + i\alpha^8$, and $a = -3.510;\ b = 18.721;\ c = -55.918;\ d = 120.90;\ e = -162.54;\ f = 131.51;\ g = -62.572;\ h = 16.10;\ i = -1.7264$, when $\alpha > \alpha_{min}$. $\alpha_{min} = 0.12$ and $C_g = 0.0035$.

The value of α_X, for non-viscous dispersed phases:

$$\alpha_X = \frac{\frac{5}{2}log\left[\frac{L\varepsilon^{2/5}\rho_c{}^{3/5}}{C_X\sigma^{3/5}}\right]}{log\left(\frac{L}{d}\right)} - 1.5 \tag{6.9}$$

Where $C_X = 0.23$. The value of L is given by:

$$L = \frac{(u')^3}{\varepsilon} = \frac{\left(\frac{2}{3}\right)^{3/2}k^{3/2}}{\varepsilon} \tag{6.10}$$

The breakage kernels were written in User Defined Function (UDF) files (Appendix C.2). The 'Population Balance Module' was not used to solve the multi-fractal breakage kernel due to high computation processing times. The breakage kernel and fragmentation distribution function were compiled in a UDF (Appendix C.2), and run separately in Fluent.

6.10.2 Breakage kernel and fragmentation distribution estimation

Models describing the rate of droplet breakage include several adjustable parameters, such as K_1 and K_2 in Eq. (2.111) and C_g in Eq. (6.8) and C_X in Eq. (6.9). These parameters should ideally be constants, however theoretical and experimental limitations result in authors presenting their own specific parameters to reproduce the experimental results, usually by trial-and-error (Ribeiro et al., 2011). Hence the constants were obtained by trial-and-error, using parameters from other studies as initial conditions. Initially, the constants reported by Bapat and Tavlarides (1985) were used in Eq. (2.111), followed by a systematic approach, which identified two further sets of constants for comparison with experimental data (Table 6.3).

Table 6.3: Constants used in the breakage kernel in Eq. (2.111).

Constants	**C1**	**C2**	**C3**
K_1	0.00481	0.00400	0.00350
K_2	0.08	0.10	0.20

In addition to selection of the constants in the breakage kernel, a daughter distribution function is required to describe the method by which the droplets fragment, known as a daughter probability density function (PDF), to define the daughter size distribution. Initally, a parabolic fragmentation distribution was investigated (ANSYS, Inc., 2009):

$$\beta(v|v') = 0.5\left[\frac{C}{v'} + \frac{1-C/2}{v'}\left\{24\left(\frac{v}{v'}\right)^2 - 24\left(\frac{v}{v'}\right) + 6\right\}\right] \quad (6.11)$$

The value of the constant C, can vary between 0 and 3 to describe the probability of drops of a certain volume being formed. If $0 < C < 2$, a concave parabola is obtained, which suggests that a parent drop is more likely to break into unequally sized daughter droplets than equally sized fragments (Figure 6.21). Initally, values of $C < 2$ were investigated as for two phases with relatively low and similar viscosities, this mechanism requires less energy to break a single drop as the surface area created is small.

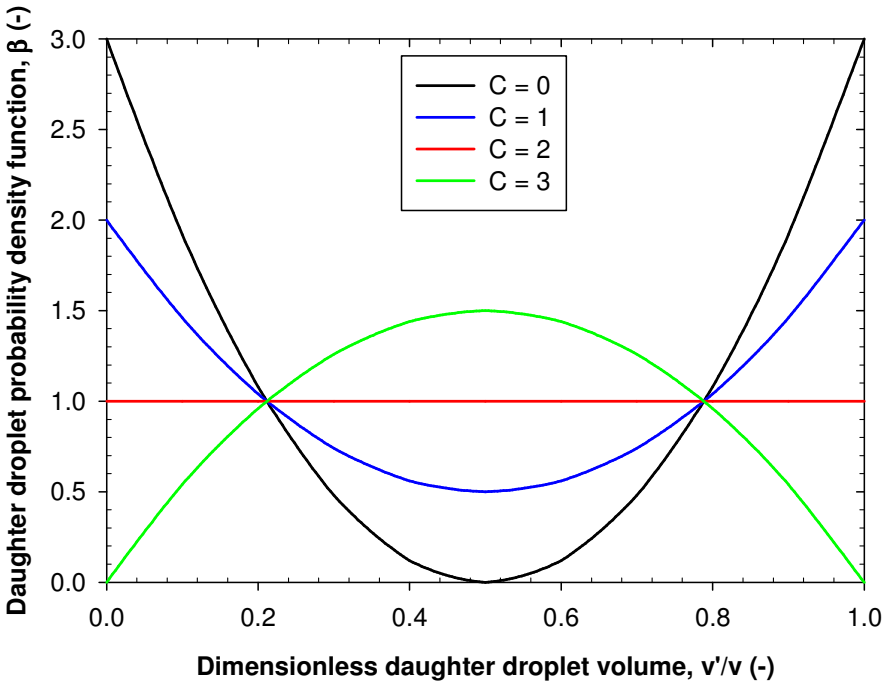

Figure 6.21: The effect of dimensionless daughter droplet volume on the daughter droplet PDF for different C values in the parabolic fragmentation distribution function.

Four cases are presented using the multi-fractal turbulence breakage kernel, with details given in Table 6.4. Initially, the constants reported by Baldyga and Podgorska (1998) were taken for C_g in Eq. (6.8) and C_X in Eq. (6.9), and after investigations, two further sets of

constants were developed (Table 6.4). For this breakage kernel, two fragmentation distribution functions were considered, the parabolic, and symmetric given by Eq. (2.112).

Table 6.4: Breakage constants in Eq. (6.8) and Eq. (6.9) and fragmentation distribution functions used to solve the multi-fractal turbulence breakage kernel.

	Case 1	**Case 2**	**Case 3**	**Case 4**
Fragmentation distribution function	Symmetric	Parabolic, $C = 0$	Symmetric	Symmetric
Constant C_g in Eq. (6.8)	0.0035	0.0035	0.07	0.105
Constant C_X in Eq. (6.9)	0.23	0.23	1.84	1.84

6.10.3 Simple breakage kernel

The distribution of number of droplets in the mixing head from numerical simulations is shown in Figure 6.22. This figure clearly shows that droplet break-up, indicated by an increase in the number of droplets per cubic metre, predominately occurs in the outer stator region. In particular, as expected, the number of droplets is highest near the tips of the outer rotor where energy dissipation rate is a maximum.

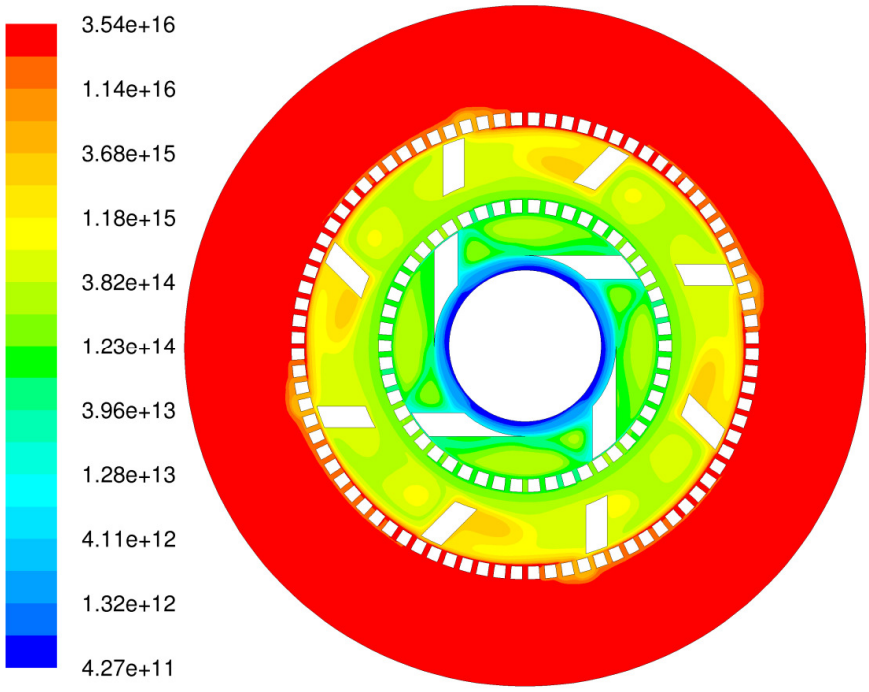

Figure 6.22: The distribution of the zeroth moment or the number concentration of drops (m^{-3}) in the mixing head at 9,000 rpm and 300 kg h^{-1}.

A comparison between experimental mean drop sizes and those calculated from numerical simulations are compared using Sauter mean diameter, and number mean diameter (d_{10}) (Eq. (A.11) in Appendix C.3), as these mean diameters contain all four calculated moments.

Predicated values of Sauter mean drop diameter based on the constants of Bapat and Tavlarides (1985) compare well at low rotor speeds, but agreement deteriorates at higher rotor speeds (Figure 6.23a). The reason for this is revealed by calculating the number mean drop diameters (Figure 6.23b), since at higher rotor speeds, the calculated number mean drop sizes were much too small. This suggests that the DSD is too broad since the model overpredicts the number of small droplets.

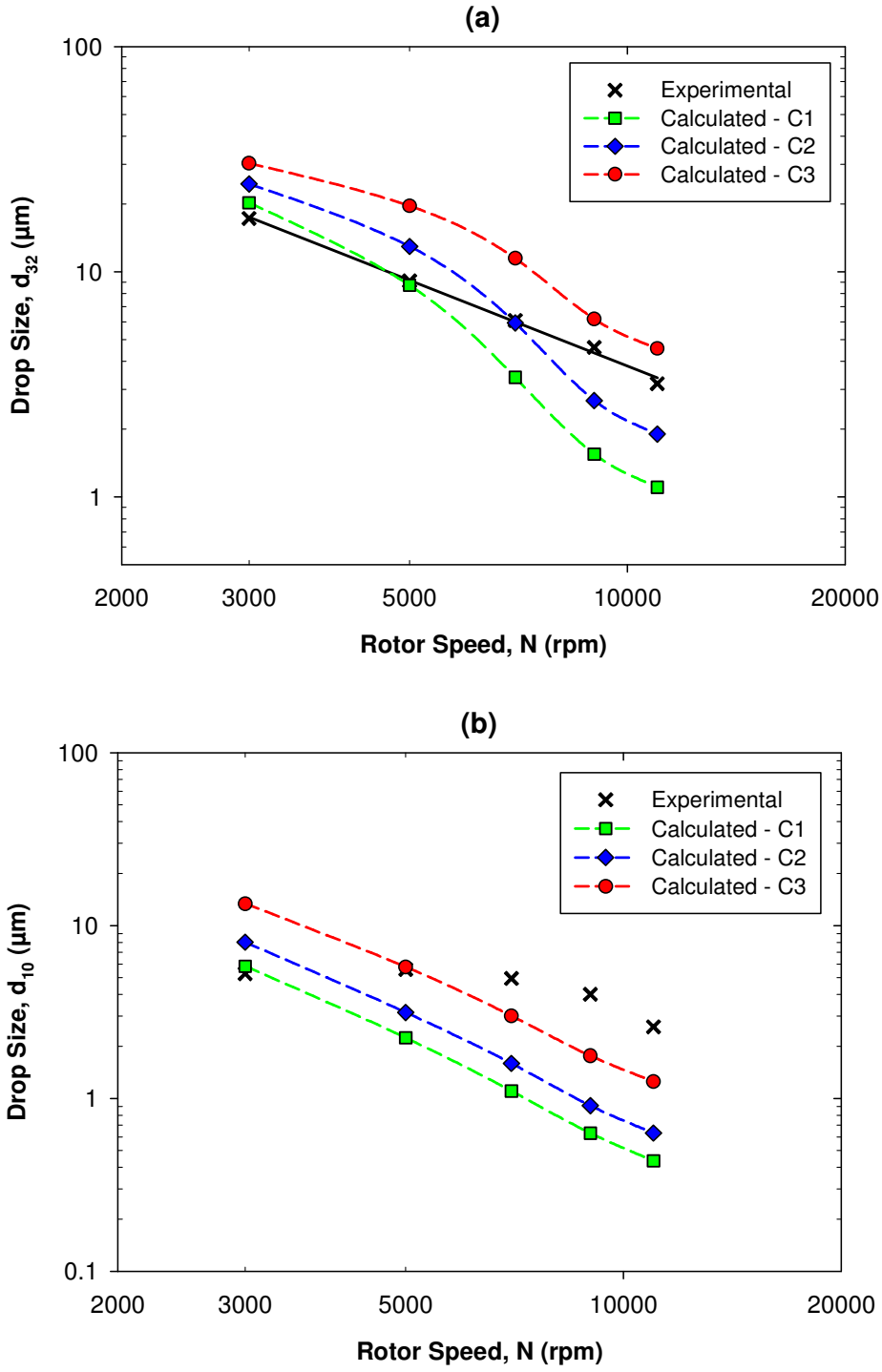

Figure 6.23: Calculated and experimental (a) Sauter mean drop diameters and (b) Number mean drop diameters, for 1% 9.4 mPa·s silicone oil emulsions, as a function of rotor speed. Calculated drop sizes from the Coulaloglou and Tavlarides (1977) breakage kernel for three sets of adjustable parameters given by C1, C2 and C3.

Additional sets of constants examined, denoted by C2 and C3 in Table 6.3, showed that the trend in droplet break-up based on d_{32} and d_{10} to differ from experiments, with low values of number mean diameter calculated in all cases. These findings suggest that a different fragmentation distribution function should be used.

6.10.4 Multi-fractal turbulence breakage kernel

Figure 6.24 shows the application of the multi-fractal turbulence breakage kernel to predict drop size in terms of d_{32} and d_{10}. Initally, different fragmentation distribution functions were investigated, following the findings from Section 6.10.3. From this investigation it was concluded that the symmetric fragmentation function in Eq. (2.112) is preferable. Figure 6.24 shows the symmetric fragmentation distribution function (Case 1) to be more favourable than the parabolic fragmentation distribution function (Case 2), and even though Sauter mean diameters for Case 2 were closer to the experimental values, number mean diameters were similar for each case, indicating poor description of the DSDs. This suggests that the silicone oil mother drops break into two equally-sized daughter droplets. Binary symmetric droplet breakage was also assumed by Raiker et al. (2009) for a high pressure homogeniser.

Mean drop sizes for Cases 3 and 4 (Figure 6.24) show that modification of the adjustable constants C_g and C_X produce good agreement between experimental and calculated mean drop sizes. For these cases, close agreement was found for both d_{32} and d_{10}, which suggests that all four moments of the distribution are in good agreement. This was examined further by reconstructing the number DSDs for Case 3.

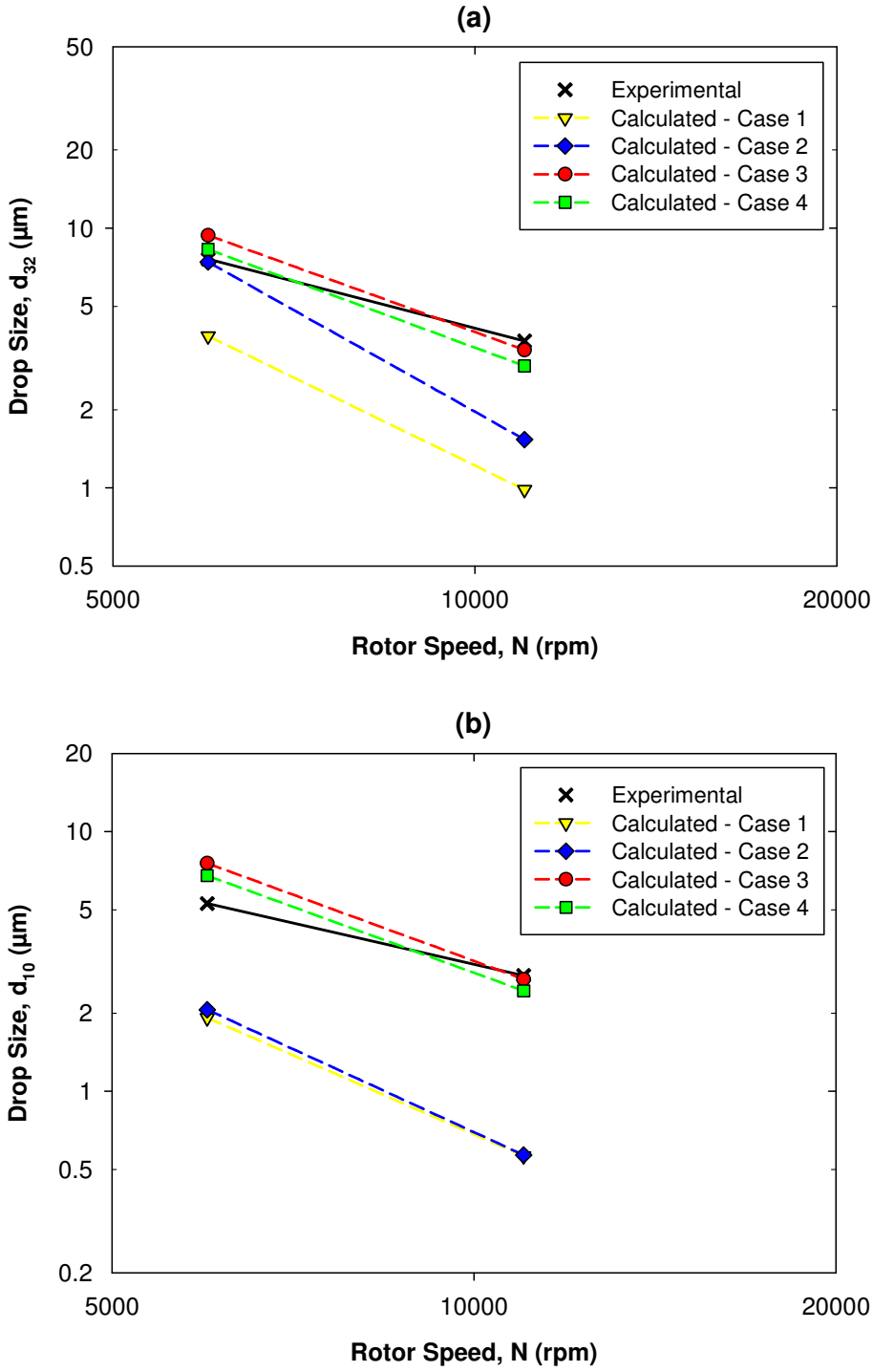

Figure 6.24: Calculated and experimental (a) Sauter mean drop diameters and (b) Number mean drop diameters, for 1% 9.4 mPa·s silicone oil emulsions, at rotor speeds of 6,000 rpm and 11,000 rpm. Calculated drop sizes from the multi-fractal turbulence breakage kernel for four cases.

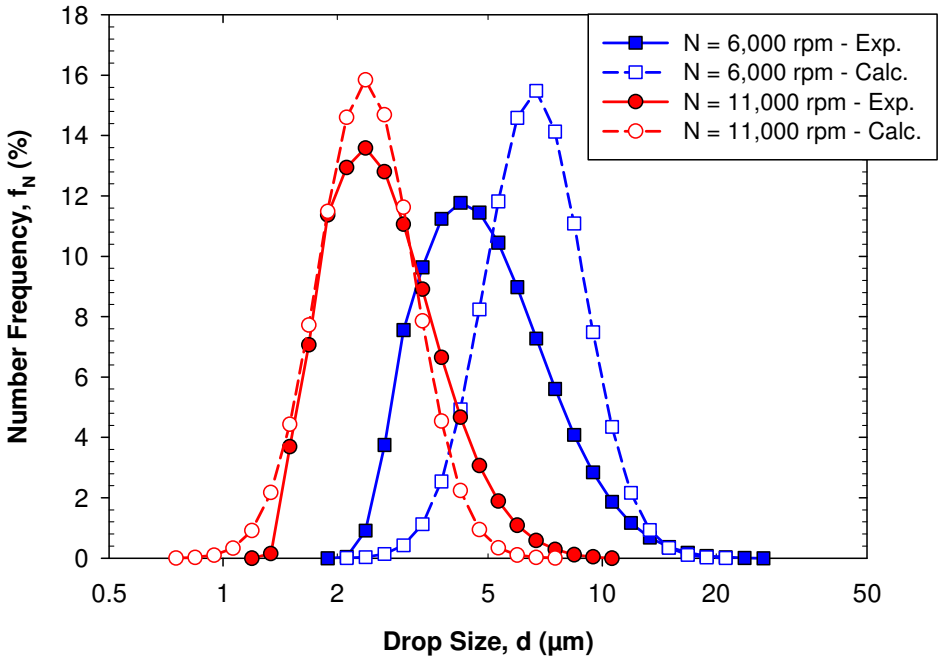

Figure 6.25: Calculated and experimental number drop size distributions, for 1% 9.4 mPa·s silicone oil emulsions, at rotor speeds of 6,000 rpm and 11,000 rpm. Calculated drop sizes from the multi-fractal turbulence breakage kernel for Case 3.

Drop size distributions were reconstructed from the first three moments using a log-normal distribution function, see Appendix C.3. Figure 6.25 shows reasonable agreement between experimental and calculated DSDs, particularly at higher rotor speed. Figure 6.26 presents calculated Sauter mean drop sizes for Case 3 for a range of rotor speeds. This figure shows good agreement, although the trends with rotor speed differ slightly. Further work is required to fully validate the selection of the adjustable constants and fragmentation distribution function, and extend the models to other process and formulation conditions, including multiple passes. Nevertheless, these results demonstrate that QMOM can be applied to solve population balance models in rotor-stator mixers.

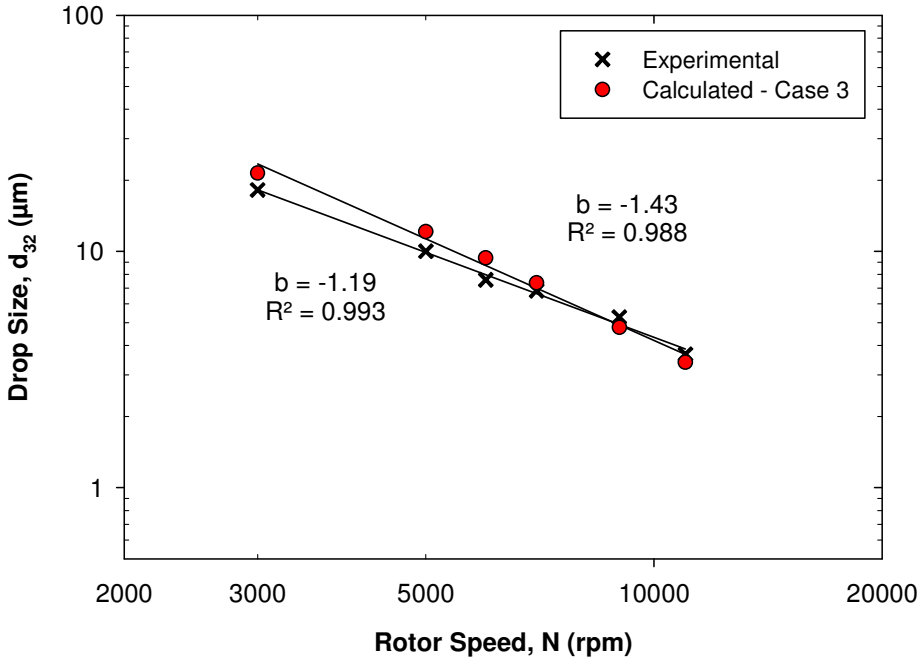

Figure 6.26: Calculated and experimental Sauter mean drop diameters for 1% 9.4 mPa·s silicone oil emulsions, as a function of rotor speed. Calculated drop sizes are from the multi-fractal turbulence breakage kernel for Case 3.

This study indicates the difficulty in solving population balance models as selection of the correct breakage model, adjustable constants and fragmentation distribution function are necessary, and the application of population balance equations was summarised by Maass and Kraume (2012), as being limited due to an increasing number of contradicting models, with the fitting of model parameters still a major challenge.

6.11 Summary

The effect of recirculation flow rate on droplet break-up is small for multiple pass systems. The effect of number of passes is most important for low viscosity oils, especially for high rotor speeds when droplet size falls below the Kolmogorov length scale. DSDs in a mixing vessel in a recirculation loop with a rotor-stator mixer were predicted. Calculated DSDs from population balance models gave reasonable agreement with experimental DSDs.

CHAPTER 7. SCALING UP OF IN-LINE SILVERSON ROTOR-STATOR MIXERS

7.1 Introduction

In collaboration with Silverson Machines Ltd., emulsification in three geometrically similar in-line rotor-stator mixers of different sizes was investigated from the lab to the factory scale. Experimental mean drop sizes at three scales were correlated with different scaling rules and the results are discussed, including the effect of number of passes and residence time on the scaling rules. Furthermore, the effect of interfacial tension on drop size was investigated using ethanol continuous phases, and by employing different surfactant concentrations, since interfacial tension is an important parameter in droplet break-up. Part of this work has been published in:

- Hall, S., Cooke, M., Pacek, A. W., Kowalski, A. J., and Rothman, D., (2011). "Scaling Up of Silverson Rotor-Stator Mixers", *The Canadian Journal of Chemical Engineering*, **89(5)**, 1040-1050.

7.2 Single pass emulsification

The effects of the mixer scale, dispersed phase viscosity and rotor tip speed (10 and 20 m s^{-1}), on drop size distributions are summarised in Figure 7.1. For low viscosity oil at the higher tip speed (20 m s^{-1}), drop size distributions were practically log-normal (Figure 7.1a) with a (log-normal) span of 1.6 to 1.8 for all three mixers. At the lower tip speed of 10 m s^{-1}, a

tail appeared on the left of the DSD containing a small volume of small drops, and as a result, span increased slightly (~ 1.85).

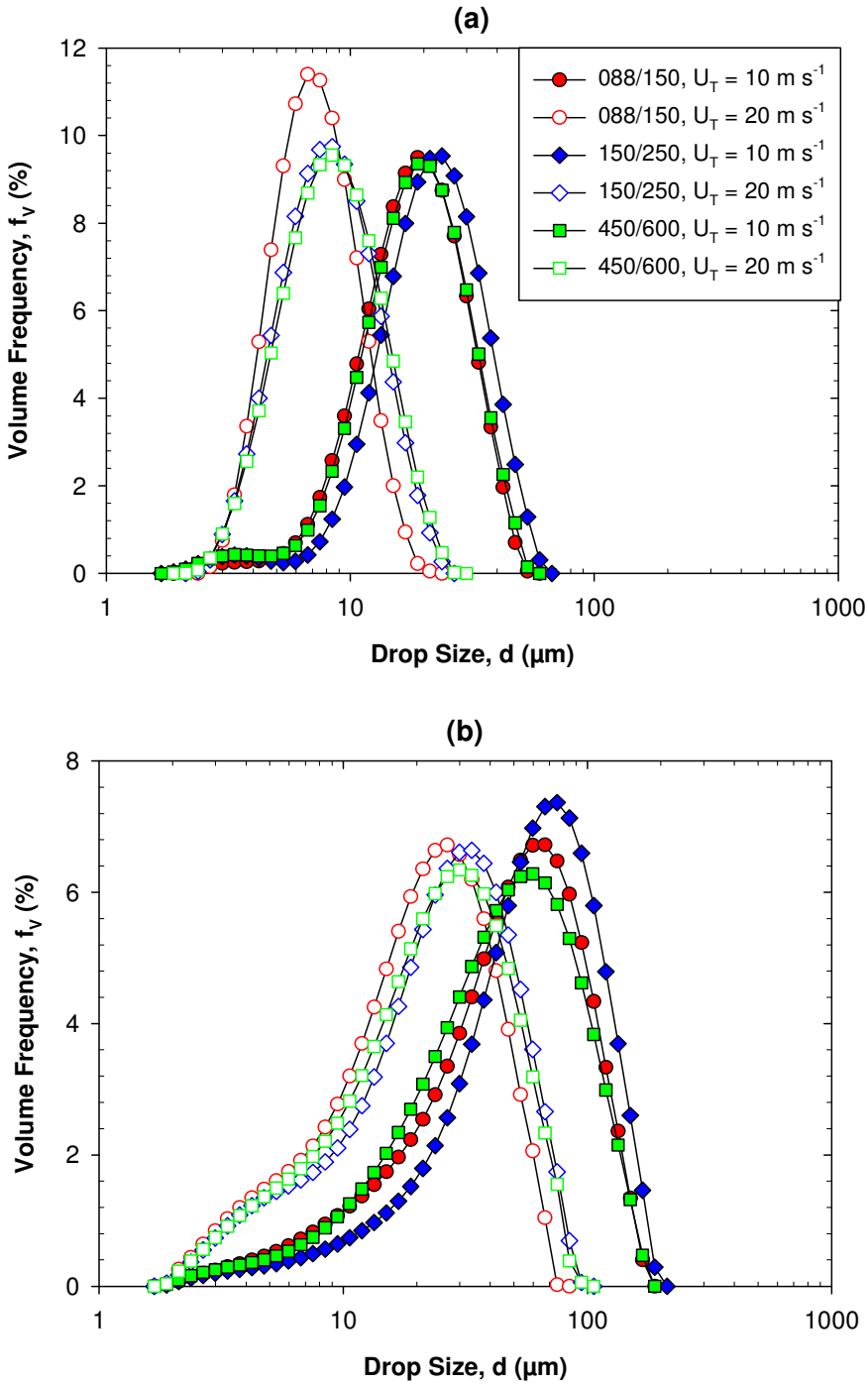

Figure 7.1: Volume drop size distributions at tip speeds of 10 and 20 m s^{-1} for three mixer scales for 1% (a) 9.4 mPa·s and (b) 339 mPa·s silicone oil emulsions at a constant residence time of 0.45 s.

As expected, the volume of oil in the smaller drops reduced at the lower tip speed; however the DSDs were very much the same shape for all scales, with skewness close to zero (-0.09 to 0.02). The tail may indicate a decrease in efficiency of droplet disruption at low tip speeds.

The high viscosity oil drop size distributions at each scale were again rather similar; however they were not log-normal but strongly skewed towards smaller drops (Figure 7.1b). At the higher tip speed (20 m s^{-1}), span was higher than for the low viscosity oil at 2.7 to 2.9, and at 10 m s^{-1}, span was similar at 2.5 to 2.8. The presence of some smaller drops forms a long tail towards small drop sizes, resulting in a negative skewness of -0.19 to -0.28 at all scales.

Table 7.1: Span and skewness of the DSDs in Figure 7.1 at three mixer scales, two tip speeds and two dispersed phase viscosities.

Scale	**Span, w (-)**			**Skewness, s (-)**		
	088/150	**150/250**	**450/600**	**088/150**	**150/250**	**450/600**
μ_d = 9.4 mPa·s, U_T = 10 m s^{-1}	1.85	1.85	1.88	-0.080	-0.081	-0.090
μ_d = 9.4 mPa·s, U_T = 20 m s^{-1}	1.64	1.78	1.81	0.017	-0.008	-0.015
μ_d = 339 mPa·s, U_T = 10 m s^{-1}	2.82	2.54	2.73	-0.280	-0.262	-0.187
μ_d = 339 mPa·s, U_T = 20 m s^{-1}	2.71	2.88	2.85	-0.246	-0.281	-0.240

In general, these figures show very good agreement in the shape of the distributions between the scales, and as expected, smaller drops are produced in dispersion of the lower viscosity oil. It is also worth noticing that the maximum drop size at all scales (for a given tip speed and viscosity) are very similar, indicating that drop breakage mechanisms are also

similar. Similarity in the shape, span, and skewness of the DSDs with no systematic trends with scale, indicates that a constant tip speed and residence time should be used for scale-up.

7.2.1 Drop size correlations

In this section, single pass drop sizes at three scales are analysed. Hence, for direct comparison of the DSDs produced at different scales, the flow rates at each scale were selected so that the mean residence times (t_R) in each mixer were equal. Therefore, Sauter mean diameters were correlated with energy dissipation rate, rotor energy dissipation rate, tip speed and Weber number, and the accuracy of these correlations is analysed below. The experimental results are compared by fitting regressions to the drop size data, where the exponents, constants and quality of fit indicators are summarised in Table 7.2.

7.2.1.1 Energy dissipation rate

One of the parameters commonly used for scale-up is energy dissipation rate. For in-line rotor-stator mixers, mean energy dissipation rate (ε) can be calculated either from total power draw (Eq. (2.21)) where both the energy from the rotor and the flow are accounted for, or from the rotor power draw only (Eq. (2.19)), to give the rotor energy dissipation rate (ε_T). The power constants (Po_z and k_1) used to calculate power consumption in Eqs. (2.19) and (2.21) are taken from Table 4.2.

In Figure 7.2, Sauter mean diameters of both oils in all the mixers are shown as a function of energy dissipation rate (Figure 7.2a) and rotor energy dissipation rate (Figure 7.2b). All measurements were undertaken at the same average residence time of 0.45 s. Figure 7.2a shows that Sauter mean diameters measured at three scales do not fall onto two straight lines particularly well for either viscosity, with a slope of -0.33 for high viscosity oil and -0.39 for low viscosity oil.

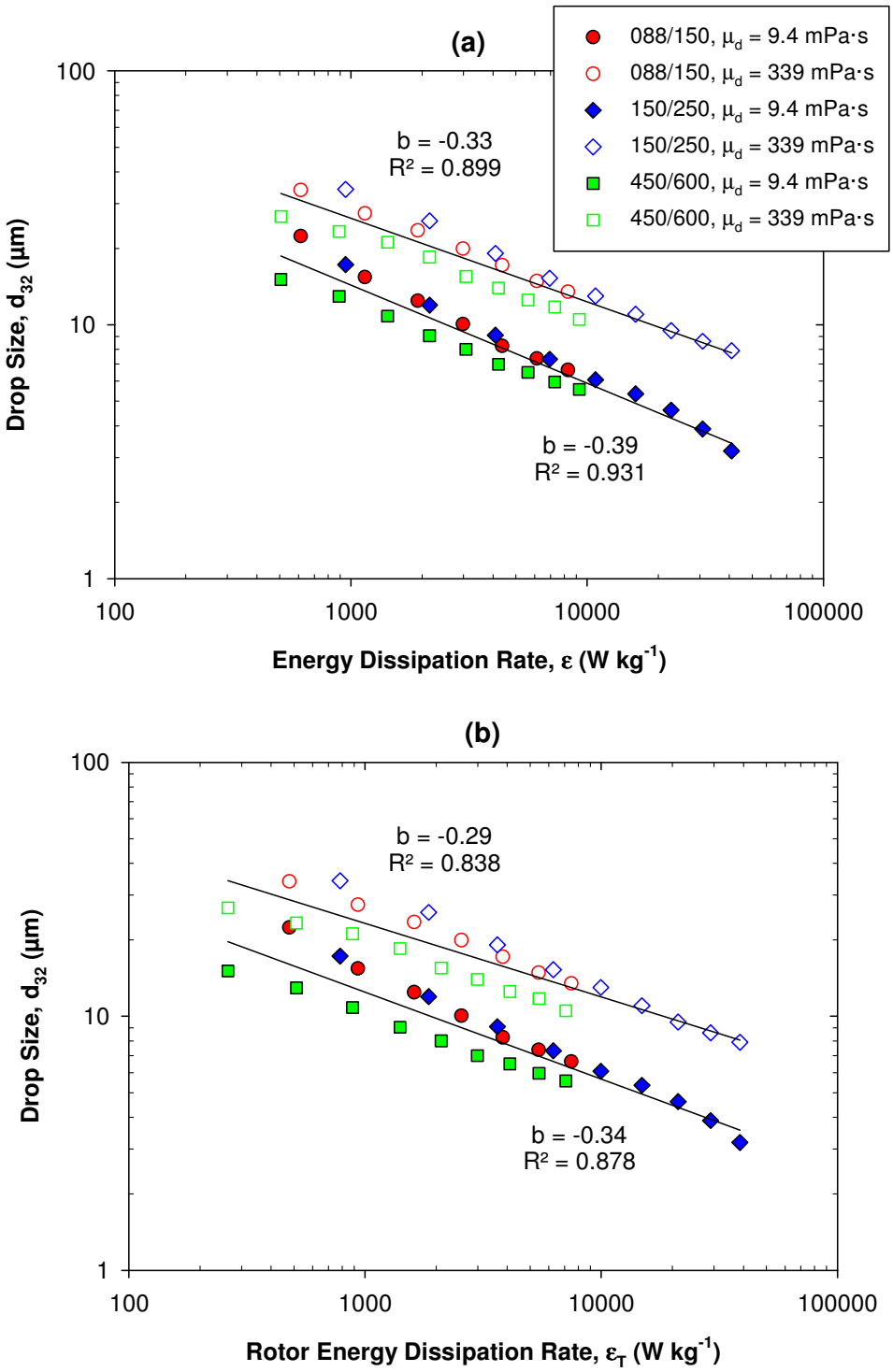

Figure 7.2: Mean drop size for 1% 9.4 and 339 mPa·s silicone oil emulsions as a function of (a) total energy dissipation rate and (b) rotor energy dissipation rate at three mixer scales, at a constant residence time of 0.45 s.

The marginal difference in the gradients indicates that all drops (at each viscosity and scale) are broken by similar mechanisms, primarily by turbulent inertial forces. The substantial differences in the intercepts (constant A) for each viscosity shows that breakage of low viscosity drops requires less energy than breakage of high viscosity drops. As the coefficients of determination are 0.899 (high μ_d) and 0.931 (low μ_d) (Table 7.2), it appears that energy dissipation rate does not correlate the data particularly well at different scales. Kamiya et al. (2010c) also used total energy dissipation rate to correlate a pilot plant and a production scale rotor-stator mixer, and reported a similar correlation of R^2 = 0.91.

Defining energy dissipation rate solely on the rotor torque power term ($P_T = Po\rho N^3 D^5$) means rotor energy dissipation rate is independent of flow rate. In addition, Figure 5.5 illustrates that the effect of flow rate on Sauter mean diameter is weak, thus the energy from the flow may not strongly influence drop break-up. Figure 7.2b shows the correlation of drop size with rotor energy dissipation rate, with constants and exponents in Table 7.2. For this correlation, the fits are slightly worse than for energy dissipation rate, with correlation coefficients of 0.838 (high μ_d) and 0.878 (low μ_d) (Table 7.2). Based on this analysis, defining energy dissipation rate using both power terms from Eq. (2.21) is preferable, and only total energy dissipation rate was considered in further analysis. Correlation of mean drop size with energy dissipation rate based solely on the flow power term ($P_F = k_1 MN^2 D^2$) is given in Table 7.2 for information.

The exponents on ε range from -0.33 to -0.47, which are close to -0.4, indicating that turbulent inertial forces are important for droplet breakage. For each viscosity, the exponents at the largest scale (~ -0.35), suggest inertial forces in the viscous sub-range may be important with an exponent close to -0.33 in Eq. (2.62). However, η_K ranges from 3 to 6 µm, indicating that droplets are in the inertial sub-range of turbulence at all scales.

Table 7.2: Results of regressions for d_{32} with scale-up terms (d_{32}/D with We) for two viscosities at three mixer scales at a constant residence time of 0.45s.

	Separate correlations						**Results from regression**			
	b			***A***						
	088/150	**150/250**	**450/600**	**088/150**	**150/250**	**450/600**	***b***	***A***	R^2	σ_{rms} (%)
9.4 mPa·s										
ε	-0.47	-0.43	-0.36	421	330	141	-0.39	207	0.931	14.3
ε_T	-0.44	-0.42	-0.32	325	277	89	-0.34	132	0.878	16.8
ε_F	-0.66	-0.62	-0.47	552	421	207	-0.55	300	0.900	23.5
U_T	-1.32	-1.25	-0.94	334	305	131	-1.13	212	0.974	8.1
We	-0.66	-0.62	-0.47	0.45	0.27	0.03	-0.70	0.63	0.956	18.9
339 mPa·s										
ε	-0.36	-0.40	-0.33	345	530	219	-0.33	255	0.899	17.4
ε_T	-0.34	-0.39	-0.29	282	450	144	-0.29	172	0.838	17.2
ε_F	-0.51	-0.58	-0.44	425	665	312	-0.49	393	0.933	27.9
U_T	-1.02	-1.16	-0.87	288	493	204	-0.98	273	0.971	7.6
We	-0.51	-0.58	-0.44	0.16	0.33	0.03	-0.66	0.76	0.922	25.9

7.2.1.2 Tip speed and Weber number

The effect of tip speed on Sauter mean diameter of emulsions shown in Figure 7.3 indicates that at the same dispersed phase viscosity, Sauter mean diameters measured at three different scales fall in one line on logarithmic coordinates. For high viscosity oil, b = -0.98 (R^2 = 0.971), and for low viscosity oil, b = -1.13 (R^2 = 0.974), which indicates that tip speed can be treated as a good scaling parameter. Tip speed was a good correlating parameter for dispersion/emulsification processes in stirred vessels (El-Hamouz et al., 2009).

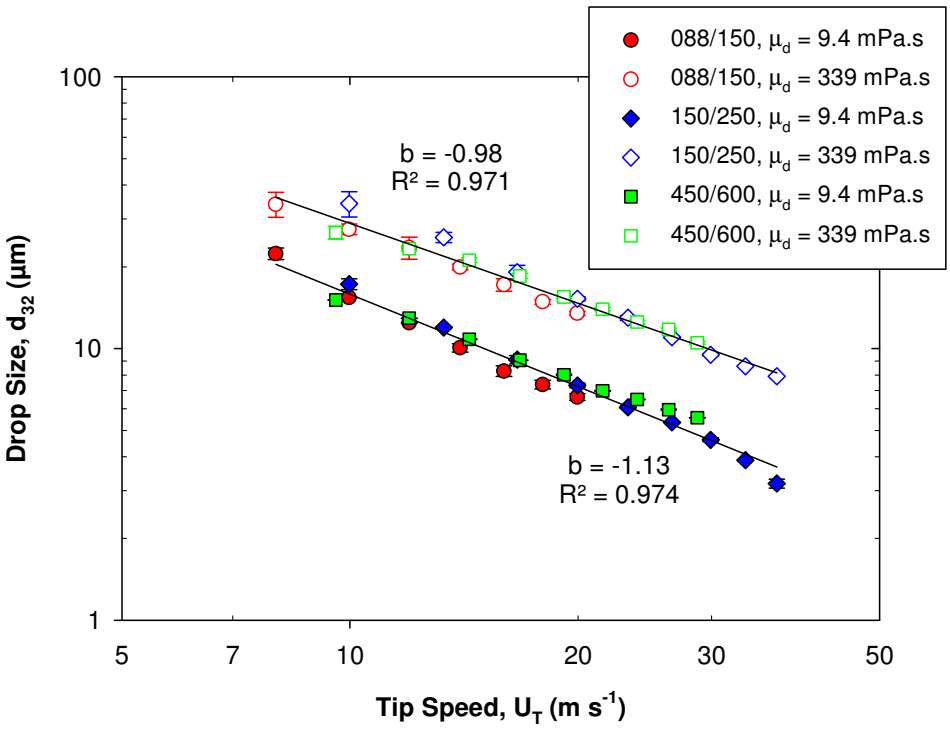

Figure 7.3: Mean drop size for 1% 9.4 and 339 mPa·s silicone oil emulsions as a function of tip speed at three mixer scales, at a constant residence time of 0.45 s with standard deviation error bars.

Dimensionless drop size as a function of Weber number (Figure 7.4) gives a slightly weaker fit than tip speed, with R^2 = 0.956 for low viscosity oil and R^2 = 0.922 for high viscosity oil. This is expected as Weber number is related to energy dissipation rate at constant Po. Figure 7.4 shows that mean drop sizes from the small and intermediate scale mixers correlate better with Weber number than the largest mixer scale. To compare the correlation constants with literature, the data for the laboratory scale (088/150) and pilot plant scale (150/250) mixers were combined and a regression undertaken to obtain separate correlations for 9.4 and 339 mPa·s viscosity oils:

$$\frac{d_{32}}{D} = 0.29We^{-0.58} \quad \text{for 339 mPa·s} \tag{7.1}$$

$$\frac{d_{32}}{D} = 0.41We^{-0.66} \quad \text{for 9.4 mPa·s} \tag{7.2}$$

These correlations have excellent fits with $R^2 > 0.996$ and compare well with findings by El-Hamouz et al. (2009), who investigated the same silicone oil-in-water and surfactant systems in a stirred tank. El-Hamouz et al. (2009) found a greater exponent of -0.64 for 32.2 mPa·s oil which fell to -0.60 at a higher viscosity of 242 mPa·s oil, which is consistent with this study as b = -0.66 for low viscosity oil (9.4 mPa·s) and b = -0.58 for high viscosity oil (339 mPa·s). This reduction in the exponents is due to larger cohesive viscous forces resisting droplet deformation at higher oil viscosities. The exponents of -0.58 and -0.66 are statistically different as the 95% confidence intervals for each exponent value do not overlap; -0.56 to -0.60 (339 mPa·s) and -0.63 to -0.68 (9.4 mPa·s). El-Hamouz et al. (2009) found the constant A to be 0.18-0.19, compared to 0.29 and 0.41 in this work, while Calabrese et al. (2000) for a batch rotor-stator mixer found a constant an order of magnitude lower at 0.040, similar to Chen and Middleman (1967) for liquid-liquid dispersion in a stirred vessel.

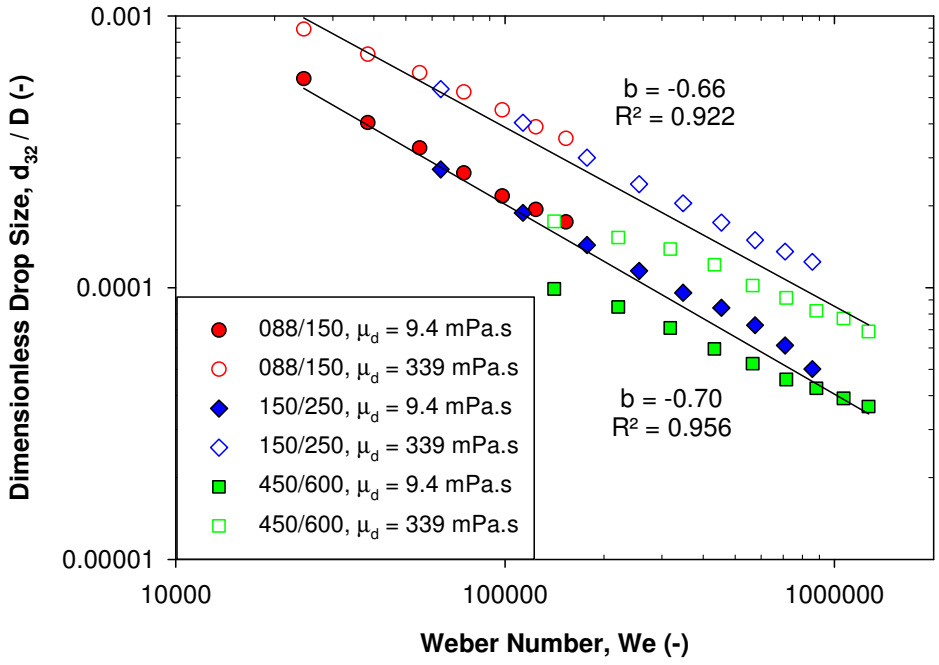

Figure 7.4: Dimensionless drop size for 1% 9.4 and 339 mPa·s silicone oil emulsions as a function of Weber number at three mixer scales, at a constant residence time of 0.45 s.

Tip speed is a scaling term commonly applied for geometrically similar systems, and based upon the coefficients of determination and root mean square values, the correlation of Sauter mean diameter and tip speed appears to be the most appropriate scaling parameter. The poorer applicability of energy dissipation rate as a scaling parameter and the variability in the exponents on ε in turbulent flow at different scales suggests that the Hinze theory cannot be completely applied to droplet break-up. The suitability of tip speed rather than energy dissipation rate suggests that droplet break-up is proportional to the velocity head in Eq. (2.2) and does not strongly depend on the circulating flow (Eq. (2.1)), and suggests that tip speed is a better approximation of the maximum shear rate (Hemrajani and Tatterson, 2004).

Table 7.3 shows the fits of mean drop size to various correlations in Table 2.2, for different droplet size ranges and mechanisms. The coefficient of determination and σ_{rms} values clearly suggest that inertial stresses are important for breakage. This is a sensible conclusion as the flow is turbulent and the drops are larger than η_K in all cases as the emulsion has only experienced a single pass. The correlation in Eq. (2.63) for inertial stresses for drops smaller than η_K gives the best fits, however as $\eta_K > d$ is not true and the gradients on ε are -0.4 (Figure 7.2a), turbulent inertial stresses for $L \gg d \gg \eta_K$ is the most likely mechanism. The similarity in the fits for all the inertial stress correlations suggests droplet breakage may not occur exclusively in one regime, since mean drop size is close to η_K.

Table 7.3: Results of regressions for d_{32} with correlations for two viscosities at three mixer scales, in the form $y=A.x$.

Range	Mechanism	Eq.	9.4 mPa·s			339 mPa·s		
			A	R^2	σ_{rms} (%)	A	R^2	σ_{rms} (%)
$L \gg d \gg \eta_K$	Inertial stresses $\mu_d \to 0$ $\tau_s \gg \tau_v$	2.52	1.226	0.954	18.9	1.314	0.914	25.9
$\eta_K > d$	Inertial stresses $\mu_d \to 0$ $\tau_s \gg \tau_v$	2.63	1.080	0.966	14.1	0.999	0.937	20.0
$\eta_K \gg d$	Inertial stresses $\mu_d \to 0$ $\tau_s \gg \tau_v$	2.66	0.995	0.933	18.7	0.920	0.912	21.9
$\eta_K > d$	Viscous stresses $\mu_d \to 0$ $\tau_s \gg \tau_v$	2.68	1.535	0.632	59.2	1.420	0.594	63.8

7.2.2 Flow rate and residence time

The effect of flow rate on Sauter mean diameter of emulsions at different scales (Figure 7.5) is rather weak, particularly for high viscosity oils, as observed in Figure 5.5.

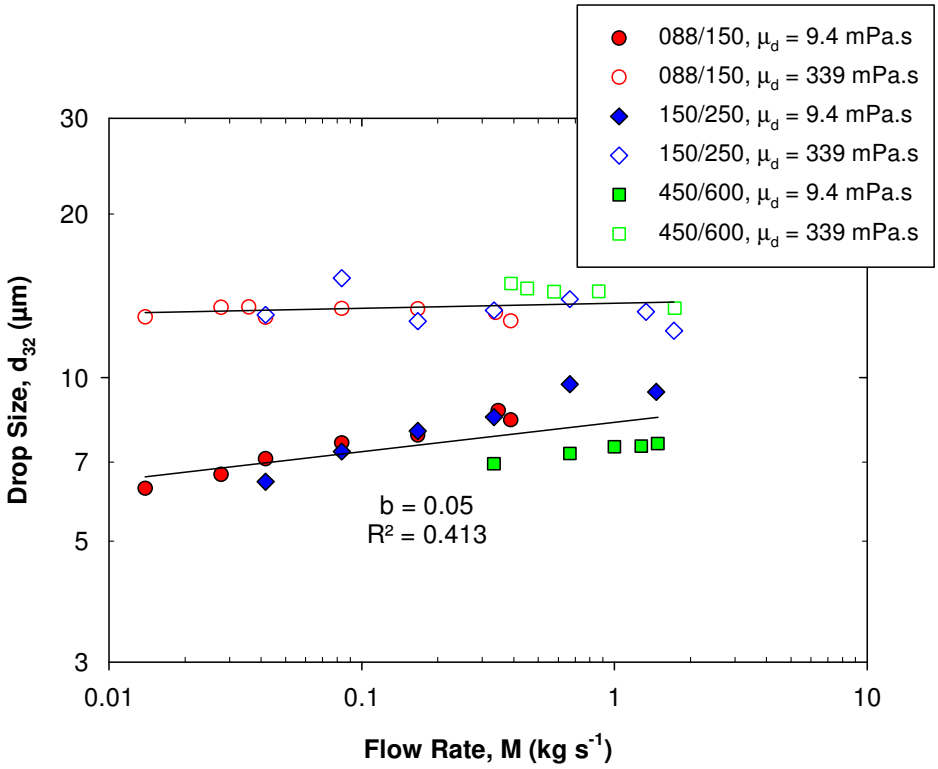

Figure 7.5: The effect of flow rate on mean drop size for 1% 9.4 and 339 mPa·s silicone oil emulsions, at a tip speed of 20 m s^{-1} at three mixer scales.

Figure 7.6 shows the Sauter mean diameters in Figure 7.5 plotted as a function of total residence time given by Eq. (6.3). For low viscosity oil, an improved fit is obtained compared to the correlation with flow rate in Figure 7.5. For high viscosity oil, since the effect of flow rate is small, there is little improvement correlating mean drop size with residence time. As expected, this figure confirms that total residence time in the mixing head helps correlate mean drop size across different scales.

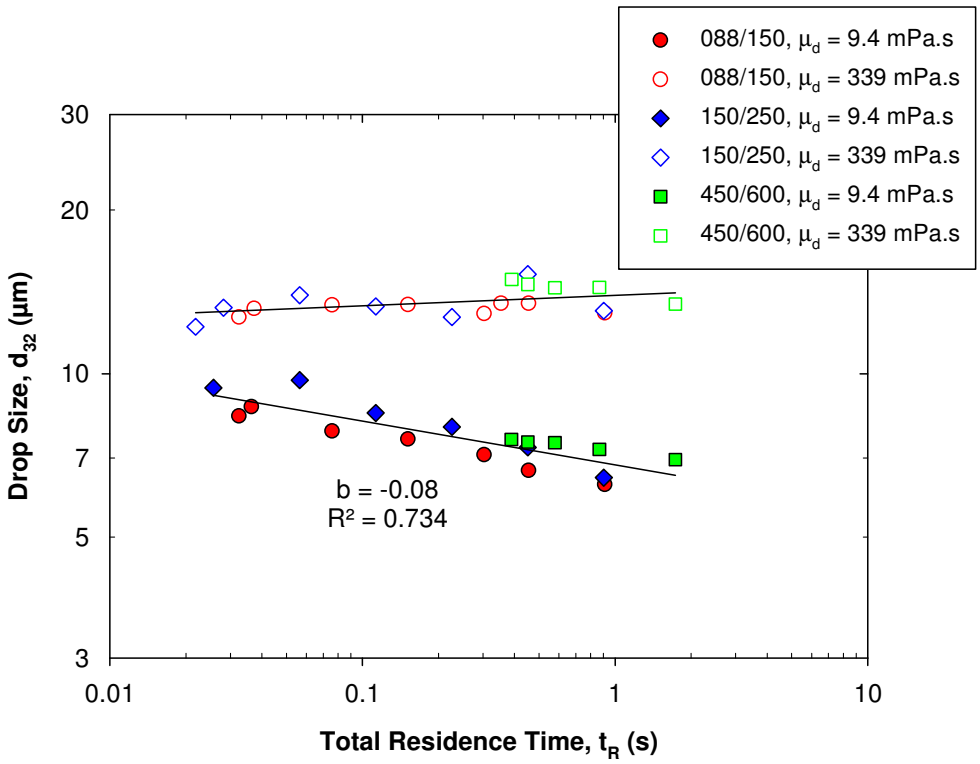

Figure 7.6: The effect of total residence time on mean drop size for 1% 9.4 and 339 mPa·s silicone oil emulsions, at a tip speed of 20 m s^{-1} at three mixer scales.

7.3 Multiple pass emulsification

The effect of number of batch turnovers (1 and 40) and mixer scale on drop size distributions from the mixer outlet are summarised in Figure 7.7, for emulsions of 9.4 mPa·s oil at a tip speed of 20 m s^{-1} ('single condition' recirculation method). For one batch turnover, DSDs were practically log-normal with span ~ 1.8 for all three mixer scales (Table 7.4). After 40 batch turnovers, as expected, the volume of oil contained in small droplets increased, and span reduced to ~ 1.4.

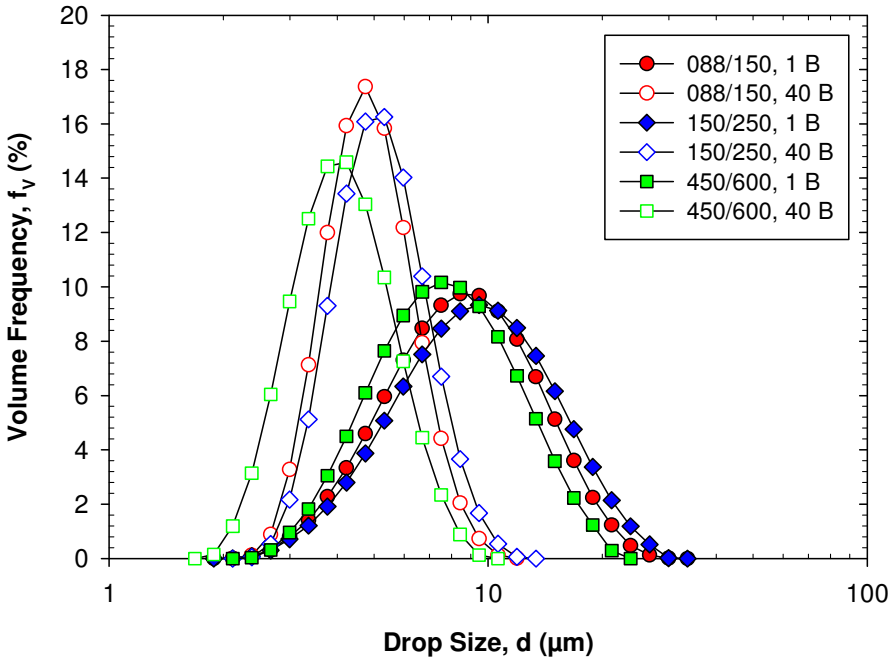

Figure 7.7: Drop size distributions for three mixer scales after 1 and 40 batch turnovers, at a tip speed of 20 m s^{-1} for 1% 9.4 mPa·s silicone oil emulsions. Residence time (τ) per pass at each scale are: laboratory scale (088/150) = 0.0757 s; pilot plant scale (150/250) = 0.0586 s; factory scale (450/600) = 0.8661 s.

Table 7.4: Span and skewness of the drop size distributions at three different scales, for 1 and 40 batch turnovers for 1% 9.4 mPa·s silicone oil emulsions for the DSDs in Figure 7.7.

μ_d = 9.4 mPa·s	Span, w (-)			Skewness, s (-)		
Scale	**088/150**	**150/250**	**450/600**	**088/150**	**150/250**	**450/600**
1 batch turnover	1.79	1.84	1.74	-0.032	-0.036	-0.003
40 batch turnovers	1.39	1.42	1.47	0.039	0.034	0.025

Figure 7.7 shows very good agreement in the shape, span and skewness (Table 7.4) of the distributions between the scales for a given number of batch turnovers, where the maximum and minimum drop sizes are very similar. In Figure 7.7, at equal energy dissipation rates, smaller drops correspond to the larger scale and larger drops to the intermediate scale, which is attributed to the largest residence time (per pass) for the factory scale (450/600)

mixer (τ = 0.87 s), and the smallest for the pilot plant scale (150/250) mixer (τ = 0.06 s). Residence time can be accounted for in correlations to enable data at single passes at different flow rates, and multiple passes to be correlated using the same expression, see Section 7.3.2.

7.3.1 Drop size correlations

The effect of multiple passes was investigated at given time points at several rotor speeds at a single flow rate using the 'step-wise' recirculation method. Sauter mean diameter correlations with energy dissipation rate and energy density (Figure 7.8), and tip speed (Figure 7.9), after 40 batch turnovers for 9.4 mPa·s silicone oil emulsions are presented. Lower viscosity oil was selected as this is more sensitive to multiple passes (see Section 6.5), and shows the differences more clearly.

Figure 7.8 shows that Sauter mean diameters measured at three scales do not correlate well with energy dissipation rate (R^2 = 0.553), or energy density (R^2 = 0.764). This is particularly true at the largest scale, and supports the findings from Section 7.2.1 for single passes, that energy dissipation rate or energy density alone are not suitable scaling parameters over a wide range of scales.

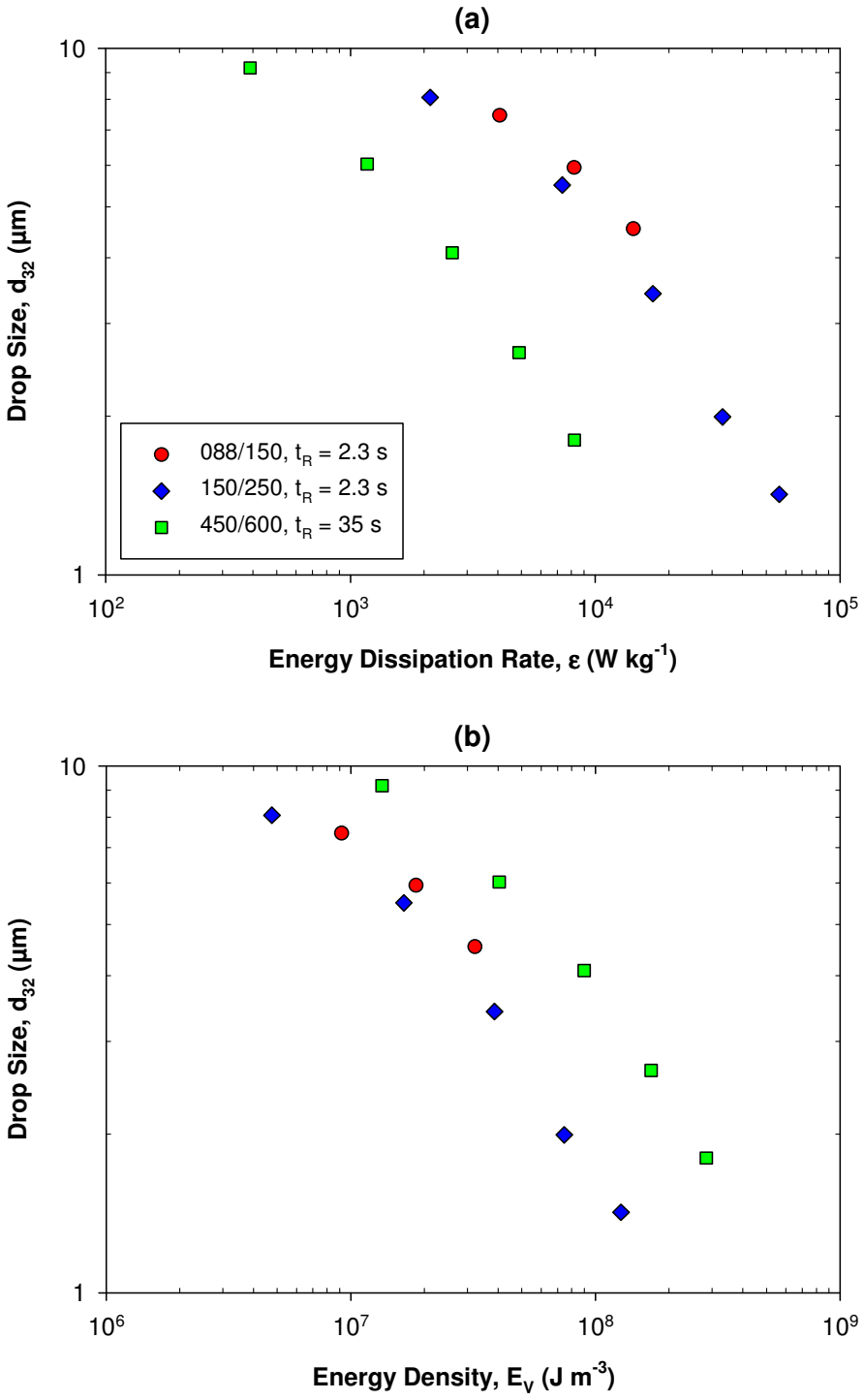

Figure 7.8: Mean drop size as a function of (a) energy dissipation rate and (b) energy density for 1% 9.4 mPa·s silicone oil emulsions at three mixer scales after 40 batch turnovers.

Figure 7.9 shows Sauter mean diameter as a function of tip speed measured at three scales, gives a good fit (R^2 of 0.949), which together with Figure 7.3 suggests that tip speed is the best scaling parameter for both single and multiple passes.

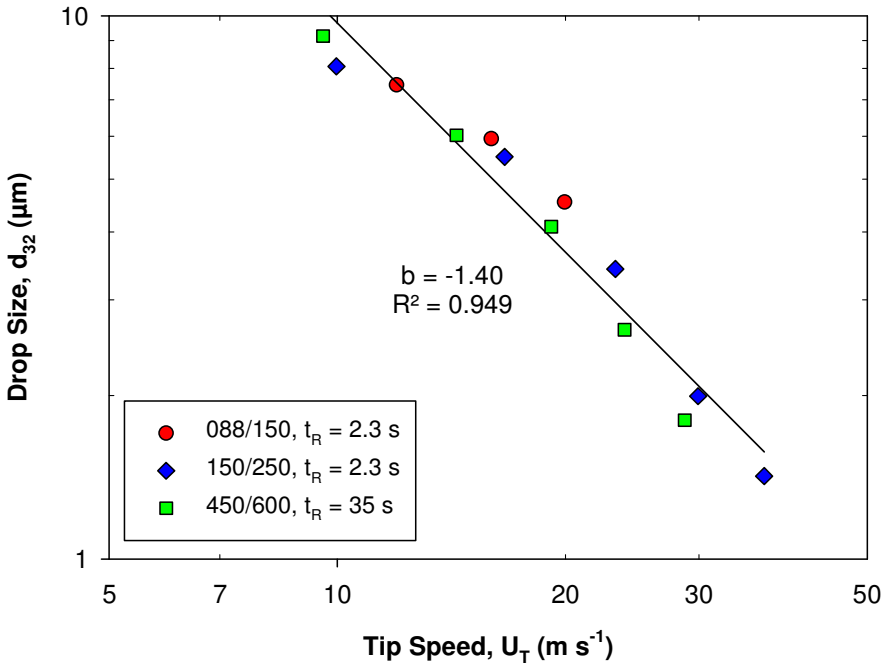

Figure 7.9: Mean drop size as a function of tip speed for 1% 9.4 mPa·s silicone oil emulsions at three mixer scales after 40 batch turnovers.

In Figure 7.8 and Figure 7.9, the number of batch turnovers at each scale was constant at 40, however total residence time (t_R) is greater at the largest scale at 35 s, compared to 2.3 s at the other scales. A higher flow rate of ~ 36,000 kg h^{-1} was required through the factory scale (450/600) mixer to match t_R with the other scales, which could not be achieved using the rig arrangement. However, Figure 7.9 confirms the results of Figure 7.6 that the effect of t_R on Sauter mean diameter is marginal as drop sizes from the factory scale (450/600) mixer are only slightly smaller than the other mixers.

The effect of number of batch turnovers at each scale was also assessed by investigating a single rotor speed and flow rate ('single condition' recirculation method). Figure 7.10 compares the effect of scale on mean droplet size using energy density in Eq. (6.5) and shows that at constant tip speed, energy density correlates drop sizes formed at different residence times, and drop size reduction trends are roughly equal at each scale. However, once tip speed was changed (from 20 m s^{-1} to 37 m s^{-1} for the pilot plant scale 150/250 mixer), energy density does not correlate drop size, which implies that energy density cannot be used for correlation unless constant tip speed is maintained.

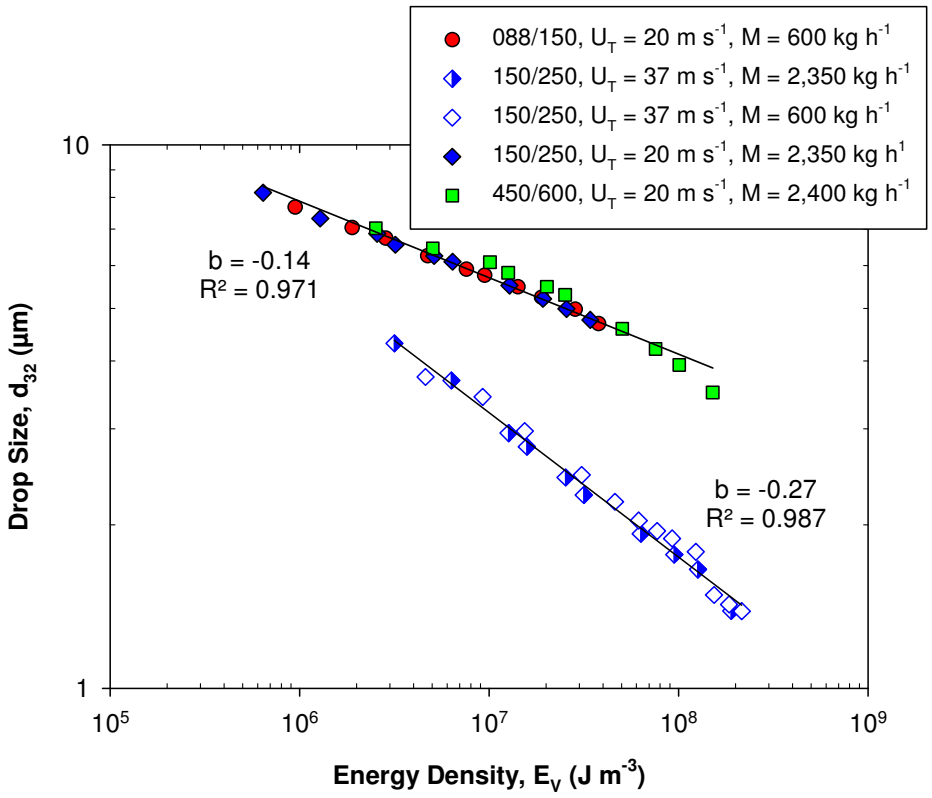

Figure 7.10: The effect of energy density on mean drop size for 1% 9.4 mPa·s silicone oil emulsions, at a tip speed of 20 m s^{-1} at three mixer scales and 37 m s^{-1} for the pilot plant scale 150/250 mixer at various flow rates.

7.3.2 Drop size and residence time correlations

Droplet size for continuous emulsification processes has been expressed in terms of energy density (Karbstein and Schubert, 1995):

$$d_{32} \propto {E_V}^{b1} \approx \left(\frac{P}{Q}\right)^{b2} \approx \Delta p^{b3} \tag{7.3}$$

Energy density is useful as it allows for comparison of many continuous flow devices using a single parameter, including high-pressure devices where droplet size is often related to the pressure drop across the nozzle (Δp). Essentially, Eq. (7.3) accounts for both energy dissipation rate (or power density) and total residence time in the mixing zone when the exponents on each parameter are similar (Jafari et al., 2008):

$$d_{32} = A.\varepsilon^x {t_R}^y \tag{7.4}$$

The poor correlations with energy density (Figure 7.8b and Figure 7.10) suggests the assumption that the exponents (x and y) in Eq. (7.4) are equal is not always correct and the specific relationship with each term can be found by decoupling the effects of energy dissipation rate and total residence time on drop size by fitting different exponents to each term. Therefore, the analysis below focuses on applying the correlation in Eq. (7.4), and comparing this expression with a similar correlation based on tip speed, as tip speed has proved to be the best correlating term:

$$d_{32} = A.{U_T}^x {t_R}^y \tag{7.5}$$

The correlations in Eqs. (7.4) and (7.5) each have a term to account for the intensity of the droplet deformation forces (how hard the drops are impacted) and a term to account for the duration of droplet deformation (how long the drops are impacted for).

Table 7.5 presents correlations of mean drop size with Eq. (7.4) and Eq. (7.5) for low and high viscosity dispersed phases. The correlations were examined using drop sizes measured at three scales, including single pass and multiple passes, containing about 200 data

points. Table 7.5 shows that each correlation provides a good relationship, with the higher viscosity oil correlating better with the tip speed based expression (R^2 of 0.944), than the energy dissipation rate based correlation (R^2 of 0.901). For the lower viscosity oil, there is less difference between the correlations, and larger σ_{rms} values due to a drift in the correlation at small drop sizes, see Figure 7.11 for the correlation in Eq. (7.4). This may be explained using the Kolmogorov theory, as for small drops there is a change in breakage mechanism to turbulent viscous stresses.

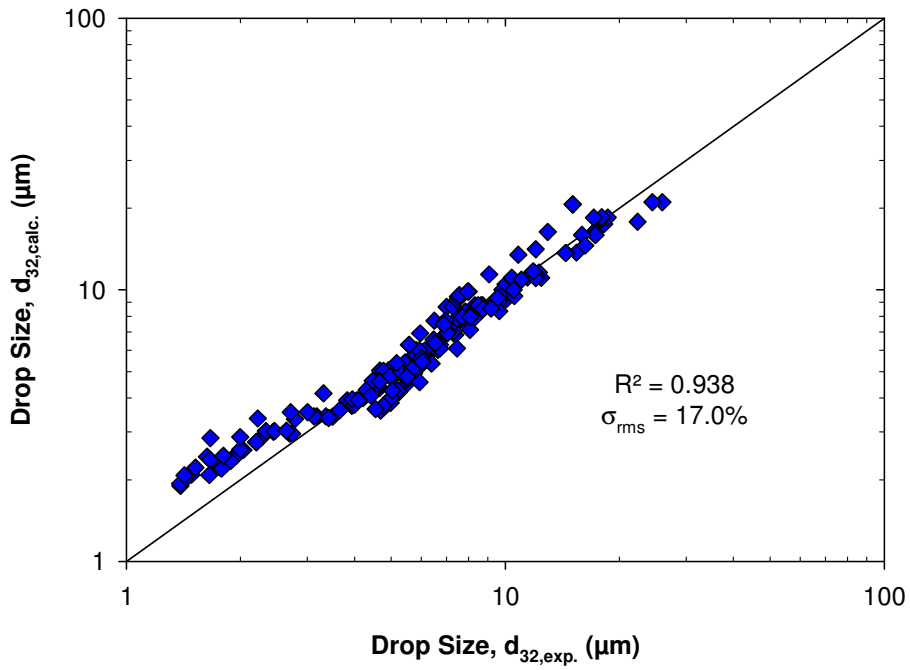

Figure 7.11: Quality of fit between mean drop size from the correlation presented by Eq. (7.4) with experimental mean drop size, for 1% 9.4 mPa·s silicone oil emulsions at three mixer scales.

Table 7.5: Constants, exponents and regression values in Eqs. (7.4) and (7.5) for 1% 9.4 and 339 mPa·s oil emulsions.

Dispersed Phase Viscosity, μ_d (mPa·s)	**Scale-Up Term**	A	x	y	R^2	σ_{rms} (%)
339	$\varepsilon^x t_R{}^y$	252	-0.327	-0.090	0.901	12.0
339	$U_T{}^x t_R{}^y$	233	-0.957	-0.043	0.944	8.3
9.4	$\varepsilon^x t_R{}^y$	219	-0.409	-0.228	0.938	17.0
9.4	$U_T{}^x t_R{}^y$	206	-1.190	-0.148	0.940	22.4

The key difference between the correlations for the two oil viscosities is the change in the exponent x (-1.19 and -0.96) on tip speed and (-0.41 and -0.33) on ε (Table 7.5). This follows that the higher oil viscosity is approaching the viscous limit in Eq. (2.56). Similarly, the exponent y for the higher viscosity oil is 60-70% below the lower viscosity oil exponent.

Overall, the correlations based on either tip speed or energy dissipation rate give a reasonable prediction of mean drop size when total residence time is included. However, y is greater for the correlation with ε than U_T, as y over compensates for the poorer applicability of ε as a scaling parameter, discussed in Section 7.3. For a constant rotor speed, a higher flow rate results in a greater power draw and hence a higher energy dissipation rate; however mean droplet size does not vary much with flow rate (Figure 7.5). Hence, a greater y value accounts for this to fit the data.

A comparison of batch and in-line rotor-stator mixers using Eq. (7.4) is presented in Appendix D.2.

The energy dissipation rate correlations in Table 7.5 are presented in Figure 7.12 on one set of axis, with the low viscosity oil data divided into two regions. Small low viscosity

drop sizes in Figure 7.11 are formed below the Kolmogorov length scale, hence separate correlations were fitted for drop sizes below 4 µm, with the constants and exponents given in Figure 7.12.

Once mean drop sizes for 9.4 mPa·s oil emulsions are separated, correlation of the larger drop sizes ($> \eta_K$) fit exactly with an exponent of -0.40 on energy dissipation rate, while the smaller drop sizes ($< \eta_K$) fit most appropriately with an exponent of -0.61. This adds further support to the fact that droplets below η_K correlate with an exponent of > 0.5 on ε. Furthermore, both x and y exponents increased by ~ 1.5 times for droplet break-up due to viscous stresses compared to inertial stresses, thus the rate of droplet break-up increased.

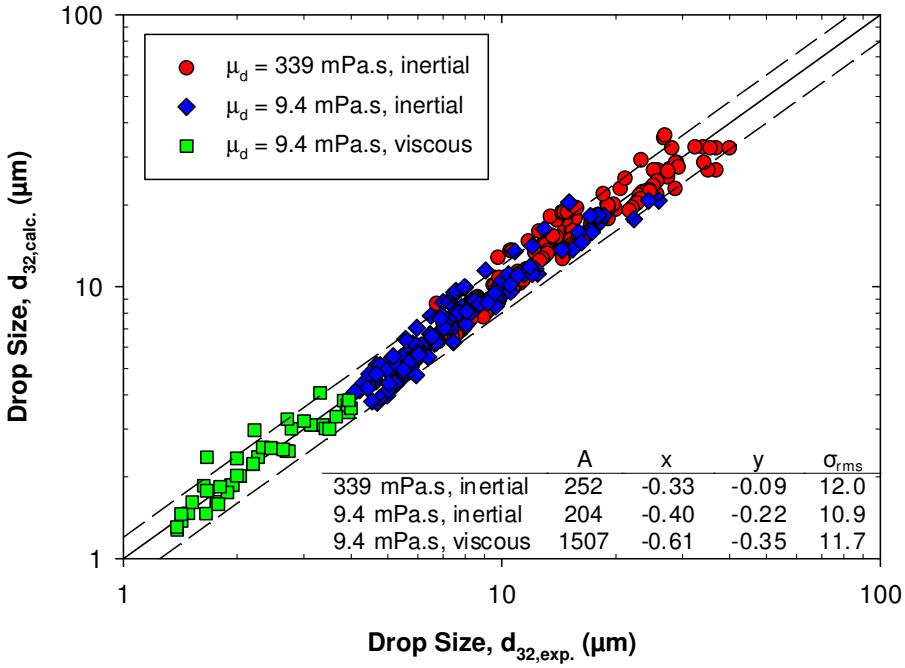

Figure 7.12: Quality of fit between mean drop size from the correlation presented by Eq. (7.4) with experimental mean drop size, for 1% 9.4 and 339 mPa·s silicone oil emulsions at three mixer scales, with 20% error lines.

7.4 Effect of interfacial tension on scale-up parameters

The interfacial tension between two immiscible liquid-liquid dispersed phases is an important parameter affecting emulsification scale-up. Interfacial tension is included in Weber number, so investigation of this physical property can further examine the applicability of Weber number as a scaling parameter. All experiments in this section were single passes through the 150/250 mixer.

7.4.1 Non-surfactant systems

The effect of interfacial tension on mean drop size of emulsions using three ethanol solutions is given in Figure 7.13. This figure shows smaller droplets were formed at a lower interfacial tension for both viscosities of silicone oil. This result is entirely expected as a lower interfacial tension reduces the surface force which resists droplet break-up. For both oil viscosities, mean drop sizes of emulsions for 27 and 18 mN m^{-1} began to converge at higher energy dissipation rates, which is mostly likely due to the coalescence of the smallest droplets formed, as stability against coalescence is reduced for low interfacial tension systems (Walstra, 2005). Sampling and emulsion stabilisation with surfactant occurs roughly 20 to 30 seconds after emulsion formation, hence coalescence may occur in this time.

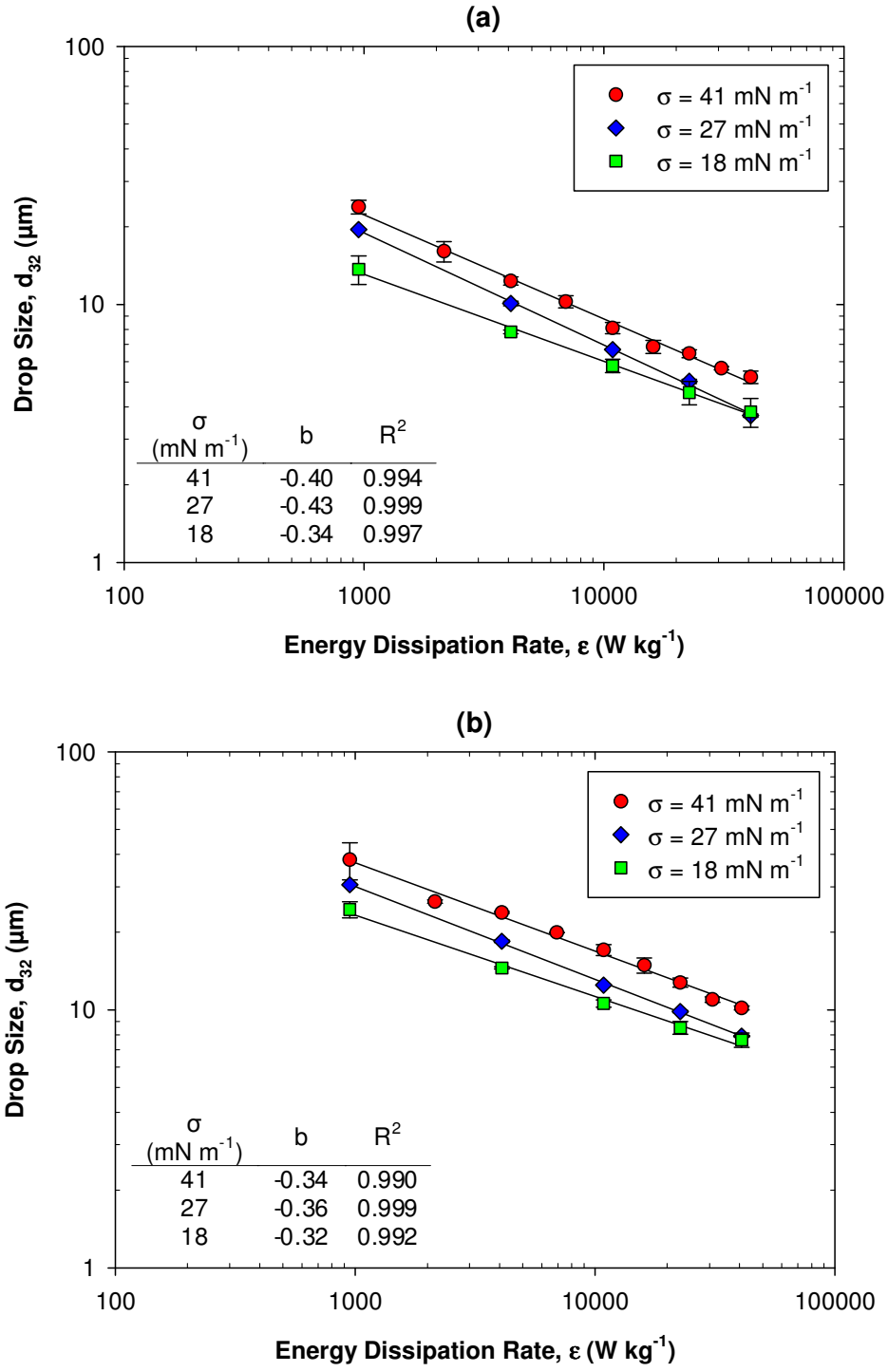

Figure 7.13: The effect of interfacial tension on mean drop size at different energy dissipation rates for 1% (a) 9.4 mPa·s and (b) 339 mPa·s silicone oil emulsions in the 150/250 mixer at 300 kg h^{-1} with standard deviation error bars.

The exponents on energy dissipation rate are close to -0.4 indicating turbulent inertial droplet break-up in all cases. As expected, the exponents are slightly lower for the high viscosity oil (see Section 5.7), also reported by Padron (2005).

For both viscosities, the gradients of the low interfacial tension mean drop sizes became slightly less shallow (-0.4 to -0.33), which is likely to be a slight coalescence effect rather than a change in the breakage mechanism. Padron (2005) found a shift from highly viscous behaviour towards inviscid behaviour as interfacial tension decreased since the exponent increased from -0.24 at 46 mN m^{-1} to -0.40 at 20 mN m^{-1}, which does not follow any mechanistic theories.

Mean drop sizes of emulsions in Figure 7.13 are correlated as a function of Weber number in Figure 7.14. This figure shows that Weber number can account well for the effect of interfacial tension for non-surfactant systems, collapsing interfacial tensions from 41 mN m^{-1} to 18 mN m^{-1} and continuous phase densities from 997 kg m^{-3} (0% EtOH) to 969 kg m^{-3} (20% EtOH) onto two lines corresponding to low and high dispersed phase viscosities. The exponents are slightly lower than the theoretical -0.6 for turbulent inertial break-up, which is particularly evident at higher Weber numbers for 18 mN m^{-1}. This suggests Weber number is suitable as a scaling parameter for interfacial tension.

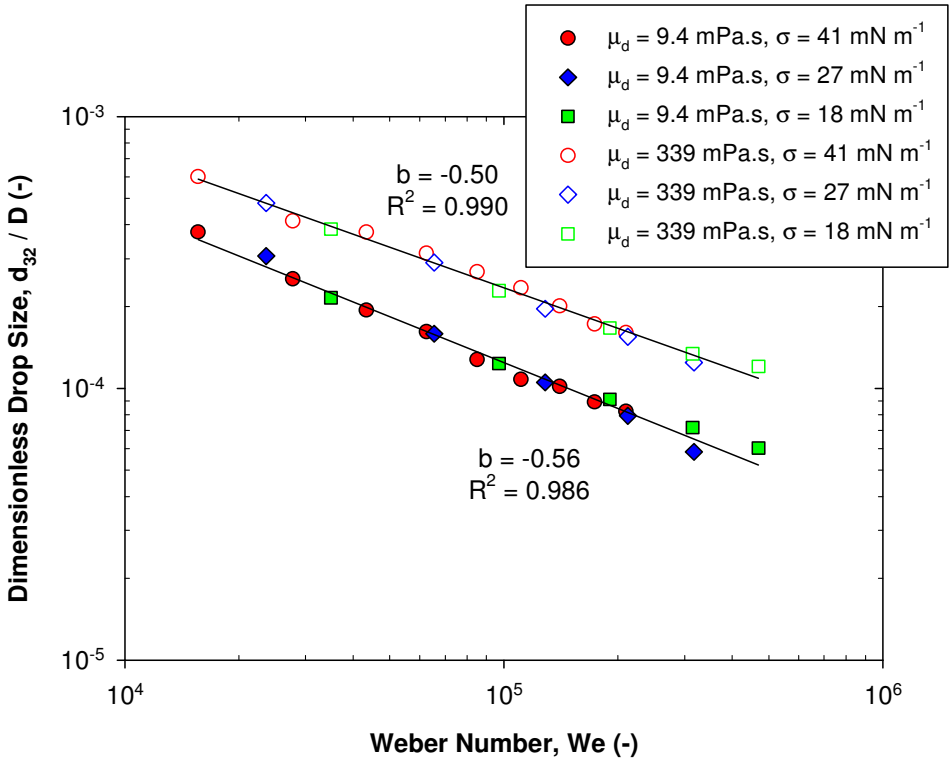

Figure 7.14: The effect of Weber number on dimensionless mean drop size at interfacial tensions of 41, 27 and 18 mN m^{-1}, for 1% 9.4 mPa·s and 339 mPa·s silicone oil emulsions in the 150/250 mixer at 300 kg h^{-1}.

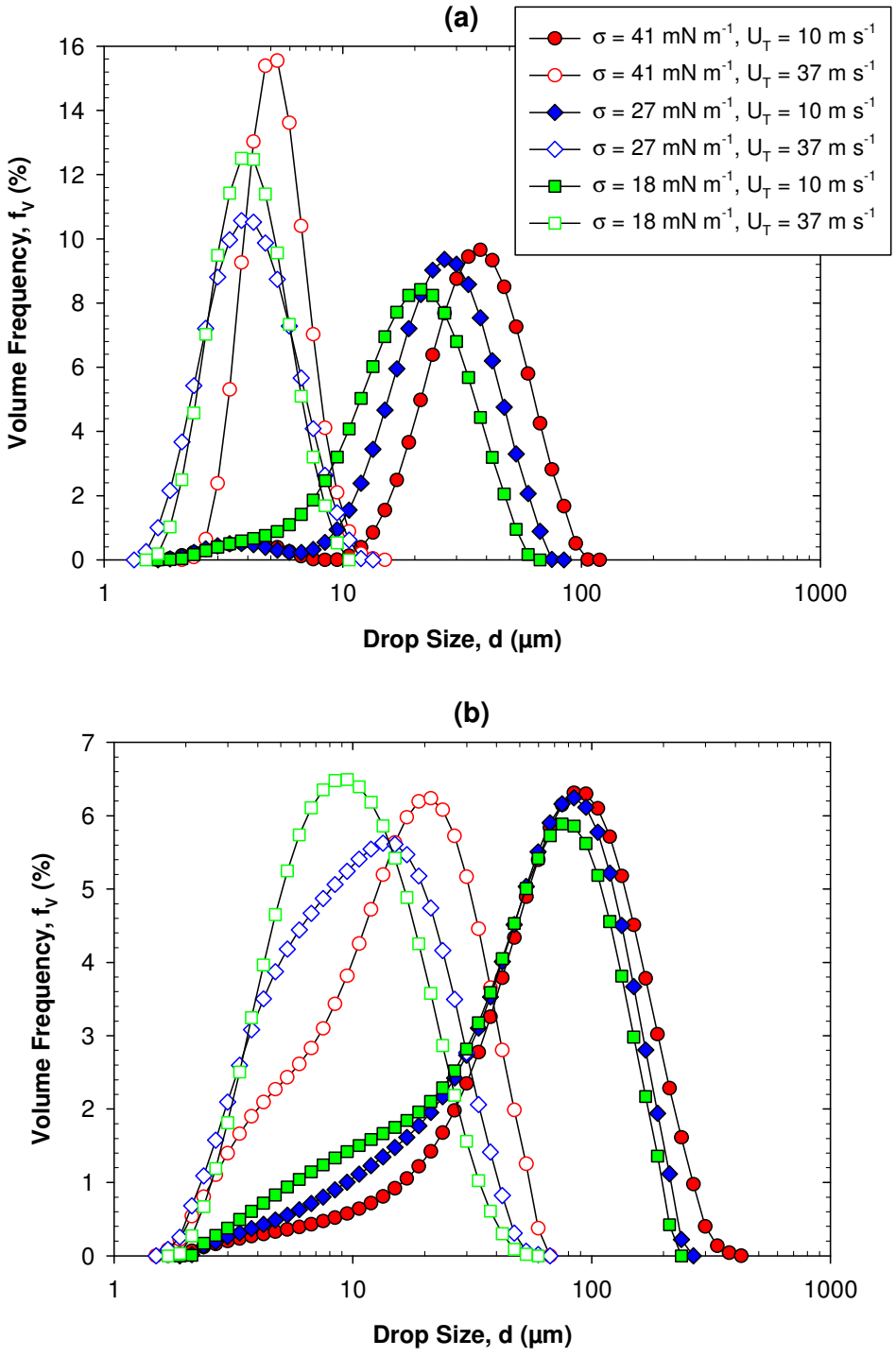

Figure 7.15: Volume drop size distributions for interfacial tensions of 41, 27 and 18 mN m^{-1}, at tip speeds of 10 and 37 m s^{-1} for 1% (a) 9.4 mPa·s and (b) 339 mPa·s silicone oil emulsions in the 150/250 mixer at 300 kg h^{-1}.

Figure 7.15a shows the effect of interfacial tension on DSDs at tip speeds of 10 and 37 m s^{-1} for 9.4 mPa·s silicone oil emulsions. Decreasing the interfacial tension clearly resulted in smaller droplets, while the shape of the distributions at each tip speed are similar. In addition at 37 m s^{-1}, the 18 and 27 mN m^{-1} distributions are very close suggesting very small droplets may be coalescing prior to stabilisation.

Figure 7.15b shows that for 339 mPa·s silicone oil emulsions, decreasing the interfacial tension resulted in a greater proportion of smaller droplets, while the shape of the distributions also becomes more symmetrical and less skewed. For tip speeds of 10 and 37 m s^{-1}, at lower interfacial tensions, d_{max} is reduced and a larger proportion of droplets with diameters in the range of 3-30 μm are greatly increased. The value of d_{min} remained roughly constant in all cases.

7.4.2 Surfactant systems

The effect of interfacial tension on mean drop size of emulsions using three SLES concentrations is presented in Figure 7.16. This figure shows that smaller drops were formed at a slightly lower interfacial tension (7.3 mN m^{-1} for 5% SLES compared to 13.8 mN m^{-1} for 0.05% SLES) for both viscosities of silicone oil investigated. In general there was little effect of surfactant concentration on mean drop size despite the 100-fold increase in SLES content, since all concentrations are above the critical micelle concentration and there is little effect on interfacial tension. In addition, the majority of the gradients are close to -0.4.

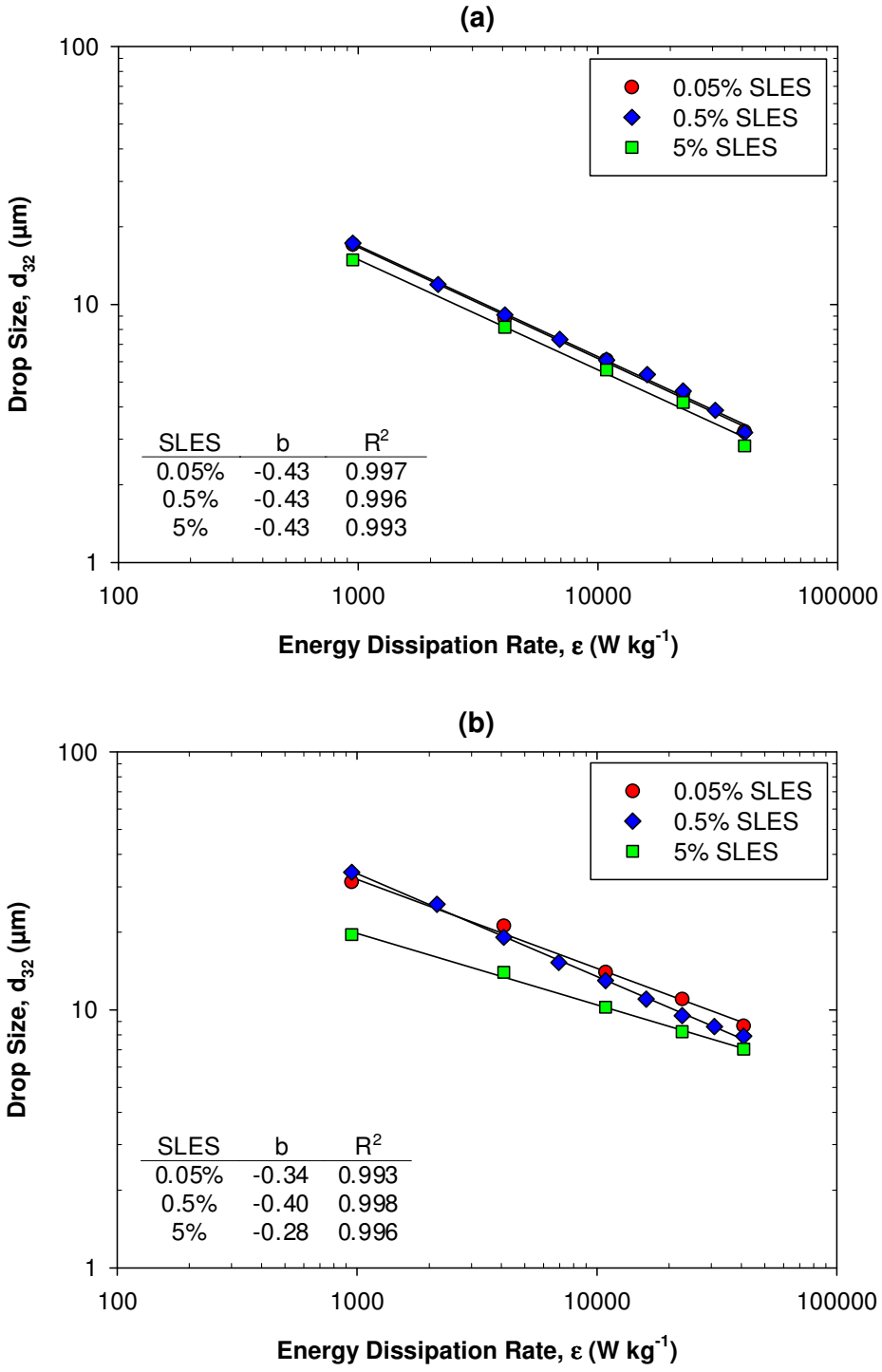

Figure 7.16: The effect of energy dissipation rate on mean drop size in surfactant solutions containing 0.05%, 0.5% and 5% SLES, for 1% (a) 9.4 mPa·s and (b) 339 mPa·s silicone oil emulsions in the 150/250 mixer at 300 kg h^{-1}.

For high viscosity oil dispersed in 5% SLES (Figure 7.16b), smaller drops were obtained at lower energy dissipation rates compared to the other SLES concentrations, and as a consequence a shallower gradient (-0.28) on ε was measured. This may be explained by examining the DSDs for the higher oil viscosity (Figure 7.17b).

Figure 7.17a shows the effect of SLES concentration on DSDs at tip speeds of 10 and 37 m s^{-1} for 9.4 mPa·s silicone oil. Overall there was little effect on the shape or position of the distributions with SLES concentration, with the highest surfactant concentration forming slightly smaller droplets.

Figure 7.17b for 339 mPa·s silicone oil, shows that at a higher tip speed of 37 m s^{-1}, the drop size distributions shifted to smaller drop sizes with increasing surfactant concentration. At the lower tip speed of 10 m s^{-1}, the 5% SLES DSD was different in shape with a higher population of smaller droplets. Coalescence is not a likely explanation for this effect since all conditions have excess surfactant and the smaller drops observed with 5% SLES were not observed for the lower oil viscosity, where drops are easier to deform.

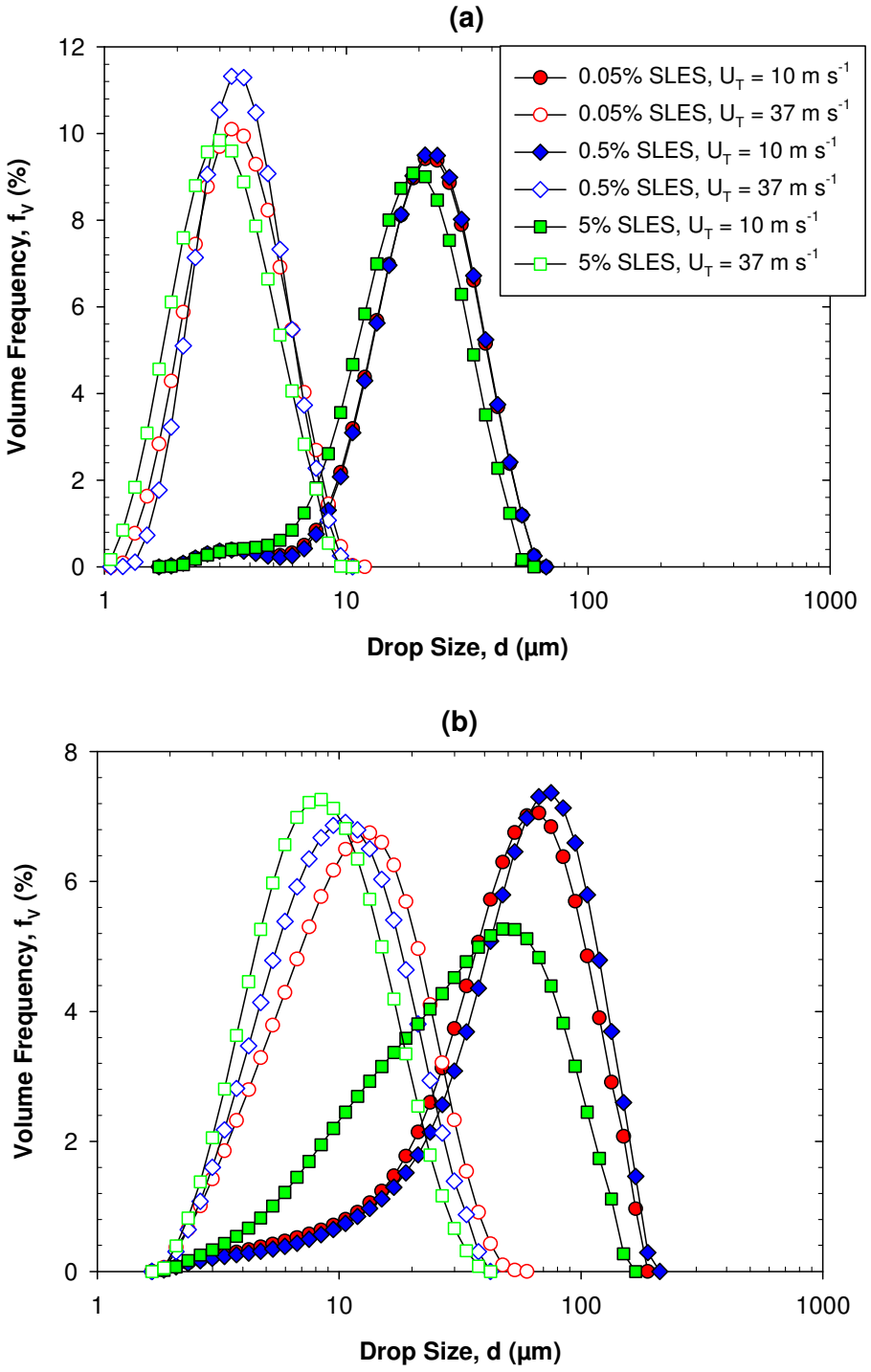

Figure 7.17: Volume drop size distributions of silicone oils in three SLES surfactant solutions, at tip speeds of 10 and 37 m s^{-1} for 1% (a) 9.4 mPa·s and (b) 339 mPa·s silicone oil emulsions in the 150/250 mixer at 300 kg h^{-1}.

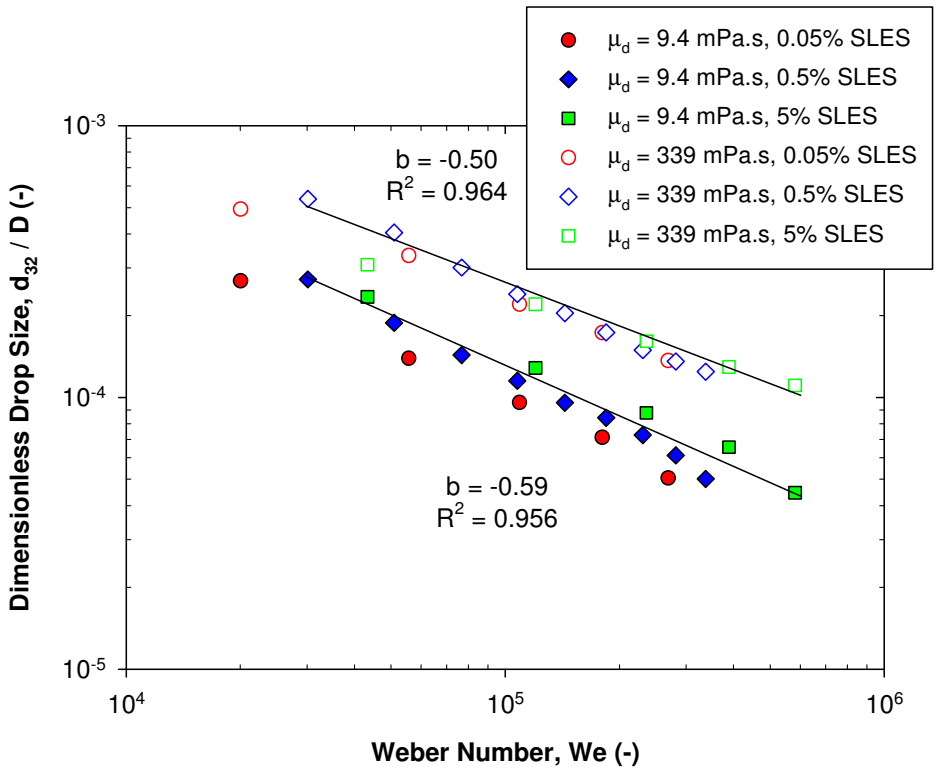

Figure 7.18: The effect of Weber number on dimensionless mean drop size in three SLES surfactant solutions, for 1% (a) 9.4 mPa·s and (b) 339 mPa·s silicone oil emulsions in the 150/250 mixer at 300 kg h^{-1}.

At higher surfactant concentrations for 339 mPa·s oil, the distributions tend to converge at small drop sizes, suggesting the distribution becomes more log-normal at high SLES concentrations.

The correlation of dimensionless drop sizes from Figure 7.16 as a function of Weber number in Figure 7.18 for surfactant systems is not as good as for non-surfactant systems, however the correlation is reasonable for small changes in interfacial tension.

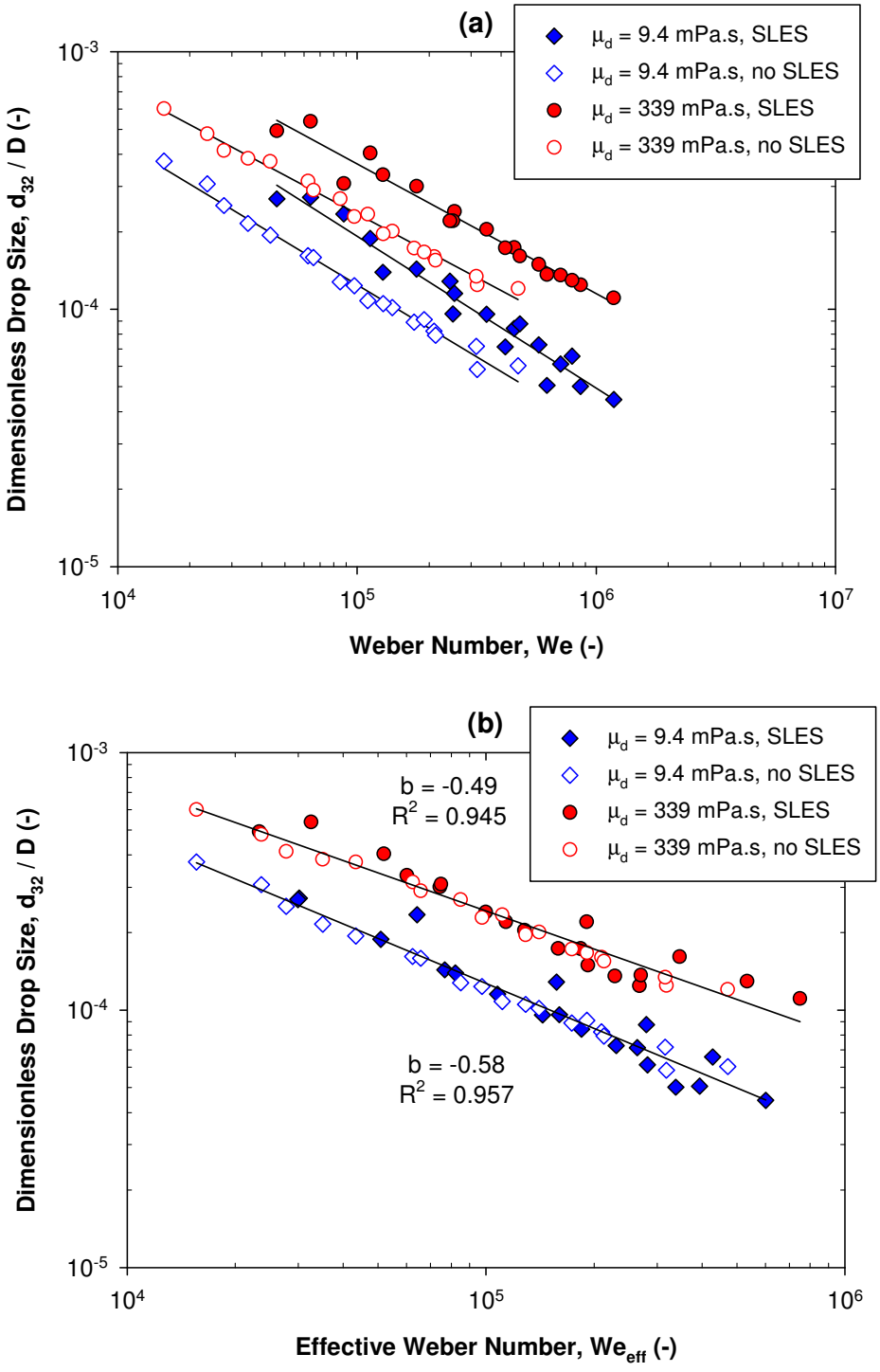

Figure 7.19: Dimensionless mean drop size for 1% 9.4 mPa·s and 339 mPa·s silicone oil in ethanol and surfactant solutions as a function of (a) Weber number and (b) effective Weber number, in the 150/250 mixer at 300 kg h^{-1}.

When the effect of interfacial tension for surfactant and non-surfactant systems, on mean drop size is correlated with Weber number, different trend lines were not only obtained for different oil viscosities but also for non-surfactant and surfactant systems (Figure 7.19a). Koshy et al. (1988) for a stirred vessel and Padron (2005) for a rotor-stator mixer reported that for the same interfacial tension and dispersed phase, oil dispersed in a surfactant system produced larger drops than in a non-surfactant system.

It was proposed that for surfactant systems, effective interfacial tension should be used instead of interfacial tension (Janssen et al., 1994b) (Eq. (2.71)), which depends on the surface excess (Γ) at the oil-water interface, and the bulk concentration of surfactant in the continuous phase, see Section 2.2.2.6. Values of Γ are taken from Walstra and Smulders (1998) for SDS, as an example molecule, to give values of 0.5 mg m^{-3} for 0.05% surfactant and 0.7 mg m^{-3} for 0.5% and 5% surfactant. The droplet deformation time was calculated using Eq. (5.5), while t_D was taken for SDS as $1x10^{-10}$ m^2 s^{-1} from Yang and Matthews (2000). Effective interfacial tension was substituted into Weber number to define an 'effective' Weber number:

$$We_{eff} = \frac{\rho_c N^2 D^3}{\sigma_{eff}} \tag{7.6}$$

Figure 7.19b shows that introducing effective interfacial tension in the Weber number correlation for surfactant systems, brings together mean drop sizes of emulsions measured in non-surfactant and surfactant systems, compared to using equilibrium interfacial tension in Figure 7.19a. The constant β in Eq. (2.71) was obtained by fitting the dimensionless mean drop sizes to the Weber number correlation, by reducing the root mean square difference, to give 0.21 (σ_{rms} = 10.5%) and 0.58 (σ_{rms} = 13.7%) for 9.4 mPa·s and 339 mPa·s oil respectively, which compares to 0.19-0.26 by Janssen et al. (1994b). Figure 7.19b suggests modification of the interfacial tension term can correlate surfactant and non-surfactant systems, however this method should be verified using a range of surfactants.

7.5 Summary

For three scales of in-line rotor-stator mixer, good agreement in DSDs was observed at constant tip speed and residence time, with energy dissipation rate providing a reasonable fit. Correlation of DSDs for multiple passes with energy dissipation rate and total residence time showed a transition from turbulent inertial to turbulent viscous breakage. The effect of interfacial tension for surfactant and non-surfactant systems correlated well with Weber number, once an effective interfacial tension term for surfactant systems was employed.

CHAPTER 8. EFFECT OF ROTOR-STATOR GEOMETRY AND DISPERSED PHASE ADDITION POINT ON EMULSIFICATION BY IN-LINE SILVERSON ROTOR-STATOR MIXERS

8.1 Introduction

The effect of rotor-stator geometry of an in-line 150/250 Silverson mixer on drop size distributions was investigated. The effects of stator hole area, hole diameter, hole design, stator thickness, number of stators, number of rotor blades and rotor-stator gap width were examined. Results were combined with the power measurements (Section 4.8) to ascertain the emulsification efficiency of the rotor-stator configurations. The effect of operating the mixer with and without the stator present has been examined, to illustrate how extreme geometry changes affect emulsification. Finally, the effect of the dispersed phase addition point on DSDs was examined, and compared to premixed DSDs using droplet deformation times.

8.2 The effect of geometry parameters on emulsification

The effect of geometry parameters were investigated in single pass experiments in the 150/250 mixer.

8.2.1 Number of rotor blades

The effect of the number of rotor blades on mean drop size of silicone oil emulsions was investigated using the single emulsor stator with (i) a 4 bladed single rotor, and (ii) an 8

bladed double rotor (Figure 3.5), corresponding to configurations (D) and (G). Mean drop size was the same for each rotor used, with drops only 2% smaller for the 8 bladed rotor (G), (Table 8.2) which is within experimental error. This parameter was not investigated further, however the modest effect on drop size suggests that increasing the number of blades does not strongly influence drop size.

8.2.2 Stator hole diameter

The effect of the stator hole diameter on emulsification was investigated in two ways using stators with spherical hole diameters (d_h) of 1.6 mm and 4.8 mm (Figure 3.5):

- Configurations (F) and (H) to maintain an equal number of holes of 72.
- Configurations (G) and (H) to maintain a similar open area of ~ 1,200 mm^2.

8.2.2.1 Equal hole number

Mean drop size was much smaller (24%) for the large hole diameter stator (H), compared to the small hole diameter stator (F). This suggests that either the hole diameter or the stator open area is significant for droplet break-up. In addition, the jet velocity in the holes is not a major factor for droplet break-up since for a constant flow rate, jet velocity and Reynolds number in the holes were nine times greater for the small hole diameter stator, but droplet break-up did not improve (Table 8.1).

Table 8.1: Stator design and flow parameters.

Configuration	Stator design	d_h (mm)	A_h (mm^2)	U_h (m s^{-1})	Re_h (x10^6)
F	Small 3 row	1.588	142.5	4.69	8.34
H	Large 3 row	4.753	1283	0.52	2.78

8.2.2.2 Equal open area

An increase in stator hole diameter by a factor of three for a similar open area, (the number of holes decreased from 560 to 72), resulted in a fall in mean drop size of 6% (comparing the large d_h stator (H) to the small d_h stator (G)). This confirms that the size of holes in the stator is not a dominant factor for improving droplet break-up, and together with the findings of Section 8.2.2.1, suggests that stator open area may be more significant. Nevertheless, Kamiya et al. (2010b) found hole diameters (1 to 6 mm) to have rather a significant effect on emulsion drop size for an equal open area.

8.2.3 Stator open area

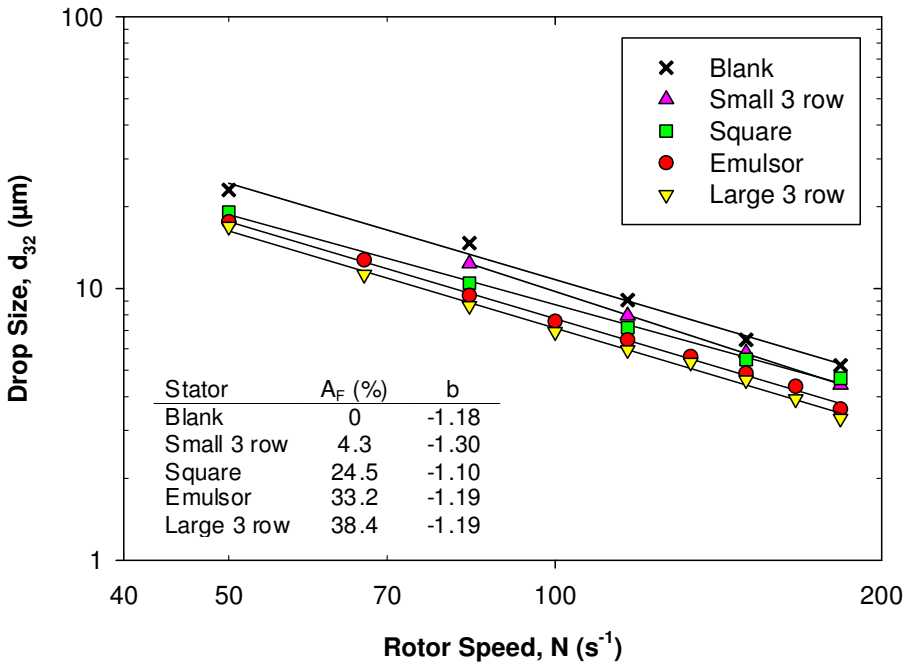

Figure 8.1: The effect of the stator design on mean drop size for 1% 9.4 mPa·s silicone oil emulsions at a flow rate of 300 kg h^{-1}.

The effect of the stator open area on mean drop size was investigated by examining 7 stator configurations using 6 single stators. These are the blank (E), small 3 row (F), large 3

row (H), fine emulsor (B), square hole (C), and standard emulsor (D) stators (Figure 3.5). Mean drop size was much smaller when stator open area was large, for example d_{32} was greatest when all the holes were blocked (Figure 8.1). In this extreme case, all the fluid enters the rotor region at one end of the stator, and flows via the rotor-stator gap out of the stator. The smallest drop size was formed in the stator with the largest open area of 38.4%. The gradients in all cases were similar (-1.2 ±0.1), indicating that droplet break-up is roughly independent of the stator geometry.

The effect of the stator geometry on drop size distributions are shown in Figure 8.2 for data in Figure 8.1 at 11,000 rpm (183 s^{-1}) and 300 kg h^{-1}. Figure 8.2 indicates that the shape of the distributions from each screen were practically equal, which is supported by the fact that averaged log-normal span values of the distributions remained roughly constant (Table 8.3).

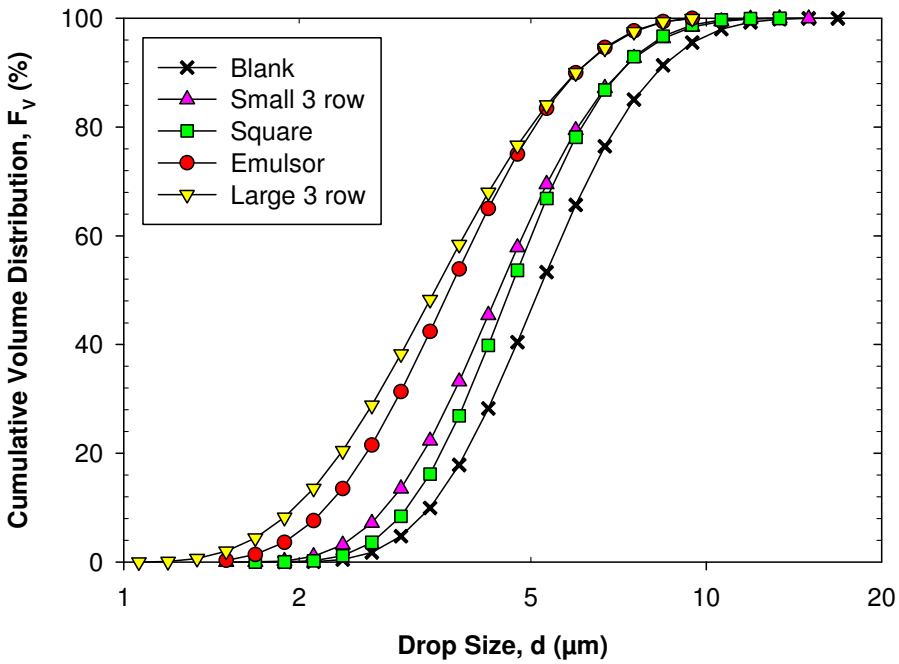

Figure 8.2: Cumulative volume drop size distributions of the five stator geometry in Figure 8.1, for 1% 9.4 mPa·s silicone oil emulsions at a rotor speed of 11,000 rpm and flow rate of 300 kg h^{-1}.

Figure 8.3 illustrates how increasing stator open area fraction (A_F) affects emulsion drop size for a stator, relative to the smallest drop size formed (for the large 3 row (H) stator), including when no stator was present (A), with a nominal A_F of 100%. Stator open area fraction was plotted as a function of drop size index (I), which is a ratio of the average Sauter mean drop size for a given rotor-stator configuration, i, to the average of the smallest mean drop size:

$$\mathrm{I} = \left(\frac{\overline{d_{32}}_i}{\overline{d_{32}}_{min}}\right) \tag{8.1}$$

The worst case (largest mean drop size) occured for the blank stator where I = 1.55, which means that drop size is on average 55% greater than the best case investigated. The removal of the stator entirely also formed relatively large drops, (I = 1.40), 40% greater than the smallest droplets formed.

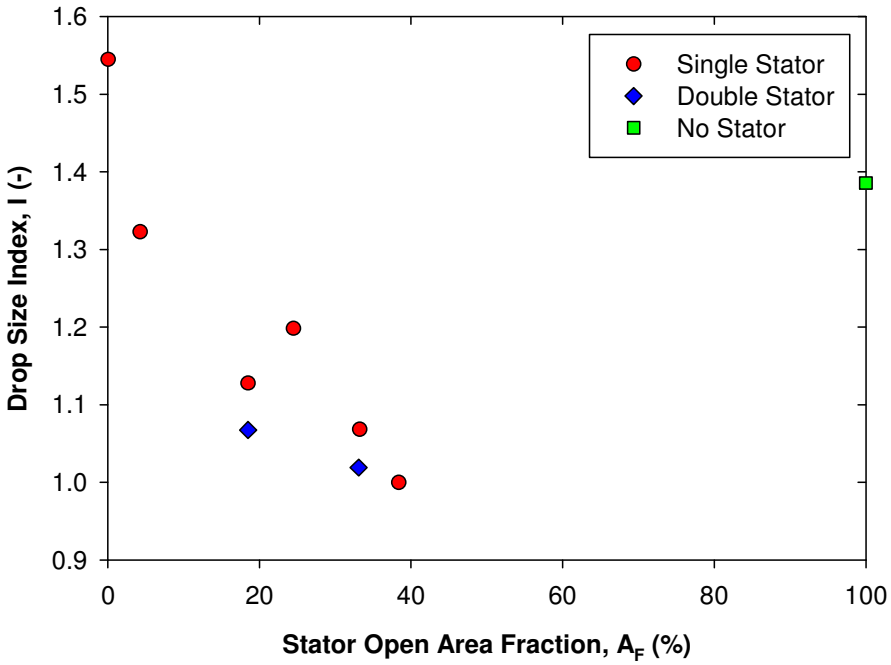

Figure 8.3: The effect of the stator open area fraction on drop size index for 1% 9.4 mPa·s silicone oil emulsions in the 150/250 mixer.

Mean drop size was larger for small A_F stators, as there is less opportunity for the fluid to be recirculated back into the rotor region, and for a given flow rate, the residence time of droplets in the jet region is reduced. For very large A_F stators, such as when the stator was removed, there is an increased chance for the fluid to bypass regions of high shear, resulting in inefficient droplet break-up. This finding suggests that there is an optimum value of A_F, where the smallest drop sizes are produced, near to 40%. Francis (1999) and Phongikaroon (2001) confirmed the trends of this study as the stator of smallest open area formed the largest drops, with a more pronounced effect at larger dispersed phase viscosities. Thapar (2004) and Kamiya et al. (2010b) both stated stator open area strongly influences emulsification performance for in-line rotor-stator mixers.

8.2.4 Rotor-stator gap width

The effect of the rotor-stator gap width on emulsification was investigated using two stators of the same design but with different gap widths:

- Case 1: Large 3 row (H) and large 3 row wide gap (I) with 0.18 mm and 1.02 mm rotor-stator gap widths, respectively.
- Case 2: Standard emulsor (L) and standard emulsor wide gap (M) with 0.24 mm and 0.48 mm rotor-stator gap widths, respectively.

Differences in mean drop size were identical for each case, with 1% greater drops for the wide gap stators (I) and (M) in Case 1 and Case 2, which is insignificant. This suggests that shear rate in the rotor-stator gap is not important for breaking droplets, as an increase in the gap width by five times (Case 1) resulted in an increase of the rotor-stator gap shear rate defined by Eq. (2.88). In Section 7.2.1, tip speed was found to be a good scaling parameter, however

this result suggests constant rotor-stator gap width is not a necessary scale-up criterion in turbulent flows.

Francis (1999) examined the effect of the gap width of 0.5 and 1.0 mm stators on drop size, and found a lower rotor speed to have no effect, while at higher rotor speeds, drop size decreased for the wider gap stator, which confirmed that shear in the gap was not the droplet break-up mechanism. For in-line rotor-stator mixers, Thapar (2004) found little effect of gap width on drop size, while Kamiya et al. (2010a,b) conversely observed a strong effect of the gap width, with smaller drops formed in narrower gap stators.

8.2.5 Stator thickness

The effect of the stator thickness on emulsification was investigated using two stators of the same design but with stator thicknesses of 2 mm (large 3 row, H) and 8 mm (large 3 row thick, J). Mean drop size increased slightly by 5% for the thicker stator (J), which suggests that residence time in the stator holes is not significant for droplet break-up, and larger drop sizes most likely result from a decrease in internal recirculation across the screens, since Po_Z decreased slightly (~ 15%) for the thicker stator (Section 4.8).

8.2.6 Number of stators

The effect of the number of stators on mean drop size was investigated by removing the inner stator. This was repeated for two stator designs:

- Case 1: Single emulsor (G) and double emulsor (L), using the same 8 bladed double rotor.
- Case 2: Single fine emulsor (B) with the 4 bladed single rotor and double fine emulsor (K) with the 8 bladed double rotor.

Mean drop size slightly decreased (by 5% for both Case 1 and Case 2) when two stators were used. This is expected since the inner rotor and stator aid initial break-up of large drops prior to reaching the outer rotor-stator region. A comparison of flow fields using CFD simulations is given in Section 8.5.

Table 8.2: Effect of geometry parameters on average mean drop size of emulsions for various mixer operating conditions in the 150/250 mixer.

Geometry parameter	**Geometry change**	**Effect on average drop size**
Number of rotor blades	4 to 8 blades	-2%
Number of stators – emulsor	1 stator (outer) to 2 stators (inner and outer)	-5%
Number of stators – fine emulsor	1 stator (outer) to 2 stators (inner and outer)	-5%
Hole diameter – equal number of holes (n_h: 72)	1.6 to 4.8 mm (A_h: 140 to 1,200 mm^2)	-24%
Hole diameter – equal open area (A_h: 1,200 mm^2)	1.6 to 4.8 mm (n_h: 560 to 72)	-6%
Stator thickness	2 to 8 mm	+5%
Rotor-stator gap width – large 3 row	0.18 mm to 1.02 mm	+1%
Rotor-stator gap width – double emulsor	0.24 mm to 0.48 mm	+1%

8.3 Stator emulsification efficiency

To assess droplet break-up efficiency of different stator designs, it is necessary to relate Sauter mean diameter with energy input. As the same formulation was used for each geometry in a single pass, the following correlation can be employed:

$$d_{32} = 100.A.\varepsilon^{-0.4}{t_R}^{-0.2} \tag{8.2}$$

In Section 7.3.2, it was shown that for 9.4 mPa·s silicone oil emulsions, exponents close to -0.4 and -0.2 are valid. For each stator design, linear regressions were applied to obtain the

constant A for a range of operating conditions, with a small A value implying that less energy is required to produce a given droplet size. Table 8.3 shows A values for the rotor-stator configurations examined.

Table 8.3: Constants in Eq. (8.2), averaged log-normal span and averaged skewness, for different rotor-stator configurations in the 150/250 mixer.

Configuration	Rotors	Stators	Stator design	A	R^2	Average span, w (-)	Average skewness, s (-)
A	2	0	No stator	2.84	0.9904	1.73	-0.014
B	1	1	Fine emulsor	2.00	0.9897	1.57	0.030
C	1	1	Square hole	1.97	0.9972	1.72	-0.011
D	1	1	Standard emulsor	2.03	0.9970	1.56	0.029
E	2	1	Blank	2.29	0.9888	1.77	-0.019
F	2	1	Small 3 row	2.19	0.9812	1.75	-0.009
G	2	1	Standard emulsor	2.07	0.9965	1.54	0.030
H	2	1	Large 3 row	2.00	0.9915	1.55	0.028
I	2	1	Large 3 row wide gap	2.13	0.9917	1.57	0.028
J	2	1	Large 3 row thick	1.98	0.9898	1.58	0.027
K	2	2	Fine emulsor	1.96	0.9897	1.54	0.027
L	2	2	Standard emulsor	2.19	0.9875	1.58	0.028
M	2	2	Standard emulsor wide gap	2.08	0.9953	1.56	0.031

Overall there is little difference in the constant A for the different rotor-stator configurations investigated (Table 8.3 and Figure 8.4). In fact, the difference between the 'most efficient' and the 'least efficient' configurations, the double fine emulsor (K) and the no stator (A) configurations, is only ~ 30%. However this clearly shows that the stator is not only significant for producing small drops, but also for improving the mixer performance.

Furthermore, span and skewness were virtually constant at ~ 1.55 and ~ 0.0028 respectively, apart from four cases (A, C, E, and F) where span was slightly higher at 1.75 and skewness became negative. For these cases the DSDs are slightly broader and skewed towards small droplets, suggesting less efficient droplet break-up.

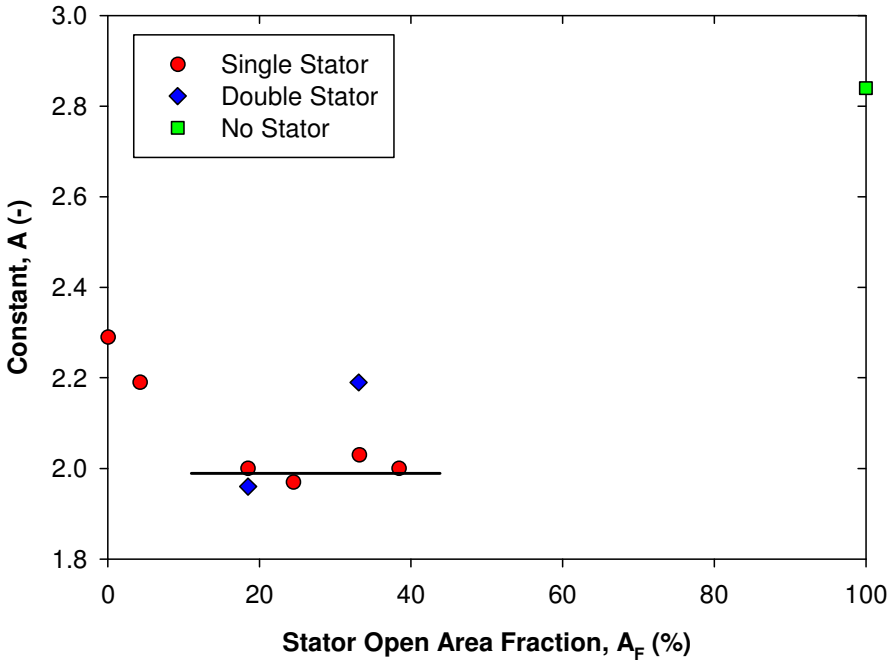

Figure 8.4: The effect of the stator open area fraction on the constant A in Eq. (8.2)

Figure 8.4 shows that correlation of mean drop size with the constant A, indicates that a greater stator open area fraction is generally more favourable for efficient droplet break-up, with higher A values for (E) and (F), the blank and small 3 row stators, where A_F is < 5%. Figure 8.4 shows that stators with A_F between 15 and 40% are the most efficient, with A ~ 2.0. This region seems to provide the best trade off between power consumption and residence time. For small A_F stators, power consumption is lower as there is less fluid flow, but the time drops are exposed to regions of high ε is also reduced. For large A_F stators, there

is increased probability for drops to bypass the regions of highest ε, resulting in inefficient energy usage as the flow is less focused and the mixer more closely resembles an agitated stirred vessel.

Looking at other parameters, the effect of hole diameter, stator thickness and number of rotor blades have a minimal effect on the constant A, with differences < 4% (Table 8.3). The effect of the rotor-stator gap width was also low for the conditions investigated (< 7%), however as for power draw (Section 4.8), conflicting results were obtained for rotor-stator gap width, with A higher (by 7%) for the wide gap stator (Case 1 in Section 8.2.4), but A was 6% higher for the narrow gap stator (Case 2).

Correlation of mean drop size and energy dissipation rate also resulted in inconsistent effects (due to experimental error), once the inner stator was removed; for the standard emulsor stator it was more favourable to emulsify using a single stator (Case 1 in Section 8.2.6), but for the fine emulsor stator it was slightly more efficient with the double stator design (Case 2). The double stator is a common characteristic of Silverson in-line mixers, but the benefits for emulsification are modest, although viscous fluids with more complex microstructure may require the inner stator to aid initial break-up. Within industry, process intensification is increasingly important, thus removing the inner stator may be preferable in certain situations to reduce energy consumption, to the slight detriment of drop size.

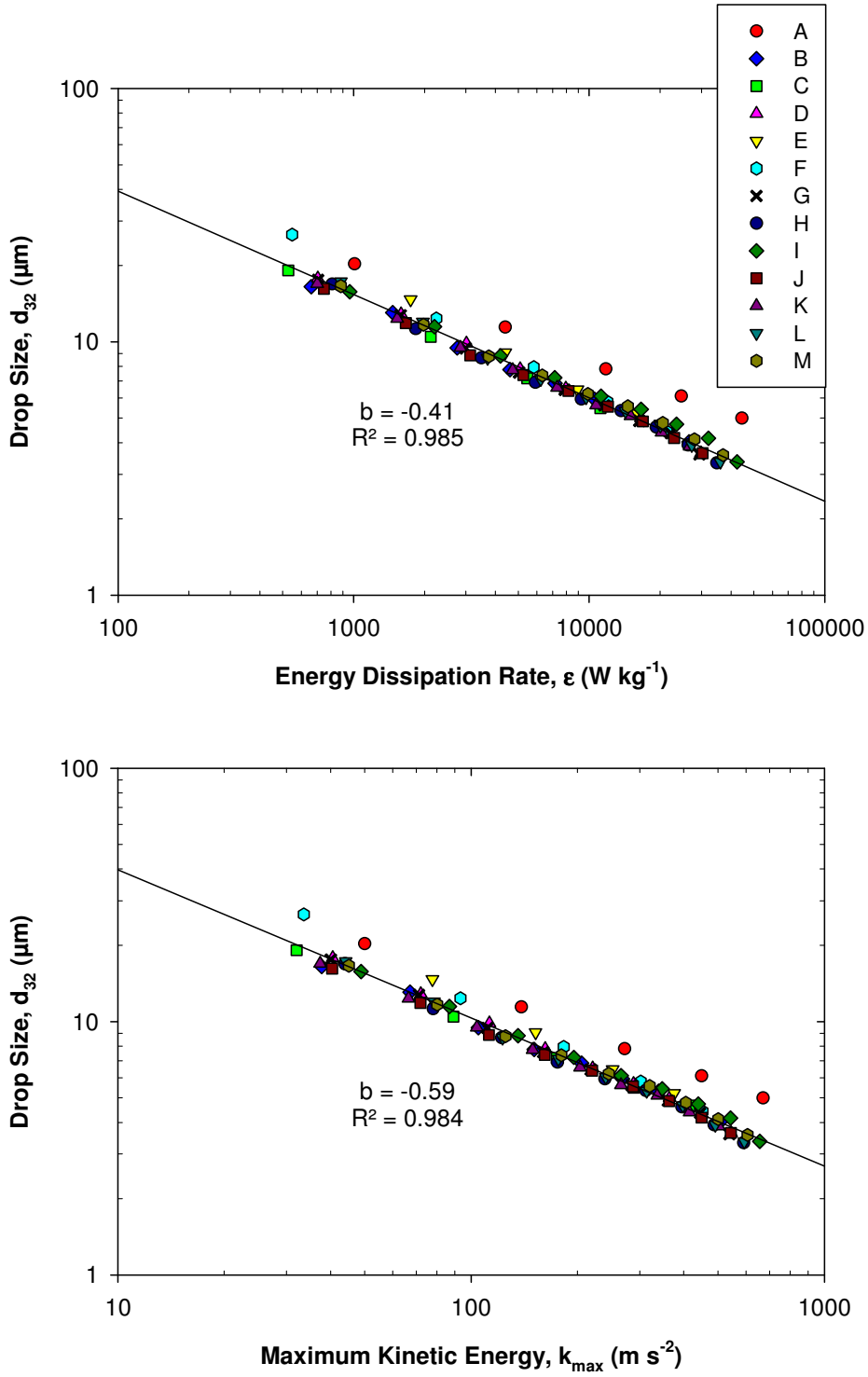

Figure 8.5: The effect of (a) energy dissipation rate and (b) maximum kinetic energy on mean drop size for all the rotor-stator geometry configurations examined (A-M), for 1% 9.4 mPa·s silicone oil emulsions at a flow rate of 300 kg h^{-1} in the 150/250 mixer.

The effect of energy dissipation rate on emulsion mean drop size is given in Figure 8.5a, for a constant flow rate so residence time was ignored. This figure shows that similar drop sizes are achieved for a given energy dissipation rate, with an excellent fit. The main anomaly occurs when no stator (A) was present, which clearly does not fall on the line with the other geometry drop sizes, as the energy is dissipated more uniformly across the mixing chamber, and the flow is less focused in the rotor region, see Section 8.5. Kamiya et al. (2010b) also used energy dissipation rate to correlate drop sizes for five rotor-stator configurations.

A further scale-up correlation for emulsification was described by Grenville et al. (2008) for bladed impellers:

$$k_{max} \propto Po^{0.5} {U_T}^2 \tag{8.3}$$

This term describes the maximum kinetic energy produced by the rotor, and was experimentally found to depend on power number. Table 8.4 shows results of regression analysis between mean drop size and correlation parameters k_{max}, ε and U_T. As expected, the correlation of mean drop size with tip speed for a range of rotor-stator geometry gives the worst relationship ($R^2 = 0.950$) as this scale-up criterion usually requires geometric similarity. For modest geometry changes, d_{32} correlates well with maximum kinetic energy and energy dissipation rate (Figure 8.5). The advantage of k_{max} is that it provides a good correlation at different scales (compared to ε), since k_{max} is a function of Po and U_T, and tip speed is a good scaling parameter (Section 7.2.1) and Po is constant with scale (Section 4.7). The condition with no stator (A) did not correlate well in all cases.

Table 8.4: Correlations of mean drop size with scaling parameters for rotor-stator geometry configurations, excluding config. A.

Scale-up term	***A***	***b***	***Lower 95% CIs***	***Upper 95% CIs***	R^2	σ_{rms} (%)
U_T	250	-1.157	-1.102	-1.212	0.950	10.1
ε	261	-0.409	-0.419	-0.399	0.985	5.8
k_{max}	153	-0.585	-0.600	-0.570	0.984	5.9

8.4 Effect of the stator

The effects of the rotor-stator geometry on emulsification in Section 8.2 are rather modest apart from the stator open area. However, a constant formulation in a single pass mode was used to examine the effect of the geometry variables, thus a full and robust study requires analysis of wider formulation and processing variables. Therefore, two geometry conditions were selected for further analysis; the double emulsor stator (L) and no stator (A) cases, since the double emulsor is the standard mixer geometry, and no stator is the most extreme geometry variation. The effect of number of passes ('step-wise' recirculation method), dispersed phase viscosity and continuous phase viscosity were examined using the 150/250 mixer.

8.4.1 Single and multiple passes

The effect of the stator was investigated by comparing configurations (L), the 'with screens' case denoted 'WS', and (A) with 'no screens', called 'NS'.

Figure 8.6 shows that for low viscosity oil, the stator removal resulted in a large increase in Sauter mean diameter, of roughly the same order for single and multiple passes; a 38% increase for single passes and ~ 30% for multiple passes. This is expected as the

presence of the stator concentrates the energy dissipation and focuses the flow in these regions.

For the high viscosity oil, the effect of the stator presence on drop size was negligible. For single passes, droplet size increased by 8% and ~ 3% when the stator was removed, for single and multiple passes, respectively. This result was supported by Rodgers and Cooke (2011) who concluded that the effect of the stator in emulsification is small.

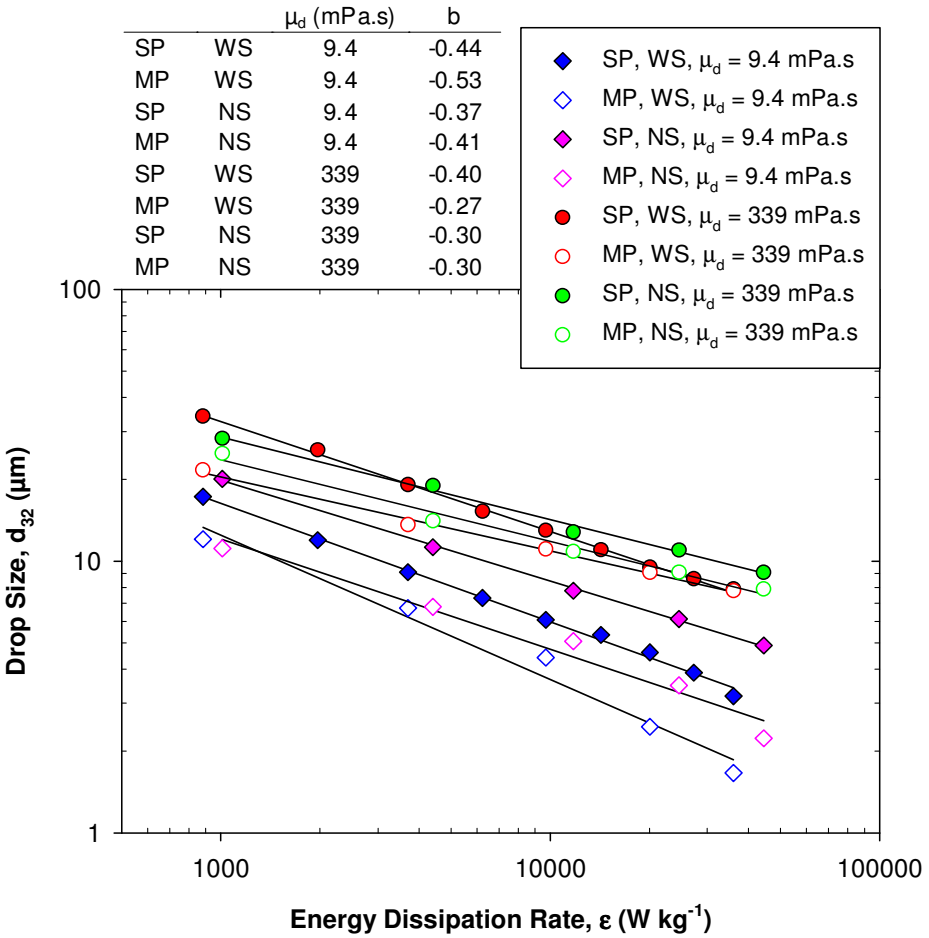

Figure 8.6: The effect of energy dissipation rate, dispersed phase viscosity (1% 9.4 and 339 mPa·s), number of passes (single pass – SP and multiple pass – MP), and stator presence (with stator – WS and no stator – NS) on emulsion mean drop size, for a flow rate of 300 kg h^{-1} (5 passes). Data for 339 mPa·s oil from Rodgers and Cooke (2011).

These results suggest that the maximum shear rate with or without the stator present is similar, since comparable drop sizes were obtained after long times for higher viscosity oil. The minimal effect of the stator on emulsion drop size for high viscosity oils, and the greater effect for low viscosity oils, is possibly akin to the greater effect of residence time for low viscosity oils. This may imply that the primary role of the stator is to focus the flow to increase the residence time in the rotor region where ε is highest.

The modest effect of geometry variables on drop size suggests that the intensity of droplet deformation was similar in all cases, which is strongly related to the tip speed (Section 7.2.1). Altering the geometry is likely to change the duration droplets are exposed to these deformation forces, and since drop size weakly depends on the flow rate (Figure 7.5), the effect of the geometry is also rather weak.

The gradients in Figure 8.6 clearly depend on the emulsion viscosity as discussed previously (Sections 5.7 and 6.5), and the number of passes for low viscosity oil where drops are below η_K. There is little difference in the exponents once the stator was removed, implying that the droplet break-up mechanism remains constant despite the large geometry modification.

Figure 8.7 presents the effect of number of passes on mean drop size with and without the stator present for 9.4 mPa·s oil emulsions. This figure reveals the rate of change of drop size remains roughly constant, with no convergence in mean drop size over time. This suggests the single pass studies in Section 8.2 using 9.4 mPa·s oil emulsions for various geometry configurations are also applicable to multiple passes as similar trends were observed with t_R.

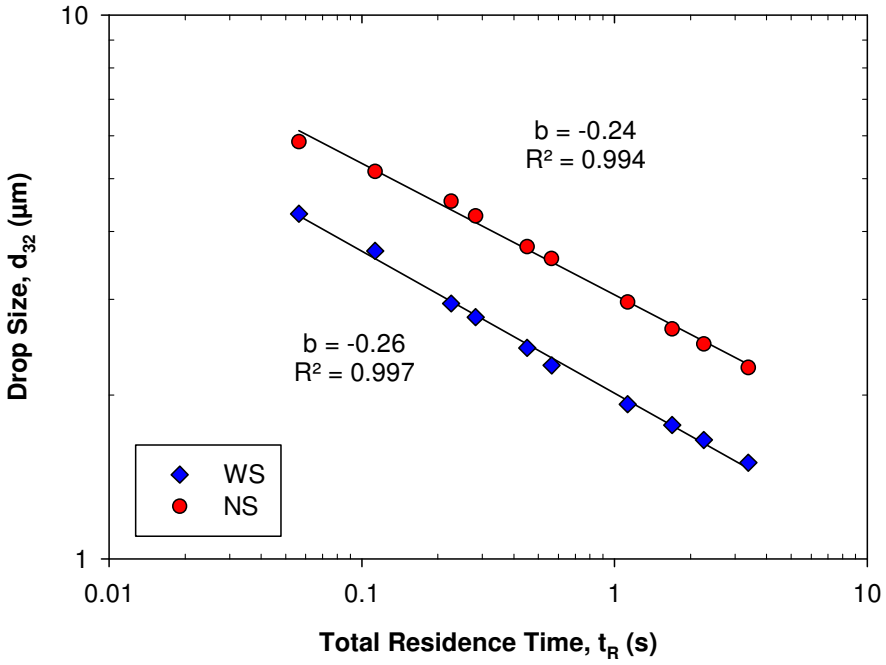

Figure 8.7: The effect of total residence time and stator presence (with stator – WS and no stator – NS) for 1% 9.4 mPa·s oil emulsions on mean drop size, for a flow rate of 300 kg h^{-1} and rotor speed of 11,000 rpm.

The effect of the stator on the cumulative volume DSDs for low viscosity oil is clear from Figure 8.8a (for the lowest and highest tip speeds investigated). In all cases, the distributions form practically a straight line on cumulative frequency axis, with a distinct difference between the WS and NS DSDs and no overlapping of the distributions. For the higher viscosity oil (Figure 8.8b), the DSDs partially lie on top of each other, as expected from the mean drop sizes in Figure 8.6. These distributions indicate that, especially for high viscosity oils, that a similar emulsion can be formed after long processing times once the stators are removed.

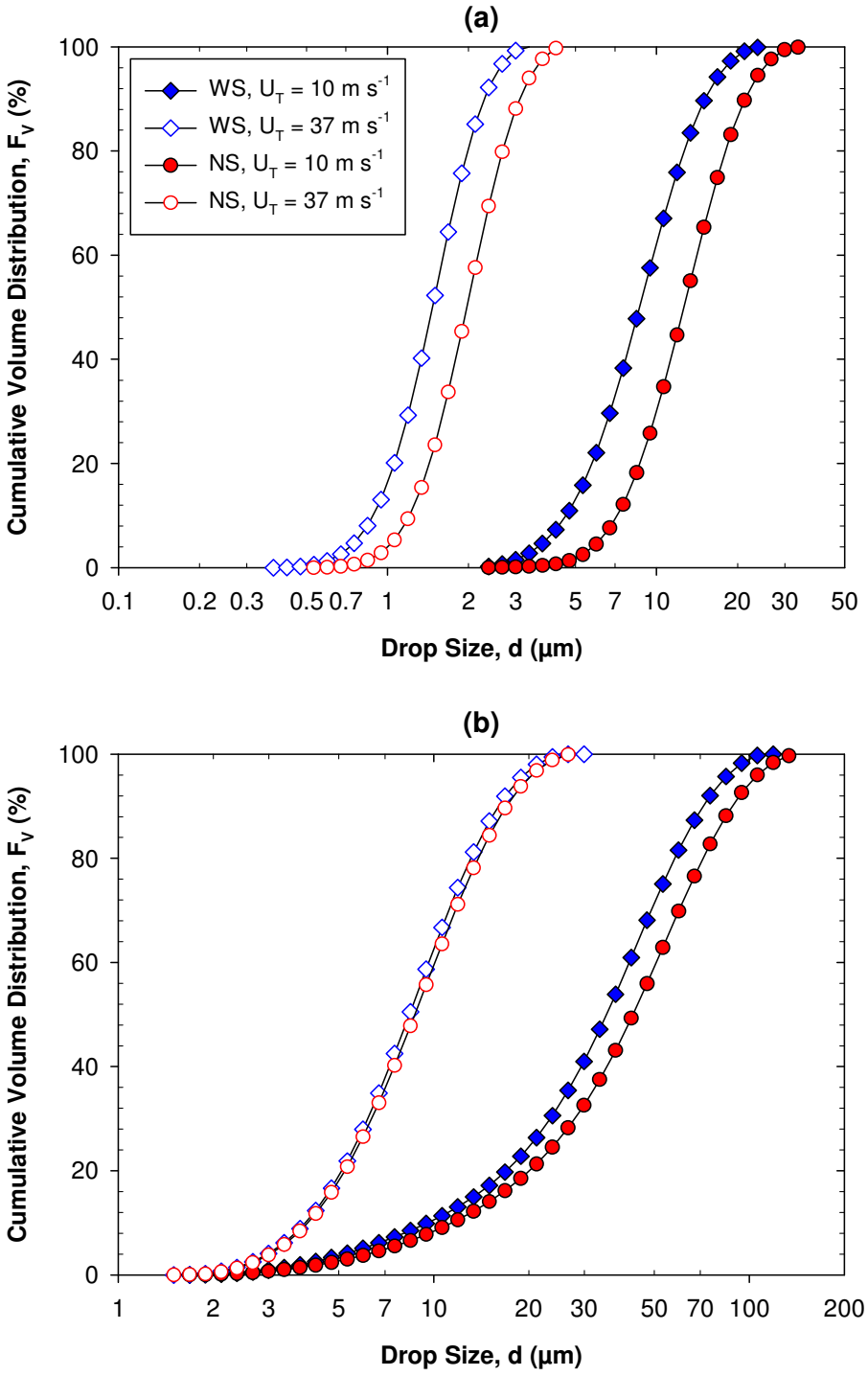

Figure 8.8: Cumulative volume drop size distributions with and without the stator at tip speeds of 10 and 37 m s^{-1} for 1% (a) 9.4 mPa·s and (b) 339 mPa·s silicone oil emulsions for multiple passes at 300 kg h^{-1} (5 batch turnovers).

8.4.2 High dispersed phase viscosity

The effect of the stator was also investigated using a high viscosity oil (9,701 mPa·s oil) dispersed phase (Figure 8.9), which as discussed previously, has a tendency to form bimodal DSDs. The 9,701 mPa·s oil showed on average a ~ 30% increase in mean drop size once the stator was removed, and drop size converged at higher ε. Mean drop sizes and trends for a single pass with the stator, were similar to the trends for multiple passes without the stator, as in each case the process is droplet deformation time limited.

The DSDs (Figure 8.9b) with and without the stator were all bimodal which confirms that bimodality does not result from elongational flow caused by the stator holes. These distributions are more likely formed by incomplete droplet deformation, which is somewhat improved with the stator as the residence time in the high shear regions is increased (see Section 8.6.3).

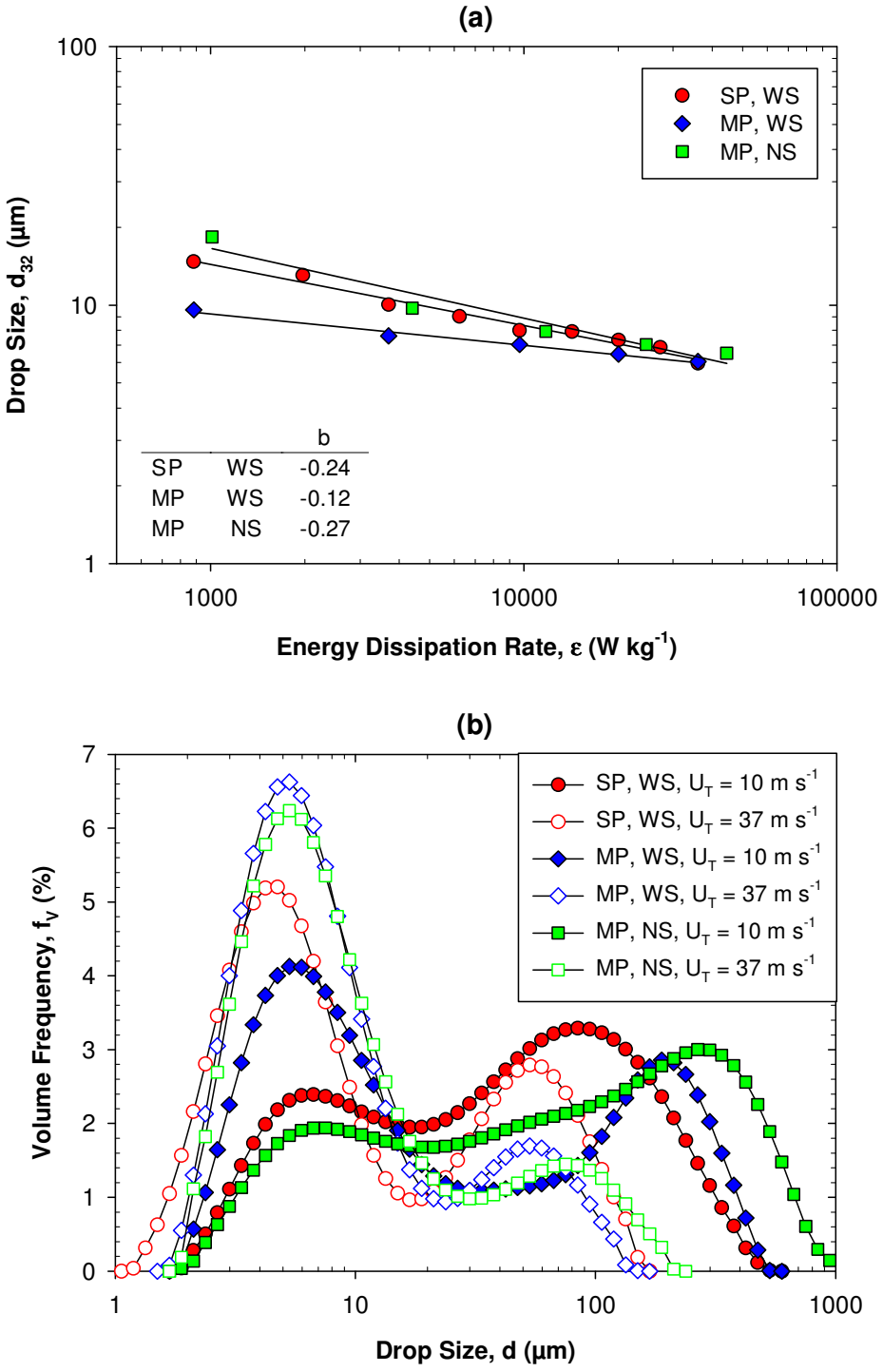

Figure 8.9: (a) The effect of energy dissipation rate, number of passes (single pass – SP and multiple pass – MP), and stator presence (with stator – WS and no stator – NS) on mean drop size, for a flow rate of 300 kg h^{-1} for 1% 9,701 mPa·s silicone oil emulsions, and the corresponding (b) volume drop size distributions at 10 and 37 m s^{-1}.

8.4.3 Continuous phase viscosity

A higher continuous phase viscosity was obtained by adding 1.35 wt.% CMC to a solution of 0.5 wt.% SLES, as the shear thinning rheology of this system was similar to many emulsion-based products (Figure 3.12). The continuous phase apparent viscosities were calculated from shear rates in Eq. (2.12), using K_S values of 46.2 (with screens) and 6.6 (without screens) from Cooke et al. (2012). It should be noted that the emulsion viscosity can be greater than the continuous phase viscosity for high dispersed phase volume fractions.

Figure 8.10 reveals that when the stator was present, little difference was observed in the mean drop diameters of emulsions with or without CMC addition, because the effect of continuous phase viscosity on drop size (Section 5.8) was minimal. For CMC systems, temperature increased from 25 ºC to 29 ºC at 11,000 rpm, and interfacial tension reduced from 10.0 to 7.3 mN m^{-1}, although these effects appear to be negligible. The increase in power consumption was measured and included in the calculation of ε, and the greatest exponent on energy dissipation rate (-0.65) occurred with the stator present for 1.35% CMC (Figure 8.10).

Once the stator was removed, two findings were observed. Firstly, larger mean drop sizes were formed in 1.35% CMC compared to 0% CMC, which was not expected as a higher continuous phase viscosity normally results in the formation of smaller droplets. Secondly, due to the increase in μ_c for 1.35% CMC, $\eta_K \gg d$ for the whole distribution (Table 8.5), thus for 1.35% CMC with no stator, an exponent of -0.5 rather than -0.38 would be expected for turbulent viscous break-up (Eq. (2.67)). One reason for this finding could be due to turbulence damping at higher continuous phase viscosities that reduce the magnitude of energy dissipation rate. Furthermore, for the 'no screens' case the flow regime is always transitional (Table 8.5), so droplet break-up may not entirely follow the models developed by Hinze based

on Kolmogorov turbulence theory. Another possibility is that the CMC may inhibit surfactant diffusion and/or absorption onto the droplet interface resulting in larger droplets.

Table 8.5: Apparent continous phase viscosities, viscosity ratios, Reynolds numbers and Kolmogorov length scales for 1.35% CMC solutions with (WS) and without (NS) screens.

Rotor speed, N (rpm)	**Apparent continuous phase viscosity, μ_A (mPa·s)**		**Viscosity ratio with 9.4 mPa·s silicone oil, μ^* (-)**		**Reynolds number, Re (-)**		**Kolmogorov length scale, η_K (µm)**	
	WS	**NS**	**WS**	**NS**	**WS**	**NS**	**WS**	**NS**
3,000	97.7	360	0.0963	0.0261	2,071	562.3	136	367
5,000	69.3	256	0.136	0.0368	4,868	1,318	87.6	203
7,000	55.3	204	0.170	0.0461	8,541	2,315	60.4	147
9,000	46.0	172	0.204	0.0545	13,201	3,531	46.8	113
11,000	37.9	151	0.248	0.0624	19,583	4,915	33.6	90.8

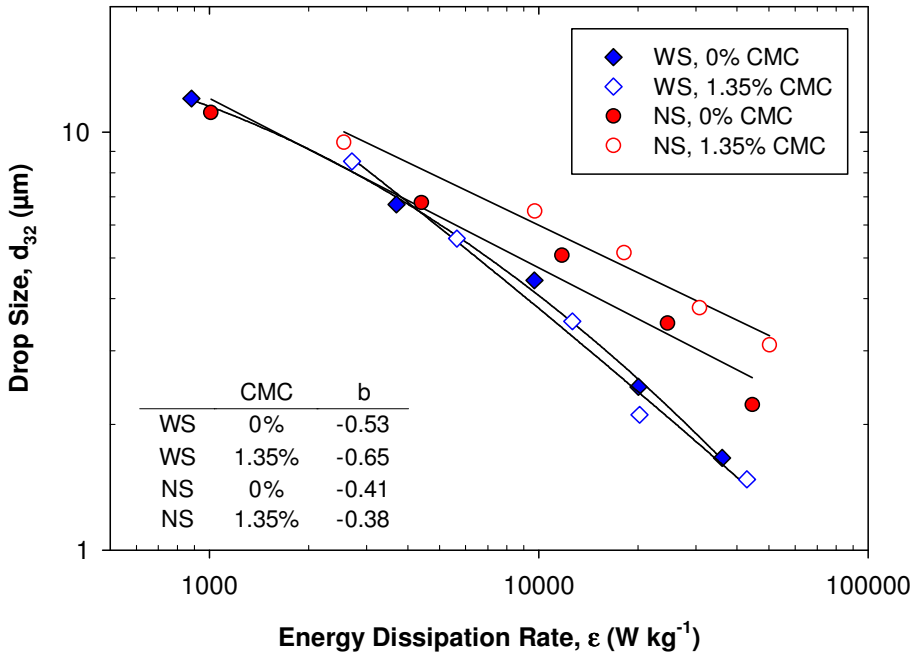

Figure 8.10: The effect of energy dissipation rate and stator presence (with stator – WS and no stator – NS) on mean drop size, for a flow rate of 300 kg h^{-1} for 1% 9.4 mPa·s silicone oil emulsions.

For $d_{32} < \eta_K$ in Figure 8.10, mean drop size correlated with ${\mu_c}^{-0.034}$, for μ^* from 0.026 to 10.6, hence the dependency of drop size upon μ_c is weak. For rotor-stator systems, Schultz et al. (2004) also found a low effect of μ_c on drop size with an exponent < -0.03.

8.5 Numerical simulations of rotor-stator geometry

Velocity and energy dissipation rate profiles (Figure 8.11) for three (150/250 mixer) rotor-stator configurations (2R2S: Double rotor and double stator; 2R1S: Double rotor and single stator; 2R0S: Double rotor and no stator) indicate that maximum velocity and energy dissipation (the key region for droplet break-up) occurs at the tips of the outer rotor blades. This is not surprising considering tip speed was a good scaling parameter (Section 7.2.1).

Comparison of the 2R2S and 2R1S configurations shows that the presence of the inner stator increases the regions of high energy dissipation rate in the outer rotor region, suggesting drops are exposed to higher energy dissipation rates for longer times. However, the removal of the stator completely (2R0S) forms a very uniform energy dissipation rate profile (and to a lesser degree uniform velocity profile), compared to the other configurations. Values of U_{max} are similar in all cases, while ε_{max} is of the same order of magnitude for single and double stators (Table 8.6).

Table 8.6: Values of parameters for different rotor-stator configurations in the 150/250 mixer for 11,000 rpm and 600 kg h^{-1}.

Parameters	**2R2S**	**2R1S**	**2R0S**
Power calculated (from torque) (W)	220	158	127
Power measured (by torque) (W)	266	213	302
Maximum velocity, U_{max} (m s^{-1})	22.7	23.4	21.5
Maximum energy dissipation rate, ε_{max} (m^2 s^{-3})	4.9×10^6	3.1×10^6	4.0×10^5
Maximum strain rate, S_{max} (s^{-1})	8.1×10^5	8.1×10^5	6.4×10^5

The predicted and measured power values for the simulations in Figure 8.11 are given in Table 8.6. In all cases, simulations under predict power consumption, especially once the stator is removed since fluid can flow next to the rotor, as details of the inflow and outflow that affect power draw cannot be modelled in 2D.

Energy dissipation rate profiles for the geometry in Figure 8.11 are given in Figure 8.12. For the 2R2S case, the distribution of ε is bimodal, with peaks at 10^1 and 10^3 W kg^{-1}, while the 2R1S case is also slightly bimodal, but the removal of the stator completely (2R0S) forms a single peak. This clearly demonstrates the action of the stator focusing the dissipated energy. Furthermore, the greater the number of stators, the greater the mixer volume in which high values of energy are dissipated ($> 10^4$ W kg^{-1}), increasing the probability for drops to reside in these regions. Hence the main function of the stator seems to be to focus ε in the rotor region to increase mean ε.

Configuration	Energy dissipation rate profiles	(m^2 s^{-3})
2R2S	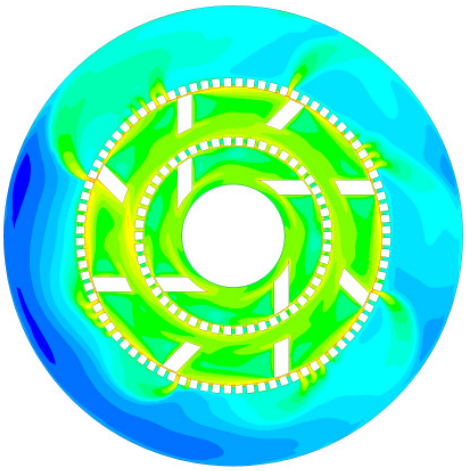	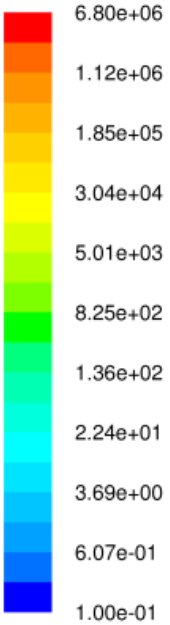
2R1S	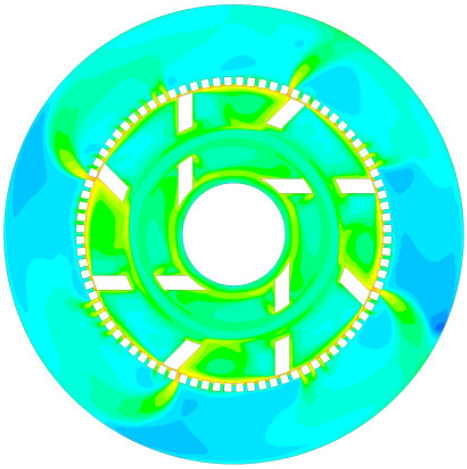	
2R0S	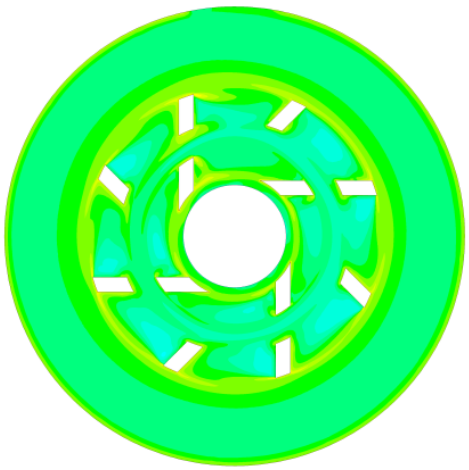	

Configuration	Velocity profiles	(m s^{-1})
2R2S	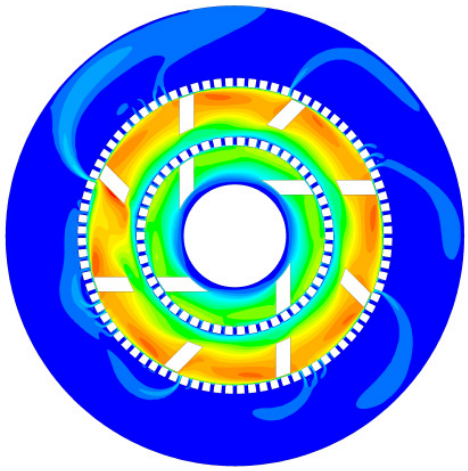	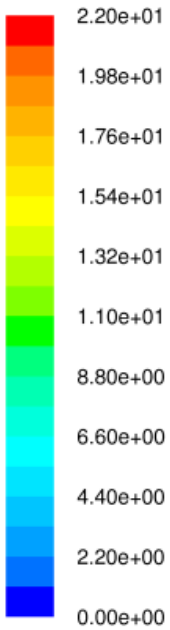
2R1S	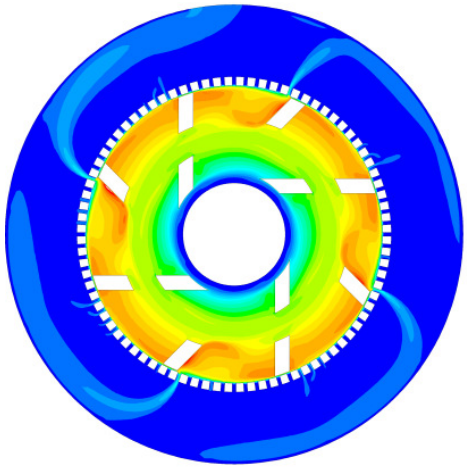	
2R0S	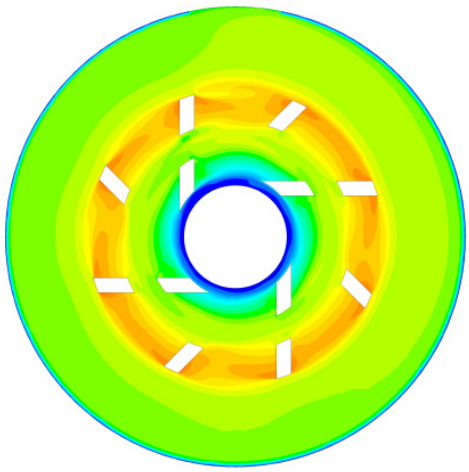	

Figure 8.11: Velocity and energy dissipation rate profiles for three rotor-stator configurations; two rotors and two stators – 2R2S (L), two rotors and one stator – 2R1S (G), and two rotors and no stators – 2R0S (A), for 6,000 rpm and 600 kg h^{-1}.

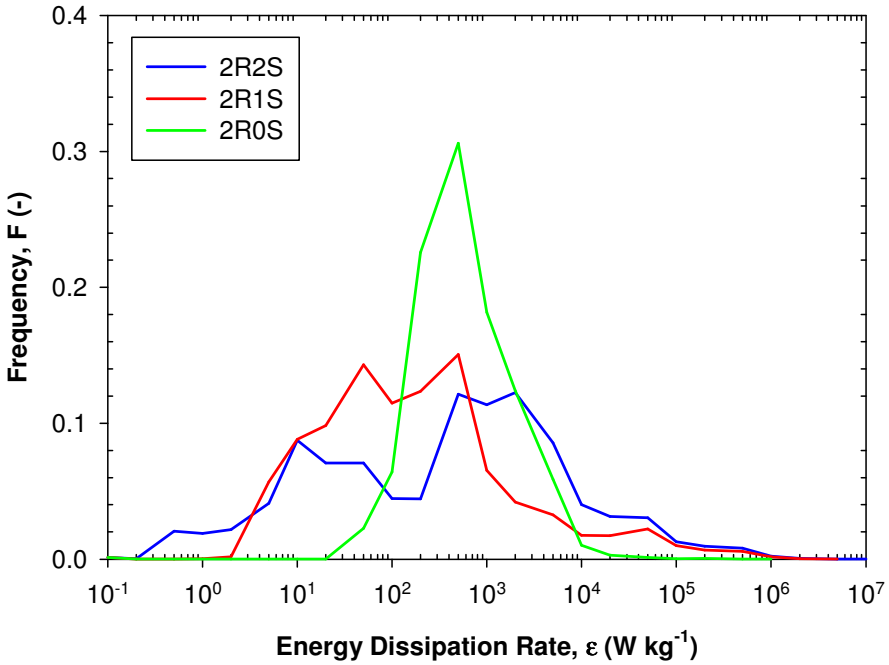

Figure 8.12: Probability frequency distribution of energy dissipation rate across the mixer volume, for three rotor-stator configurations; 2R2S (L), 2R1S (G) and 2R0S (A), for 6,000 rpm, 600 kg h^{-1}.

8.5.1 Strain rate

For an incompressible Newtonian fluid, the mean strain rate is defined as (Fluent Inc., 2006):

$$S_{ij} = \frac{1}{2}\left(\frac{\partial U_j}{\partial x_i} + \frac{\partial U_i}{\partial x_j}\right) \tag{8.4}$$

The strain rate represents the rate at which velocity varies with distance from a given point (Bai et al., 2011) and includes both rotation and strain tensors, so more correctly accounts for the effects of rotation on turbulence. Strain rate is useful as it is comparable to Metzner-Otto shear rates (Bakker, 2006).

Table 8.7: Ratio of average mean drop sizes for various processing conditions, and the ratio of maximum velocity, maximum energy dissipation rate and maximum strain rates for three rotor-stator configurations; 2R2S (L), 2R1S (G) and 2R0S (A), for 6,000 rpm and 600 kg h^{-1}.

Configuration	U_{max}	ε_{max}	S_{max}	$1/\overline{d_{32}}$
2R0S/2R2S	0.94	0.08	0.79	0.76
2R1S/2R2S	1.03	0.63	0.99	0.96

Table 8.7 compares the effect of the ratio of maximum velocity, maximum energy dissipation rate and maximum strain rates for the 2R0S and 2R1S configurations to the 2R2S configuration, in addition to the inverse of the ratio of average drop size between the respective configurations, to investigate the correlation of the 2R0S (A) configuration in Figure 8.5. Table 8.7 shows that the ratio of average mean drop diameters compares most appropriately with maximum strain rate. This result implies that maximum strain rate could be used in correlations of different mixer geometry, although further work using 3D simulations should be employed for verification.

8.5.2 Particle tracking

Particle tracking using the discrete random walk model in Fluent illustrates the actual residence time drops spend in different regions of the mixing head. Figure 8.13a shows that a droplet can travel through the inner and outer stators several times prior to exiting the mixing head due to internal recirculation patterns. A typical residence time profile (Figure 8.13b) shows that droplets reside in high energy dissipation rate zones for very small times, of the order of microseconds. However, this figure shows that droplets experience a reasonably high ε (> 10^3 W kg^{-1}) for a sufficiently long time to result in droplet break-up in a single pass.

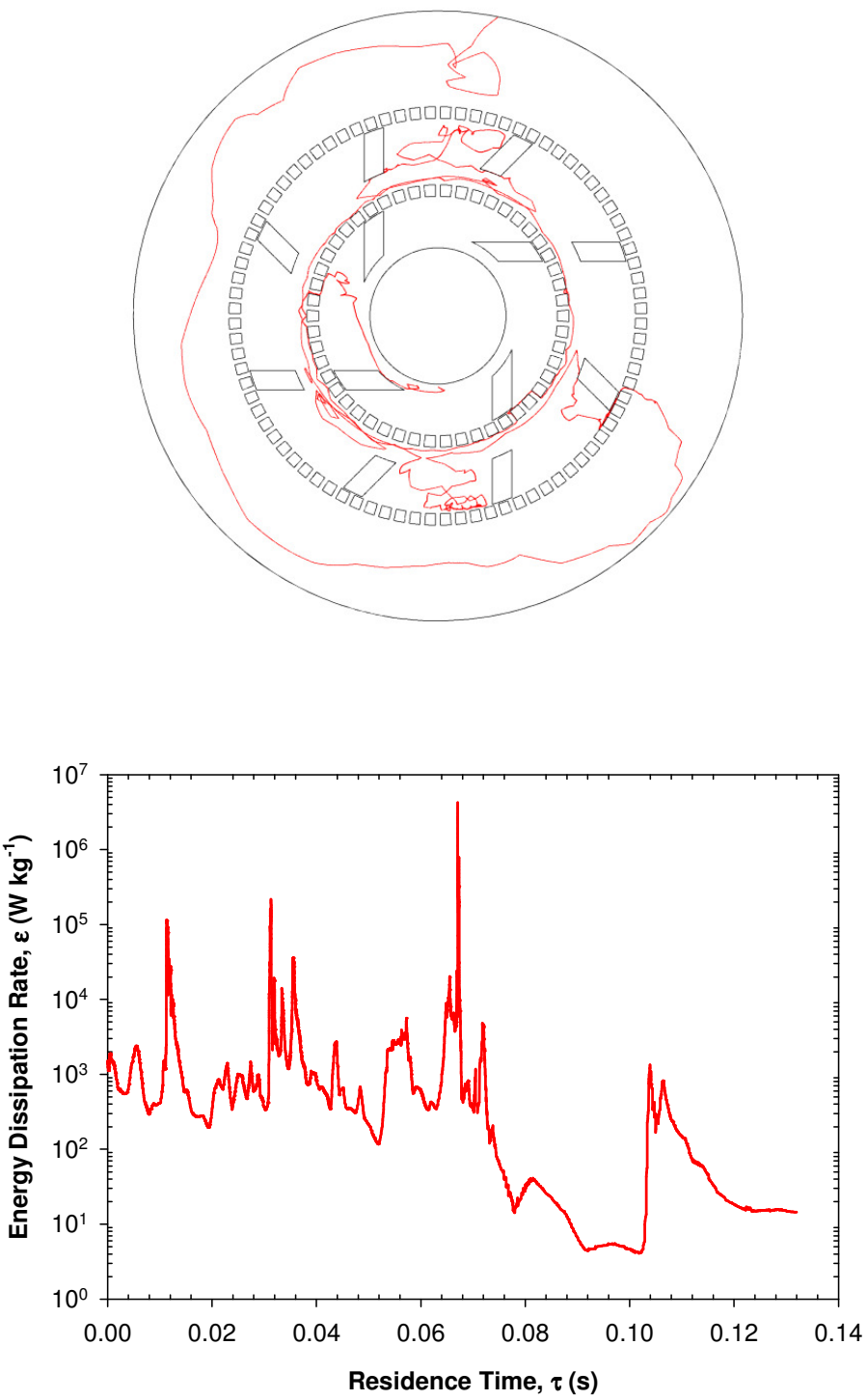

Figure 8.13: (a) An example of particle tracking for two rotors and two stators – 2R2S (L), for 6,000 rpm, 600 kg h^{-1} and (b) energy dissipation rate as a function of residence time for a particle.

8.6 Dispersed phase addition point

A comparison between injecting the dispersed phase into the mixing head, as opposed to creating a coarse emulsion premix was also investigated, since oil injection is a common operating mode, but current information in literature is practically non-existant. The effect of processing conditions and dispersed phase viscosity on DSDs were studied for single passes through the 150/250 mixer, as these were found to be the primary factors influencing drop size (Chapters 5 and 6).

8.6.1 Dispersed phase viscosity

Figure 8.15 compares addition of the dispersed phase into the continuous phase by injection into the inner stator, injection into the outer stator, or by forming a premix in a stirred vessel (as for all previous sections) on emulsification (Figure 8.14).

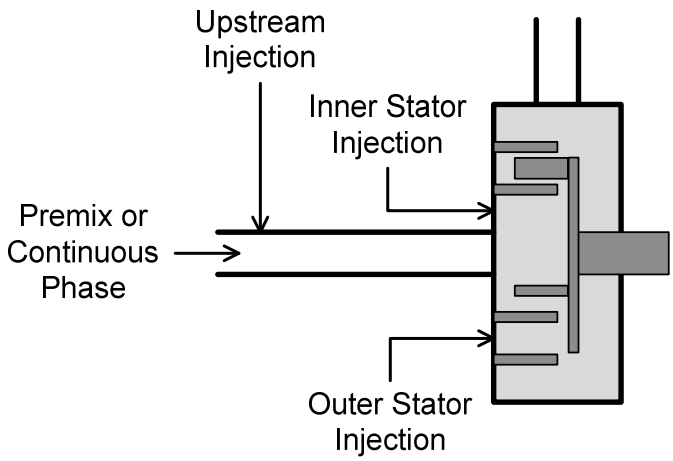

Figure 8.14: Methods of injecting the dispersed phase into the in-line Silverson mixer.

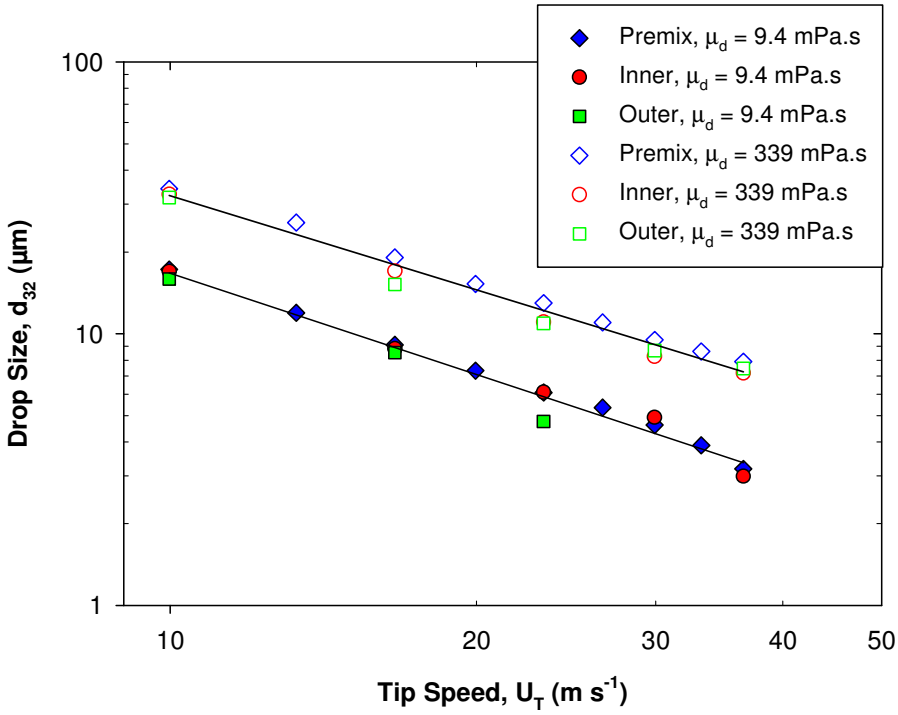

Figure 8.15: Mean drop size of emulsions as a function of tip speed at 300 kg h^{-1} for 1% silicone oil viscosities of 9.4 and 339 mPa·s, comparing addition of the dispersed phase either as a premix, or injection into the inner or the outer stator.

Mean drop size remained practically constant despite the mode of oil addition, for oil viscosities of 9.4 and 339 mPa·s (Figure 8.15). A similar finding was observed when flow rate was varied at rotor speeds of 6,000 and 11,000 rpm (Figure 8.16). Since the effect of the inlet droplet size on the outlet drop size was small (Section 5.2), it is perhaps not surprising that varying the initial drop size by changing the point of oil addition is not a major factor in emulsification.

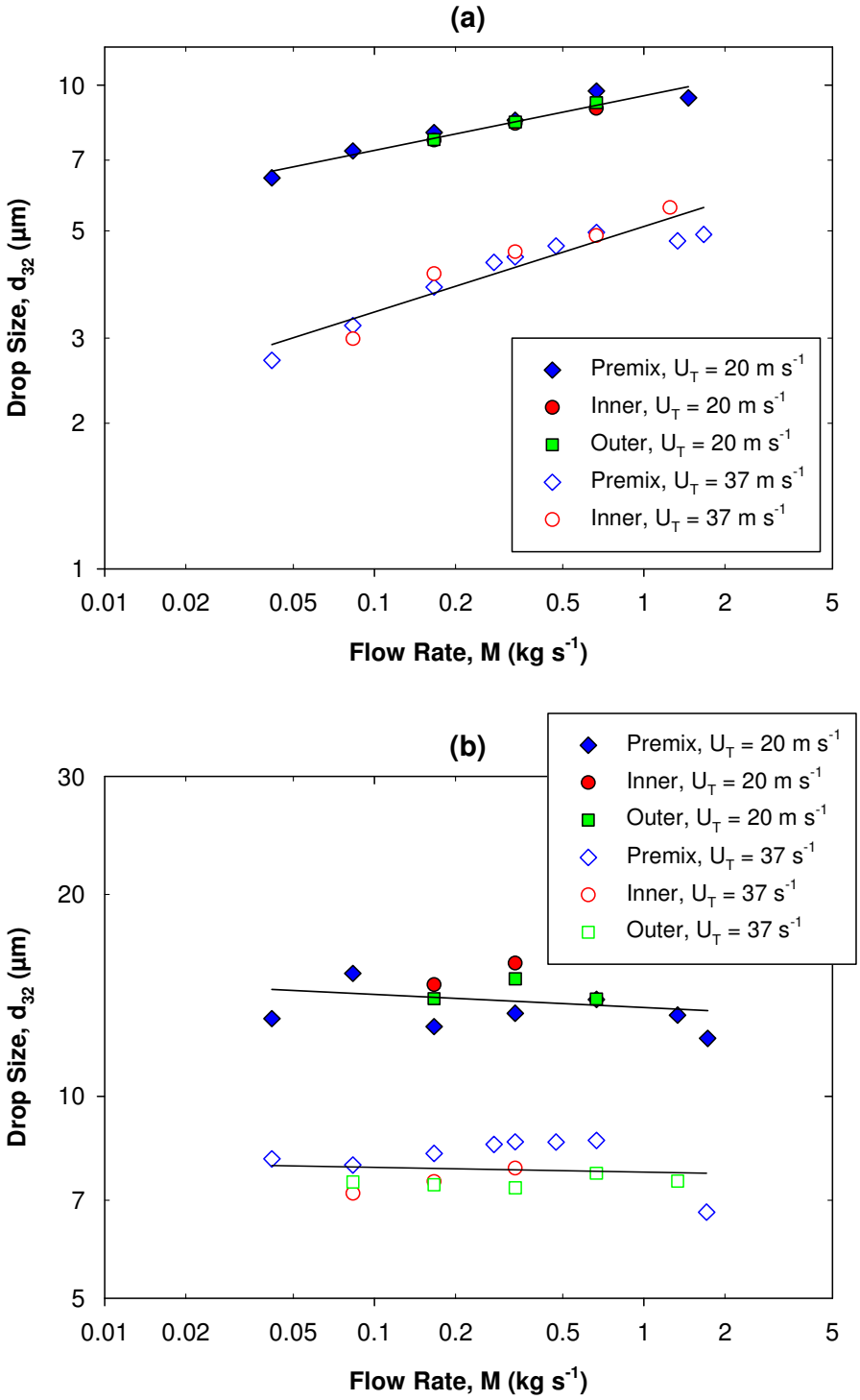

Figure 8.16: Mean drop size of emulsions as a function of flow rate at 20 and 37 m s^{-1} for 1% silicone oil viscosities of (a) 9.4 and (b) 339 mPa·s, comparing addition of the dispersed phase either as a premix, or injection into the inner or the outer stator.

8.6.2 High dispersed phase viscosity

The effect of the dispersed phase addition point on mean drop size of emulsions for high viscosity oil drops is presented in Figure 8.17. The effect of tip speed in Figure 8.17a clearly shows that smaller drops were formed by injecting the dispersed phase into the continuous phase rather than dispersing an emulsion premix. Furthermore, injection into the outer screen consistently delivered a smaller drop size compared to injection into the inner screen. A fourth method of dispersed phase addition was examined, by injecting the oil into the continuous phase ~ 0.5 m upstream of the mixing head. This method was examined as oil injection into the stators against a high pressure head was difficult, and the flow rate of oil often pulsed at low flow rates, while oil injection upstream was easier as the suction of the mixer can be harnessed. For this condition, mean drop size was more closely related to mean drop sizes formed by injection into the stator than from the emulsion premix. However, d_{32} went through a minimum of 5.4 µm around 20 to 30 m s^{-1}, rising to 5.8 µm at 37 m s^{-1}, equal to that from the emulsion premix.

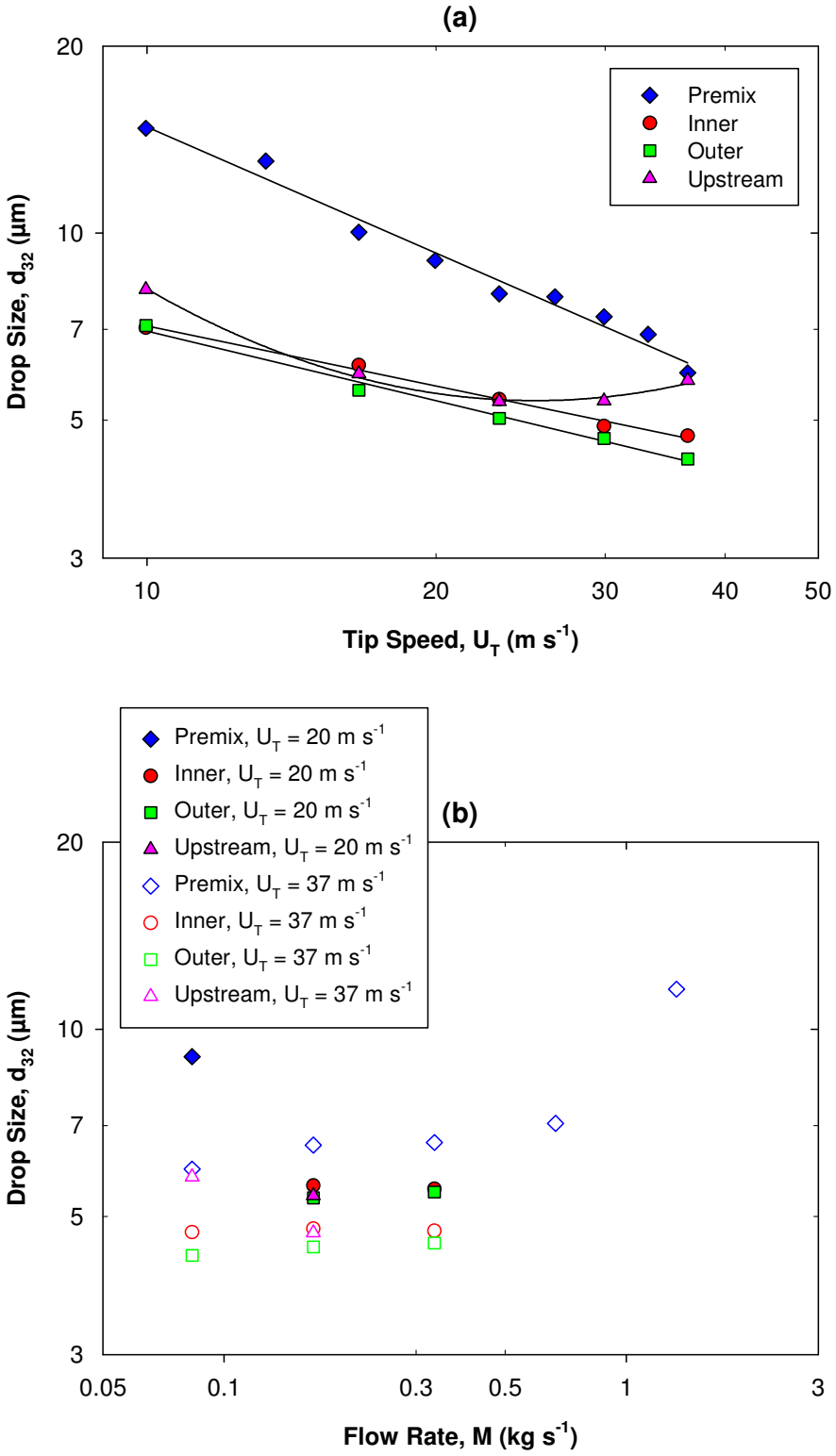

Figure 8.17: Mean drop size as a function of (a) tip speed at 0.083 kg s^{-1} (300 kg h^{-1}) or (b) flow rate at 20 m s^{-1} and 37 m s^{-1} for 1% 9,701 mPa·s silicone oil emulsions, comparing addition of the dispersed phase either as a premix, or injection into the inner stator, the outer stator, or upstream of the mixing head.

The enhanced droplet break-up for 9,701 mPa·s oil is stark compared to the other oil viscosities examined (Figure 8.15 and Figure 8.16), and may be explained by examining the droplet deformation times. Creation of a premix forms mother droplets which are difficult to deform in a given flow field. Injection of the dispersed phase forms larger mother droplets which are easier to deform, resulting in more complete droplet break-up. Injection of the dispersed phase into the outer stator where energy dissipation rates are higher (Figure 8.11) enables large viscous mother drops to deform faster, resulting in smaller droplets.

Injection of the dispersed phase upstream of the mixing head differs as there is opportunity for drops to break-up prior to entering the mixing head. Figure 8.17a suggests this does not occur to any large degree until very high tip speeds (> 30 m s^{-1}). Despite a constant flow rate (and constant Re in the pipeline), at high tip speeds it is likely that suction in the mixer inlet causes a degree of droplet break-up before the drops experience high levels of shear in mixing head. Nevertheless, injection of oil upstream does offer benefits over premixing an emulsion. Similar findings were observed for a batch rotor-stator mixer, see Appendix D.3.

Figure 8.17b shows the effect of dispersed phase addition point and flow rate on drop size for 9,701 mPa·s oil emulsions. At equal rotor speeds, injection into the outer screen is the most favourable mode of operation, followed by injection into the inner screen, injection upstream of the mixing head, with premixing the emulsion giving the largest droplet sizes. At high flow rates (> 1 kg s^{-1}), an increase in drop size for the premix condition (at 37 m s^{-1}) was observed, as residence time was reduced. Highly viscous oils could not be pumped at a sufficiently high flow rate using the rig arrangement to examine higher flow rates for the injection cases (> 0.4 kg s^{-1}).

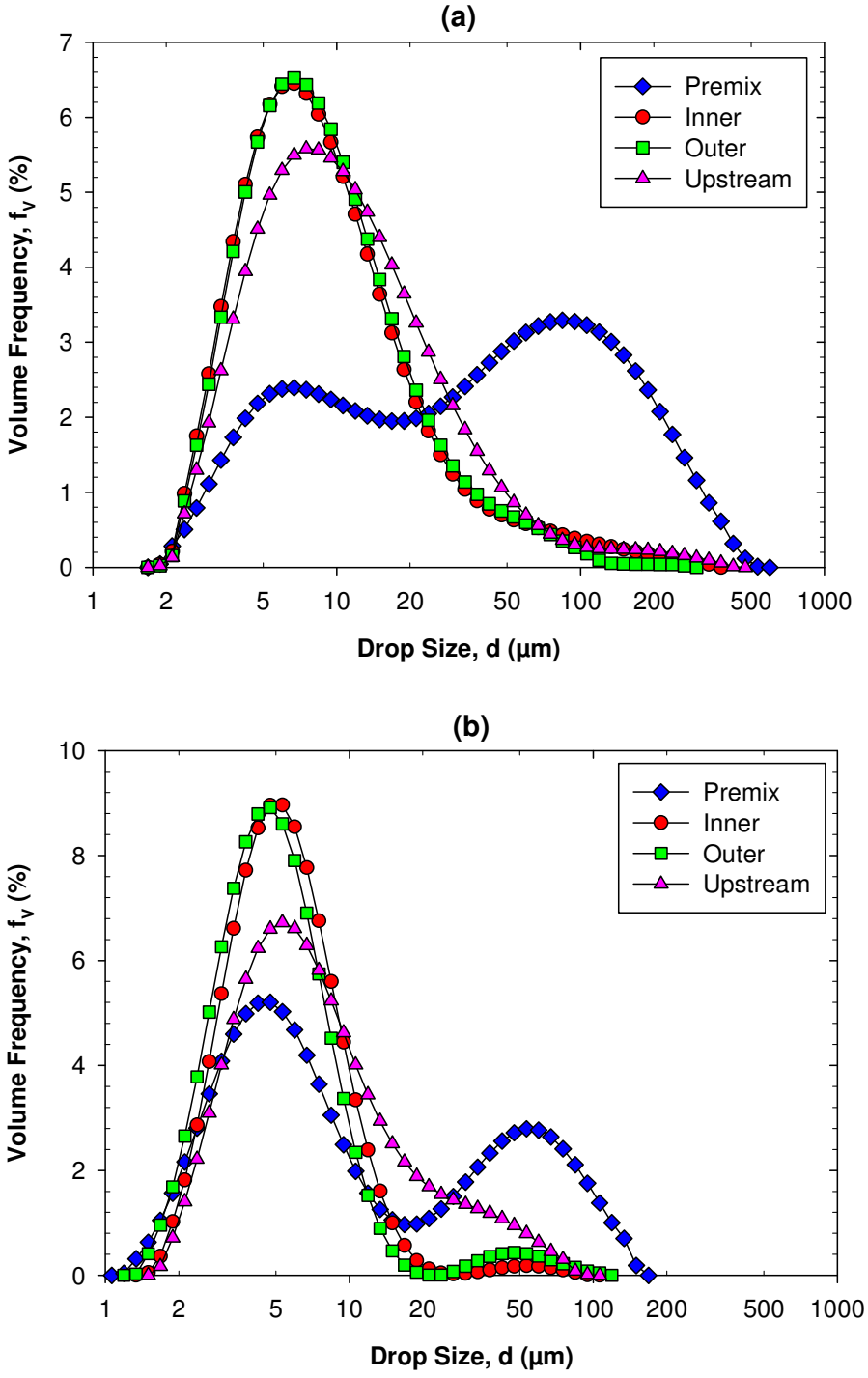

Figure 8.18: Volume drop size distributions at tip speeds of (a) 10 m s^{-1} and (b) 37 m s^{-1} for 1% 9,701 mPa·s silicone oil emulsions at 300 kg h^{-1}, comparing addition of the dispersed phase either as a premix, or injection into the inner stator, the outer stator, or upstream of the mixer.

The volume DSDs in Figure 8.18 clearly show that creation of a premix resulted in distinct bimodal DSDs at tip speeds of 10 and 37 m s^{-1}, compared to oil injection where the distributions became more monomodal. At the lower tip speed (Figure 8.18a), injection into the inner or outer stator formed a single modal distribution with a long tail containing a small volume of large drops. Injection upstream of the mixing head produced a similar shape of distribution, with a slight shift towards larger drop sizes. These results plainly show that the breakage mechanism differs for the injection cases.

At the higher tip speed (Figure 8.18b) the same trend was observed as for the lower tip speed, with a shift from bimodal to single modal distributions once the oil was injected, with a reduction in d_{max}. The DSD for oil injection upstream of the mixing head less closely resembled the DSDs for injection into the stator, due to a large population of larger droplets.

These results indicate that droplet break-up is not only a function of the processing conditions but also how the materials are brought together. The importance of this is shown in Figure 8.19 as at 10 m s^{-1}, mean drop size of the highest viscosity oil was lowest at 7.0 µm, compared to 17.0 µm and 32.6 µm for 9.4 mPa·s and 339 mPa·s oil, respectively, when oil is injected into the inner stator. At 37 m s^{-1}, the 9,701 mPa·s oil DSD falls between that of the 9.4 mPa·s and 339 mPa·s oils.

According to Gelest Inc. (2004), high viscosity silicone oils (> 1,000 cSt) exhibit pseudoplastic behaviour beyond a critical velocity gradient, hence the findings from this study may be attributed to a reduction in the apparent viscosity of 9,701 mPa·s oil. The most likely mechanism is breakage of viscous drops in the form of long threads in extensional flow, discussed in Section 5.7. Nevertheless, these findings imply that the role of the initial droplet size may be critical in certain circumstances, and tip speed or energy dissipation rate alone cannot predict droplet size.

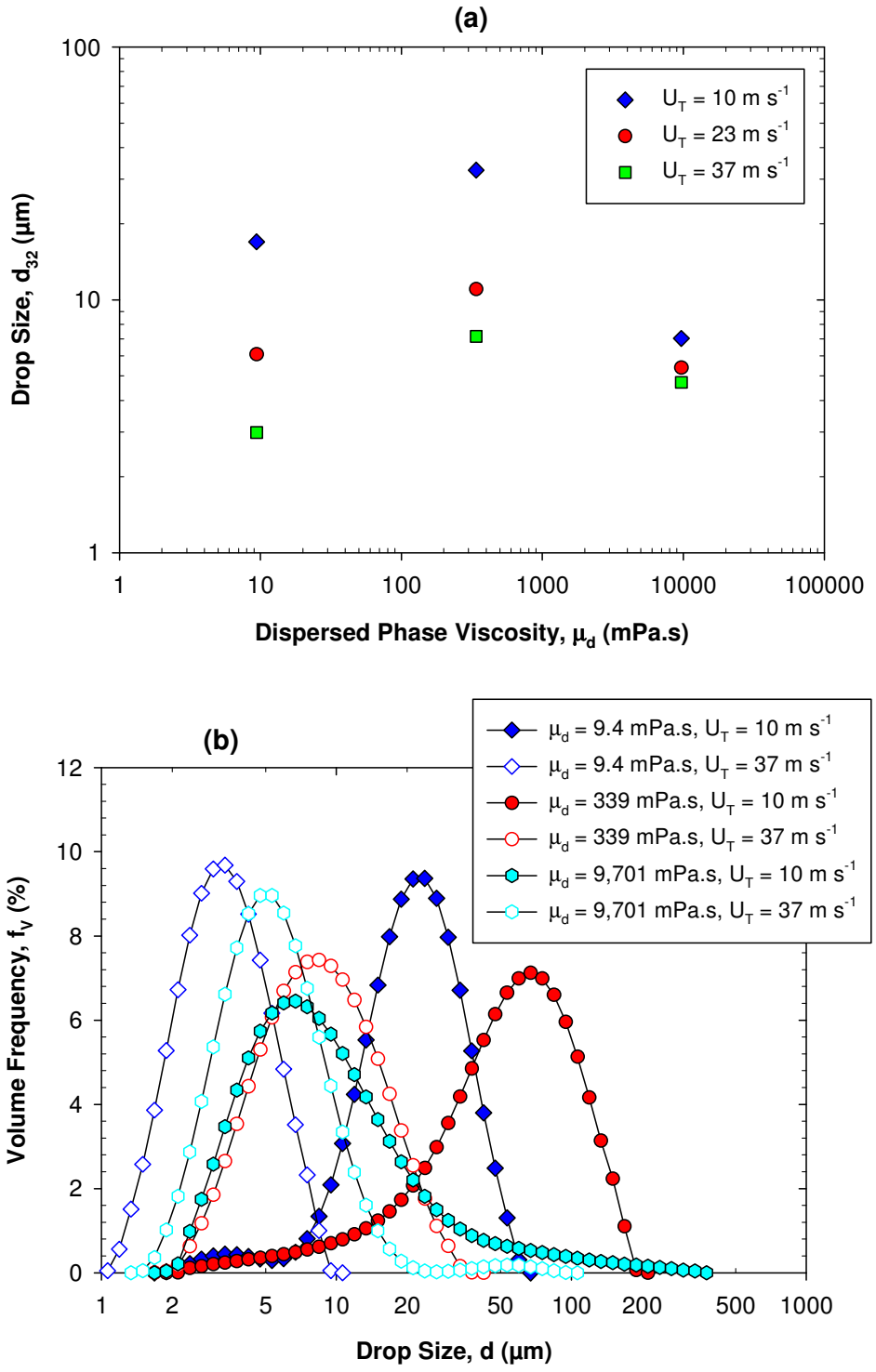

Figure 8.19: (a) Mean drop size of emulsions by injection into the inner stator as a function of dispersed phase viscosity for three tip speeds, and (b) Volume drop size distributions at 10 and 37 m s^{-1} for 1% 9.4, 339 and 9,701 mPa·s silicone oil emulsions at 300 kg h^{-1} by injection into the inner stator.

8.6.3 Droplet deformation times

To better understand droplet break-up of 9,701 mPa·s oil emulsions, it is useful to compare the droplet deformation times, (calculated from Eq. (5.5) for the turbulent inertial sub-range, using d_{32} as mean drop diameter) and internal recirculation residence times in the mixer. Residence time has been defined using Eq. (6.2), and while this provides a good estimate for correlations, it is not truly representative as it does not account for internal recirculation. For example, Eq. (6.2) for single passes assumes τ tends to infinity when flow rate is zero, hence the real expression is:

$$\tau_{IR} = \frac{V_H}{Q+Q_L} \tag{8.5}$$

This expression includes total flow rate (Q) through the mixing head, and local flow rate (Q_L), which is the component of the total flow rate through the screen due to internal recirculation (Figure 8.20). Thus, when total flow rate is zero, internal recirculation residence time is a maximum.

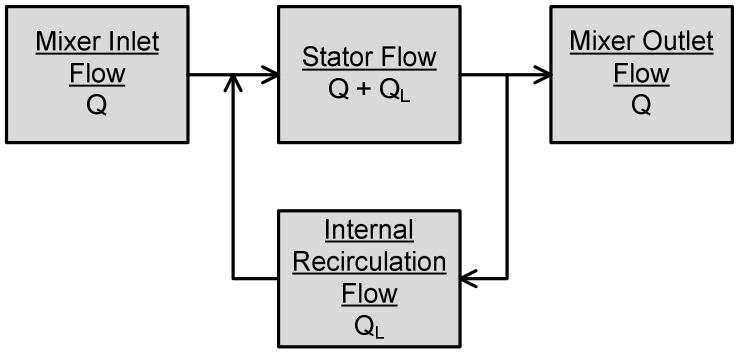

Figure 8.20: Diagram of the stator flow rates in the mixing head.

To apply Eq. (8.5), Q_L should be estimated, which may be achieved simply from the power number, since $Po \propto Q$ (Utomo et al., 2009). From Section 4.6, it is known that Po_U = 0.66 for unrestricted flow, and Po_Z = 0.24 for zero flow. Power number for the blank stator is

~ 0.08 (Table 4.3 in Section 4.8), therefore power draw due to internal recirculation across the holes can be approximated by:

$$Po_{Q_L} \approx (0.24 - 0.08) \approx 0.16 \tag{8.6}$$

From $Po \propto Q$:

$$\frac{Po_U}{Po_{Q_L}} \propto \frac{Q_{max}}{Q_L} \tag{8.7}$$

The application of Eq. (8.7) gives $4Q_L \approx Q_{max}$, which was supported by numerical simulations. At 6,000 rpm, Q_L was estimated as 893 kg h^{-1} from CFD (Figure 4.25 in Section 4.9), compared to a relatively similar value of 1,221 kg h^{-1} calculated from Eq. (8.7). The simulated value of Q_L = 893 kg h^{-1} is slightly lower than predicted from the power numbers for several reasons, see Section 4.9.

Values of Q_{max} from Section 4.5 for each rotor speed, were used in Eq. (8.7) to estimate Q_L. From this analysis, two extremes of τ_{IR} are defined:

$$Q = 0, \tau_{IR} = \tau_{IR,max} \tag{8.8}$$

$$Q = Q_{max}, \tau_{IR} = \tau_{IR,min} \tag{8.9}$$

The estimate of τ_{IR} for these extreme conditions is shown in Figure 8.21. The calculation of residence time ranges from 54 to 222 ms at 3,000 rpm to 15 to 61 ms at 11,000 rpm.

Figure 8.21 compares the estimated values of τ_{IR} with droplet deformation times for premixed emulsions of 9.4, 339 and 9,701 mPa·s oil, and 9,701 mPa·s oil injected upstream of the mixing head. The initial droplet size of the premixed emulsions was measured as 45 µm for 9.4 and 339 mPa·s oil, and 32 µm for 9,701mPa·s oil. A value of 4,570 µm for 9,701 mPa·s oil injected was taken as the initial droplet size, which is the pipe diameter (4.57 mm) used to pump the oil into the mixer.

Figure 8.21 shows that the lower the oil viscosity, the easier drops deform, with deformation times of 6 to 77 µs for 9.4 mPa·s oil emulsions. Interestingly, the deformation times of the premixed 9,701 mPa·s oil drops are of the order of the mixer internal recirculation residence time, from 8 to 100 ms. However, once the 9,701 mPa·s oil was injected to form a dispersion of larger drops, the droplet deformation time falls by roughly two orders of magnitude. This may explain why bimodal DSDs were observed for high viscosity oil premix emulsions, but not for emulsions once the oil was injected.

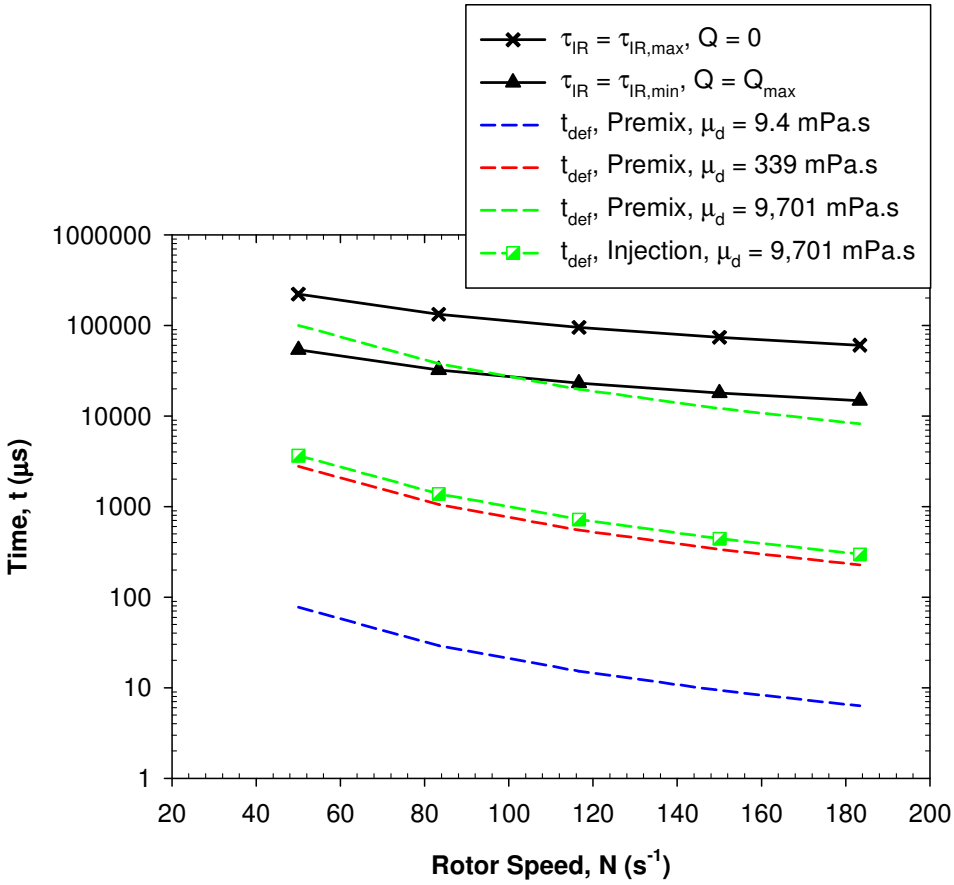

Figure 8.21: A comparison of the estimated maximum and minimum internal recirculation residence times, with droplet deformation times of emulsions of 9.4, 339 and 9,701 mPa·s oil premixed, and 9,701 mPa·s oil injected upstream.

Figure 8.22 presents the ratio of the maximum internal recirculation residence time to the droplet deformation time for systems with different initial emulsion droplet sizes. In reality these ratios are an overestimate as $\tau_{IR} < \tau_{IR,max}$, however the values are useful for comparison. For lower viscosity oil emulsions, $\tau_{IR} \gg t_{def}$. For 9,701 mPa·s oil emulsions, it is clear that τ_{IR} is only greater than t_{def} once the oil was injected. For premixed oil drops, and for emulsion droplets formed after a single pass, $\tau_{IR} \approx t_{def}$ and incomplete droplet deformation occurs, resulting in bimodal DSDs, while for the injected oil, the DSDs were not bimodal (Figure 8.18). Furthermore, this may explain the limited effect of multiple passes on drop size reduction for higher viscosity oil emulsions.

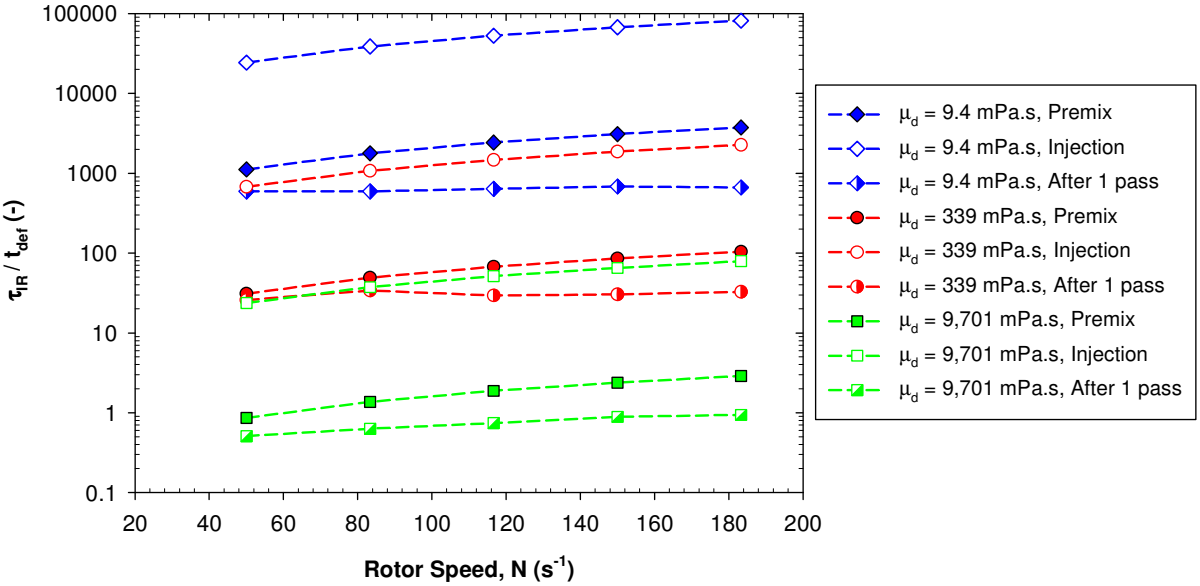

Figure 8.22: Internal recirculation residence time to deformation time ratios for emulsions of three dispersed phase oil viscosities, for initial droplet sizes created as a premix, by injection and after one pass, where $\tau_{IR} = \tau_{max}$.

For a 1 wt.% emulsion, the oil flow rate (0.017 m s^{-1}) was five times lower than the continuous phase flow rate (0.09 m s^{-1}). Hence, the injected oil formed no appreciable jet into the continuous phase, so the assumption of large droplet injection into the pipeline may be

correct. For higher phase volumes (> 5 wt.%), the oil velocity would exceed the velocity of the continuous phase, resulting in a jet which may cause droplets to break-up prior to entering the mixer.

8.6.4 Summary of droplet break-up

Droplet break-up in in-line rotor-stator mixers may be divided into five regimes based on the observations from Chapters 7 and 8. The regimes depend on the ratio of internal recirculation residence time to droplet deformation time (τ_{IR}/t_{def}), and the ratio of drop size to the Kolmogorov length scale (d/η_K), see Table 8.8.

Table 8.8: Droplet break-up summary.

μ_d	d/η_K	τ_{IR}/t_{def}	x in ε^{-x}	y in ${t_R}^{-y}$	Comments
High	Large	Small	-	-	Incomplete droplet break-up
High	Large	Large	0.25	< 0.1	
Intermediate	Large	Large	0.3-0.35	~ 0.1	
Low	Large	Large	0.4	~ 0.2	Sensitive to multiple passes
Low	Small	Large	0.5-0.75	> 0.3	

8.7 Summary

The stator open area was found to be the key rotor-stator geometry parameter affecting emulsion mean drop size, while rotor-stator gap width, stator thickness and number rotor of blades had less effect. Geometry parameters also had a limited effect on emulsification efficiency, apart from removal of the stator which resulted in inefficient droplet break-up. Injection of the dispersed phase into the mixing head formed similar DSDs to emulsion premixes, apart from highly viscous oil drops which formed smaller drops by injection, which may be related to smaller droplet deformation times of larger mother drops.

CHAPTER 9. CONCLUSIONS AND FURTHER WORK

9.1 Conclusions

The main conclusions from this study are summarised below in sections corresponding to the findings from Chapters 4 to 8.

9.1.1 Power draw

- Power draw of in-line rotor-stator mixers scaled with rotor speed to the 3rd power, as for conventional stirred vessels, and flow rate to the 2nd power. A two-term expression (Kowalski, 2009) for turbulent power draw of an in-line rotor-stator mixer successfully correlated power measurements. It describes the effect of rotor speed and flow rate containing two constants, the first akin to classical power number in the absence of flow (Po_Z), and the second to account for the effect of flow rate (k_1).
- The torque and calorimetric methods gave similar values of power draw. The accuracy of the calorimetry method was better at lower flow rates (as temperature rises were larger), while accuracy of the torque technique improved at higher flow rates.
- The power curve for in-line rotor-stator mixers was similar in shape to conventional stirred tanks, except in the turbulent regime two power numbers were defined corresponding to zero flow (Po_Z) and unrestricted flow (Po_U) conditions.
- Experimentally measured values of turbulent power draw constants, Po_Z and k_1, were weakly dependent on scale, and can be assumed to be constant with scale for geometrically similar in-line rotor-stator mixers.

- The stator open area, more specifically, the number and diameter of the stator holes, had the greatest effect on power draw and Po_Z. This is most likely due to enhanced recirculation loops at larger open areas sucking fluid back into the rotor region. Additional geometric variables, such as the rotor-stator gap width, had a small effect on power draw in turbulent flow.
- Values of k_1 did not to correlate well with geometry parameters, although k_1 was inversely proportional to pumping efficiency.
- Good agreement between experimental and calculated (from CFD) power values were obtained at lower rotor speeds, while at higher rotor speeds experimental values exceeded simulated values by ~ 30%. The presence of the stator resulted in a few regions of very high energy dissipation and broad distributions of energy.

9.1.2 Droplet break-up

- Emulsion droplet size in an in-line Silverson high shear rotor-stator mixer was primarily influenced by the rotor speed and was almost independent of flow rate. Drop size correlations with energy density indicated that to obtain a given droplet size it is more energy efficient to operate the mixer at high flow rates.
- The outlet droplet size was not greatly affected by the inlet droplet size after a single mixer pass. In the presence of excess surfactant, the dispersed phase volume fraction did not affect the droplet size significantly.
- Droplet size increased as dispersed phase viscosity increased, but began to reach a plateau at approximately 100 mPa·s and decreased near 1,000 mPa·s. The width of the distributions broadened as the dispersed phase viscosity increased, with more pronounced bimodality at higher rotor speeds and flow rates. In general, reducing the

continuous phase viscosity resulted in smaller drop sizes as a consequence of improved transmission of stresses to the droplet surface.

- The drop sizes obtained in rotor-stator mixers are of the same order of magnitude as the Kolmogorov length scale, and thus droplet breakage is likely to occur by several mechanisms. Droplet break-up was consistent with the well established theory based on Kolmogorov, where high viscosity droplets larger than the Kolmogorov length scale are most likely broken by turbulent inertial stresses, while droplets smaller than the Kolmogorov length scale are broken by a combination of inertial and viscous stresses.

9.1.3 Single and multiple pass emulsification and modelling

- The effect of recirculation flow rate on emulsion droplet size at a given total residence time was small. The effect of rotor speed also had a limited effect on the rate of droplet break-up, except at higher rotor speeds and lower dispersed phase viscosities when droplet size was near or below the Kolmogorov length scale, and the breakage mechanism changed from turbulent inertial to turbulent viscous.
- For higher dispersed phase viscosities (> 339 mPa·s), the effect of multiple passes on drop size was limited, since the probability of further droplet break-up is restricted by the droplet deformation times of small highly viscous drops. Low viscosity oil distributions were practically log-normal while high viscosity oil distributions were broader and strongly skewed towards smaller drops.
- The difference between single and multiple passes droplet size distributions is minimal at higher dispersed phase viscosities and higher energy dissipation rates, while at lower dispersed phase viscosities, smaller drops were obtained from multiple pass operation at equal total residence times.

- A model to predict droplet size distributions in a mixing vessel (Baker, 1993) in a recirculation loop with a rotor-stator mixer was successfully applied, with equal drop size distributions in the vessel and at the mixer outlet after roughly five batch vessel turnovers.
- Application of population balance equations produced reasonable agreement between experimental and predicted (from CFD) drop size distributions, for an inviscid non-coalescing system, by applying a multi-fractal turbulence breakage kernel.

9.1.4 Scaling up

- Very good agreement in the shape and position of drop size distributions between three mixer scales was observed, which suggests that the droplet breakage mechanism was similar at all scales. For a single pass, at constant residence time in the mixing head, tip speed was found as the best scaling parameter across three scales.
- Energy dissipation rate was also a reasonable scaling parameter, however the suitability of this scaling term reduced when residence time was not constant. Application of the rotor energy dissipation rate which neglects power due to the flow rate, produced a less favourable correlation.
- The effect of multiple passes was successfully correlated with energy dissipation rate and total residence time. The exponent on energy dissipation rate describing droplet break-up compared well with theoretical models for turbulent inertial stresses, but not for turbulent viscous stresses.
- The effect of interfacial tension for non-surfactant systems was accounted for using the Weber number correlation. A comparison of mean drop sizes from surfactant and non-surfactant systems may be achieved by including an effective interfacial tension term in Weber number.

9.1.5 Rotor-stator geometry and dispersed phase addition point

- The stator open area was the most important geometry parameter influencing droplet size distributions, most likely as a result of higher recirculation flow rates, increasing the probability of further droplet break-up in each pass. The optimum stator open area for droplet break-up was near to 40%, and the shape of the drop size distributions were not greatly affected by the rotor-stator geometry.
- Additional geometry parameters including the number of rotor blades, rotor-stator gap width, stator thickness and number of stators had little effect on emulsification performance. In particular, the negligible effect of the rotor-stator gap width confirms that droplet break-up does not depend on laminar shear stresses.
- In general, emulsification efficiency was not strongly affected by the rotor-stator geometry, apart from removal of the stator which significantly reduced emulsification efficiency. At higher dispersed phase viscosities, there was little effect of the stator presence on drop size, which implies that the primary role of the stator is to increase residence time in the rotor region where energy dissipation rates are highest, since break-up of highly viscous drops are less residence time dependent.
- The effect of continuous phase viscosity did not affect drop size significantly with or without the screens present, indicating that continuous phase viscosity is not an important parameter in droplet break-up.
- For low and intermediate viscosities, similar drop size distributions were formed from coarse emulsions and by injecting the dispersed phase into the mixing head, confirming that the effect of the initial drop size is not important. However, highly viscous oils formed smaller mean drop sizes when injected, with monomodal distributions compared to bimodal distributions for premixed emulsions. This was

attributed to a decrease in droplet deformation times when large highly viscous drops were injected, as opposed to premixed emulsions where the drops were smaller and the corresponding deformation times were larger.

9.2 Further work

The key recommendations for further work arising from this study are detailed below:

- The application of 3D numerical simulations is required to fully understand the effect of rotor-stator geometry parameters on emulsification. CFD could be utilised to examine the recirculation flow rates observed, possible correlating parameters such as maximum energy dissipation and strain rate, and to solve population balance equations.
- Behaviour such as a maximum in droplet size for low viscosity oil emulsions with increasing continuous phase viscosity was observed when investigating high continuous phase viscosities. Further analysis of the effect of high continuous phase viscosities, in transitional and turbulent flow, for industrially relevant Newtonian and non-Newtonian fluids, on emulsification should be examined. The effect of viscoelastic rheology of emulsions on rotor-stator mixer performance should also be considered, particularly at high shear rates.
- Population balance modelling is potentially a powerful tool in scale-up of emulsification processes, as a result, more work is required to develop appropriate breakage and fragmentation models to describe droplet break-up. The models should account for the effect of processing conditions such as flow rate and multiple passes, and describe drop size distributions of emulsions with different physical properties.
- The scaling parameters investigated should be extended to other rotor-stator manufacturers and other mixing devices, since this work focused on Silverson mixers.

The trends and constants should be examined further using different formulations to develop a full understanding of emulsification.

- Further analysis of different surfactant systems, in particular large molecular weight surfactants, is required to fully examine correlations with effective interfacial tension. Application of surfactants with high diffusivities should be examined further, as for some process conditions droplet break-up may become diffusion time limited. It is recommended to reanalyse the data using calculated surface dilational modulus values and surfactant diffusion times for SLES instead of using values for SDS.
- The effect of rotor-stator geometry should be examined in transitional and laminar flow conditions. Whilst these conditions are of less importance in industry, it is highly likely that geometry parameters such as the rotor-stator gap will play an important role in droplet break-up when laminar shear is important. It would also be useful to examine the effect of rotor-stator geometry using more complex emulsions containing multiple components, similar to emulsion-based products, as the role of certain geometry parameters may increase in importance.
- It would be interesting to examine further the rotor design in droplet break-up since the main focus of this work was the stator. Impeller design in stirred vessels can drastically affect droplet break-up so an advantage could be gained, although in a rotor-stator mixer the rotor should also be designed for pumping.
- The role of droplet deformation time in the deformation of highly viscous dispersed phases should be examined further by measuring the actual inlet droplet size to the mixer. It would also be interesting to extend this investigation to other emulsification devices to confirm that bimodal drop size distributions are a result of incomplete droplet breakage rather than a change in the breakage mechanism.

APPENDIX A. POWER DRAW MEASUREMENT

A.1 Power draw data

In this section, examples of the orders of magnitude of the raw power number measurements as a function of time, for the calorimetry and torque methods, including temperature difference across the mixing head for the calorimetry. Data are shown (Figure A.1) to demonstrate the reliability of power measurements at various rotor speeds and flow rates.

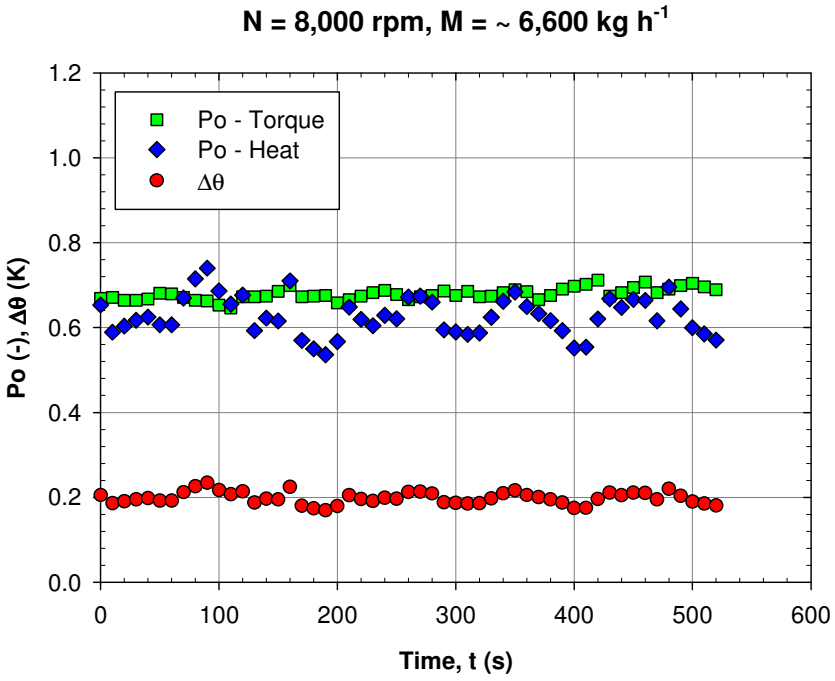

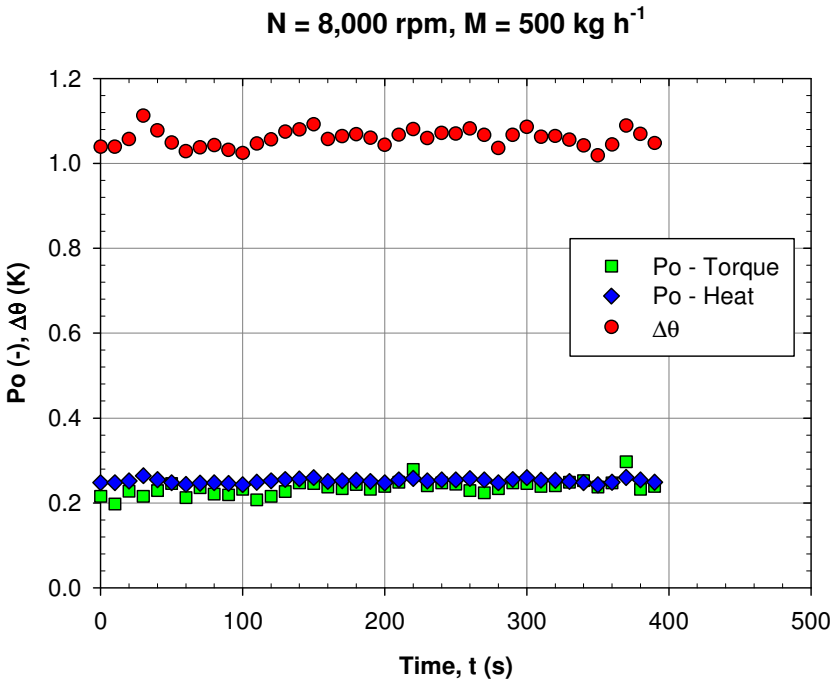
N = 8,000 rpm, M = 500 kg h-1
Po (-), Δθ (K)
Time, t (s)
Po - Torque
Po - Heat
Δθ
0.0
0.2
0.4
0.6
0.8
1.0
1.2
0
100
200
300
400
500

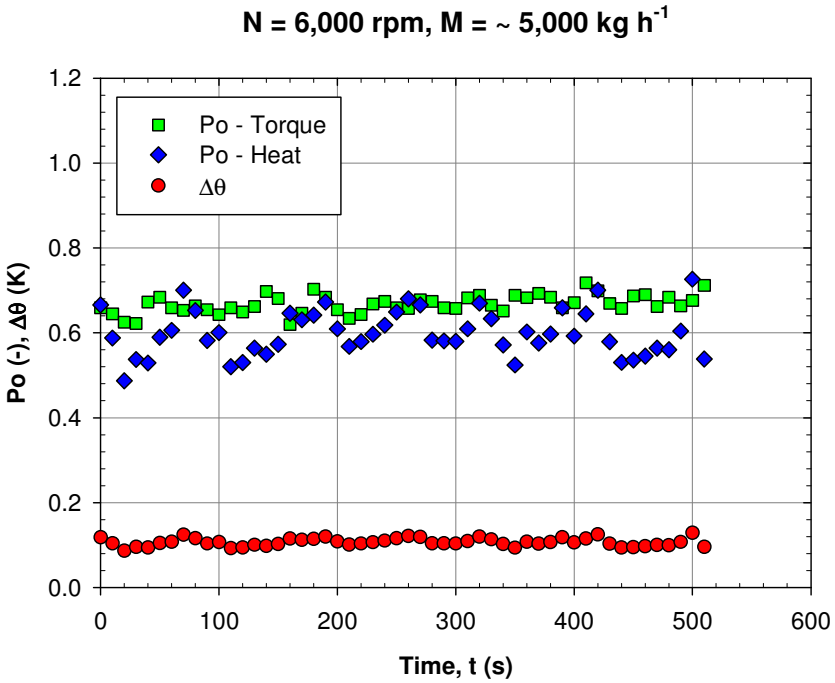
N = 6,000 rpm, M = ~ 5,000 kg h-1
Po (-), Δθ (K)
Time, t (s)
Po - Torque
Po - Heat
Δθ
0.0
0.2
0.4
0.6
0.8
1.0
1.2
0
100
200
300
400
500
600

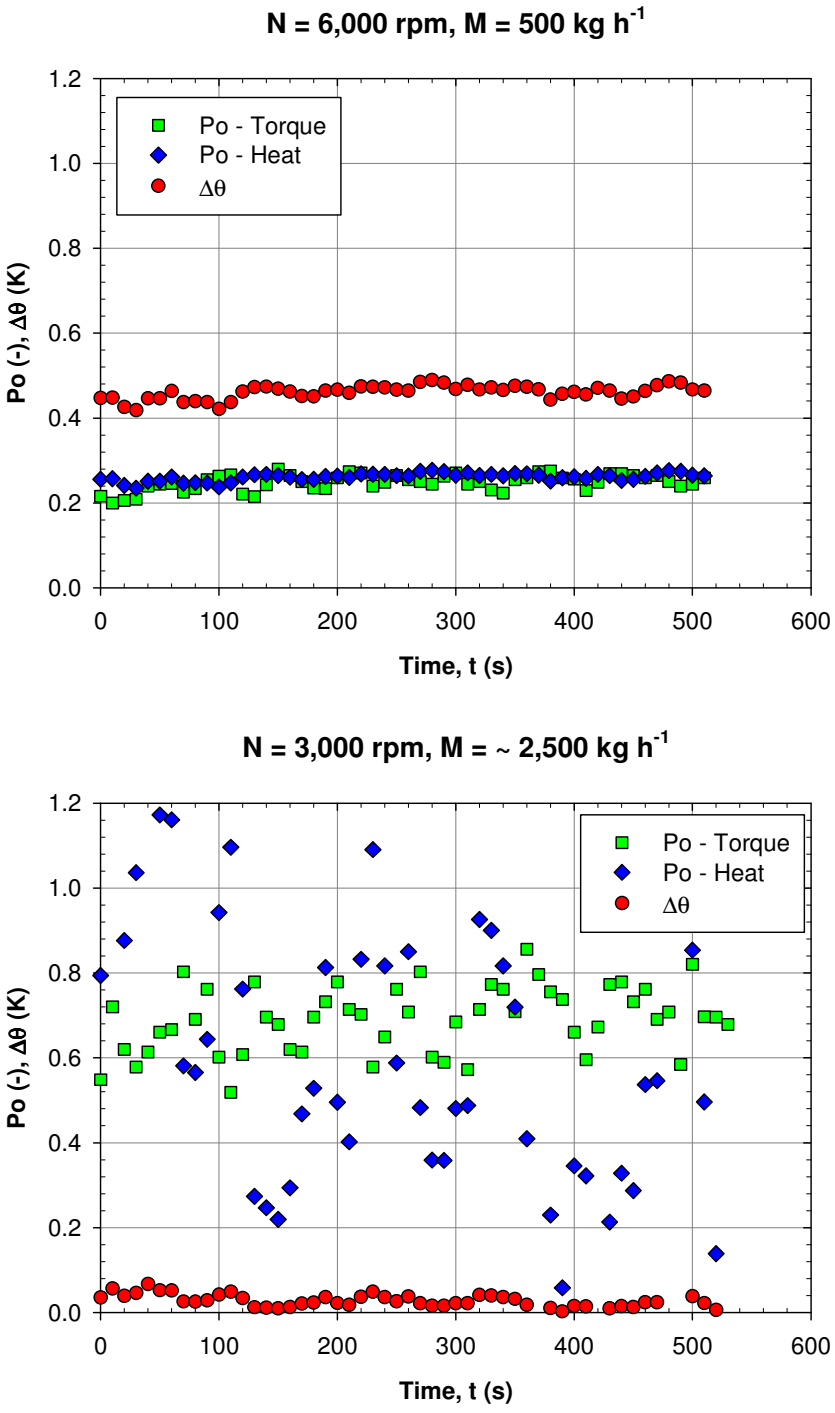

Figure A.1: A comparison of power number obtained from the calorimetry and torque methods for a range of rotor speeds and flow rates, including temperature differences.

A.2 Power draw repeatability

The reproducibility of power draw measurements are shown in Figure A.2, with torque measurements showing good repeatability (Figure A.2a). Errors can reach ~ 20% at lower rotor speeds, but on average the error is 4%. Figure A.2b shows repeats of power draw from the calorimetry method to be also reasonably good. However in certain conditions (low rotor speeds and high flow rates), the error between measurements can be ~ 60%, but on average the error is ~ 15%. For this reason, the torque method was the preferred technique, however the use of a torque meter was not possible in all cases.

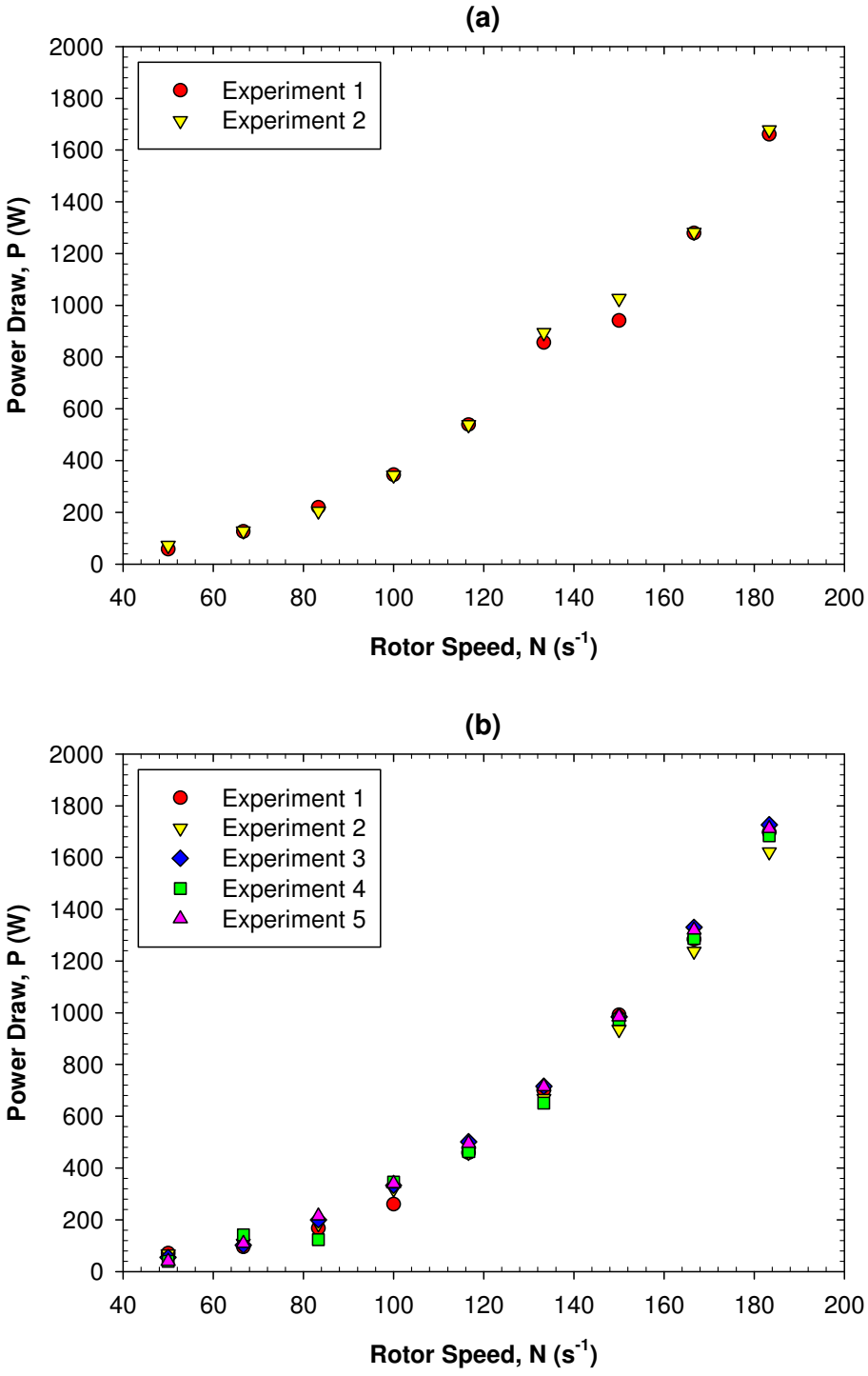

Figure A.2: Comparison of power draw measured by (a) torque and (b) calorimetry from several experiments at 1,200 kg h^{-1}.

APPENDIX B. DROP SIZE MEASUREMENT

B.1. Particle refractive index determination

The 'correct' particle refractive index was determined by a trial-and-error method by examining the residuals and weighted residuals of the drop size distribution. Graphically, the residual is the difference between the measured scattering data detected (in red) and the theoretical scattering data (in green) (Figure B.1). The residual values are for unadjusted data, while the weighted residuals are normalised for low intensity sub-micron particles. For a normal size distribution the residual is typically less than 1%.

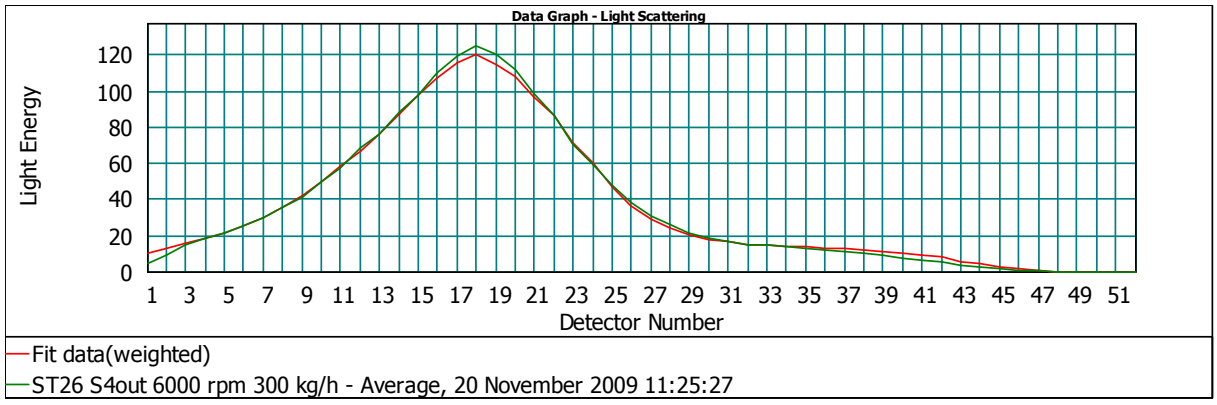

Figure B.1: Image showing measured (red) and theoretical scattering data (green).

In order to obtain the correct relative refractive index for the Mie model, weighted and unweighted residuals were plotted against particle refractive index and the correct refractive index was selected by inspection (Figure B.3a, Figure B.4a and Figure B.5a). For larger particles a minimum in the unweighted residuals is a priority, while for smaller particles a

minimum in the weighted residuals is more important. The refractive index was selected based on the following criteria (Flanagan, 2008):

- Low weighted and unweighted residuals
- Weighted and unweighted residuals of a similar order
- Believable drop size distribution

Figure B.3a, Figure B.4a and Figure B.5a show weighted and unweighted residuals plotted against particle refractive index for three oil viscosities. These plots show that both residuals achieve a minimum at roughly 1.42, which was selected as the most appropriate n_{ri} value. By inspection of several oil viscosities and operating conditions, this n_{ri} value was found to be most appropriate to produce a drop size distribution that best fits a range of light scattering patterns.

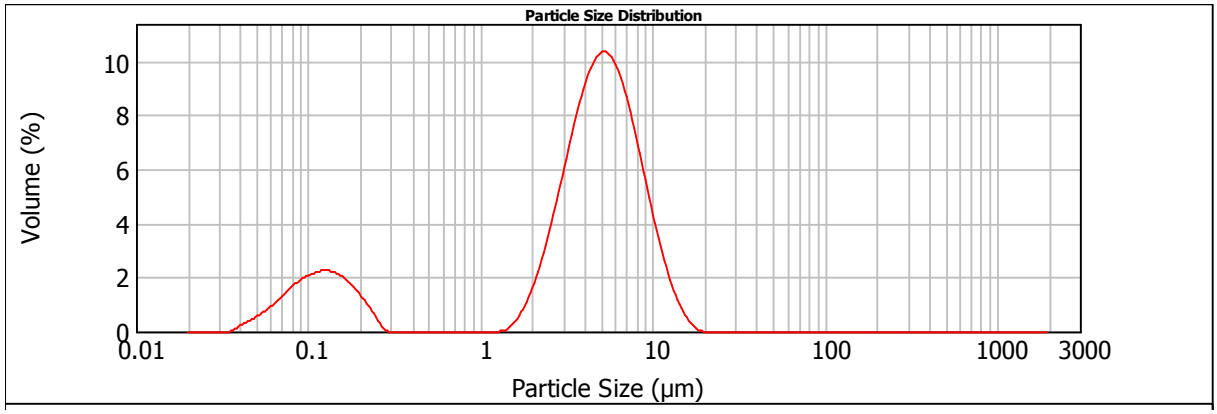

Figure B.2: Image showing errors as multiple peaks in the measured drop size distribution.

Without this procedure, errors manifest themselves by adding an extra peak either at the lower or higher ends of the drop size distribution, distorting the results (Figure B.2). Figure B.3b, Figure B.4b and Figure B.5b show the effect of particle refractive index on mean drop size. These figures clearly show that n_{ri} values < 1.42 form much smaller mean drop

sizes due to multiple peaks which are an artefact of the measurement technique, hence the DSDs are not believable. Interestingly, higher values of n_{ri} (for silicone oil) have little effect on mean drop size, although the selected value should meet all three criteria given above.

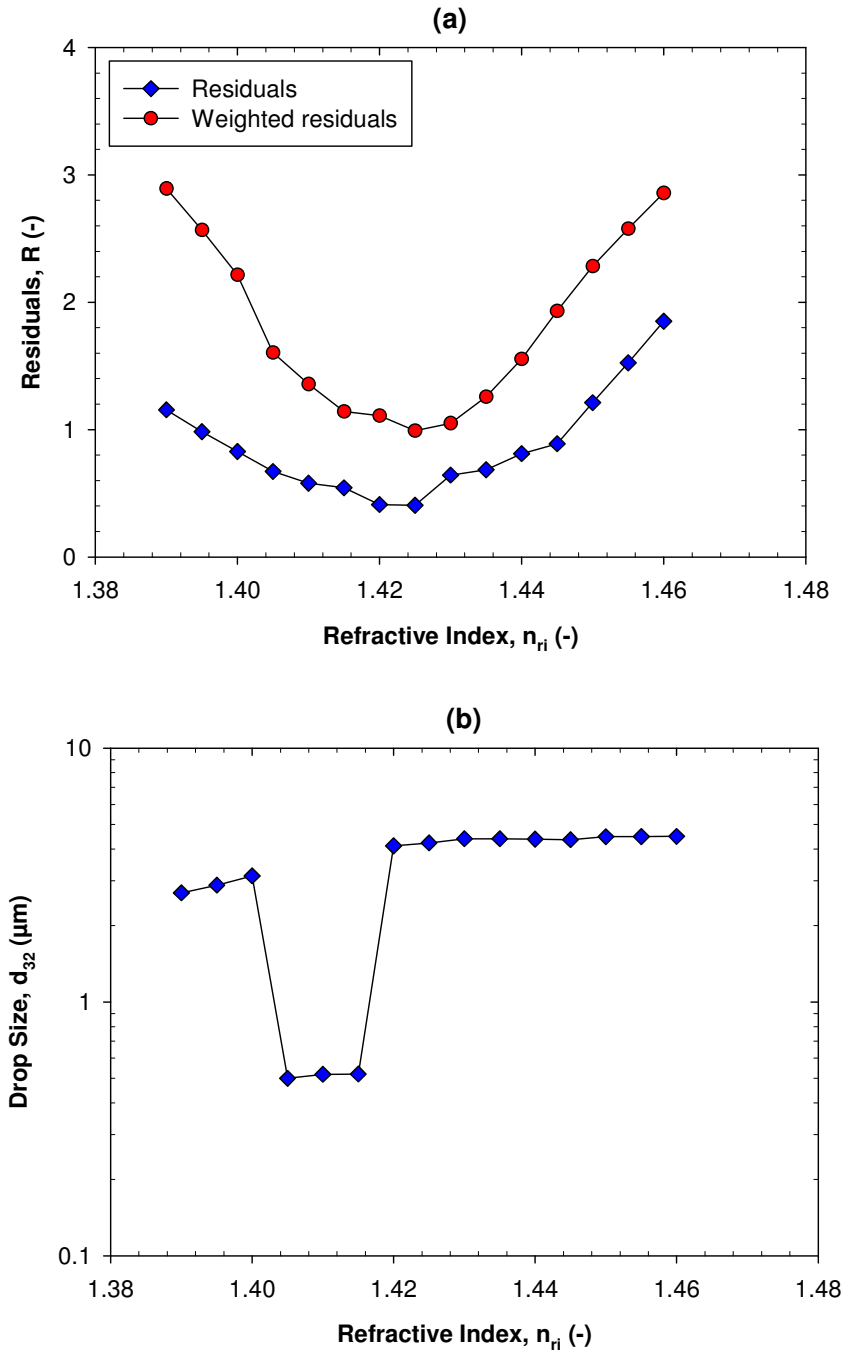

Figure B.3: (a) Mean drop size and (b) weighted and unweighted residuals as a function of particle refractive index for 1% 9.4 mPa·s silicone oil emulsions.

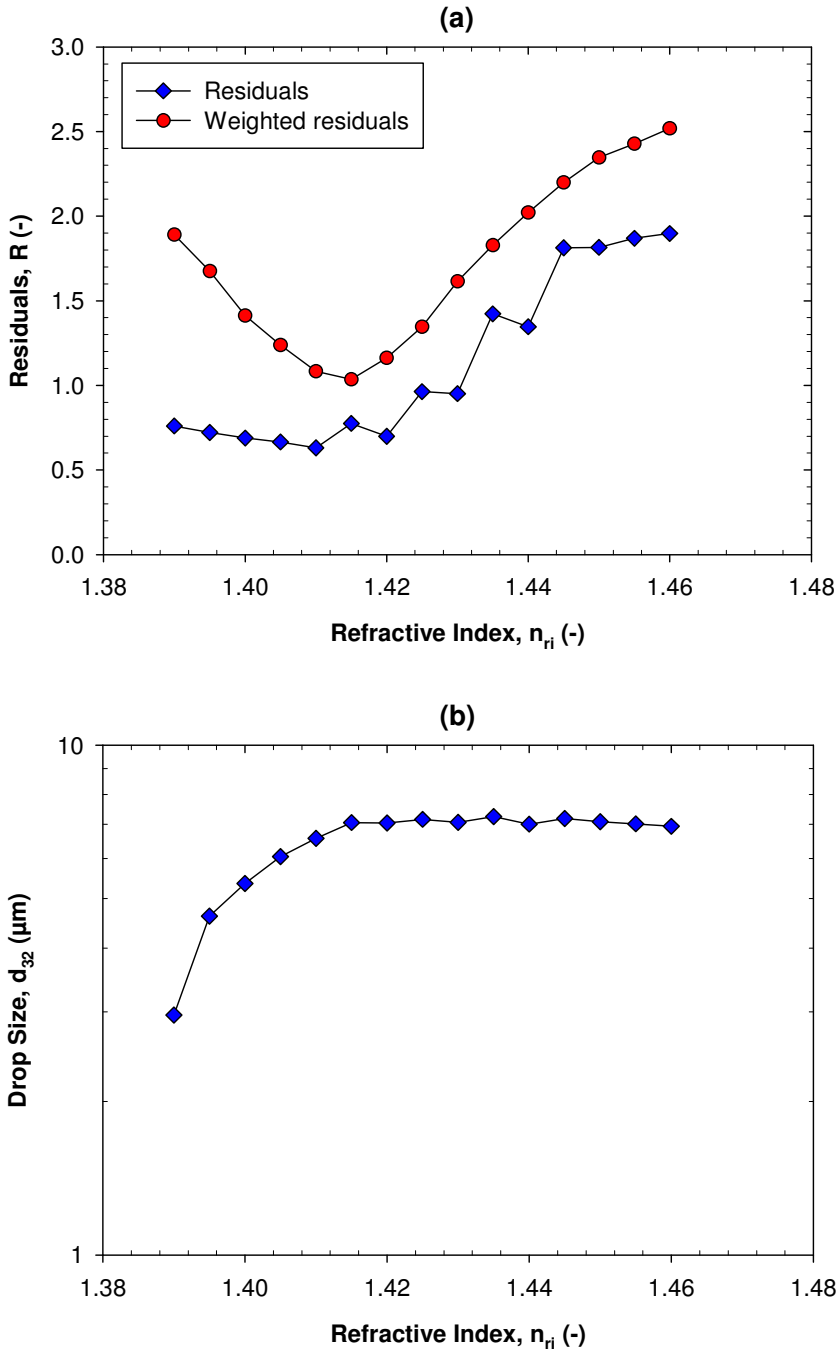

Figure B.4: (a) Mean drop size and (b) weighted and unweighted residuals as a function of particle refractive index for 1% 339 mPa·s silicone oil emulsions.

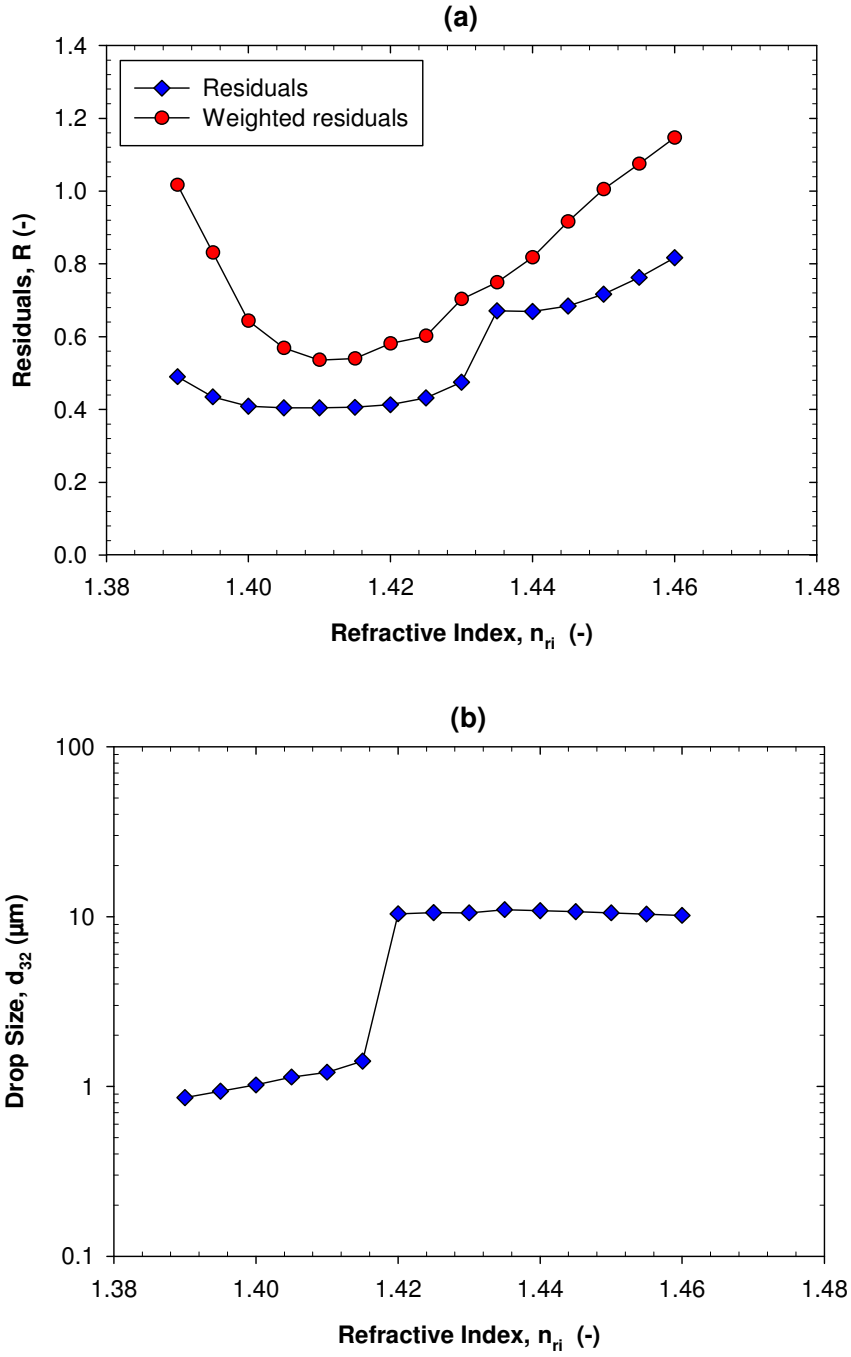

Figure B.5: (a) Mean drop size and (b) weighted and unweighted residuals as a function of particle refractive index for 1% 9,701 mPa·s silicone oil emulsions.

B.2. Comparison between Mastersizer X and 2000 models

Two models of Malvern Mastersizer particle analyser were employed to measure drop size distributions; the Mastersizer X long bed and the Mastersizer 2000.

The Mastersizer X long bed has a series of lenses that can measure different particle size ranges (Table B.1). The selected lens with a focal length of 300 mm was employed as this provided the most suitable range of drop size measurement of 1.2-600 µm.

Table B.1: Particle size measurement ranges of the Mastersizer X and 2000 particle analysers.

Analyser	**Lens (mm)**	**Particle size (µm)**
Mastersizer X	45	0.1-80
	100	0.5-180
	300	1.2-600
Mastersizer 2000	-	0.02-2,000

The Malvern Mastersizer 2000 particle size analyser measures drops in the range of 0.02 to 2000 µm using two light sources, red light, and blue light which scatters at lower angles, resulting in two significant advantages. Firstly, the more intense scattering from large particles is scattered to lower angles, giving improved sensitivity to weaker higher angle scattering from smaller particles. Secondly, some weak very high angle scattering that falls outside the angular detection range for red light, now falls within the detection range, hence further improving sensitivity for smaller particles. This capability increases the data quality, especially for small particle systems (Flanagan, 2008).

Figure B.6 shows that good fits were obtained using each sizer, with the Mastersizer 2000 reporting slightly larger mean drop sizes than the Mastersizer X, as a multiplier of 1.16 to 1.18 was required to compare each analyser.

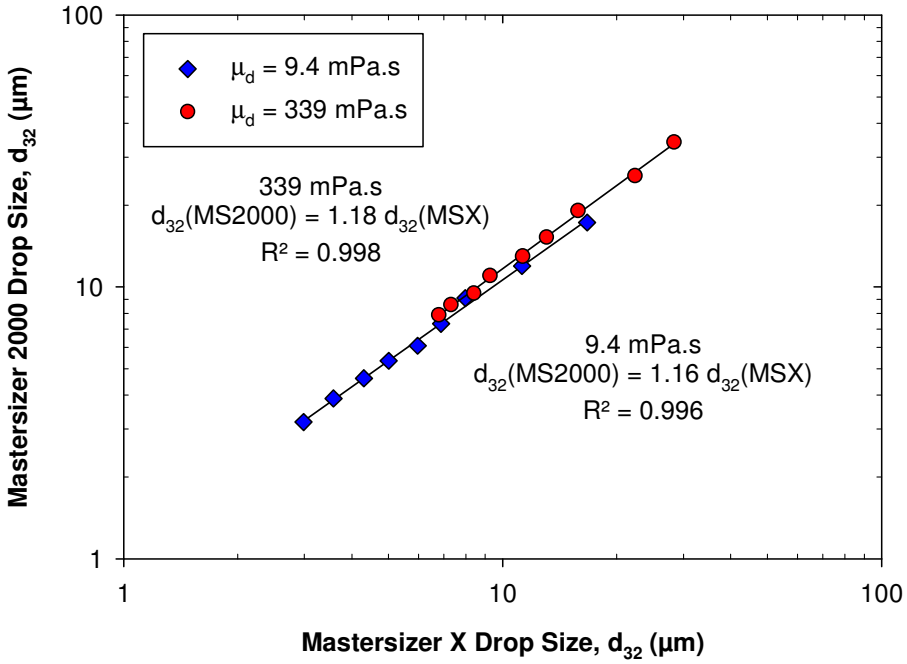

Figure B.6: Comparison between mean drop sizes measured using the Mastersizer 2000 and X for 1% silicone oil emulsions at 300 kg h^{-1}.

Figure B.7 shows that the trends of mean drop size with energy dissipation rate were practically identical from either particle analyser, however the Mastersizer 2000 gave slightly larger droplets for the same emulsion sample. This confirms that the trends obtained in correlations using each machine are comparable, however the absolute drop sizes and constants in the correlations may give some errors up to ~ 20%. As the majority of this study is concerned with scale-up, the trends are of more importance, thus the results from each analyser can be used. However, the Mastersizer X has a far smaller drop size measurement range than the Mastersizer 2000, therefore only measured data that falls within this range were considered. Furthermore, the Mastersizer 2000 is a superior machine; hence measurements from this machine were taken wherever possible.

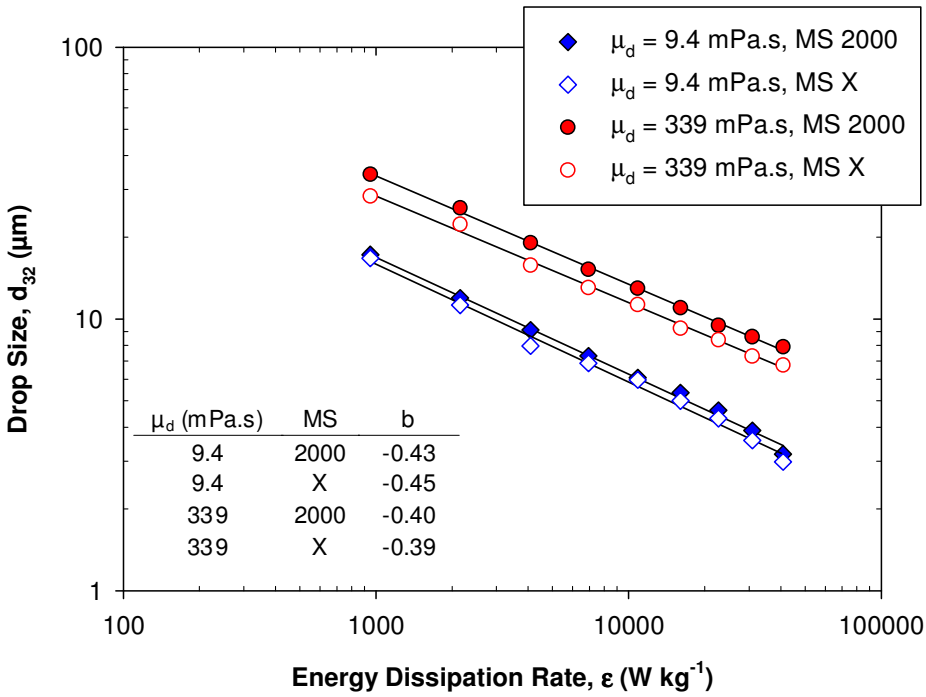

Figure B.7: Mean drop size measured using the Mastersizer 2000 and X as a function of energy dissipation rate for 1% silicone oil emulsions at 300 kg h^{-1}.

B.3. Emulsion stability

The DSDs of emulsion samples measured directly after production did not to change after many months, due to the presence of excess anionic SLES surfactant. Figure B.8 shows mean drop size for 1% 9.4 mPa·s oil emulsions to remain unchanged after 19 months. This finding was observed since SLES was present in each sample. The only analysis issue occurred for large droplets of highly viscous oil emulsion (9,701 mPa·s oil), as over time the large droplets creamed and attached themselves to the wall of the sample container, reducing the overall mean drop size. This was particularly a problem at low rotor speeds when drop sizes were larger, thus emulsions were measured soon after production, within 48 hours. This problem was also minimised by using 1% 9.4 mPa·s oil emulsions as the standard formulation, to examine the effect of geometry parameters.

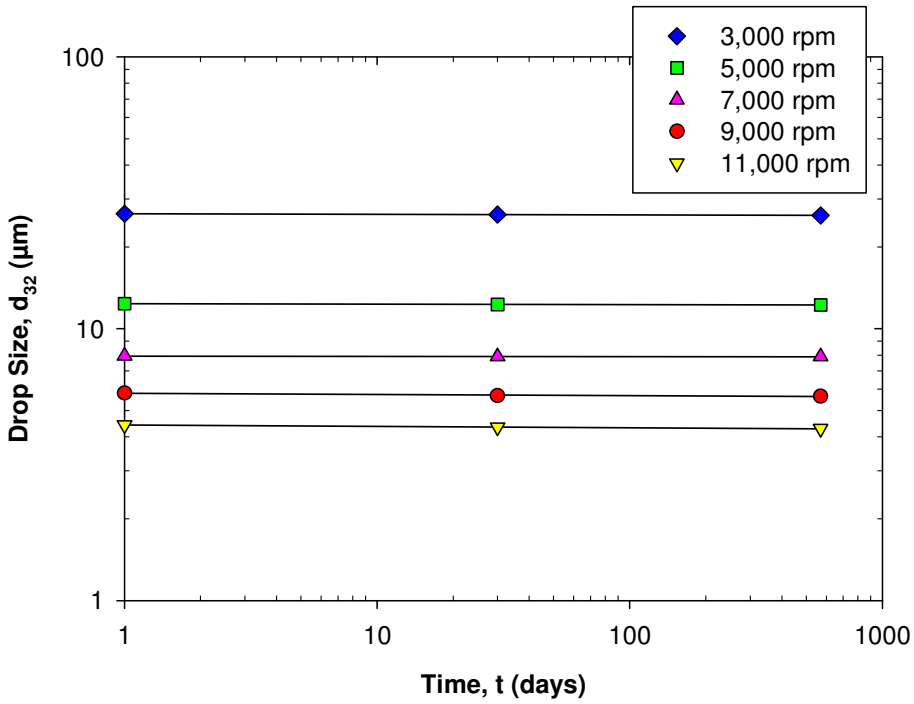

Figure B.8: Effect of time (after production) on mean drop size of emulsion samples for 1% 9.4 mPa·s silicone oil emulsions.

B.4. Drop size repeatability

Mean drop sizes of emulsions from two or three experiments as a function of rotor speed are given in Figure B.9 for three oil viscosities. All samples were analysed by the same procedure using the Mastersizer 2000, although the experimental error was virtually the same using the Mastersizer X. Figure B.9a shows the reproducibility of drop sizes of low viscosity oil emulsions was extremely good, with an error < 5%. For 339 mPa·s oil emulsions (Figure B.9b), the agreement between experiments was also excellent at high rotor speeds, with more error at lower rotor speeds, athough the error is still within 10% in all cases, and < 5% at 5,000 rpm and above. For 9,701 mPa·s oil emulsions (Figure B.9c), only at the highest rotor speeds was the error excellent, as at lower rotor speeds the droplet size increased, and

consequently for the same dispersed phase volume fraction, the number of droplets decreased (by the cube root of drop diameter). This results in high sampling errors for large drops as the probability of consistently measuring a uniform range of droplets is difficult. Errors at high viscosity reached 20%, falling to < 5% at 9,000 rpm and above.

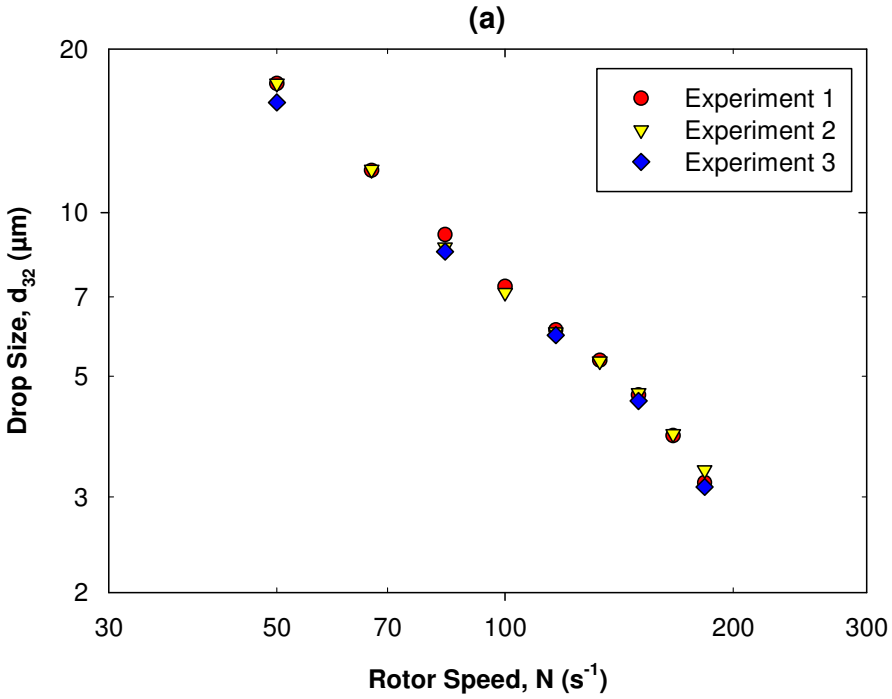

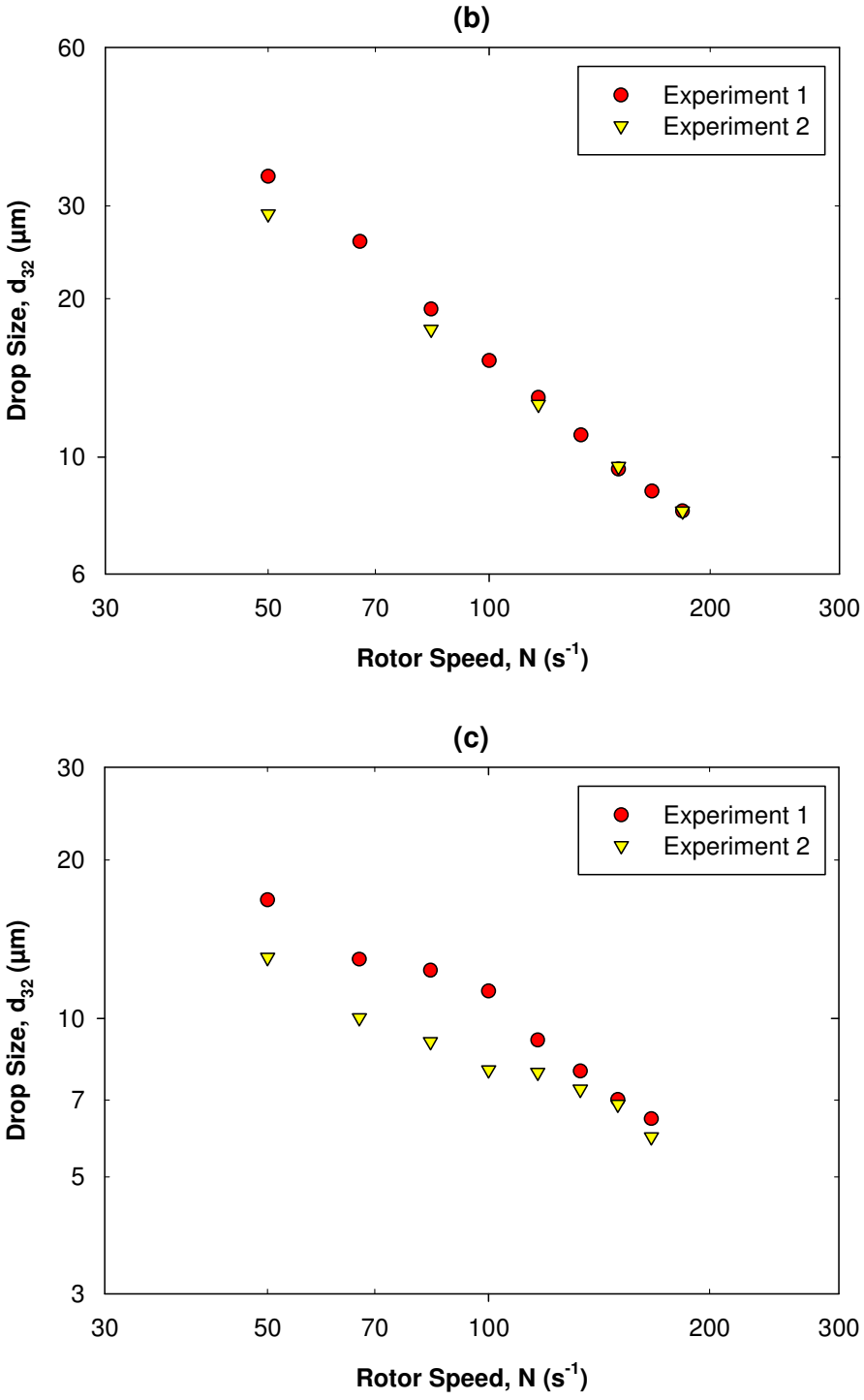

Figure B.9: Comparison of mean drop sizes of 1% (a) 9.4 mPa·s, (b) 339 mPa·s and (c) 9,701 mPa·s oil emulsions measured from various experiments using the Mastersizer 2000 particle analyser at 300 kg h^{-1}.

B.5. Analysis of bimodal drop size distributions

The bimodal drop size distributions of highly viscous oil emulsions were analysed by splitting the peaks to find the mean drop size of each peak. In the vast majority of drop size distributions, peaks 1 and 2 overlap to some extent (Figure B.10), making it difficult to easily split the peaks. The procedure used to extract the separate peaks involved fitting two log-normal distributions to the whole distribution. Each log-normal distribution was characterised by a seperate mean and standard deviation. An adjustable multiplier constant for each peak was also required to fit the data. The best fit for the peaks was obtained using the solver in Microsoft Excel to minimise the sum of the difference between the two fitted peaks and the original bimodal distribution. The mean, standard deviation and multiplier constant values were all adjusted using the solver to obtain the best fit while maintaining the same volume fraction in the two new distributions as for the original bimodal distribution. An example of how the two fitted peaks compare to the bimodal distribution is shown in Figure B.10. Appropriate mean drop diameters were then calculated for each peak using Eq. (2.36).

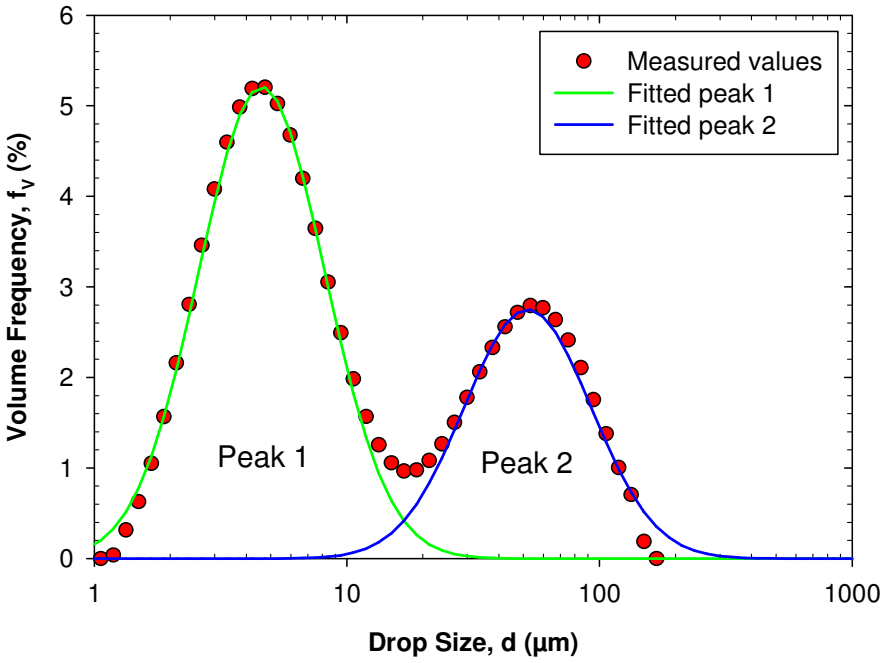

Figure B.10: Comparison of the fits of two single peaks to a bimodal drop size distribution, for 1% 9,701 mPa·s oil emulsion at 11,000 rpm and 300 kg h^{-1}.

APPENDIX C. NUMERICAL SIMULATIONS

C.1 Geometry

For 2D numerical simulations, it was necessary to transform 3D rotor-stator geometry into a 2D simplification whilst capturing aspects of the 3D geometry. For example, holes in the 3D stator geometry are transformed to slots in 2D, so a method to capture geometric parameters such as hole design, the number of rows of holes and distance between these rows was required.

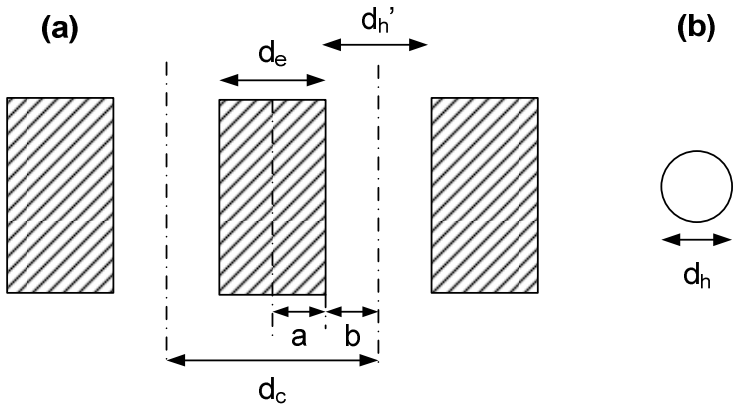

Figure C.1: Schematic diagram of the stator holes with characteristic dimensions (Baldyga et al., 2009).

The geometric parameters used for transformation are given in Figure C.1, where d_e denotes the transformed distance between the holes and d_h' the transformed hole size (Baldyga et al., 2009). Also $d_h \neq d_h'$, so the transformed hole size (a) is not equal to the real hole size (b). The fraction of free space (ratio of surface area of holes to the complete surface area):

$$A_F = \frac{Surface\ area\ of\ holes}{Surface\ area\ of\ screen} = \frac{A_h}{A_s} \quad (A.1)$$

The perimeter of all holes per unit surface area of the screen:

$$P_F = \frac{Perimeter\ of\ holes}{Surface\ area\ of\ screen} = \frac{P_h}{A_s} \quad (A.2)$$

By correct selection of a and b, the same A_F and P_F characteristics for the 2D geometry can be found as for the 3D geometry. These parameters were chosen because the flow through the screen experiences resistance which depends on the stator open area and the perimeter of the holes (Baldyga et al., 2009). This gives:

$$A_F = \frac{bh_s}{(a+b)h_s} = \frac{b}{a+b} \quad (A.3)$$

$$P_F = \frac{h_s}{(a+b)h_s} = \frac{1}{a+b} \quad (A.4)$$

This gives:

$$b = \frac{A_F}{P_F} \quad (A.5)$$

$$a = \frac{1-A_F}{P_F} \quad (A.6)$$

Therefore the effective hole size is:

$$d_h{}' = \frac{2A_F}{P_F} \quad (A.7)$$

The distance between hole edges:

$$d_e = \frac{2(1-A_F)}{P_F} \quad (A.8)$$

The distance between hole centres:

$$d_c = \frac{2}{P_F} \quad (A.9)$$

Applying this method, the calculated geometric parameters for Silverson double emulsor screens are given in Table C.1.

Table C.1: Geometric distances in the 2D model compared to the 3D geometry for Silverson double emulsor stators (Baldyga et al., 2009).

Geometry	Effective hole size, d_h' (m)	Distance between hole centres, d_c (m)	Number of holes, n_h (-)
2D – Inner stator	0.794	1.641	50
3D – Inner stator	1.588	-	300
2D – Outer stator	0.794	1.597	84
3D – Outer stator	1.588	-	560

C.2 Population balance breakage kernels

The user defined functions (UDF) used to describe the rate of droplet breakage in Fluent (ANSYS) are given below. The Coulaloglou and Tavlarides (1977) breakage kernel:

```
#include "udf.h"
#include "sg.h"
#include "prop.h"
#include "sg_pb.h"
#include "sg_mphase.h"

DEFINE_PB_BREAK_UP_RATE_FREQ(break_up_freq, cell, thread, d_1)
{
  double eps, alpha;
  double g;

  eps = C_D(cell,thread);
  alpha = C_VOF(cell,thread);

      g = (0.00481*pow(eps,1./3.)*pow(d_1,-2./3.)/(1.+alpha))*exp(-
0.08*0.01*(1.+alpha)*(1.+alpha)/(937*pow(eps,2./3.)*pow(d_1,5./3.)));

C_UDMI(cell,thread,0) = g;

return g;
}
```

The code to solve the multi-fractal turbulence breakage kernel (Baldyga and Podgorska, 1998), developed by M. Jasinska (2012):

```
#include "udf.h"
#include "sg.h"
#include "prop.h"
#include "imsl.h"

#define TRUE_ (1)
#define FALSE_ (0)
```

```
typedef long int logical;

struct {double integraL,d_1,d_2;} bob;

DEFINE_ADJUST(adjust_fcn, domain)
{
  extern double sub_integral_fun1 (double alfa);
  extern double sub_integral_fun2 (double alfa);
  extern double sub_fun (double alfa);
  extern double fun1 (double F);

  double M0, M1, M2, M3, AA, BB, CC, PD, L1, L2, W1, W2, B0b, B1b, B2b,
B3b, D0b, D1b, D2b, D3b;
  double a1, a2, b1_0, b2_0, b1_1, b2_1, b1_2, b2_2, b1_3, b2_3;

  double d_1, d_2, integraL, sub_integral_1, sub_integral_2, alfa_min,
alfa_x1, alfa_x2;
  double int1, int2, dp1, dp2, const_a, const_b, eps;
  double cx, cg;

  Thread *t;
  cell_t c;

  thread_loop_c(t,domain)
  {

      begin_c_loop_all(c,t)
      {

             cx = 8.0*0.23;
             cg = 30.0*0.0035;

             integraL =
pow((2./3.),(3./2.))*pow(C_K(c,t),(3./2.))/C_D(c,t);
             bob.integraL = integraL;
             eps = C_D(c,t);

             M0 = C_UDSI(c,t,0)*998.2;
         M1 = C_UDSI(c,t,1)*998.2;
         M2 = C_UDSI(c,t,2)*998.2;
         M3 = C_UDSI(c,t,3)*998.2;

         AA = M1*M1 - M0*M2;
         BB = M0*M3 - M1*M2;
         CC = M2*M2 - M1*M3;
             if ((BB*BB - 4.*AA*CC)<=0)
             {
              PD = 0.0;
             }
             else
              {
               PD = pow((BB*BB - 4.*AA*CC),0.5);
              }


             if (AA == 0.)
              {
                  L2 = 0.;
              }
```

```
            else
             {
                 L2 = (-BB + PD)/(2.*AA);
             }

          if ((M1-M0*L2) == 0.)
             {
                 L1 = 0.;
             }
            else
             {
                 L1 = (M2-M1*L2)/(M1-M0*L2);
             }


             if ((L2-L1) == 0.)
             {
                 W2 = 0.;
             }
            else
             {
               W2 = (M1-M0*L1)/(L2-L1);
             }

            W1 = M0 - W2;

  d_1 = L1;
  d_2 = L2;
  alfa_min = 0.12;

  bob.d_1 = d_1;
  bob.d_2 = d_2;


  if (d_1 <=  integraL)
  {

   if (d_1 <=  0.1e-6)
   {
     a1 = 0.0;
   }
   else
   {
    alfa_x1 =
((5./2.)*log10(integraL*pow(eps,0.4)*pow(998.2,0.6)/(cx*pow(0.0096,0.6)))/(
log10(integraL/d_1))) - 1.5; /*Cx*/
      if (alfa_x1 <= alfa_min)
      {
        sub_integral_1 = 0.;
        a1 = 0.;
      }
    else
      {
        sub_integral_1 = imsl_d_int_fcn (sub_integral_fun1, alfa_min,
alfa_x1, IMSL_RULE, 1, 0);
        a1 = cg*pow(log(integraL/d_1),(1./2.))*pow(eps,(1./3.))*pow(d_1,(-
2./3.))*sub_integral_1; /*Cg*/
      }
   }
```

```
  }
  else
  {
   a1 = cg*pow(eps,(1./3.))*pow(integraL,(-2./3.)); /*Cg*/
  }

  if (d_2 <=  integraL)
  {
   if (d_2 <=  0.1e-6)
   {
     a2 = 0.0;
   }
   else
   {
      alfa_x2 =
((5./2.)*log10(integraL*pow(eps,0.4)*pow(998.2,0.6)/(cx*pow(0.0096,0.6)))/(
log10(integraL/d_2))) - 1.5; /*Cx*/
      if (alfa_x2 <= alfa_min)
      {
        sub_integral_2 = 0.;
        a2 = 0.;
      }
    else
      {
        sub_integral_2 = imsl_d_int_fcn (sub_integral_fun2, alfa_min,
alfa_x2, IMSL_RULE, 1, 0);
        a2 = cg*pow(log(integraL/d_2),(1./2.))*pow(eps,(1./3.))*pow(d_2,(-
2./3.))*sub_integral_2; /*Cg*/
      }
   }
  }
  else
  {
     a2 = cg*pow(eps,(1./3.))*pow(integraL,(-2./3.)); /*Cg*/
  }


              C_UDMI(c,t,4) = integraL;
              C_UDMI(c,t,5) = d_1;
              C_UDMI(c,t,6) = d_2;
              C_UDMI(c,t,7) = W1;
              C_UDMI(c,t,8) = W2;

              C_UDMI(c,t,9)  = M0;
              C_UDMI(c,t,10) = M1;
              C_UDMI(c,t,11) = M2;
              C_UDMI(c,t,12) = M3;

              C_UDMI(c,t,13) = a1;
              C_UDMI(c,t,14) = a2;
              C_UDMI(c,t,15) = sub_integral_1;
              C_UDMI(c,t,16) = sub_integral_2;
              C_UDMI(c,t,17) = alfa_x1;
              C_UDMI(c,t,18) = alfa_x2;

          b1_0 = 2.;
              b2_0 = 2.;
              b1_1 = pow(2.,(2./3.))*L1;
              b2_1 = pow(2.,(2./3.))*L2;
```

```
            b1_2 = pow(2.,(1./3.))*L1*L1;
            b2_2 = pow(2.,(1./3.))*L2*L2;
            b1_3 = pow(L1,3.);
            b2_3 = pow(L2,3.);

            B0b = a1*b1_0*W1 + a2*b2_0*W2;
            B1b = a1*b1_1*W1 + a2*b2_1*W2;
            B2b = a1*b1_2*W1 + a2*b2_2*W2;
            B3b = a1*b1_3*W1 + a2*b2_3*W2;

            D0b = a1*W1 + a2*W2;
            D1b = L1*a1*W1 + L2*a2*W2;
            D2b = L1*L1*a1*W1 + L2*L2*a2*W2;
            D3b = pow(L1,3.)*a1*W1 + pow(L2,3.)*a2*W2;

            C_UDMI(c,t,0) = B0b - D0b;
            C_UDMI(c,t,1) = B1b - D1b;
            C_UDMI(c,t,2) = B2b - D2b;
            C_UDMI(c,t,3) = B3b - D3b;

        }
      end_c_loop_all(c,t)
  }
}


DEFINE_DIFFUSIVITY(diffusivity,c,t,i)
{
return (1e-9+(0.1*C_K(c,t)*C_K(c,t)/C_D(c,t)))*998.2;
}

DEFINE_SOURCE(source_0, c, t, dS, eqn) /* m0 */
{
real X;
X = C_UDMI(c,t,0);
dS[eqn]=0.;
return X; }

DEFINE_SOURCE(source_1, c, t, dS, eqn) /* m1 */
{
real X;
X = C_UDMI(c,t,1);
dS[eqn]=0.;
return X; }

DEFINE_SOURCE(source_2, c, t, dS, eqn) /* m2 */
{
real X;
X = C_UDMI(c,t,2);
dS[eqn]=0.;
return X; }

DEFINE_SOURCE(source_3, c, t, dS, eqn) /* m3 */
{
real X;
X = C_UDMI(c,t,3);
dS[eqn]=0.;
return X; }
```

```
double sub_integral_fun1 (double alfa)
{
 double x, fun, p;
 double a1 = -3.510, b1 = 18.721, c1 = -55.918, d1 = 120.90, e1 = -162.54,
f1 = 131.51, g1 = -62.572, h1 = 16.10, i1 = -1.7264;
 fun = a1 + b1*alfa + c1*pow(alfa,2) + d1*pow(alfa,3) + e1*pow(alfa,4) +
f1*pow(alfa,5) + g1*pow(alfa,6) + h1*pow(alfa,7) + i1*pow(alfa,8);
 p = (alfa + 2. - 3*fun)/3.;
 x = pow((bob.d_1/bob.integraL),p);
 return x;
}

double sub_integral_fun2 (double alfa)
{
 double x, fun, p;
 double a1 = -3.510, b1 = 18.721, c1 = -55.918, d1 = 120.90, e1 = -162.54,
f1 = 131.51, g1 = -62.572, h1 = 16.10, i1 = -1.7264;
 fun = a1 + b1*alfa + c1*pow(alfa,2) + d1*pow(alfa,3) + e1*pow(alfa,4) +
f1*pow(alfa,5) + g1*pow(alfa,6) + h1*pow(alfa,7) + i1*pow(alfa,8);
 p = (alfa + 2. - 3*fun)/3.;
 x = pow((bob.d_2/bob.integraL),p);
 return x;
}

double sub_fun (double alfa)
{
 double x, fun, p;
 double a1 = -3.510, b1 = 18.721, c1 = -55.918, d1 = 120.90, e1 = -162.54,
f1 = 131.51, g1 = -62.572, h1 = 16.10, i1 = -1.7264;
 fun = a1 + b1*alfa + c1*pow(alfa,2) + d1*pow(alfa,3) + e1*pow(alfa,4) +
f1*pow(alfa,5) + g1*pow(alfa,6) + h1*pow(alfa,7) + i1*pow(alfa,8);
 p = (alfa + 2. - 3*fun)/3.;
 x = pow((0.001/0.01),p);
 return x;
}
```

C.3 Reconstructed drop size distributions

The theoretical DSDs were reconstructed from the four moments at the mixer outlet by assuming a log-normal distribution (John et al., 2007):

$$f(d) = \frac{1}{dln\sigma_g\sqrt{2\pi}} exp\left(-\frac{ln^2\left(d/\bar{d}_g\right)}{2ln^2\sigma_g}\right) \tag{A.10}$$

The following distribution properties are based on the first three moments:

$$\bar{d} = \frac{m_1}{m_0} \tag{A.11}$$

$$c_v = \sqrt{\frac{m_0 m_2}{m_1^2} - 1} \tag{A.12}$$

$$\bar{d}_g = \frac{\bar{d}}{\exp(0.5 ln^2 \sigma_g)} \tag{A.13}$$

$$\sigma_g = \exp(\sqrt{c_v^2 + 1}) \tag{A.14}$$

The reconstructed DSDs were compared with experimental DSDs in Section 6.10.

APPENDIX D. BATCH ROTOR-STATOR MIXERS

D.1 Experimental set-up

A study using a Silverson L4R batch rotor-stator mixer (Figure D.1) was undertaken using the same silicone emulsions dispersed in 0.5 wt.% SLES as for the in-line rotor-stator mixers, for comparison. The emulsion was processed in stages at tip speeds of 5.9, 7.4, 8.9, 10.3 and 11.8 m s^{-1}, for 30 minutes. A 1 L jacketed vessel was used at a temperature of 25 ºC and DSDs were sampled and measured using the method described in Section 3.3.

Figure D.1: Batch L4R rotor-stator mixer.

D.2 Application of scale-up correlations for in-line and batch rotor-stator mixers

The applicability of the scale-up correlations developed for in-line rotor-stator mixers in Chapter 7 was extended to a batch rotor-stator mixer. The correlation applied for batch and in-line mixers in Figure D.2 is for inertial stresses for $L \gg d \gg \eta_K$, given by Eq. (7.4) using the constants in Table 7.5. For the batch mixer, t_R was calculated from Eq. (6.2) using flow rate through the batch mixing head estimated from CFD simulations as 0.34 kg s^{-1} by Utomo et al. (2009).

Figure D.2 shows a good correlation for the higher viscosity oil emulsions (where the effect of residence time is small) is obtained between the batch and in-line mixers, while the fit for the lower viscosity oil emulsion data is reduced. Yang (2011) simulated batch and in-line Silverson mixers and found the flow patterns to be rather different and suggested scale-up may be difficult, which would explain the less favourable fit in Figure D.2 for the low viscosity oil. Furthermore, the difficulty in scaling from batch to in-line mixers prompted Silverson Machines Ltd. to develop the lab scale 088/150 mixer to maintain geometric similarity and more comparable flow fields.

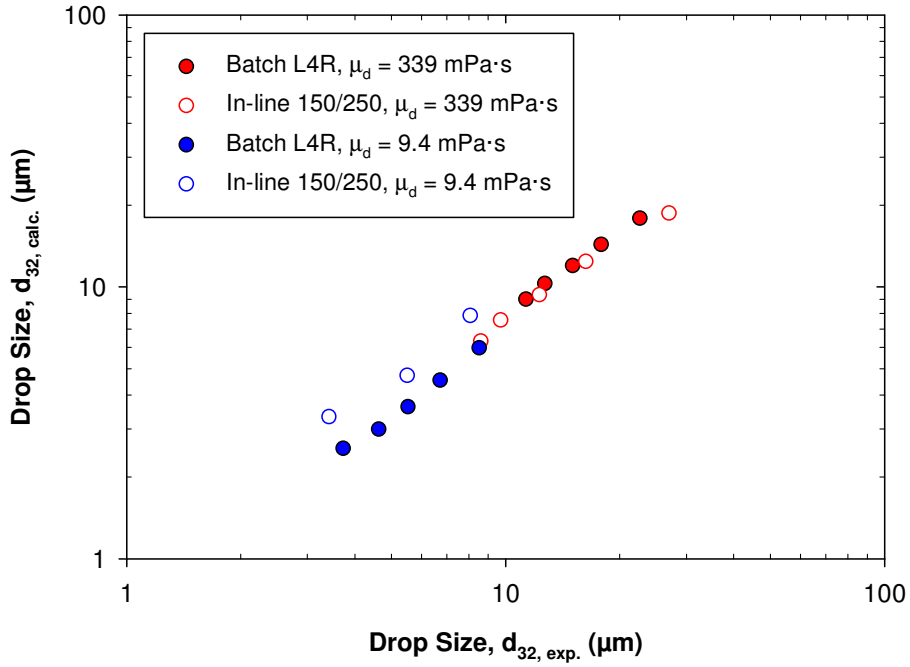

Figure D.2: Quality of fit between mean drop size from the correlation presented by Eq. (7.4) with experimental mean drop size, for 1% 9.4 and 339 mPa·s silicone oil emulsions for an in-line 150/250 mixer and a batch L4R mixer. Constants used are from Table 7.5.

D.3 Effect of initial droplet size on final droplet size in a batch rotor-stator mixer

The premise behind Table 8.8 can be summarised using Figure D.3 (similar to Figure 8.19a). This figure shows a study using a Silverson L4R batch mixer to compare the effect of initial d_{32} on the final d_{32} of silicone oil-in-water emulsions. This was achieved by creating coarse emulsions at U_T of 4.4 and 7.4 m s^{-1}, before processing at 8.9 m s^{-1} for 30 minutes.

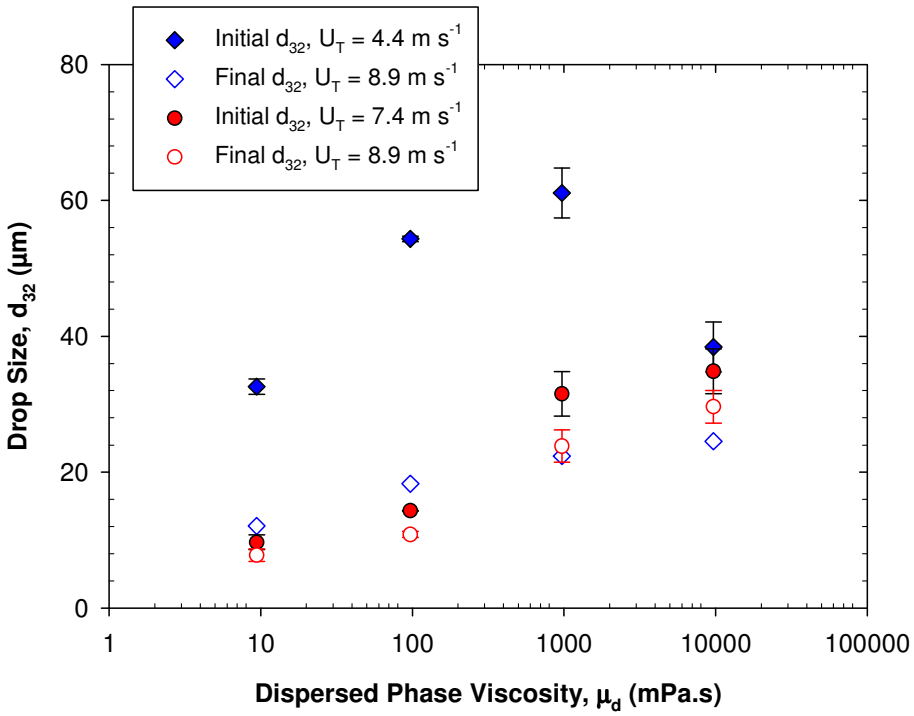

Figure D.3: Effect of dispersed phase viscosity and initial droplet size on final droplet size for 1% silicone oil emulsions dispersed using a batch Silverson L4R mixer with standard deviation error bars.

Figure D.3 shows that for lower μ_d oils, a larger initial drop size results in a larger final drop size, which corresponds to the greater dependence on τ_{IR} in Table 8.8. Thus, drop sizes of lower μ_d oils decrease more after a greater number of passes since $\tau_{IR}\ /t_{def}$ is high (Figure D.3). For higher μ_d oils the converse is true, a larger initial drop size forms a smaller drop size, since $\tau_{IR}\ /t_{def}$ is reduced.

REFERENCES

Adler-Nissen, J., Mason, S. L., and Jacobsen, C., (2004). "Apparatus for emulsion production in small scale and under controlled shear conditions", *Food and Bioproducts Processing*, **82(C4)**, 311-319.

ANSYS Inc., (2009). "*Population balance module manual*", ANSYS Fluent 12.0.

Arai, K., Konno, M., Matunaga, Y., and Saito, S., (1977). "Effect of dispersed-phase viscosity on the maximum stable drop size for breakup in turbulent flow", *Journal of Chemical Engineering of Japan*, **10**, 325-330.

Ascanio, G., Castro, B., and Galindo, E., (2004). "Measurement of power consumption in stirred vessels – A review", *Chemical Engineering Research and Design*, **82(A9)**, 1282-1290.

Atiemo-Obeng, V. A., and Calabrese, R. V., (2004). "Rotor-stator mixing devices", in *Handbook of Industrial Mixing: Science and Practice*, Paul, E. L., Atiemo-Obeng, V. A., and Kresta, S. M., (Eds.), John Wiley & Sons, Inc., Hoboken, New Jersey, USA, pp. 479-505.

Averbukh, Yu. N., Nikoforov, A. O., Kostin, N. M., and Korshakov, A. V., (1988). "Computation of dispersion for emulsions formed in a rotor-stator unit*", Journal of Applied Chemistry of the USSR*, **61(2)**, 396-397.

Bai, G., Wang, Y., and Armenante, P. M., (2011). "Velocity profiles and shear strain rate variability in the USP dissolution testing apparatus 2 at different impeller agitation speeds", *International Journal of Pharmaceutics*, **403**, 1-14.

Baker, M. R., (1993). "Droplet breakup using in-line mixers located in recirculation loops around batch vessels", *Chemical Engineering Science*, **48(22)**, 3829-3833.

Baker, M. R., (1996). "The use of in-line mixers located in recirculation loops around batch vessels to intensify droplet breakup processes", in *Advances in Engineering Fluid Mechanics: Mixed-flow hydrodynamics*, Cheremisinoff, N. P. (Ed.), Gulf Publishing Company, Houston, USA.

Bakker, A., (2006). "Reacting flows – Lecture 7", in "*Modeling Flow Fields in Stirred Tanks*", available from: http://www.bakker.org/dartmouth06/engs199/ (accessed on 01/09/12).

Baldyga, J., and Podgorska, W., (1998). "Drop break-up in intermittent turbulence: Maximum stable and transient sizes of drops", *The Canadian Journal of Chemical Engineering*, **76(3)**, 456-470.

Baldyga, J., and Bourne, J. R., (1999). "*Turbulent mixing and chemical reactions*", John Wiley & Sons, New York, USA.

Baldyga, J., Bourne, J. R., Pacek, A. W., Amanullah, A., and Nienow, A. W., (2001). "Effects of agitation and scale-up on drop size in turbulent dispersions: Allowance for intermittency", *Chemical Engineering Science*, **56**, 3377-3385.

Baldyga, J., Kowalski, A., Cooke, M., and Jasinska, M., (2007a). "Investigations of micromixing in a rotor-stator mixer", *Chemical and Process Engineering*, **28**, 867-877.

Baldyga, J., Orciuch, W., Makowski, L., Malski-Brodzicki, M., and Malik, K., (2007b). "Break up of nano-particle clusters in high-shear devices", *Chemical Engineering and Processing*, **46**, 851-861.

Baldyga, J., Orciuch, W., Makowski, L., Malik, K., Ozcan-Taskin, G., Eagles, W., and Padron, G., (2008). "Dispersion of nanoparticle clusters in a rotor-stator mixer*", Industrial Engineering Chemical Research*, **47**, 3652-3663.

Baldyga, J., Jasinska, M., and Makowski, L., (2009). "CFD prediction of Silverson mixer performance", *WP1 Report*, Warsaw University of Technology, Poland.

Bapat, P. M., and Tavlarides, L. L., (1985). "Mass transfer in a liquid-liquid CFSTR", *AIChE Journal*, **31(4)**, 659-666.

Barailler, F., Heniche, M., and Tanguy, P. A., (2006). "CFD analysis of a rotor-stator mixer with viscous fluids", *Chemical Engineering Science*, **61**, 2888-2894.

Black, D. L., McQuay, M. Q., and Bonin, M. P., (1996). "Laser-based techniques for particle-size measurement: A review of sizing methods and their industrial applications", *Progress in Energy and Combustion Science*, **22(3)**, 267-306.

Bourne, J. R., and Garcia-Rosas, J., (1986). "Rotor-stator mixers for rapid micromixing", *Chemical Engineering Research and Design*, **64,** 11-17.

Bourne, J. R., and Studer, M., (1992). "Fast reactions in rotor-stator mixers of different size", *Chemical Engineering and Processing*, **31**, 285-296.

Brocart, B., Tanguy, P. A., Magnin, C., and Bousquet, J., (2002). "Design of in-line emulsification processes for water-in-oil emulsions", *Journal of Dispersion Science and Technology*, **23**, 45-53.

Brown, D. E., and Pitt, K., (1972). "Drop size distribution of stirred non-coalescing liquid-liquid system", *Chemical Engineering Science*, **27**, 577-583.

Burdin, F., Tsochatzidis, N. A., Guiraud, P., Wilhelm, A. M., and Delmas, H., (1999). "Characterisation of the acoustic cavitation cloud by two laser techniques", *Ultrasonics Sonochemistry*, **6**, 43-51.

Calabrese, R. V., Chang, T. P. K., and Dang, P. T., (1986). "Drop breakup in turbulent stirred-tank contactors Part I: Effect of dispersed-phase viscosity", *AIChE Journal*, **32(4)**, 657-666.

Calabrese, R. V., Francis, M. K., Mishra, V. P., and Phongikaroon, S., (2000). "Measurement and analysis of drop size in a batch rotor-stator mixer", in *Proceedings of the 10th European Conference on Mixing*, van den Akker, H. E. A., and Derksen, J. J., (Eds.), The Netherlands, July 2-5, 2000, Elsevier Science, Amsterdam, pp. 149-156.

Calabrese, R. V., Francis, M. K., Kevala, K. R., Mishra, V. P., Padron, G. P., and Phongikaroon, S., (2002). "Fluid dynamics and emulsification in high shear mixers*",* in *Proceedings of the 3rd World Congress on Emulsions*, Lyon, France.

Calabrese, R. V., and Padron, G. A., (2008). "Power draw in radial flow batch rotor-stator mixers", presented at the *Sixth International Symposium on Mixing in Industrial Process Industries-ISMIP VI*, Niagara on the Lake, Niagara Falls, Ontario, Canada, August 17-21, 2008.

Chen, H. T., and Middleman, S., (1967). "Drop size distribution in agitated liquid-liquid systems," *AIChE Journal*, **13(5)**, 989-995.

Colenbrander, G. W., (2000). "Experimental findings on the scale-up behaviour of the drop size distribution of liquid/liquid dispersions in stirred vessels," in *Proceedings of the 10th European Conference on Mixing*, van den Akker, H. E. A., and Derksen, J. J., (Eds.), Delft, The Netherlands, July 2-5, 2000, Elsevier Science, Amsterdam, pp. 173-180.

Cooke, M., (2005). "*Design of mechanically agitated contactors or reactors with 'attitude'*", PhD Thesis, The University of Manchester, UK.

Cooke, M., Naughton, J., and Kowalski, A. J., (2008). "A simple measurement method for determining the constants for the prediction of turbulent power in a Silverson MS 150/250 in-line rotor stator mixer", presented at the *Sixth International Symposium on Mixing in Industrial Process Industries- ISMIP VI*, Niagara on the Lake, Niagara Falls, Ontario, Canada, August 17-21, 2008.

Cooke, M., Rodgers, T. L., and Kowalski, A. J., (2012). "Power consumption characteristics of an in-line Silverson high shear mixer", *AIChE Journal*, **58(6)**, 1683-1692.

Coulaloglou, C. A., and Tavlarides, L. L., (1977). "Description of interaction processes in agitated liquid-liquid dispersions", *Chemical Engineering Science*, **32**, 1289-1297.

Davies, J. T., and Rideal, E. K., (1961). "*Interfacial phenomena*", Academic Press, New York, USA.

Davies, J. T., (1985). "Drop sizes of emulsions related to turbulent energy dissipation rates", *Chemical Engineering Science*, **40(5)**, 839-842.

Davies, J. T., (1987). "A physical interpretation of drop sizes in homogenizers and agitated tanks, including the dispersion of viscous oils", *Chemical Engineering Science*, **42(7)**, 1671-1676.

Deutsch, D., (1998). "How to select rotor-stator mixers: Laboratory testing is the key to fine-tuning a high-performance mixing system", *Chemical Engineering*, **105(8)**, 76-79.

Doucet, L., Ascanio, G., and Tanguy, P. A., (2005). "Hydrodynamics characterization of rotor-stator mixer with viscous fluids", *Chemical Engineering Research and Design*, **83(A10)**, 1186-1195.

Edwards, M. F., Baker, M. R., and Godfrey, J. C., (1997). "Mixing of liquids in stirred tanks", in *Mixing in the Process Industries*, 2nd Ed., Harnby, N., Edwards, M. F., Nienow, A. W., (Eds.), Butterworth Heinemann, Oxford, pp 137-158.

El-Hamouz, A., (2007). "Effect of surfactant concentration and operating temperature on the drop size distribution of silicon oil water dispersion". *Journal of Dispersion Science and Technology*, **28(5)**, 797-804.

El-Hamouz, A., Cooke, M., Kowalski A., and Sharratt, P., (2009). "Dispersion of silicone oil in water surfactant solution: Effect of impeller speed, oil viscosity and addition point on drop size distribution", *Chemical Engineering and Processing*, **48(2)**, 633-642.

Flanagan, M., (2008). "Principles of particle sizing by light scattering with reference to the Mastersizer X and 2000", Unilever R&D Port Sunlight, UK.

Fluent Inc., (2006). "*User's guide*", Fluent 6.3.

Fradette, L., Brocart, B., and Tanguy, P. A., (2007). "Comparison of mixing technologies for the production of concentrated emulsions", *Chemical Engineering Research and Design*, **85(A11)**, 1553-1560.

Francis, M. K., (1999). "*The development of a novel probe for the in situ measurement of particle size distributions, and application to the measurement of drop size in rotor-stator mixers*", PhD Thesis, University of Maryland, College Park, MD, USA.

Gelest, Inc., (2004). "*Silicone fluids: Stable, inert media*".

Gingras, J.-P., Tanguy, P. A., Mariotti, S., and Chaverot, P., (2005). "Effect of process parameters on bitumen emulsions", *Chemical Engineering and Processing*, **44(9)**, 979-986.

Goloub, T., and Pugh, R. J., (2003). "The role of the surfactant head group in the emulsification process: Single surfactant systems", *Journal of Colloid and Interface Science*, **257**, 337-343.

Grenville, R. K., Tilton, J. N., Simpson, T. A., Brown, D. A. R., Padron, G. A., and Etchells III, A. W., (2008). "Flow and shear in agitated vessel", presented at the *AIChE Annual Meeting*, November 16-21, Philadelphia, PA, USA.

Hanselmann, W., and Windhab, E., (1999). "Flow characteristics and modelling of foam generation in a continuous rotor/stator mixer", *Journal of Food Engineering*, **38**, 393-405.

Hemrajani, R. R., and Tatterson, G. B., (2004). "Mechanically stirred vessels", in *Handbook of Industrial Mixing: Science and Practice*, Paul, E. L., Atiemo-Obeng, V. A., and Kresta, S. M. (Eds.), John Wiley & Sons, Inc., Hoboken, New Jersey, USA, pp. 345-390.

Hinze, J. O., (1955). "Fundamentals of the hydrodynamic mechanism of splitting in dispersion processes", *AIChE Journal*, **1(3)**, 289-295.

IKA, (2012). Available from: http://www.ikausa.com (accessed on 01/09/12).

Jafari, S. M., Assadpoor, E., He, Y., and Bhandari, B., (2008). "Re-coalescence of emulsion droplets during high-energy emulsification", *Food Hydrocolloids*, **22**, 1191-1202.

Janssen, J. M. H., and Meijer, H. E. H., (1993). "Droplet breakup mechanisms: Stepwise equilibrium versus transient dispersion", *Journal of Rheology*, **37(4)**, 597-608.

Janssen, J. J. M., Boon, A., and Agterof, W. G. M., (1994a). "Droplet break-up in simple shear flow in the presence of emulsifiers", *Colloids and Surfaces A*, **91**, 141-148.

Janssen, J. J. M., Boon, A., and Agterof, W. G. M., (1994b). "Influence of dynamic interfacial properties on droplet break-up in simple shear flow", *AIChE Journal*, **40(12)**, 1929-1939.

Jaworski, Z., Pianko-Oprych, P., Marchisio, D. L., and Nienow, A. W., (2007). "CFD modelling of turbulent drop breakage in a Kenics static mixer and comparison with experimental data", *Chemical Engineering Research and Design*, **85(A5)**, 753-759.

Jaworski, Z., (2010). "On generalized rheological characteristics of carboxymethylcellulose solutions", *Chemical and Process Engineering*, **31**, 873-888.

John, V., Angelov, I., Oncul, A. A., and Thevenin, D., (2007). "Techniques for the reconstruction of a distribution from a finite number of its moments", *Chemical Engineering Science*, **62**, 2890-2904.

Kamiya, T., Kaminoyama, M., Nishi, K., and Misumi, R., (2010a). "Scale-up factor for mean drop diameter in batch rotor-stator mixers", *Journal of Chemical Engineering of Japan*, **43(4)**, 326-332.

Kamiya, T., Sasaki, H., Toyama, Y., Hanyu, K., Kaminoyama, M., Nishi, K., and Misumi, R., (2010b). "Evaluation method of homogenization effect for different stator configurations of

internally circulated batch rotor-stator mixers", *Journal of Chemical Engineering of Japan*, **43(4)**, 355-362.

Kamiya, T., Sugawara, T., Sasaki, H., Tomita, T., Kaminoyama, M., Nishi, K., and Misumi, R., (2010c). "Scale-up factor for mean drop diameter in batch rotor–stator mixers with internal circulation", *Journal of Chemical Engineering of Japan*, **43(9)**, 737-744.

Karbstein, H., and Schubert, H., (1995). "Developments in the continuous mechanical production of oil-in-water macro-emulsions", *Chemical Engineering and Processing*, **34**, 205-211.

Kevala, K. R., Kiger, K. T., and Calabrese, R. V., (2005). "Single pass drop size distributions in an inline rotor-stator mixer", presented at the *APS Division of Fluid Dynamics 58th Annual Meeting (DFD05)*, Chicago, IL, USA, Paper No. GB.00004.

Khopkar, A. R., Fradette, L., and Tanguy, P. A., (2007). "Hydrodynamics of a dual shaft mixer with Newtonian and non-Newtonian fluids", *Chemical Engineering Research and Design*, **85(A6)**, 863-871.

Khopkar, A. R., Fradette, L., and Tanguy, P. A., (2009). "Emulsification capability of a dual shaft mixer", *Chemical Engineering Research and Design*, **87**, 1631-1639.

King, R. L., Hiller, R. A., and Tatterson, G. B., (1988). "Power consumption in a mixer", *AIChE Journal*, **34(3)**, 506-509.

Klausen Trading Company, (2012). Available from: http://www.klausen.net.au (accessed on 01/09/12).

Koglin, B., Pawlowski, J., and Schnoring, H., (1981). "Kontinuierliches emulgieren mit rotor/stator-maschinen: Einfluss der volumenbezogenen dispergierleistung und der verweilzeit auf die emulsionsfeinheit", *Chemie Ingenieur Technik*, **53(8)**, 641-647.

Kolmogorov, A. N., (1949). "The breakup of droplets in a turbulent stream", *Dokaldy Akademii Nauk Uzbekskoi SSR*, **66**, 825-828

Koshy, A., Das, T. R., and Kumar, R., (1988). "Effect of surfactants on drop breakage in turbulent liquid dispersions", *Chemical Engineering Science*, **43(3)**, 649-654.

Kowalski, A. J., (2009). “An expression for the power consumption of in-line rotor-stator devices”, *Chemical Engineering and Processing*, **48**, 581-585.

Kroezen, A. B. J., Groot Wassink, J., and Bertlein, E., (1988). “Foam generation in a rotor-stator mixer”, *Chemical Engineering and Processing*, **24**, 145-156.

Leng, D. E., and Calabrese, R. V., (2004). “Immiscible liquid-liquid systems,” in *Handbook of Industrial Mixing: Science and Practice,* Paul, E. L., Atiemo-Obeng, V. A. and Kresta, S. M., (Eds.), John Wiley & Sons, Inc., Hoboken, New Jersey, USA, pp. 639-753.

Levich, V. G., (1962). “*Physicochemical hydrodynamics*”, Prentice Hall, Englewood Cliffs, New Jersey, USA.

Liao, Y., and Lucas, D., (2009). “A literature review of theoretical models for drop and bubble breakup in turbulent dispersions”, *Chemical Engineering Science*, **64**, 3389-3406

Liao, Y., and Lucas, D., (2010). “A literature review on mechanisms and models for the coalescence process of fluid particles”, *Chemical Engineering Science*, **65**, 2851-2864

Lucassen-Reynders, E. H., and Kuijpers, K. A., (1992). “The role of interfacial properties in emulsification”, *Colloids and Surfaces*, **65**, 175-184.

Ludwig, A., Flechtner, U., Pruss, J., and Warnecke, H-J., (1997). “Formation of emulsions in a screw loop reactor”, *Chemical Engineering Technology*, **20**, 149-161.

Ma, Z., Merkus, H. G., de Smet, J. G. A. E., Heffels, C., and Scarlett, B., (2000). “New developments in particle characterization by laser diffraction: size and shape”, *Powder Technology*, **111**, 66-78.

Maa, Y-F., and Hsu, C., (1996). “Liquid-liquid emulsification by rotor/stator homogenization”, *Journal of Controlled Release*, **38**, 219-228.

Maass, S., and Kraume, M., (2012). “Investigation of discrete population balance models and its parameters for turbulent emulsification processes,” in *Proceedings of the 14th European Conference on Mixing*, Baldyga, J., (Ed.), Warsaw, Poland, September 10-13, 2012, Warsaw University of Technology, Warsaw, pp. 251-256.

Marchisio, D. L., Vigil, R. D., and Fox, R. O., (2003). "Quadrature method of moments for aggregation-breakage processes", *Journal of Colloid and Interface Science*, **258**, 322-334.

Marden Marshall, E., and Bakker, A., (2004). "Computational fluid mixing" in *Handbook of Industrial Mixing: Science and Practice,* Paul, E. L., Atiemo-Obeng, V. A. and Kresta, S. M., (Eds.), John Wiley & Sons, Inc., Hoboken, New Jersey, USA, pp. 257-343.

Masmoudi, H., Le Dreau, Y., Piccerelle, P., and Kister, J., (2005). "The evaluation of cosmetic and pharmaceutical emulsions aging process using classical techniques and a new method: FTIR", *International Journal of Pharmaceutics*, **289**, 117-131.

McClements, D. J., (2005). "*Food Emulsions: Principles, Practices, and Techniques*", CRC Press, Boca Raton, USA.

Metzner, A. B., and Otto, R. E., (1957). "Agitation of non-Newtonian fluids", *AIChE Journal*, **3(1)**, 3-10.

Middleton, J. C., (Ed.), (1984). "*ICI agitation and mixing manual*", ICI.

Mortensen, H. H., Calabrese, R. V., Innings, F., and Rosendahl, L., (2011). "Characteristics of batch rotor-stator mixer performance elucidated by shaft torque and angle resolved PIV measurements", *The Canadian Journal of Chemical Engineering*, **89(5)**, 1076-1095.

Muller-Fischer, N., Suppiger, D., and Windhab, E. J., (2007). "Impact of static pressure and volumetric energy input on the microstructure of food foam whipped in a rotor-stator device", *Journal of Food Engineering*, **80**, 306-316.

Myers, K. J., Reeder, M. F., Ryan, D., and Daly, G., (1999). "Get a fix on high-shear mixing", *Chemical Engineering Progress*, **95**, 33-42.

Myers, K. J., Reeder, M. F., and Ryan, D., (2001). "Power draw of a high-shear homogenizer", *The Canadian Journal of Chemical Engineering*, **79**, 94-99.

Noro, S., (1978). "Studies on liquid-liquid dispersion by mechanical agitation", *Progress in Organic Coatings*, **6**, 271-314.

Okufi, S., Perez de Ortiz, E. S., and Sawistowski, H., (1990). "Scale-up of liquid-liquid dispersions in stirred tanks", *The Canadian Journal of Chemical Engineering*, **68**, 400-406.

Orr, C., (1983). "Emulsion droplet size data", in *Encyclopedia of Emulsion Technology, Volume 1*, Becher, P., (Ed.), Marcel Dekker, New York, USA.

Ozcan-Taskin, G., Kubicki, D., and Padron, G., (2011). "Power and flow characteristics of three rotor-stator heads", *The Canadian Journal of Chemical Engineering*, **89(5)**, 1005-1017.

Pacek, A. W., Moore, I. P. T., Nienow, A. W., and Calabrese, R. V., (1994). "Video technique for measuring dynamics of liquid-liquid dispersion during phase inversion", *AIChE Journal*, **40(12)**, 1940-1949.

Pacek, A. W., and Nienow, A. W., (1995). "Measurement of drop size distribution in concentrated liquid-liquid dispersions: Video and capillary techniques", *Trans IChemE*, **73(A)**, 512-518.

Pacek, A. W., Man, C. C., and Nienow, A. W., (1998). "On the Sauter mean diameter and size distributions in turbulent liquid/liquid dispersions in a stirred vessel", *Chemical Engineering Science*, **53(11)**, 2005-2011.

Pacek, A. W., Chamsart, S., Nienow, A. W., and Bakker, A., (1999). "The influence of impeller type on mean drop size and drop size distribution in an agitated vessel", *Chemical Engineering Science*, **54**, 4211-4222.

Pacek, A. W., Ding, P., and Utomo, A. T., (2007). "Effect of energy density, pH and temperature on de-aggregation in nano-particles/water suspensions in high shear mixer", *Powder Technology*, **173**, 203-210.

Padron, G. A., (2001). "*Measurement and comparison of power draw in batch rotor-stator mixers*", MSc Thesis, University of Maryland, College Park, MD, USA.

Padron, G. A., (2005). "*Effect of surfactants on drop size distribution in a batch rotor-stator mixer*", PhD Thesis, University of Maryland, College Park, MD, USA.

Pedrocchi, L., and Widmer, F., (1988). "Formation of emulsions in a turbulent shearfield", presented at the *6th European Conference on Mixing*, Pavia, Italy, 24-26 May, 205-212.

Phongikaroon, S., (2001). "*Drop size distribution for liquid-liquid dispersions produced by rotor-stator mixers*", PhD Thesis, University of Maryland, College Park, MD, USA.

Puel, F., Briancon, S., and Fessi, H., (2006). "Chapter 6: Industrial technologies and scale-up", in *Microencapsulation: Methods and Industrial Applications*, 2nd Ed., Benita, S., (Ed.), Drugs and the Pharmaceutical Sciences, Vol. 158, CRC Press Taylor & Francis Group, 149-182.

Raikar, N. B., Bhatia, S. R., Malone, M. F., and Henson, M. A., (2009). "Experimental studies and population balance equation models for breakage prediction of emulsion drop size distributions", *Chemical Engineering Science*, **64**, 2433-2447.

Ramkrishna, D., (2000). "*Population balances: Theory and applications to particulate systems in engineering*", Academic Press, San Diego, USA.

Rawle, A., (1993). "Basic principles of particle size analysis", *Technical Paper MRK034*, Malvern Instruments, Malvern, UK.

Ribeiro, M. M., Regueiras, P. F., Guimaraes, M. M. L., Madureira, C. M. N., and Cruz Pinto, J. J. C., (2011). "Optimization of breakage and coalescence model parameters in a steady-state batch agitated dispersion", *Industrial and Engineering Chemistry Research*, **50**, 2182-2191.

Rodgers, T. L., and Cooke, M., (2012). "Rotor-stator devices: The role of shear and the stator", *Chemical Engineering Research and Design*, **90(3)**, 323-327.

Rothman, D., (2009). "*Mixing for formulated products*", IChemE Formulated Product Engineering Subject Group.

Rothman, D., (2011). Private Communication.

Schramm, L. L., (2005). "*Emulsion, foams and suspensions: Fundamentals and applications*", Wiley-VCH, Verlag GmbH & Co., Weinheim, Germany.

Schubert, H., and Engel, R., (2004). "Product and formulation engineering of emulsions", C*hemical Engineering Research and Design*, **82(A9)**, 1137-1143.

Schultz, S., Wagner, G., Urban, K., and Ulrich, J., (2004). "High-pressure homogenization as a process for emulsion formation", *Chemical Engineering Technology*, **27(4)**, 361-368.

Seville, J. P. K., Tuzun, U., and Clift, R., (1997). "*Processing of particle solids*", Chapman and Hall, London, UK.

Shaw, D. J., (2003). "*Introduction to colloid and surface chemistry*", 4th Ed., Butterworth Heinemann, Oxford, UK.

Shinnar, R., and Church, J. M., (1960). "Statistical theories of turbulence in: predicting particle size in agitated dispersions", *Industrial and Engineering Chemistry*, **52**, 253-256.

Shinnar, R., (1961). "On the behaviour of liquid dispersions in mixing vessels", *Journal of Fluid Mechanics,* **10**, 259-275.

Silverson, (2012). Available from: http://www.silverson.com (accessed on 01/09/12).

Sparks, T., (1996). "*Fluid mixing in rotor-stator mixers*", PhD Thesis, Cranfield University, UK.

Sprow, F. B., (1967). "Distribution of drop sizes produced in turbulent liquid-liquid dispersion", *Chemical Engineering Science*, **22**, 435-442.

Summets, A. M., (1966). "Continuous reactor-mixer for liquid media", *Khimicheskoei Neftyanoe Mashinostroenie*, **10**.

Szalai, E. S., Alvarez, M. M., and Muzzio, F. J., (2004). "Laminar mixing: A dynamical systems approach," in *Handbook of Industrial Mixing: Science and Practice,* Paul, E. L., Atiemo-Obeng, V. A. and Kresta, S. M., (Eds.), John Wiley & Sons, Inc., Hoboken, New Jersey, USA, pp. 89-143.

Thapar, N., (2004). "*Liquid-liquid dispersions from in-line rotor-stator mixers*". PhD Thesis, Cranfield University, UK.

Triton, S., (1982), "*Physical fluid mechanics*", CUP.

Uhl, V. W., and Gray, J. B., (1966). "*Mixing: Theory and practice*", Academic Press Inc., London, UK.

Urban, K., Wagner, G., Schaffner, D., Roglin, D., and Ulrich, J., (2006). "Rotor-stator and disc systems for emulsification processes", *Chemical Engineering Technology*, **29**, 24-31.

Utomo, A. T., Baker, M., and Pacek, A. W., (2008). "Flow pattern, periodicity and energy dissipation in a batch rotor-stator mixer", *Chemical Engineering Research and Design*, **86**, 1397-1409.

Utomo, A., Baker, M., and Pacek, A. W., (2009). "The effect of stator geometry on the flow pattern and energy dissipation rate in a rotor-stator mixer", *Chemical Engineering Research and*

Design, **87**, 533-542.

Utomo, A. T., (2009). "*Flow patterns and energy dissipation rates in batch rotor-stator mixers*", PhD Thesis, University of Birmingham, UK.

Vankova, N., Tcholakova, S., Denkov, N. D., Ivanov, I. B., Vulchev, V. D., and Danner, T., (2007). "Emulsification in turbulent flow: 1. Mean and maximum drop diameters in inertial and viscous regimes", *Journal of Colloid and Interface Science*, **312**, 363-380.

Vanoni, V. A., (2006). "*Sedimentation engineering*", American Society of Civil Engineers, Reston, Virginia, USA.

Walstra, P., (1983). "Formation of emulsions", in *Encyclopedia of Emulsion Technology, Volume 1*, Becher, P., (Ed.), Marcel Dekker, New York, USA.

Walstra, P., and Smulders, P. E. A., (1998). "Emulsion formation", in *Modern Aspects of Emulsion Science*, Binks, B. P., (Ed.), The Royal Society of Chemistry, Cambridge, UK.

Walstra, P., (2005). "Emulsions", in *Fundamentals of Interface and Colloid Science*, Vol. 5, Lyklema, J., (Ed.), Academic Press, London, UK.

Wang, C. Y., and Calabrese, R. V., (1986). "Drop breakup in turbulent stirred-tank contactors: Part II: Relative influence of viscosity and interfacial tension", *AIChE Journal*, **32(4)**, 667-676.

Wu, J., Graham, L. J., and Mehidi, N. N., (2006). "Estimation of agitator flow shear rate", *AIChE Journal*, **52(7)**, 2323-2332.

Yang, X., and Matthews, M. A., (2000). "Diffusion coefficients of three organic solutes in aqueous sodium dodecyl sulfate solutions", *Journal of Colloid and Interface Science*, **229**, 53-61.

Yang, M., (2011). "*CFD simulations for scale up of wet milling in high shear mixers*", PhD Thesis, University of Maryland, College Park, MD, USA.

Yuan, Q., Williams, R. A., and Biggs, S., (2009). "Surfactant selection for accurate size control of microcapsules using membrane emulsification", *Colloids and Surfaces A: Physiochemical and Engineering Aspects*, **347**, 97-103.

Zaidi, S. H., Altunbas, A., and Azzopardi, B. J., (1998). “A comparative study of phase Doppler and laser diffraction techniques to investigate drop sizes in annular two-phase flow”, *Chemical Engineering Journal*, **71**, 135-143.

Zhang, J., Xu, S., and Li, W., (2012). “High shear mixers: A review of typical applications and studies on power draw, flow pattern, energy dissipation and transfer properties”, *Chemical Engineering and Processing*, **57-58**, 25-41.

Zhou, G., and Kresta, S. M., (1998). “Evolution of drop size distribution in liquid-liquid dispersions for various impellers”, *Chemical Engineering Science*, **53(11)**, 2099-2113.